

Design and Benchmarking of a Combustor Simulator Relevant to Gas Turbine Engines

Michael Barringer

Thesis submitted to the Faculty of the
Virginia Polytechnic Institute and State University
in partial fulfillment of the requirements for the degree of

Master of Science
in
Mechanical Engineering

Dr. Karen Thole, Chair
Dr. Wing Ng
Dr. Thomas Diller

September 20, 2001
Blacksburg, Virginia

Keywords: Combustion Chamber, Gas Turbines

© 2001, Michael Barringer

Design and Benchmarking of a Combustor Simulator Relevant to Gas Turbine Engines

Michael Barringer

(ABSTRACT)

An experimental facility was designed and benchmarked that could simulate the non-uniformities in the flow and thermal fields exiting real gas-turbine combustors. The design of the combustor simulator required analyses of the flow paths within a real combustor in a gas turbine engine. Modifications were made to an existing wind tunnel facility to allow for the installation of the combustor simulator. The overall performance of the simulator was then benchmarked through measurements of velocity, pressure, temperature, and turbulence using a straight exit test section to provide a baseline set of data. Comparisons of the measured quantities were made between two test cases that included a flow field with and without dilution flow.

One of the major findings from this study was that the total pressure profiles exiting the combustor simulator in the near-wall region were different from a turbulent boundary layer. This is significant since many studies consider a turbulent boundary layer as the inlet condition to the turbine. Turbulent integral length scales were found to scale well with the dilution hole diameters and no dominant frequencies were observed in the streamwise velocity energy spectra. Dilution flow resulted in an increase in turbulence levels and mixing causing a reduction in the variation of total pressure and velocity. Adiabatic effectiveness levels were significantly reduced for the case with dilution flow in both the near combustor exit region and along the axial length of the straight exit test section.

Acknowledgements

This research work was conducted with the help of several people of whom are acknowledged here. First and foremost, I would like to greatly thank Dr. Karen Thole for her guidance and direction in helping me to conduct and complete this work. I would like to thank United Technologies and Pratt & Whitney for sponsoring this research. I would also like to thank several other graduate students that have worked with me in the VT ExCCL research group including: Andrew Lethander, Andrew Lyman, Roger Radomsky, Sarah Stitzel, Joe Walter, and Owen Richard. Finally, I would like to thank my family for their support and understanding while I conducted this work.

Table of Contents

Abstract.....	i
Acknowledgements.....	ii
Nomenclature.....	v
List of Tables.....	ix
List of Figures.....	x
1. Introduction.....	1
2. Literature Review.....	6
2.1 Combustor Simulator Model Studies.....	7
2.2 Effects of Combustor Flowfields on Turbine Performance.....	18
2.3 Summary of Past Literature.....	20
3. Design of the Combustor Simulator and Instrumentation.....	38
3.1 Description of Engine Combustor.....	38
3.2 Overall Design of the Combustor Simulator.....	43
3.3 Primary Flow Path in the Combustor Simulator.....	47
3.4 Secondary Flow Path in the Combustor Simulator.....	49
3.5 Test Section Downstream of the Combustor Simulator.....	50
3.6 Instrumentation.....	51
3.7 Uncertainty Analysis.....	60
4. Benchmarking of the Combustor Simulator.....	78
4.1 Primary Flow Benchmarking.....	78
4.2 Liner Flow Benchmarking.....	80
4.3 Dilution Flow Benchmarking.....	83
4.4 Combustor Exit Flow Conditions.....	85

5. Flow and Thermal Field Measurements at the Combustor Simulator Exit.....	98
5.1 Flow Field Measurements.....	98
5.2 Thermal Field Measurements.....	106
5.3 Endwall Adiabatic Effectiveness Measurements.....	109
6. Conclusions and Future Work.....	127
6.1 Facility Benchmarking.....	127
6.2 Combustor Exit Profiles.....	128
6.3 Recommendations for Future Work.....	130
References.....	132
Appendix A.....	139
Appendix B.....	158
Appendix C.....	160
Appendix D.....	166
Appendix E.....	167
Vita.....	171

Nomenclature

ALP	=	air loading parameter, $ALP = \frac{P_0^{1.75} \cdot A_{ref} \cdot D_{ref}^{0.75} \cdot e^{\frac{T}{300}}}{\dot{m}}$
A_{ref}	=	reference area
C	=	chord of stator vane in engine turbine
C_d	=	discharge coefficient, $C_d = \frac{\dot{m}_{actual}}{\dot{m}_{theoretical}}$
D	=	diameter of film cooling holes
D_1	=	dilution hole diameter (row 1)
D_2	=	dilution hole diameter (row 2)
D_{ref}	=	reference diameter
$E_{11}(f)$	=	turbulent kinetic energy associated with the frequencies of the streamwise velocity fluctuations, $E_{11}(f) = \frac{ FFT(u') ^2}{\Delta f_s}$
f	=	frequency
f_{resp}	=	frequency response, $f_{resp} = \frac{1}{\tau_s}$
f_s	=	sampling frequency
f_{Nyq}	=	Nyquist frequency, $f_{Nyq} = \frac{f_s}{2}$
h	=	exit slot height
H_{inlet}	=	mainstream inlet height of combustor simulator
H	=	total exit height of combustor simulator

- I = momentum flux ratio, $I = \frac{\rho_{jet} V_{jet}^2}{\rho_{\infty} V_{\infty}^2}$
- K = acceleration parameter, $K = \frac{v}{V_{\infty}^2} \frac{\partial V_{\infty}}{\partial x}$
- K_L = loss coefficient
- L = combustor length
- M = mass flux ratio, $M = \frac{\rho_{jet} V_{jet}}{\rho_{\infty} V_{\infty}}$
- \dot{m} = mass flow rate, $\dot{m} = \rho VA$
- Ma = Mach number, $Ma = \frac{V}{\sqrt{\gamma RT}}$
- N = number of film-cooling holes, $N = \frac{\dot{m}_{panel}}{\rho_{jet} V_{jet} A_{jet}}$
- N_s = number of data samples
- P = static pressure
- P_o = total pressure
- $P_{o_{ms-ave}}$ = average total pressure at mid-span
- P_{loss} = pressure drop across perforated plate, $P_{loss} = K_L \frac{1}{2} \rho V^2$
- R = gas constant
- Re = Reynolds number based on vane chord length, $Re = \frac{\rho VC}{\mu}$
- $R_{u'}(\tau)$ = autocorrelation of u' , $R_{u'}(\tau) = \frac{\overline{u'(t) \cdot u'(t + \tau)}}{\left(u'_{rms}\right)^2}$
- S_s = film-cooling hole spacing parameter

S_p	=	film-cooling hole spacing parameter
t	=	time
T	=	static temperature
T_0	=	total temperature
T_{aw}	=	adiabatic wall temperature
T_c	=	coolant temperature
T_∞	=	mass averaged freestream temperature
Tu	=	turbulence intensity, $Tu = \frac{u_{rms}}{U}$
u	=	local streamwise velocity
U	=	average streamwise velocity
U_∞	=	average streamwise freestream velocity
u_{rms}	=	root-mean-square of local streamwise velocity
u'	=	streamwise velocity fluctuation, $u' = u - U$
Vol	=	combustion chamber volume
W	=	one vane pitch
x,y,z	=	local coordinate system
X,Y,Z	=	global coordinate system

Greek

α	=	contraction angle
Δf_s	=	frequency bandwidth, $\Delta f_s = \frac{f_s}{N_s}$

ΔP	=	normalized total pressure, $\Delta P = \frac{P_o - P_{o_{ms-ave}}}{0.5 \rho U_{ave}^2}$
ε	=	emmissivity
η	=	adiabatic effectiveness level, $\eta = \frac{T_\infty - T_{aw}}{T_\infty - T_c}$
η_θ	=	loading parameter, $\eta_\theta = \frac{\dot{m}}{Vol \cdot P_0^{1.8} \cdot 10^{0.00145(T-400)}}$
φ	=	flow parameter, $\varphi = \frac{\dot{m} \sqrt{T_0}}{P_0}$
γ	=	specific heat ratio
Λ_x	=	integral length scale, $\Lambda_x = U \cdot T$
κ_l	=	wave number, $\kappa_l = \frac{2\pi f}{U}$
κ_E	=	$\frac{0.75}{\Lambda_x}$
μ	=	dynamic viscosity
ρ	=	density
τ	=	time lag
τ_s	=	time constant
T	=	integral time scale, $T = \int_{\tau=0}^{\tau=\infty} R(\tau) d\tau$
θ	=	temperature difference ratio, $\theta = \frac{T_{ave} - T}{T_{ave} - T_c}$
ν	=	kinematic viscosity

List of Tables

Table 3-1	Distribution of Mass Flow in the Engine Combustor	62
Table 3-2	Engine Data at Combustor Exit.....	62
Table 3-3	Flow Field Parameters in the Engine Combustor (Inner Diameter Liner).....	62
Table 3-4	Flow Field Parameters in the Engine Combustor (Outer Diameter Liner).....	63
Table 3-5	Total Film-Cooling Hole Area (per sector) in the Engine Combustor.....	63
Table 3-6	Summary of Flow Field Conditions Used to Design the Combustor Simulator.....	63
Table 3-7	Summary of the Combustor Simulator Geometry.....	64
Table 3-8	Liner Panel and Dilution Hole Geometry in the Combustor Simulator.....	64
Table 3-9	Total Mass Flow Rate and Mass Averaged Freestream Velocity at the Trailing Edge of Each Liner Panel.....	64
Table 3-10	Plenum Pressure Drops and Mass Flow Rates in the Combustor Simulator....	65
Table 3-11	Uncertainties in the Flow and Thermal Field Measurements.....	65
Table 4-1	Summary of the Flow Field Conditions for the Two Flow Cases.....	88

List of Figures

Figure 1-1	Schematic of a simple gas-turbine engine cycle.	4
Figure 1-2	Schematic of the Pratt & Whitney F-119 turbofan engine.	4
Figure 1-3	Picture of the Lockheed F-22A Raptor.	5
Figure 2-1	Schematic of an annular combustion chamber.	21
Figure 2-2	Schematic of a cannular combustion chamber.	21
Figure 2-3	Schematic of a typical mass flow distribution in a gas-turbine engine combustor.	22
Figure 2-4	Schematics of combustor liner cooling techniques.	22
Figure 2-5	Schematic of Koutmos and McGuirk (1989) combustor model.	23
Figure 2-6	Schematic of Stevens and Carrotte (1990) combustor model.	23
Figure 2-7	Graph indicating results of Stevens and Carrotte (1990) experimental results.	24
Figure 2-8	Schematic of Liou and Wu (1992) combustor model.	24
Figure 2-9	Schematics of Holdeman (1993) combustor model and orifice configurations.	25
Figure 2-10	Schematic of Anacleto et al. (1996) combustor models.	26
Figure 2-11	Schematic of Doerr et al. (1997) combustor model.	27
Figure 2-12	Schematic of Ahmed (1998) combustor models.	27
Figure 2-13	Schematic of Gritsch et al. (1998) combustor model.	28
Figure 2-14	Schematic of measurement plane and graphs indicating results of Gritsch et al.(1998) experiments.	29
Figure 2-15	Schematic of Blomeyer et al.(1999) combustor model.	30
Figure 2-16	Schematic of the non-uniform temperature profile from Halls (1970).	30
Figure 2-17	Schematic of Bicen et al. (1988) combustor models.	31

Figure 2-18	Graphs indicating results from Bicen et al. (1988) experimental work.	32
Figure 2-19	Graphs indicating results from Bicen et al. (1988) experimental work.	33
Figure 2-20	Schematic of Cameron et al. (1989) combustor models.	33
Figure 2-21	Schematic of Richards and Samuelsen (1992) combustor models.	34
Figure 2-22	Schematic of Goebel et al. (1993) combustor model.	34
Figure 2-23	Schematic of Crocker et al. (1994) combustor model.	35
Figure 2-24	Graphs indicating results from Crocker et al. (1994) experiments.	35
Figure 2-25	Schematic of Gulati et al. (1995) combustor model.	36
Figure 2-26	Schematic of Krishnamoorthy et al. (1988) experimental setup.	36
Figure 2-27	Schematic of Burd and Simon (2000) experimental setup.	37
Figure 3-1	Schematic shows a plan view of the existing wind tunnel facility with its scaled-up (9x) turbine vane cascade.	66
Figure 3-2	Schematic shows a cross-sectional view of a Pratt & Whitney annular. combustor geometry.	66
Figure 3-3	Schematic of the engine combustor indicating the axial locations used to perform flow calculations.	67
Figure 3-4	Graph indicating the axial Mach number distribution and the acceleration of the mainstream flow in the engine combustor.	67
Figure 3-5	Schematics showing portions of an arbitrary liner panel indicating film- cooling hole pattern.	68
Figure 3-6	Schematic showing the general shape of the combustor simulator.	68
Figure 3-7	Schematic indicating the flat liner panels and straight exit section.	69
Figure 3-8	Schematic indicating design concept modifications to the existing facility. ...	69

Figure 3-9	Graph showing a comparison of the acceleration in the engine combustor and the combustor simulator.	70
Figure 3-10	Schematic indicating the dilution hole pattern relative to the down stream vanes.	70
Figure 3-11	Schematic indicating the primary flow path arrangement.	71
Figure 3-12	Schematic of the perforated plate design with the final hole pattern.	71
Figure 3-13	Schematic indicating the secondary flow path arrangement.	72
Figure 3-14	Schematic of the combustor simulator illustrating the components within the secondary path supply chamber.	72
Figure 3-15	Schematic indicating the details of the exit slot region (Stitzel, 2001).	73
Figure 3-16	Schematic of the straight test section downstream of the combustor simulator.	73
Figure 3-17	Schematic of the Plexiglas cover indicating the locations of the infrared camera ports.	74
Figure 3-18	Schematic of a thermocouple embedded in a portion of the flat foam endwall.	74
Figure 3-19	Schematic showing an enlarged view of the head of a Keil Probe.	75
Figure 3-20	Schematic of the thermocouple rake.	75
Figure 3-21	Graph of a typical hot-wire calibration curve.	76
Figure 3-22	Graph showing a typical autocorrelation curve for a turbulence level of 15 %.	76
Figure 3-23	Schematic of the traverse system.	77
Figure 4-1	Schematic indicating the location of the measurement plane for	

benchmarking the primary path of the combustor simulator.	89
Figure 4-2 Schematic of the initial primary path flow arrangement.	89
Figure 4-3 Graph of the velocity profiles at the combustor simulator inlet in both the pitch and span directions.	90
Figure 4-4 Graph of the pitch and span temperature profiles at the combustor simulator inlet.	90
Figure 4-5 Schematic of the discharge coefficient experiment setup.	91
Figure 4-6 Graph of the discharge coefficient data.	91
Figure 4-7 Graph of the vertical velocity profiles indicating uniform film-cooling conditions at the end of the first liner panel ($x/D = 7.7$ downstream of the last row of film-cooling holes).	92
Figure 4-8 Graph of the vertical turbulence profiles indicating uniform film-cooling conditions at the end of the first liner panel ($x/D = 7.7$ downstream of the last row of film-cooling holes).	92
Figure 4-9 Graph of velocity profiles taken across the diameters of the first row of dilution holes.	93
Figure 4-10 Graph of velocity profiles taken across the diameters of the second row dilution holes.	93
Figure 4-11 Schematic of the combustor simulator indicating the measurement locations used for the mass balance study.	94
Figure 4-12 Graph of the spanwise velocity profiles taken at combustor simulator exit (upstream of exit slot) indicating proper upstream mass flow rate conditions.	94
Figure 4-13 Graph of the pitchwise velocity profile taken at the combustor simulator	

exit (upstream of exit slot) indicating proper upstream mass flow rate conditions (data taken at $z / H = 0.0$).	95
Figure 4-14 Schematic showing the exit slot flow region and the measurement location.	95
Figure 4-15 Schematic of the exit slot region indicating the measurement locations.	96
Figure 4-16 Graph of the exit slot total pressure profile with a schematic of the upstream component orientation.	97
Figure 5-1 Schematic indicating the measurement Plane A located upstream of the exit slot.	112
Figure 5-2 Schematic indicating the measurement Plane B located downstream of exit slot.	112
Figure 5-3 Graph comparing pitchwise velocity profiles in Plane A at mid-span ($z / H = 0.5$) with and without dilution flow.	113
Figure 5-4 Graph comparing spanwise velocity profiles in Plane A at mid-pitch ($y / W = 0.0$) with and without dilution flow.	113
Figure 5-5 Contour plot showing normalized streamwise velocity with dilution flow in Plane A.	114
Figure 5-6 Contour plots of non-dimensional total pressure without dilution flow in (a) Plane A and (b) Plane B.	115
Figure 5-7 Contour plots of non-dimensional total pressure with dilution flow in (a) Plane A and (b) Plane B.	116
Figure 5-8 Comparison of non-dimensional total pressure contours with dilution flow in Plane A indicating the variation of pressure on (a) original scale and (b) refined scale.	117

Figure 5-9 Graph showing the spatially averaged non-dimensional total pressure profiles.	118
Figure 5-10 Graph showing a comparison of pitchwise turbulence intensity with and without dilution flow in Plane A ($z/H = 0.5$).	118
Figure 5-11 Graph showing a comparison of spanwise turbulence intensity for the cases with and without dilution flow in Plane A ($y/W = 0.0$).	119
Figure 5-12 Contour plot of the turbulence intensity with dilution flow in Plane A.	119
Figure 5-13 Graph showing the spatially averaged turbulence intensity profile with dilution flow in Plane A.	120
Figure 5-14 Plot of the integral length scales in Plane A ($z/H = 0.5$) with dilution flow.	120
Figure 5-15 Plot of the turbulent energy spectra at $y/W = 0.0$ and 0.5 in Plane A ($z/H = 0.5$) with dilution flow.	121
Figure 5-16 Contour plot of non-dimensional temperature without dilution flow in Plane B.	121
Figure 5-17 Contour plots of non-dimensional temperature with dilution flow in (a) Plane A and (b) Plane B.	122
Figure 5-18 Graph showing the spatially averaged non-dimensional temperature profiles.	123
Figure 5-19 Contours of adiabatic effectiveness levels in the near exit slot region for (a) without dilution flow and (b) with dilution flow.	124
Figure 5-20 Contours of adiabatic effectiveness levels downstream of the exit slot for the cases without dilution flow and (b) with dilution flow.	125

Figure 5-21 Graph showing adiabatic effectiveness levels downstream of the exit slot taken with thermocouples and the infrared camera for the cases with and without dilution flow (data taken at mid-pitch). 126

1. Introduction

Modern gas turbine engines are used for a variety of functions including electric power generation as well as jet propulsion. A simple gas turbine engine in an aircraft, shown in Figure 1-1, consists of a compressor, a combustor, a turbine, and an exit nozzle. Atmospheric air is drawn into the compressor where it is compressed to pressures that are typically 10 to 15 times higher than the inlet for power generation and 25 to 40 times higher than the inlet for aircraft engines. The air is then directed into a combustion chamber in which fuel is injected and combusted at nearly constant pressure thus significantly increasing the air temperature. The combustion rate in aircraft engines at sea level is on the order of $500,000 \text{ kJ/m}^3\text{s}$, which is more than 100 times as intense as the combustion in large, power-generation gas turbines (Hill and Peterson, 1992). The combustion products then expand through a turbine that produces work. A large percentage of the turbine work is used to drive the compressor and a small percentage is used to drive auxiliary engine devices. The high pressure, high temperature air exiting the turbine is then used to either produce electric power or to produce thrust.

After sixty years of development with considerable design modifications to improve overall efficiencies and increase the output power, today's gas turbine engines, for example the General Electric GE90-B4 and the Pratt & Whitney PW4084, are both capable of producing 387 kN of thrust during take-off (Mattingly, 1996). Burd et al. (2000) stated that the turbine inlet temperatures in current commercial aircraft engines are approaching 3000 °F. Modern gas turbine engines have also allowed aircraft to attain speeds exceeding 2000 miles per hour. These significant improvements, however, have also led to gas turbine engines becoming very expensive and very complex machines. The Pratt & Whitney F-119 turbofan engine, shown in Figure 1-2, can produce nearly 156 kN of thrust and costs on the order of six to eight million dollars. This engine has been successfully implemented into the Lockheed F-22A Raptor, an advanced tactical fighter plane, shown in Figure 1-3. The main manufacturers of current industrial gas turbines include ABB, General Electric, Siemens, and Westinghouse, all of whom design single shaft gas turbine engines that are capable of producing over 200 MW per unit (Cohen et al., 1996).

It is known within the gas turbine community that the turbine operating temperature is one of the most important factors that affects a gas turbine's work output. Increasing the gas temperature exiting the combustor, and thus entering the downstream turbine, leads to an overall increase in engine work output. As a result of the push for higher temperatures, the gas temperatures exiting combustors of today's gas turbines are well above the melting temperature of the metal alloy engine components. Durability and maintainability of the engine components are therefore primary concerns of gas turbine engine designers. Of particular interest are the nozzle guide vanes and endwall platform regions in the turbine. The nozzle guide vanes and endwall regions are subjected to very harsh and highly turbulent non-uniform thermal and flow fields. These non-uniformities significantly influence flow development and temperature potentials for the vane and endwall surfaces. Because of these extreme conditions, it is imperative to cool the vane and endwall surfaces to prolong engine component life.

The purpose of this investigation was to design and benchmark an experimental facility that could simulate the non-uniformities in the flow and thermal fields exiting real gas-turbine combustors. The intent of this facility is to understand how to best integrate the combustor and turbine. The design of the combustor simulator required analyzing the flow paths within a gas turbine combustor representative of a commercial engine. The design also required an extensive literature review to find experimental combustor models that have been previously used. Upon completion of the design, modifications were made to an existing wind tunnel facility to allow for the installation of such a simulator. The overall performance of the facility was then benchmarked through velocity, pressure, temperature, and turbulence measurements.

This research is considered to be unique in the sense that it analyzes the impact of combustor exit flows on turbine heat transfer. The flow and thermal fields in combustors and turbines have typically been studied independently from one another. This investigation served as an initial step to bring the two components together by studying the effects of the flow and thermal fields exiting a combustor simulator on downstream heat transfer using a straight exit

section to establish baseline results. Note that the majority of this research is also documented in Barringer et al. (2001).

The following chapter presents a discussion of the relevant studies that are present in the current literature in the areas of combustor flow models as well as combustor-turbine flowfield interactions in gas turbine engines. Chapter 3 discusses the design of the combustor flow field simulator including the facility design, instrumentation, and experimental uncertainties. Chapter 4 then discusses the benchmarking of the combustor simulator facility. The combustor simulator exit flow and thermal fields are then analyzed in Chapter 5. Finally, Chapter 6 discusses the conclusions from performing this work as well as recommendations for further studies.

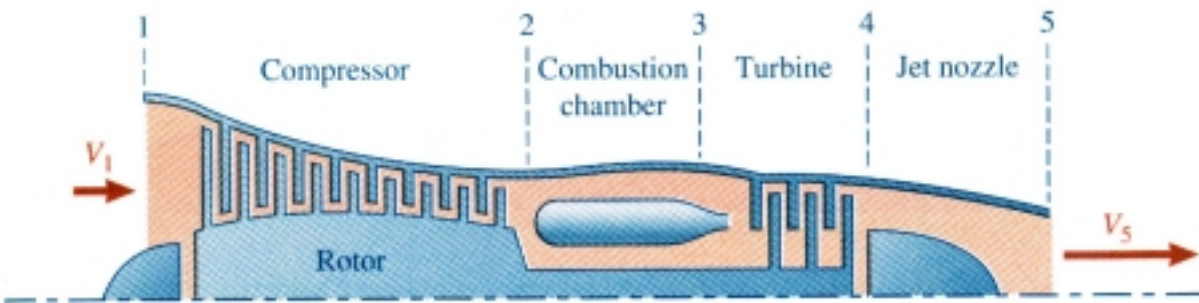


Figure 1-1 Schematic of a simple gas-turbine engine cycle (Jones and Dugan, 1996).



Figure 1-2 Schematic of the Pratt & Whitney F-119 turbofan engine.



Figure 1-3 Picture of the Lockheed F-22A Raptor.

2. Literature Review

The flow field conditions at the combustor exit in real gas turbine engines are highly non-uniform in temperature, pressure, and velocity. These non-uniformities are a function of the combustion chamber flow arrangement and geometry. Typical gas-turbine engine combustors have either an annular combustion chamber arrangement, shown in Figure 2-1, or a cannular (tubo-annular) combustion chamber arrangement, shown in Figure 2-2. The cannular combustion system contains individual flame tubes uniformly spaced around the annular casing. This arrangement is advantageous to industrial engines with centrifugal compressors in which the flow is divided into separate streams in the diffuser. Also, the development of the cannular combustion chamber can be performed on a single can using only a portion of the overall air and fuel flow (Cohen et al., 1996). The cannular combustor is undesirable, however, in aircraft applications due to weight, volume, and frontal area considerations. Instead, a more light weight and smaller sized annular combustion chamber is used which contains a flow area defined by an open annulus containing more evenly-spaced fuel-injection nozzles. One disadvantage of this flow arrangement is the difficulty in obtaining an even air-fuel distribution and thus an even outlet temperature distribution. Other disadvantages of the annular combustor type are that it is weaker structurally (the metal casing is more prone to buckling) and the development work has to be performed on a complete combustor. This requires a facility that can supply the full engine air flow.

The major features of these combustion chambers include the chamber liners, entrance swirlers, fuel nozzles, liner cooling slots and holes, as well as primary and secondary dilution holes. One major consideration in the designing of a combustor is the division of the inlet mass flow into separate flow paths. Figure 2-3 shows a typical mass flow distribution within an annular gas-turbine combustor. As can be seen from the figure, a large portion of the combustor inlet flow is used for cooling the metal casing and diluting the combustion products. Figure 2-4 shows several different techniques that are used to cool the combustion chamber walls. The

interaction of all of these combustor components results in a very complex flowfield exiting the combustor and entering the downstream turbine section.

Several experimental studies have been performed to analyze and model combustor flows. Very few of these studies, however, have focused on the effects of this flowfield on the downstream turbine blades and endwalls. The following section discusses relevant studies that are in the current literature that have used combustor simulator models. Following the discussion of the combustor simulator studies, studies focusing on the effects of combustor flow fields on turbine performance are discussed.

2.1 Combustor Simulator Model Studies

An extensive effort was made to find open literature studies using combustor models. This section gives descriptions of those studies including the combustor model geometries that were used, the types of measurements that were conducted, and the significant results and conclusions that were made from performing the research. The analysis of these research efforts that is presented below is separated into non-reacting flows and reacting flows. Appendix A contains a complete set of the combustor models that were found in the literature while this section of the thesis presents the highlights of some of these studies.

A non-reacting water channel model of a can-type combustor was studied by Koutmos and McGuirk (1989). The combustor simulator model is shown in Figure 2-5 and it consists of a swirl driven primary zone (velocities in the tangential direction), annularly fed dilution jets, and an exit contraction nozzle. Fifteen percent of the exit mass flow passed through the swirler, 33 percent flowed through the first row of dilution holes, and 52 percent flowed through the second row of dilution holes. They found that decreasing the swirler exit area resulted in a reduction in strength of the recirculation and turbulence associated with the primary zone due to the first row of dilution holes experiencing weak penetration into the mainstream. They also found that the flow mixed rapidly and efficiently throughout the first and second dilution hole zones, which led

to a reduction in the velocity and turbulence non-uniformities at the combustor exit. A 50 % reduction of turbulence was noted between the dilution region and the combustor exit.

Ames and Moffat (1990) studied the effects of high-intensity large-scale turbulence on boundary layer heat transfer by using a non-reacting, simulated, combustor flow field. The experimental combustor model contained slot film-cooling, two rows of in-line dilution holes ($d = 6.25$ cm), and a 2:1 exit contraction. The combustor simulator generated turbulence levels up to 19 % and integral length scales of 4 to 6 centimeters. The integral length scales scaled very well with the dilution hole diameters. They also reported that heat transfer was augmented by up to 26 % for a turbulent boundary layer over a flat plate with constant velocity.

Stevens and Carrotte (1990) also experimentally investigated the combustor dilution zone and jet development by focusing on the downstream thermal field in a non-reacting, annular combustor simulator. The experimental combustor model, shown in Figure 2-6, contained a row of 16 heated jets that were injected normally into a confined annular crossflow at a momentum flux ratio of 4. The momentum flux ratio is the ratio of momentum associated with the jet to that of the mainstream. The jet flow was heated to identify the trajectory of the core flow and the dispersal of the jet fluid. A complex flowfield in the rear of each dilution jet was observed as it exited into the crossflow. This flow field was found to vary in a random manner from one jet to another. The complexity of the flowfield at this location was highly dependent on the direction of the approach flow in the feed annulus and its deflection as it flowed through the dilution holes. The temperature distribution within this region was found to be distorted about each hole centerplane as a result of the complex flowfield into which the jet develops. These temperature distributions, shown in Figure 2-7, were taken two hole diameters downstream of the jet and they revealed that although each jet exhibited the characteristic kidney-shaped profile, a lack of symmetry of the distributions between the dilution jets was apparent. They also concluded that since this complex flowfield varied from one dilution hole to the next, each jet had its own mixing characteristics which in turn led to an overall non-uniform temperature distribution downstream. They believed their results to be representative of real, combustor-exit temperature non-uniformities.

Liou and Wu (1992) constructed a non-reacting combustor simulator, shown in Figure 2-8, with an isothermal flowfield that consisted of a rectangular duct with two opposing side inlets. One major finding from the study was that the turbulence was inhomogeneous and anisotropic throughout most regions of the combustor simulator.

Holdeman (1993) simulated a non-reacting gas turbine combustion chamber by conducting computations and experiments on the mixing of single, double, and opposed rows of dilution jets with an isothermal or variable temperature mainstream in a confined subsonic crossflow. The focus was on the three-dimensional flowfield in the dilution zone. The experimental combustor model is shown in Figure 2-9. The principle finding from the investigation was that the momentum flux ratio of the jets dictated the exit velocity and temperature profiles. The exit temperature distributions for single-sided injection were found to be very similar for both the single and double row jet injection cases and indicated only slightly better mixing for the double row case. The results from the cases involving opposed-rows of jets revealed that for in-line jets the two streams mixed very rapidly and that the effective mixing height was half the duct height for equal momentum flux ratios on both sides. For opposed-rows of staggered jets it was found that the optimum ratio of orifice spacing to duct height was double the value for single-sided injection at the same momentum flux ratio. The computational models, using the standard k- ϵ turbulence model, did not accurately predict the mixing of the dilution jets for the case with the opposed jet centerlines in-line but predicted very well the jet penetration by showing good agreement with the data.

Anacleto et al. (1996) studied the flow patterns typical of rich-burn, quick-quench, lean-burn (RQL) gas-turbine combustors by taking detailed velocity measurements of the flow in a non-reacting water model (1:1 scale) of a can-type combustor shown in Figure 2-10. The study consisted of a basic flow configuration with a series of geometrical modifications to determine the influence of several parameters on the overall performance of the combustor. These parameters included the swirl level in the rich zone, the geometry of the quench holes, and the momentum of the inflowing jets. One of the major findings from this study was that the

impingement of the opposed jets in the center of the combustor greatly enhanced turbulent production giving rise to large velocity fluctuations. These results are in agreement with those stated earlier from Holdeman.

Doerr et al. (1997) conducted a simulation of the rich-burn, quick-quench, lean-burn (RQL) combustion concept by experimentally investigating a non-reacting multiple jet configuration with a confined crossflow. Jets were perpendicularly injected through one row of opposed circular orifices (in-line) into a heated crossflow in a rectangular duct, as shown in Figure 2-11. Spacing and hole size were varied according to real combustor applications. The analogy between heat and mass transfer allowed measurements of the time-averaged temperature distribution to be used as an indicator of the mixing. The temperature distribution and mixing rates were determined at several downstream locations. They found that the best mixing in terms of temperature uniformity depended strongly on the momentum flux ratio of the jet to the mainstream. This is also in agreement with the findings by Holdeman. An optimum momentum flux ratio for all geometries studied resulted in a homogeneous temperature distribution downstream of the injection plane.

The effects of a swirl driven inlet flow were studied by Ahmed (1998) who used a laser doppler velocimeter to measure the flow field turbulence characteristics of a non-reacting, isothermal, swirling flowfield in an axisymmetric sudden expansion research combustor. The experimental combustor simulator is shown in Figure 2-12. One of his major findings was that swirling enhanced the production and distribution of turbulence energy and resulted in thorough flow mixing. These turbulence results differ from those presented earlier by Koutmos and McGuirk because the combustor simulator experiments performed by Koutmos and McGuirk included the use of inlet swirl flow coupled with downstream dilution jets whereas the experiments performed by Ahmed did not include the use of dilution jets. A swirl driven inlet flow by itself enhances mixing of the entire flow field and leads to increased turbulence levels. Dilution jets are sometimes used in parallel with swirl to actually counteract the effects of the swirl driven inlet flow to produce lower levels of turbulence.

Gritsch et al. (1998) studied the effect of mixing jets on slot cooling performance in a non-reacting simulated combustor liner. A scaled-up test model, shown in Figure 2-13, was constructed consisting of a flat wall with a film-cooling slot and a perpendicular dilution jet. The mainstream Reynolds number was 5800, which is representative of real combustor flows. Three combinations of film-cooling blowing ratio (M), defined as the ratio of the slot mass flow to the mainstream mass flow, and jet to mainstream momentum flux ratio (I) were studied. The three cases studied included $M=1$ and $I=10$, $M=1$ and $I=7$, and $M=2$ and $I=7$. It was found that the jet penetration was the highest for the case with the strongest jet momentum flux ratio and lowest slot-cooling blowing ratio ($M=1$ and $I=10$) as can be seen in Figure 2-14. The penetration of the jet was smallest for the case with the strongest film-cooling blowing ratio and lowest jet momentum flux ratio ($M=2$ and $I=7$). They determined that the film-cooling lifted off the wall just downstream of the dilution jet leading to weaker film-cooling coverage in this area. This phenomenon was attributed to counter-rotating vortices produced by the jet-mainstream interaction. The downstream heat transfer coefficient and adiabatic effectiveness were also determined downstream of the dilution jet. They reported heat transfer coefficients that increased downstream of the jet injection and then gradually decreased.

Blomeyer et al. (1999) conducted an experimental investigation of the mixing process of the hot primary zone gases with secondary air in a RQL combustor similar to that of Doerr et. al.. The mixing process was also simulated using a non-reacting flow, shown in Figure 2-15, consisting of multiple jets that were injected through one stage of opposed rows of circular orifices into a slightly heated cross-flow within a rectangular duct. The analogy between heat and mass transfer was again used to allow measurements of the time-averaged temperature distribution to be used as an indicator of the mixing. Emphasis was placed on high momentum flux ratios with high mass flow addition. Although the mainstream Reynolds number had little affect on the mixing process, the addition of swirl to the mainstream and the high turbulence that it produced in the shear layer of the jets significantly influenced the mixing process. These results were consistent with the findings from Anacleto et. al. They also found that jet penetration depth increased with increasing ratios of duct height to jet diameter and with increasing relative spacing. The mixing process was found to be best for a jet configuration such

that the jets were opposed to one another with their centerlines aligned. This is in agreement with the results reported by Doerr et. al.

Stitzel (2001) computationally modeled the non-reacting combustor simulator that is presented in this thesis that contained liners with film-cooling holes and two rows of in-line dilution jets. The computations were performed using the RNG k- ϵ turbulence model and the results agree with those found by Holdeman. The mixing of the dilution jets was not accurately predicted but good agreement was obtained in predicting the jet penetration. Overall, there was good qualitative agreement between the predictions and the experimental measurements presented in this thesis for a flow case that did not include dilution flow. Non-uniformities in the combustor exit profiles of pressure, velocity, and temperature were predicted.

One of the first reacting combustor flow experiments was conducted by Halls (1970) using a Conway engine. The results from his experiments, shown in Figure 2-16, indicated a highly non-uniform temperature profile at the combustor exit, which is consistent with the findings from the studies mentioned earlier that did not include reaction. Bicen et al. (1988) conducted an investigation of the flow and combustion characteristics of an annular combustor for two different air-fuel ratios and two different geometric arrangements. The combustor models used in the experiments, shown in Figure 2-17, consisted of two rectangular sectors including liner cooling slots as well as two rows of dilution jets. The first geometry consisted of positioning the vaporizer in line with the primary dilution holes, which were in line with the gaps between the secondary dilution holes. The second geometry had the primary dilution holes in line with the secondary dilution holes, which were both out of line with the vaporizer. The results indicated non-uniform distributions of velocity in the combustor exit plane for both flow configurations and turbulence levels near 20% over the majority of the exit plane, which were attributed to the upstream jets. These levels are consistent with the results presented earlier for the non-reacting combustor studies indicating that reactions do not contribute to turbulence levels. The exit plane characteristics, including localized hot spots and velocity peaks and deficiencies, were influenced by the opposing rows of dilution jets that tend to prevent the mainstream cross-flow from penetrating. The temperature profiles at the combustor exit plane,

shown in Figures 2-18 and 2-19, as well as the species concentration distributions were also found to be non-uniform.

Cameron et al. (1989) conducted detailed spatial mappings of velocity and temperature in the non-reacting and reacting environment of a model gas turbine combustor with wall injection. The experimental model is shown in Figure 2-20. They concluded that the strong on-axis recirculation zone located upstream of the primary jets that was present in the non-reacting case was dissipated in the case of reaction. Evidence of a hot streak was also observed near the primary jets for the reaction case and was attributed to fuel nozzle asymmetry. The hot streak persisted downstream due to the fact that the swirl was very weak beyond the primary jets. They found that the temperature profile at the exit of the combustor still contained evidence of the hot streak. The mean and rms velocities were also measured at several axial locations using a laser anemometer. These velocity measurements in the exit plane indicated turbulence levels, defined as the rms velocity divided by the mean velocity, to be approximately 25% for the reaction case, which is consistent with the turbulence levels mentioned earlier in studies without reaction. For this particular study, no information was given with respect to the rms velocities in the exit plane for the case without reaction.

Moss (1992) measured turbulence levels and calculated integral length scales for several reacting, can-type, gas turbine combustors. The combustors differed mainly in the design of the burner and head region, but were similar in both overall size and appearance. The calculated integral length scales ranged from 5.6 mm to 15.6 mm for the combustors studied. A major result from this study was the very good agreement between the calculated length scales for the non-reacting flow versus reacting flow for a particular combustor design.

Richards and Samuelsen (1992) conducted an experimental investigation into the role of primary jets on the overall performance of a gas turbine combustor. The experiments were performed in the reacting model combustor shown in Figure 2-21 that contains entrance swirl and two rows of dilution jets. The effects of the location of the first row of dilution holes (the primary holes) relative to the dome swirler and the number of jets in the primary row were

explored. Flow and thermal fields were measured with the principle findings being that the location of the primary holes relative to the dome swirler significantly influenced the percent mass recirculated into the dome region. The location of the primary jets and their momentum flux ratios also influenced the overall mixing uniformity and combustion efficiency. The influence of the dilution hole momentum flux ratio is consistent with the results presented earlier for the non-reacting combustor flow studies. They also found that increasing the number of primary jets per row resulted in decreased jet injection velocities. The increased number of jets also spread the mixing more uniformly about the duct circumference.

Goebel et al. (1993) measured velocity, turbulence, and temperature profiles downstream of a reacting small-scale combustor, shown in Figure 2-22, using laser doppler velocimetry and an insertion thermocouple. The effects of the combustor geometry including nozzle swirl, liner mixing, and dilution holes were studied. The operating conditions including mass flow, pressure, and combustion were studied independently. They found that with an appreciable swirl velocity the dilution jets acted to disrupt the swirl and actually reduced turbulence levels. This is in agreement with the results presented earlier from Koutmos and McGuirk. Without swirl and at low swirl velocities, the transverse dilution jets increased the turbulence levels. They also found that the combustor exit velocity profiles were affected by closing and opening the dilution jets. The exit temperature profiles were found to be strongly affected by the dilution jets. They also found that for low swirl velocities the turbulence levels were nearly constant with and without combustion.

Lawson (1993) computationally modeled an aircraft engine combustor to achieve target exit temperature profiles. The goal of the study was to determine the effects of changing the cooling and dilution flow to achieve a certain exit temperature profile. Two profiles were desired including an inboard peaked temperature profile and a flat temperature profile. To achieve the inboard peaked profile, 35% of the inner diameter liner cooling was moved to the outer diameter liner. The computational results were applied to an actual combustor in a GE high bypass turbofan aircraft engine. Excellent agreement was obtained between the engine tests and the computations. The flat temperature profile was computationally obtained by reducing

the liner cooling by 20% to raise the temperatures near the walls. This 20% of the total exit mass flow was redirected into the primary dilution flow in which the inner diameter liner holes received a larger portion of it to cool down the inboard peaked profile. Engine test data again agreed very well with the computations. Since only a single rig test was needed to verify the changes prescribed by the computational models, it was concluded that the modeling provided a cost savings of over \$50,000 and a time savings of nearly one month. No information with regards to turbulence levels was given.

Crocker et al. (1994) also experimentally investigated ways to reduce the temperature pattern factor at the combustor exit of an Allied Signal F109 reverse flow annular combustor, shown in Figure 2-23. The temperature pattern factor is the difference between the radially averaged temperature at the combustor exit and the local radial temperature all divided by the difference between the radially averaged temperature at the combustor exit and the combustor inlet temperature. A baseline case was conducted with the conventional engine configuration with the test results indicating non-uniform circumferential temperatures at the turbine inlet. These non-uniformities were caused by fuel flow variations between fuel nozzles. Dilution jets were then modified to enhance circumferential mixing. The dilution jets on the outer liner were angled in one direction and the dilution jets on the inner liner were angled in the opposite direction. The only modification made to the combustor was the dilution hole orientation. Test results indicated that the circumferential temperature variations experienced in the baseline case were significantly reduced. Figure 2-24 shows the results from both of these tests. This study is consistent with the findings by Lawson in that the dilution flow can be tailored to achieve certain combustor exit temperature profiles.

Gulati et al. (1995) measured the mean and rms temperatures at the exit plane of a full-scale, 10-cup, double annular research combustor as shown in Figure 2-25. Their results also indicated that the dilution air had a significant affect on the mean and rms temperature profiles. As the outer row of dilution air was increased, the jets pushed the combustion zone toward the inner liner and increased the peak temperature. Increasing the dilution air on the inner row of dilution holes shifted the peak temperature towards the combustor centerline and reduced the

peak value. The drop in the peak value suggested that the inner dilution air penetrated the combustion zone and led to enhanced mixing. Both of these trends were predicted well by computational models using the standard k- ϵ turbulence model. The overall effect of the inner and outer dilution air was to make the temperature profile peak at the centerline with an overall lower peak temperature. The dilution jets were also found to generally increase the rms temperature fluctuations. The model consistently underpredicted the temperature fluctuations at the exit, although the trend of increased turbulence with dilution air was predicted correctly. These computational results are in agreement with the findings of Holdeman and Stitzel.

Malecki et al. (2001) used an advanced computational analysis system to optimize the combustor exit temperature in the Pratt & Whitney PW6000 engine. The standard k- ϵ turbulence model with wall function near-wall modeling was used. They recognized that this turbulence model underpredicts the mixing that occurs for flows with jets in crossflow. To overcome this turbulence modeling problem associated with the mixing and to match combustor exit temperature validation data, it was stated that some studies reduced the Schmidt number (Sc) from typical values between 0.7 and 0.9 to values ranging from 0.25 to 0.6. The Schmidt number is the ratio of momentum diffusivity to mass diffusivity. They mentioned that reducing Sc enhances mixing of the product species downstream of the dilution jets thus enhancing mixing of the temperature field. They reported using $Sc = 0.2$ which was the optimal Sc to use according to studies performed by He et al. (1999) for Reynolds averaged Navier-Stokes analyses of jet-in-crossflow flow fields using the standard k- ϵ turbulence model with typical gas turbine combustor momentum flux ratios. The computational analysis system was applied to three different Pratt & Whitney combustor geometries to determine its generality for predicting combustor exit temperature profiles under sea-level take off conditions. The combustor geometries included a film-cooled liner with three rows of dilution holes and a fuel injector with axial swirl vanes, a film-cooled liner with two rows of dilution holes and a fuel injector with radial inflow swirlers, and one row of dilution holes and a fuel injector with radial inflow swirlers. Each of the three combustors was also experimentally tested to provide a complete set of validation data for the computations. There was very good agreement between circumferentially-averaged exit temperature profiles from the test rig data and the analyses for all

three combustor geometries. The first combustor geometry produced a center-peaked temperature profile with slightly higher temperatures near the outer wall. The second geometry produced higher temperatures in the outer half of the span. The third geometry resulted in a much more uniform exit temperature profile with slightly higher temperatures near the outer wall. The maximum rms difference between measured and calculated temperatures among the three geometries was 22 K.

Snyder et al. (2001) used the same advanced computational analysis system as Malecki et al. (2001) to optimize the combustor exit temperature in the Pratt & Whitney PW6000 engine. They successfully used this computational design tool to tailor combustor exit temperature profiles to within design limits by performing a parametric study of dilution hole patterns. Although, no information with respect to the hole pattern geometry was given, the optimized dilution hole pattern was incorporated into the PW6000 engine to improve durability and prolong turbine life indicating the computational effort was successful.

In comparing the results from the studies presented above on non-reacting and reacting combustor flows there are many important similarities and some differences. The differences in the flow fields between the two cases seem to lie in the near primary zone where combustion stability is controlled. For example, Cameron et. al. (1989) found that the recirculation zone located upstream of the primary jets present in the non-reacting case was not present in the case of reaction. Further downstream within the combustor, near the dilution zone and at the combustor exit, many similarities exist in the results reported by the non-reacting and reacting studies. A common finding was the evidence of non-uniform exit profiles in velocity, temperature, and turbulence. The studies indicated that the dilution jets played the most dominant role in creating these profiles and that the exit profiles could be tailored by altering the dilution and cooling flow. The turbulence levels at the combustor exit that were reported for the studies with reaction were very similar to those found in the studies without reaction. Moss (1992) also found very similar integral length scales between a reacting and non-reacting flow for a given combustor design. There was good agreement between computations, which used both the standard k- ϵ and the RNG k- ϵ turbulence models, and the experiments in predicting

dilution jet penetration and combustor exit temperature profiles. It was noted in one study, Lawson (1993), that implementing the computational modeling saved a significant amount of money and time. The computational models seemed to lack, however, the ability to accurately model the turbulent mixing that occurs in the dilution zone and at the combustor exit.

2.2 Effects of Combustor Flowfields on Turbine Performance

There have been very few experimental and computational studies performed regarding the effects of combustor flow fields on downstream turbine performance. Although the emphasis of this research is not on the turbine section, understanding the impact of combustor exit flows on turbine heat transfer is the motivating factor. Schwab et al. (1983) and Stabe et al. (1984) conducted analytical and experimental studies of flow through an axial turbine stage with uniform and non-uniform inlet radial temperature profiles. The turbine inlet radial temperature profiles were experimentally generated by a Combustor Exit Radial Temperature Simulator (CERTS) that injected coolant air through circumferential slots in the hub and tip endwalls upstream of the stator vanes. Coolant flowrates were adjusted to produce design inlet temperature profiles in terms of local to mean temperature ratios. Measurements of total temperature and total pressure were conducted at the stator inlet and rotor exit with and without coolant injection. In addition to the non-uniform temperature profile, a non-uniform total pressure profile at the stator inlet was indicated and used as an inlet boundary condition for analytical modeling of the flow. Measured profiles at the rotor exit plane were more mixed out than those predicted by the analytical solution. The reason for this difference was attributed to a lack of viscous effects in the computations. These computational results are consistent with those mentioned earlier that did not accurately predict turbulent mixing processes.

Krishnamoorthy et al. (1988) experimentally investigated the influence of a combustor flow field on the heat flux distribution in a turbine vane cascade located just downstream of the combustor. The experimental setup is shown in Figure 2-26. Surface temperature measurements were made around the convectively cooled vanes for a low-turbulence uniform hot gas stream,

high-turbulence uniform hot gas stream, and high-turbulence non-uniform hot gas stream exiting the combustor. The results from this study indicate that the effect of the high turbulence at the combustor exit was to reduce the cooling effectiveness on the vane by 10 %. It was also shown that the effect of temperature non-uniformities at the combustor exit was to reduce the overall cooling effectiveness on the vane by as much as 21 % indicating the importance of these non-uniformities. Information regarding the combustor geometry that was used in the experiments was not given.

Burd and Simon (2000) conducted experimental investigations of the effects of slot bleed injection over a contoured endwall on nozzle guide vane cooling performance. Bleed flow was injected through angled slots upstream of the nozzle guide vane section, shown in Figure 2-27, for a range of bleed flow ratios between 1.0% and 6.0%. Experiments were conducted with an approach flow containing high turbulence (9.5%). It was also stated that the approach flow was uniform in total pressure, however, this is questionable considering only a single total pressure measurement was made in the approach flow. Total pressure measurements were made over the entire exit plane of the cascade and were non-dimensionalized by the total pressure and velocity head of the approach flow into a total pressure loss coefficient. For the two flow cases in which the bleed to mainstream mass flow ratios were 2.0 % and 4.5 % it was found that the values of the loss coefficient were nearly zero over the vast majority of the exit plane. Thin regions of high loss coefficient were measured in the near endwall regions indicating large total pressure gradients associated with the bleed flow. Measurements of the core flow temperature distribution were also taken at several axial positions within the cascade. These temperature measurements indicated that the bleed coolant could provide thermal protection over large regions of the endwall, including regions on the pressure and suction surfaces of the airfoils, as long as the combustor bleed flow was strong enough to overcome the influence of the endwall region secondary flows.

Hermanson and Thole (2000) performed a computational study to study the effects of temperature, velocity, and total pressure on endwall secondary flows. They showed that with a large total pressure in the endwall region, which is opposite of that associated with a turbulent

boundary layer, the rotation of the passage vortex was reversed from that occurring for a turbulent boundary layer. This is important because most turbine vane experiments and computations in the past have assumed a two-dimensional turbulent boundary layer as in inlet condition. Another major result was the complete absence of a leading edge vortex or passage vortex when there was no total pressure gradient present near the airfoil leading edges.

2.3 Summary of Current Literature

All of the relevant experimental and computational studies in the current literature indicate that the interaction of the individual combustor components results in a very complex flow field at the combustor exit. The literature indicates that the most significant combustor components that contribute to the exiting non-uniform thermal and pressure fields are swirlers, film-cooling slots and holes, and dilution holes. The results from the studies presented earlier indicate that in a combustor the flow and thermal fields downstream of the primary zone are very similar with or without reaction. The only noteworthy differences occur upstream of the primary zone where combustion is stabilized. This is very important because it allows a flow field representative of one exiting a real gas turbine combustor to be simulated under non-reacting conditions.

There is insufficient research to date, however, that incorporates the effects of realistic combustor flow and thermal fields on downstream turbine vanes and endwall regions. In particular, very little experimental data exists that documents total pressure profiles at the combustor exit. This information is paramount since it has been shown that the total pressure field is a driving force in the development of secondary flows that are present in the downstream nozzle guide vane passages (Hermanson and Thole, 2000). These secondary flow patterns dictate the overall heat transfer to the endwall regions by lifting cooler fluid near the endwall and replacing it with hotter mainstream fluid. The non-uniformities in velocity, pressure, temperature, and turbulence at the combustor exit can have detrimental effects on the turbine vanes. A more complete understanding of the effects of combustor flows on the downstream nozzle guide vanes and endwall regions is needed.

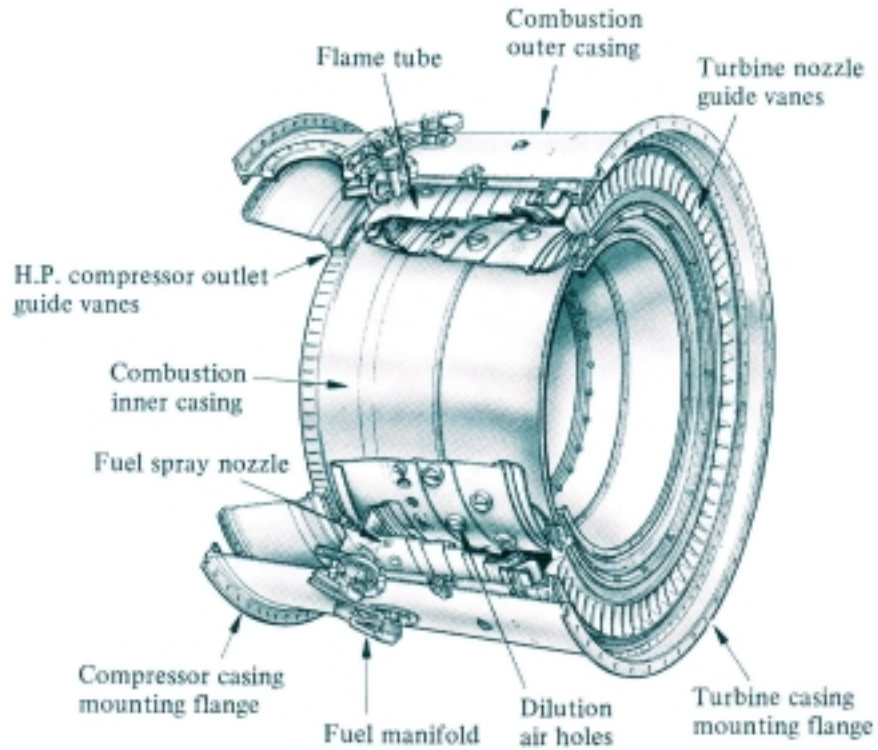


Figure 2-1 Schematic of an annular combustion chamber (Hill and Peterson, 1992).

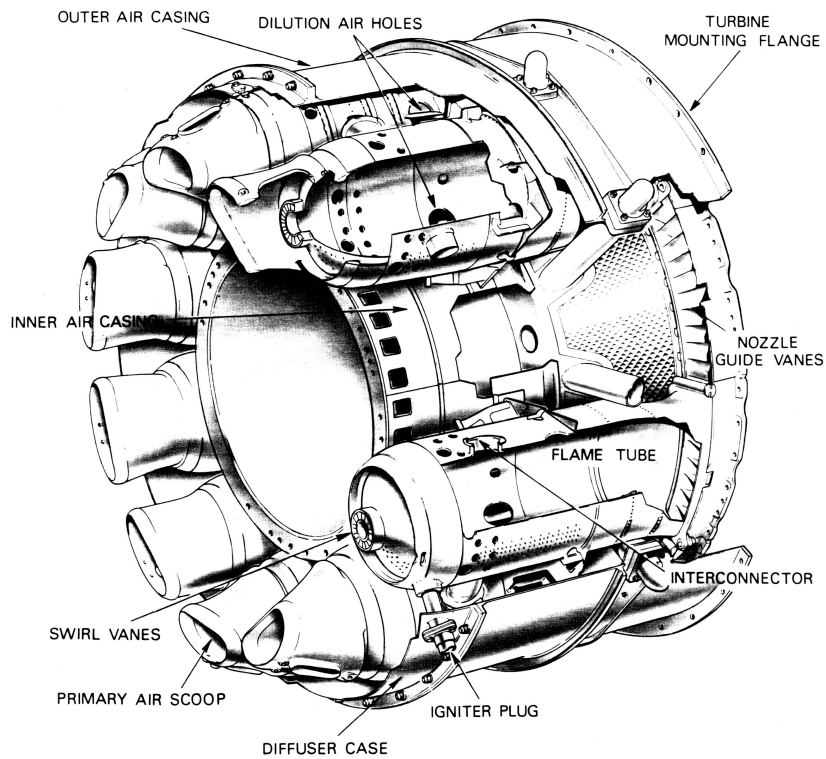


Figure 2-2 Schematic of a cannular combustion chamber (Hill and Peterson, 1992).

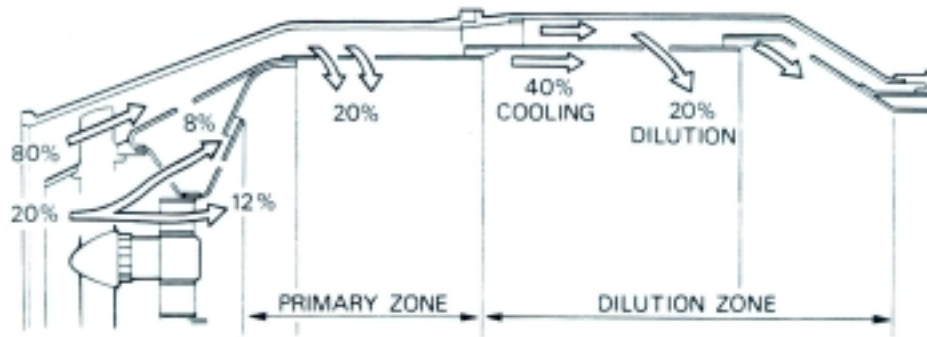


Figure 2-3 Schematic of a typical mass flow distribution in a gas-turbine engine combustor (Hill and Peterson, 1992).

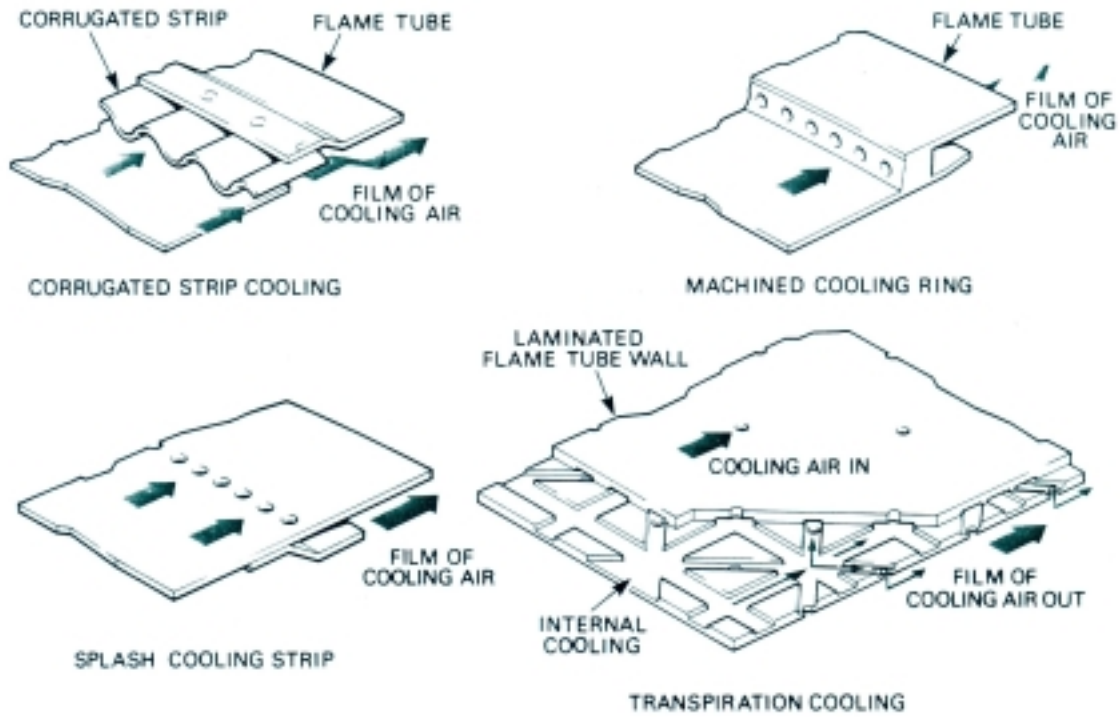


Figure 2-4 Schematics of combustor liner cooling techniques (Rolls Royce, 1992).

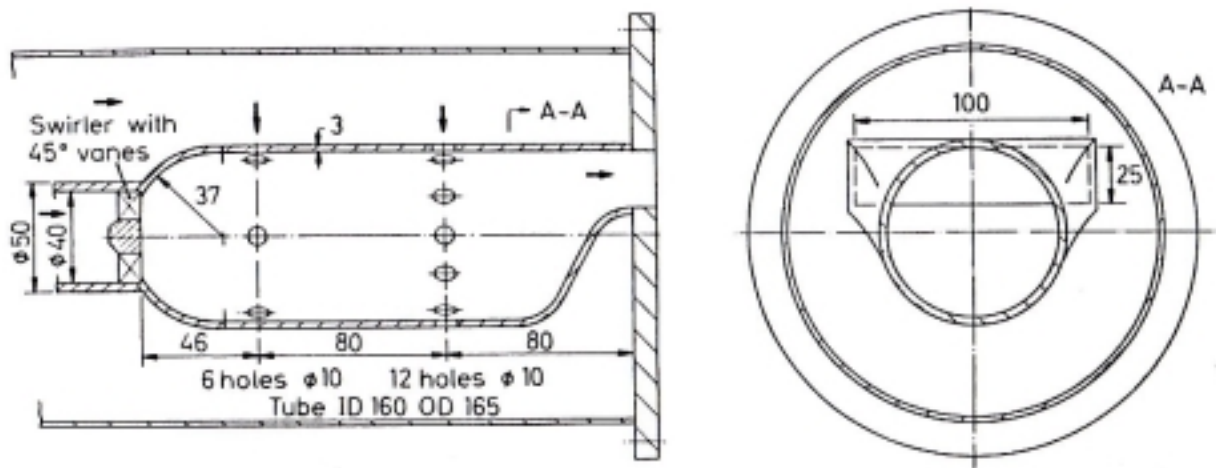


Figure 2-5 Schematic of Koutmos and McGuirk (1989) combustor model.

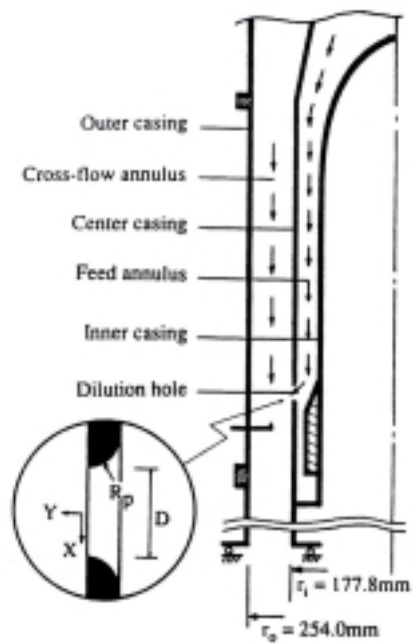


Figure 2-6 Schematic of Stevens and Carrotte (1990) combustor model.

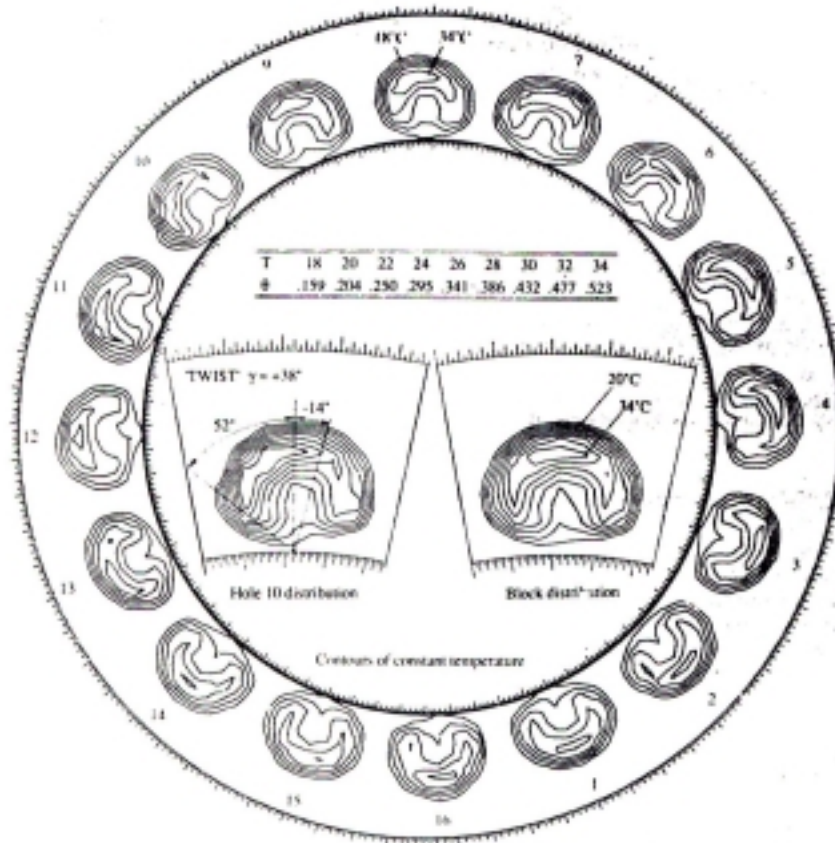


Figure 2-7 Graph indicating results of Stevens and Carrotte (1990) experimental results.

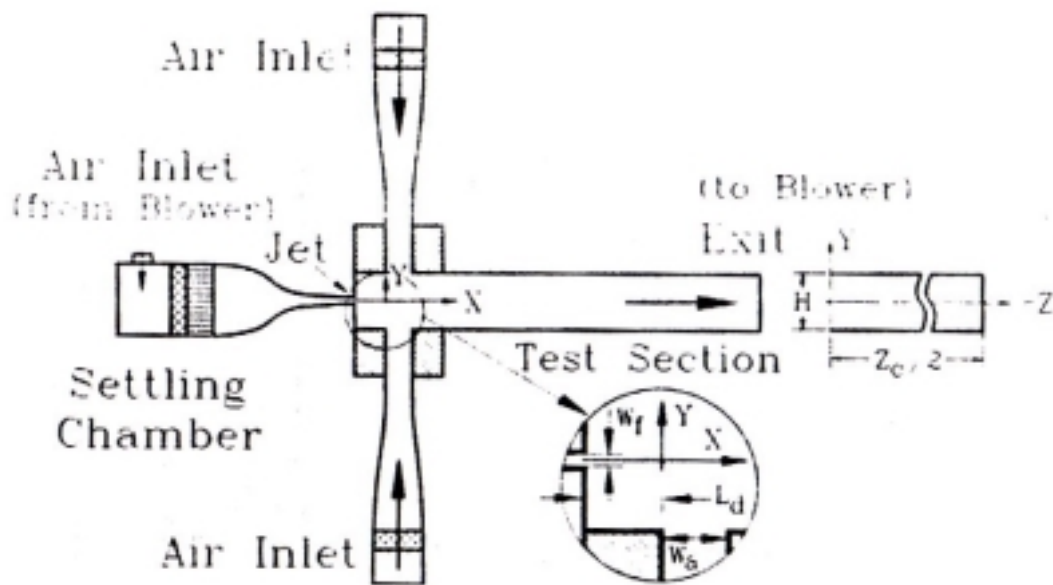
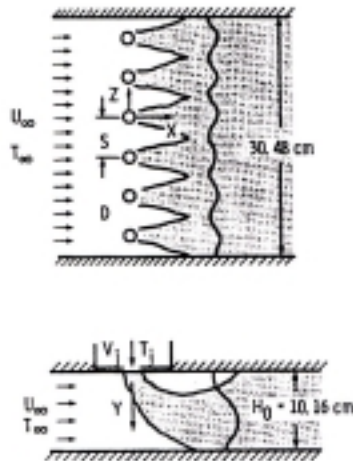


Figure 2-8 Schematic of Liou and Wu (1992) combustor model.



	S/H_0	H_0/D	S_x/H_0	Type
A	0.5	8	—	
B	.5	5.7	—	
C	.5	4	—	
D	.5	4	—	0° Slot
E	.5	4	—	90° Slot
F	.5	4	—	45° slot
G	1.0	4	—	
H	1.0	4	—	
I	1.0	4	—	Square
J	—	9.9	—	2-D Slot
K	—	19.8	—	2-D slot
L	.25	8	—	
M	.5	5.7	0.5	In-Line
	.5	5.7	—	
N	.5	5.7	.25	Disimilar
	.25	8	—	
O	1.0	4	.5	Staggered
	1.0	4	—	

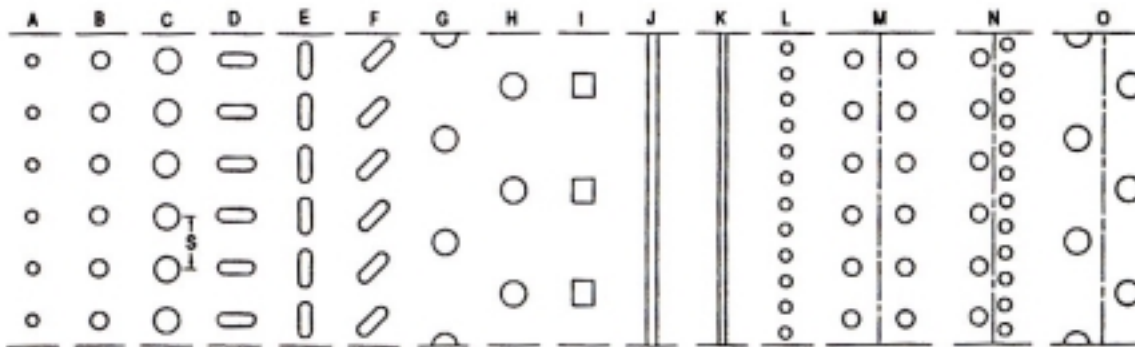


Figure 2-9 Schematics of Holdeman (1993) combustor model and orifice configurations.

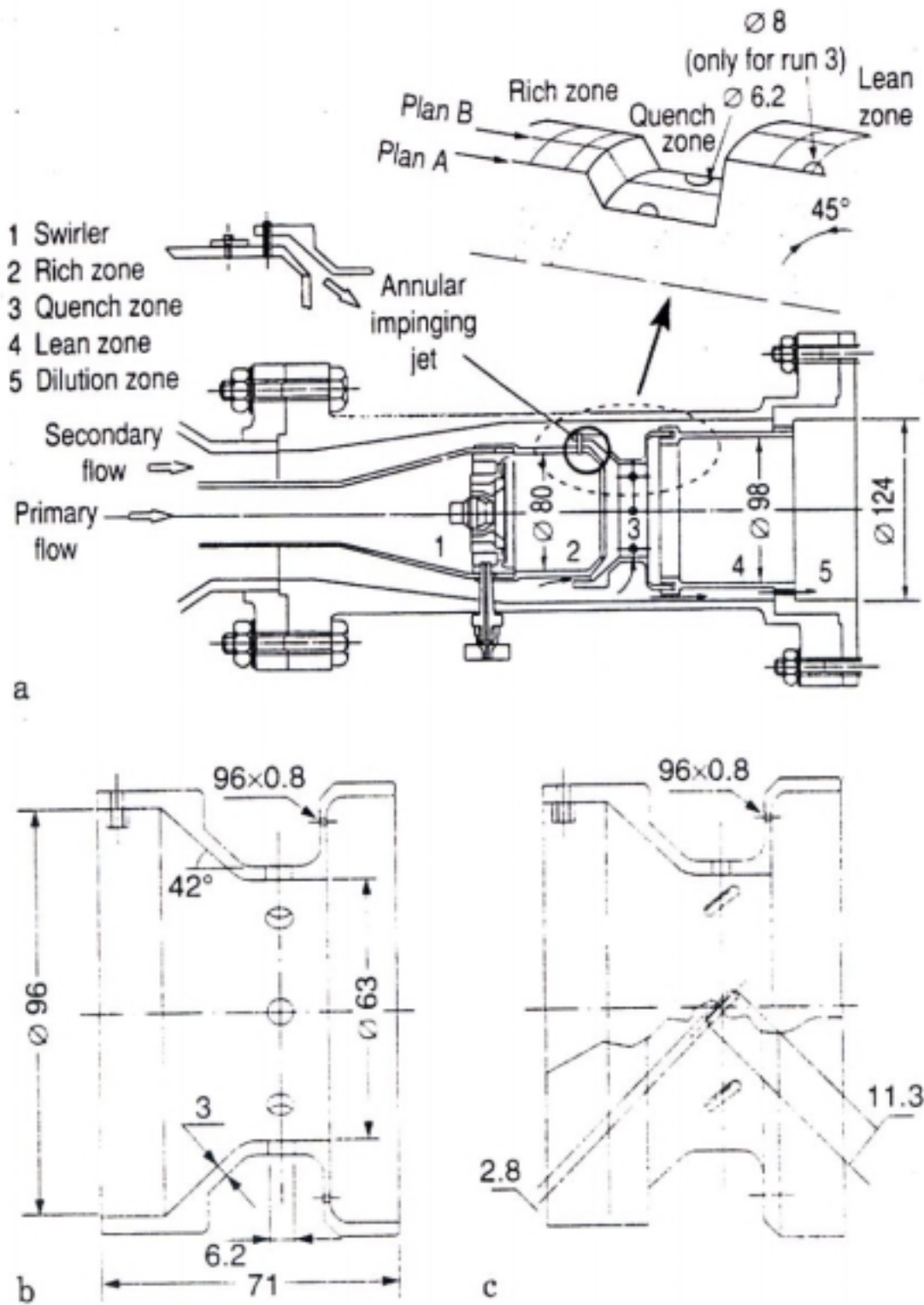


Figure 2-10 Schematic of Anacleto et al. (1996) combustor models.

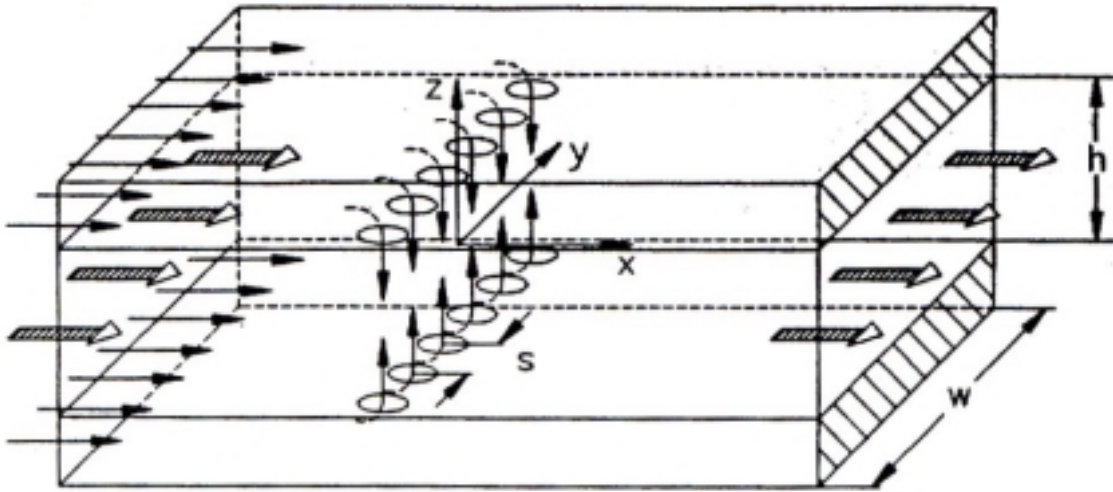


Figure 2-11 Schematic of Doerr et al. (1997) combustor model.

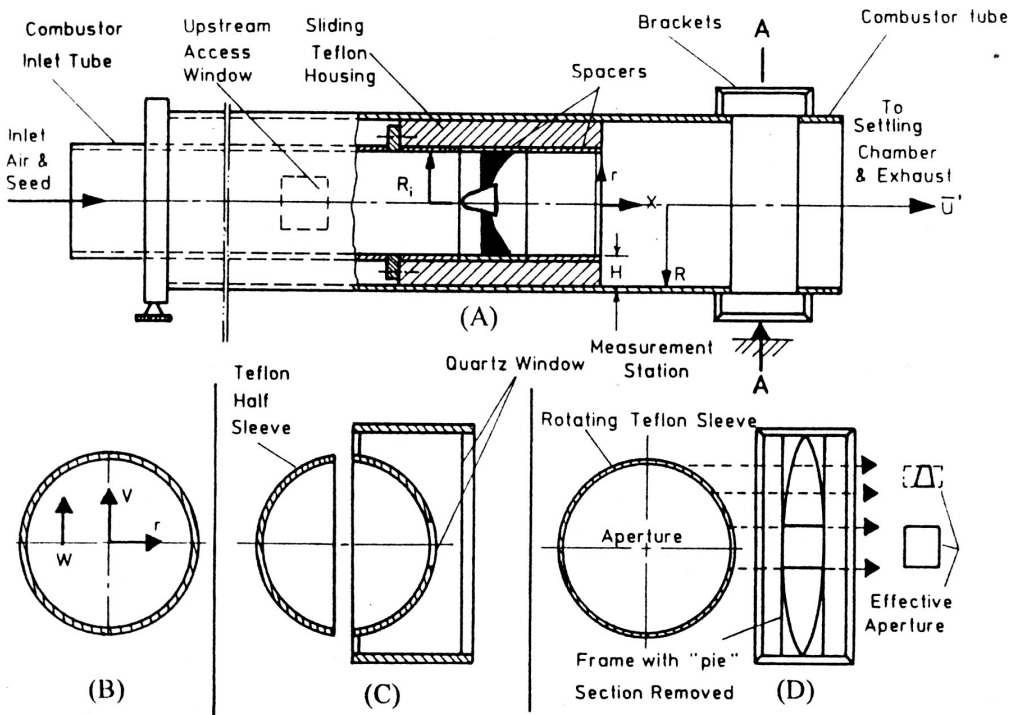


Figure 2-12 Schematic of Ahmed (1998) combustor models.

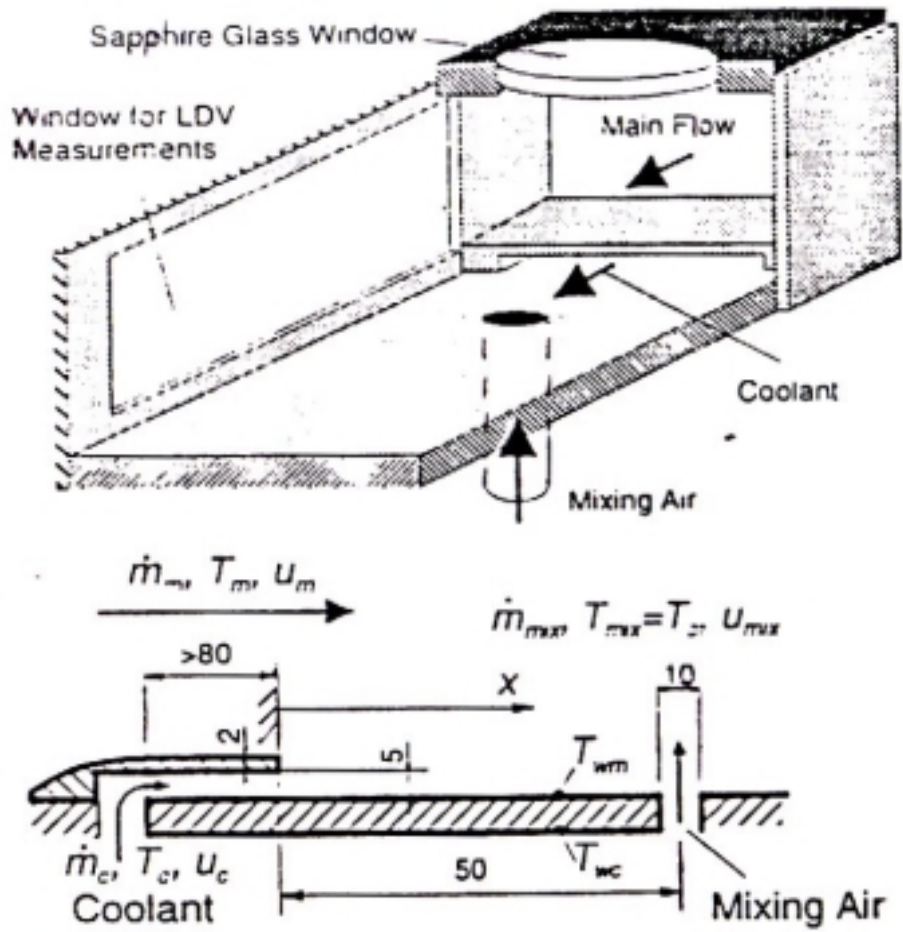


Figure 2-13 Schematic of Gritsch et al. (1998) combustor model.

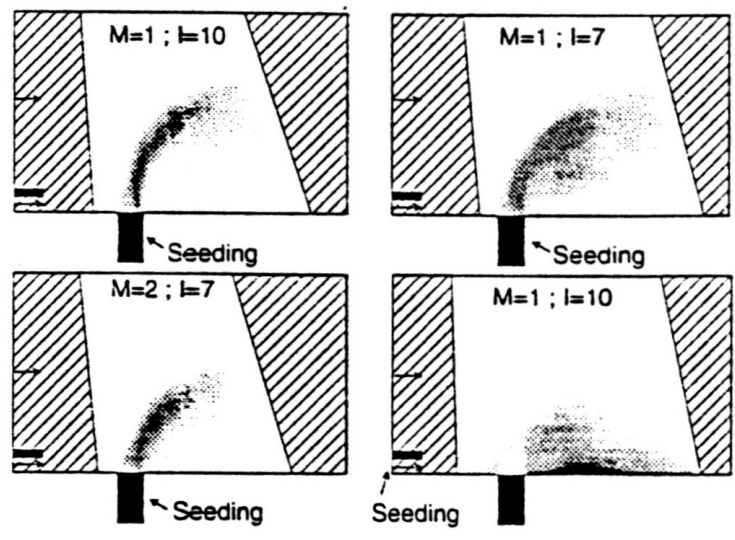
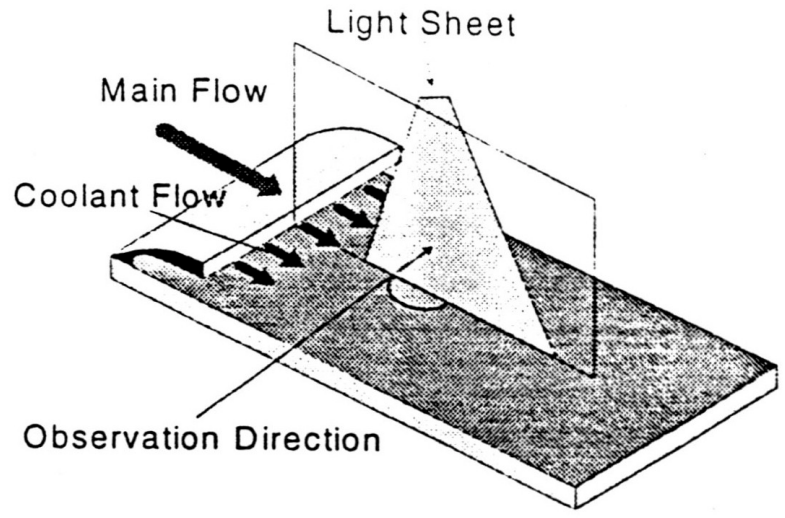


Figure 2-14 Schematic of measurement plane and graphs indicating results of Gritsch et al. (1998) experiments.

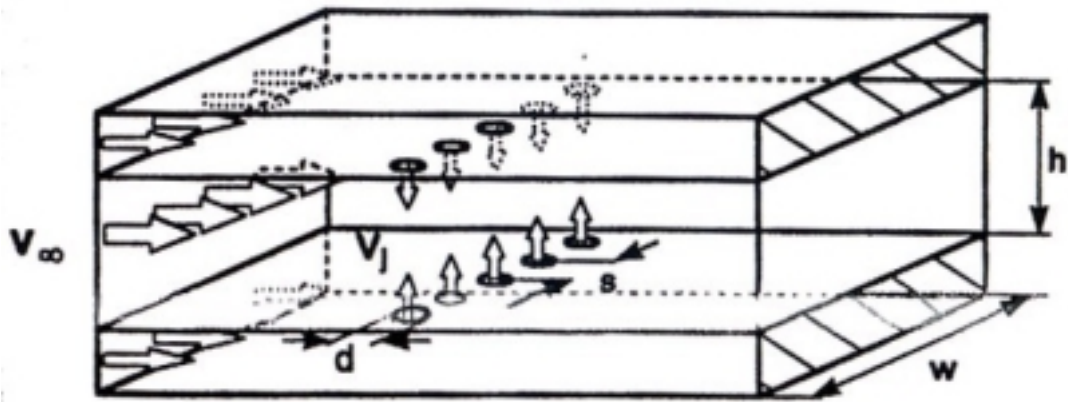


Figure 2-15 Schematic of Blomeyer et al.(1999) combustor model.

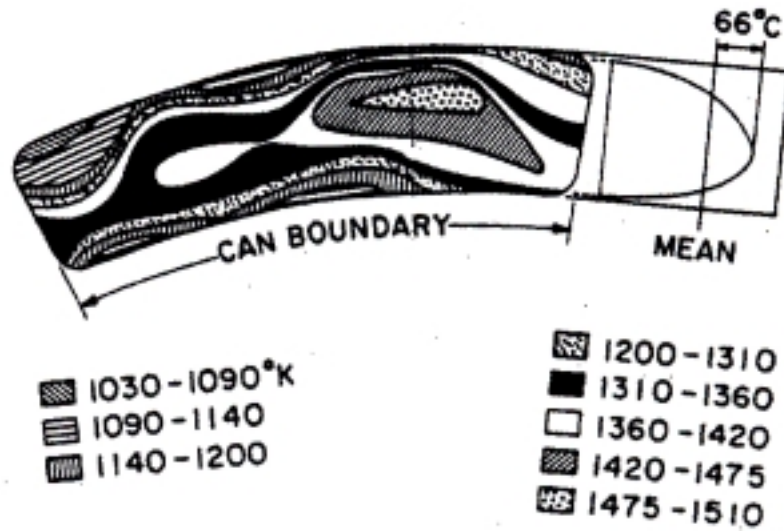
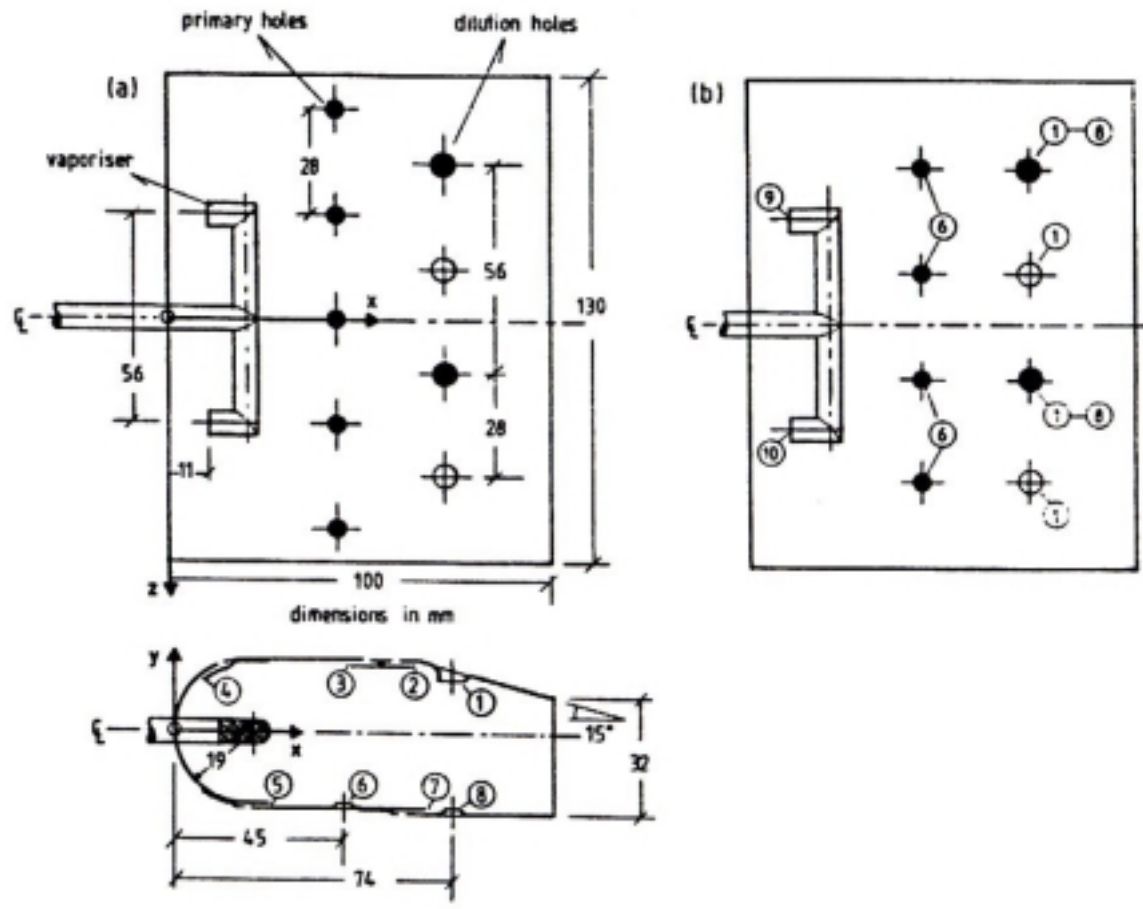
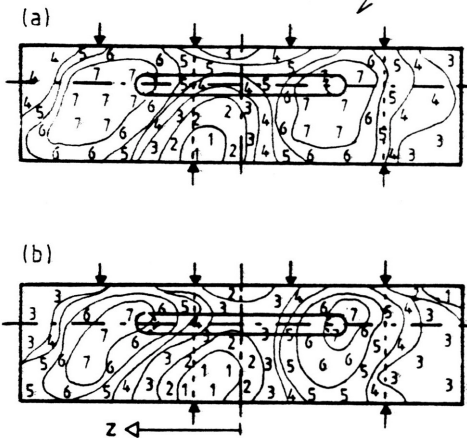
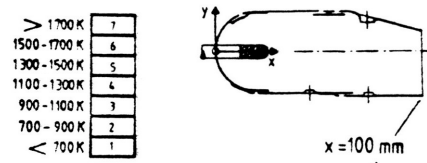


Figure 2-16 Schematic of the non-uniform temperature profile from Halls (1970).

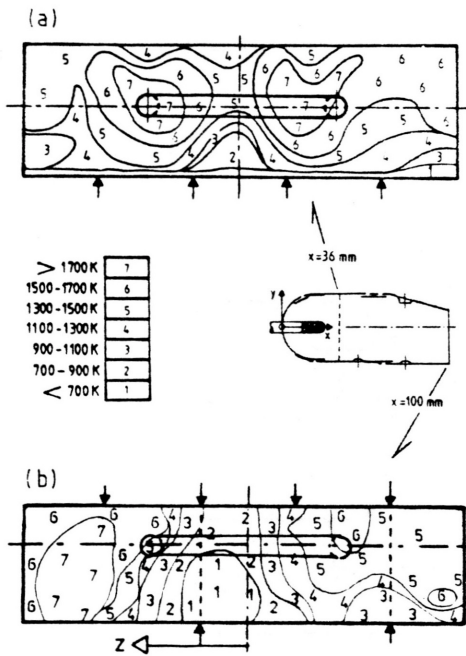


Combustor geometries: (a) Combustor 1; (b) Combustor 2.

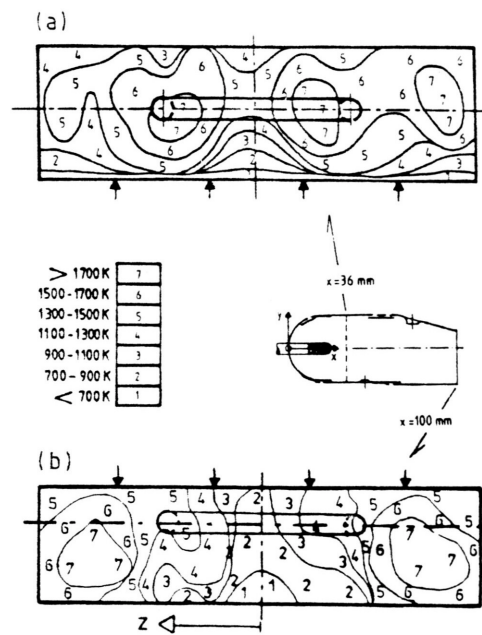
Figure 2-17 Schematic of Bicen et al. (1988) combustor models.



Exit-plane distributions of mean temperature with Combustor 1: (a) air-fuel ratio of 29; (b) air-fuel ratio of 37.

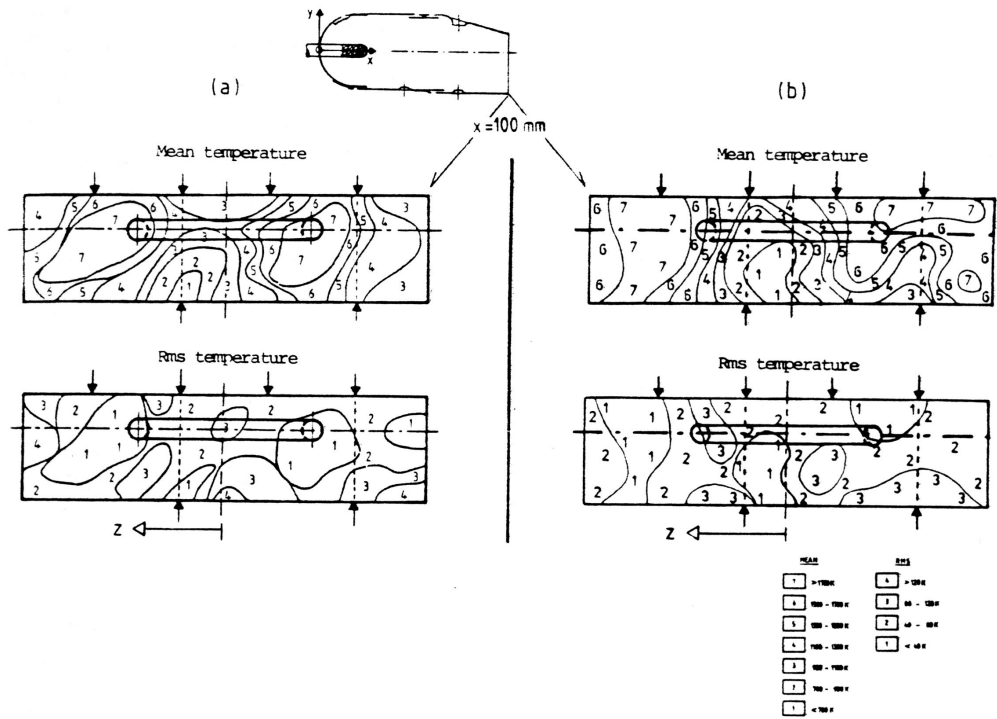


Cross-plane distributions of mean temperature with Combustor 2 and air-fuel ratio of 37: (a) primary zone; (b) exit plane.



Cross-plane distributions of mean temperature with lower dilution holes of Combustor 2 blocked and air-fuel ratio of 37: (a) primary zone; (b) exit plane.

Figure 2-18 Graphs indicating results from Bicen et al. (1988) experimental work.



Exit-plane distributions of mean and rms of temperature fluctuations obtained with digitally compensated $40\ \mu\text{m}$ -wire thermocouple: (a) Combustor 1 with air-fuel ratio of 29; (b) Combustor 2 with air-fuel ratio of 29.

Figure 2-19 Graphs indicating results from Bicen et al. (1988) experimental work.

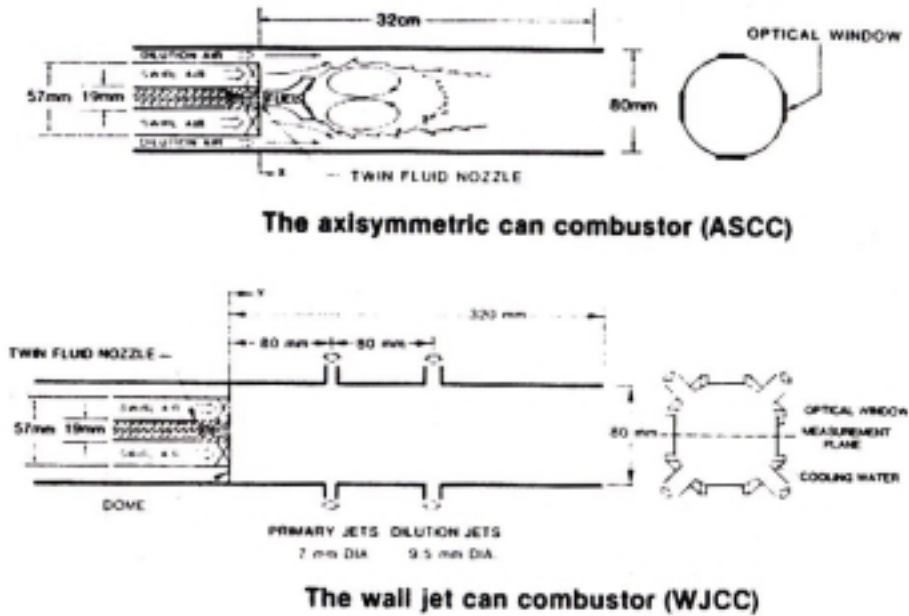
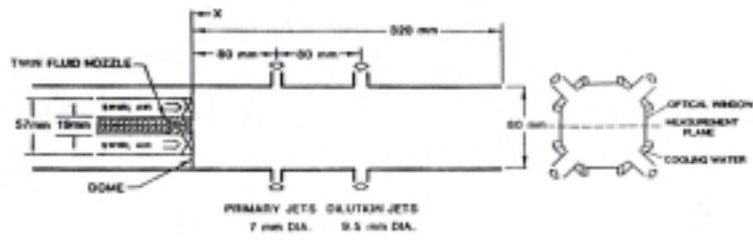


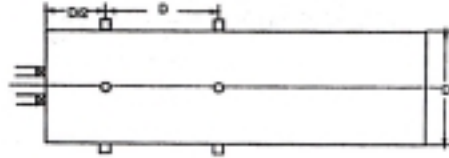
Figure 2-20 Schematic of Cameron et al. (1989) combustor models.



b) Module 1.



c) Module 2.



d) Module 3.

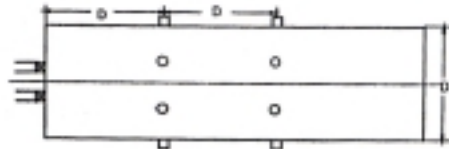


Figure 2-21 Schematic of Richards and Samuelsen (1992) combustor models.

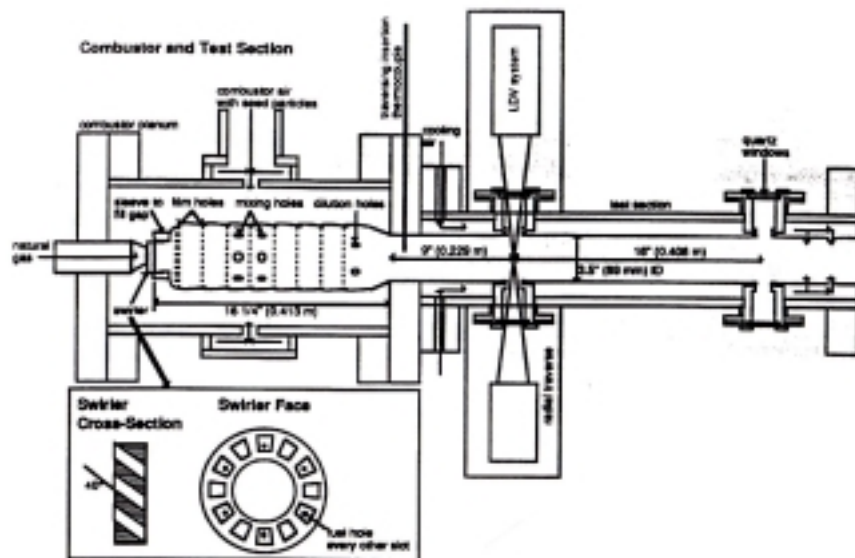


Figure 2-22 Schematic of Goebel et al. (1993) combustor model.

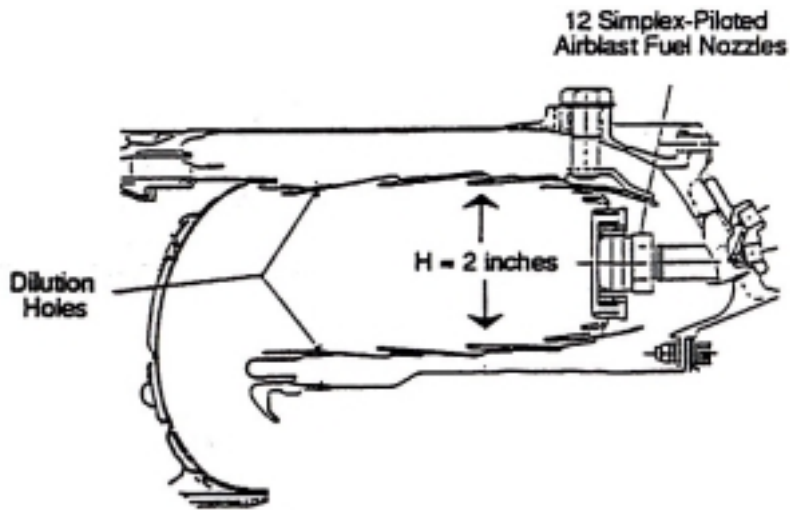


Figure 2-23 Schematic of Crocker et al. (1994) combustor model.

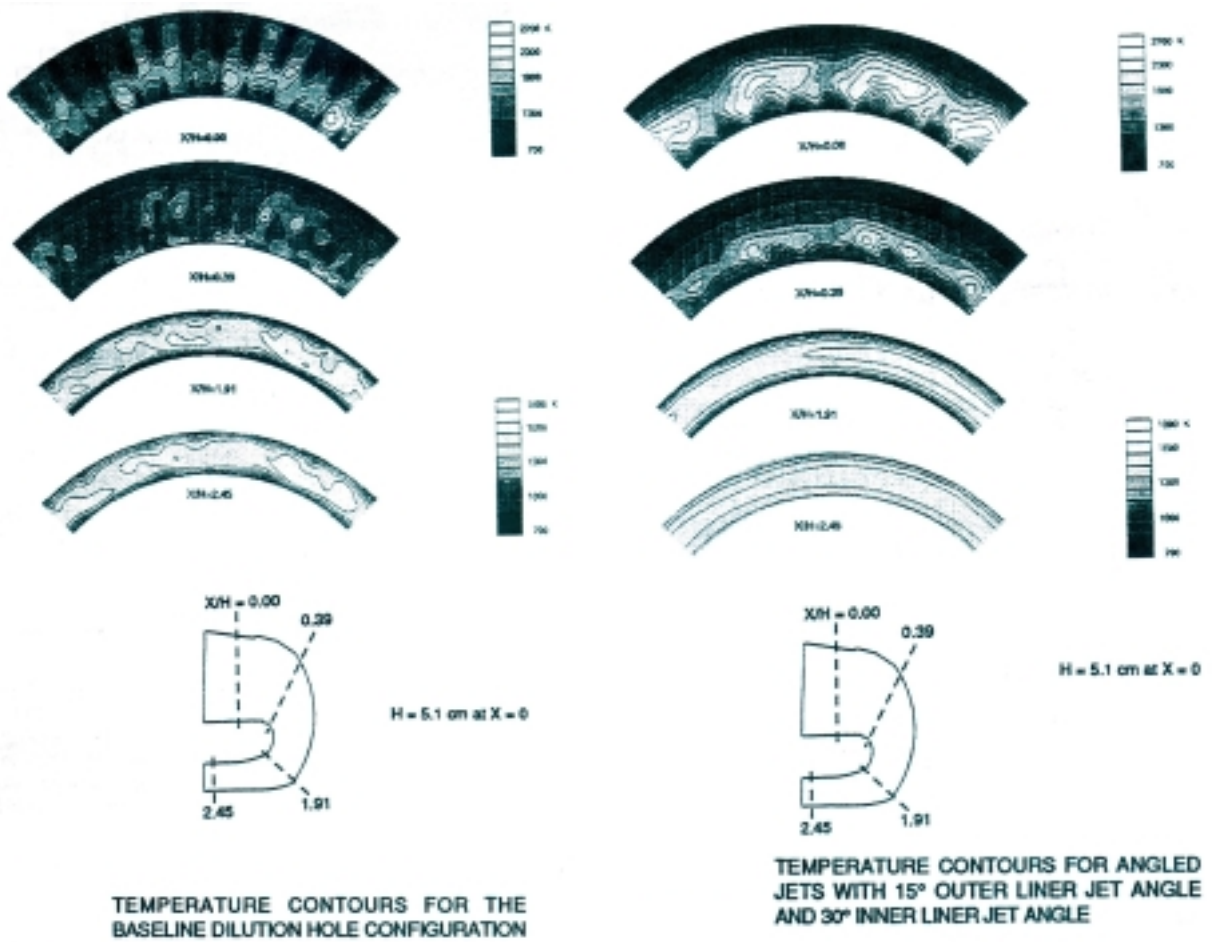


Figure 2-24 Graphs indicating results from Crocker et al. (1994) experiments.

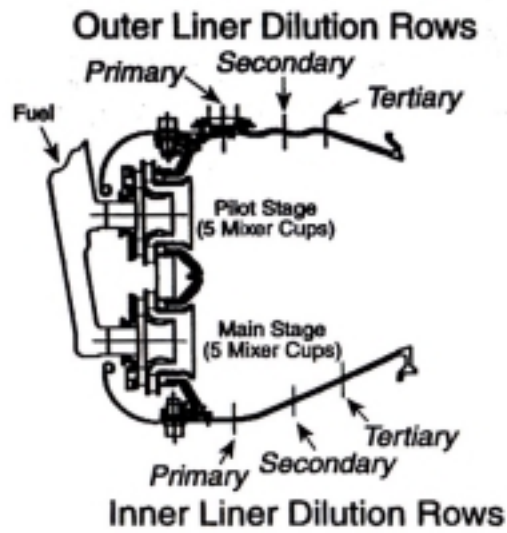


Figure 2-25 Schematic of Gulati et al. (1995) combustor model.

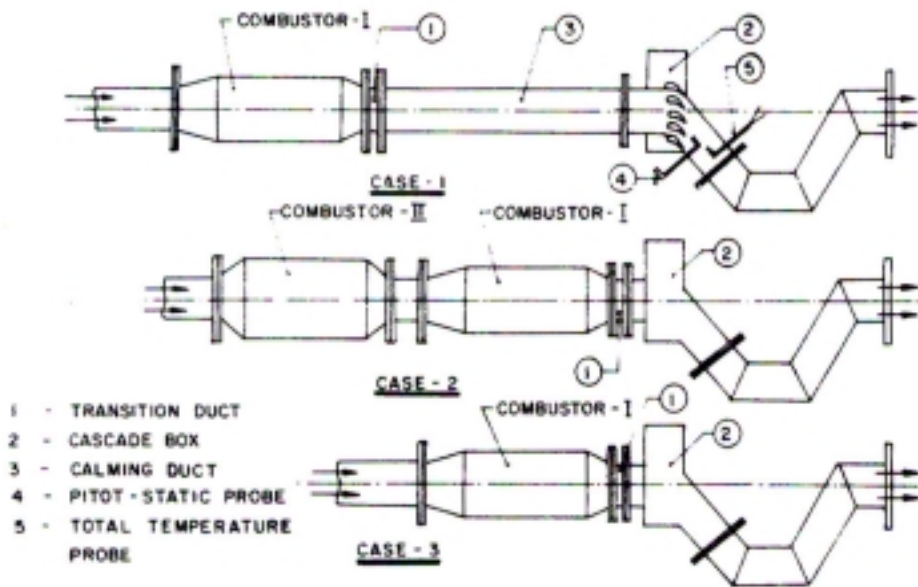


Figure 2-26 Schematic of Krishnamoorthy et al. (1988) experimental setup.

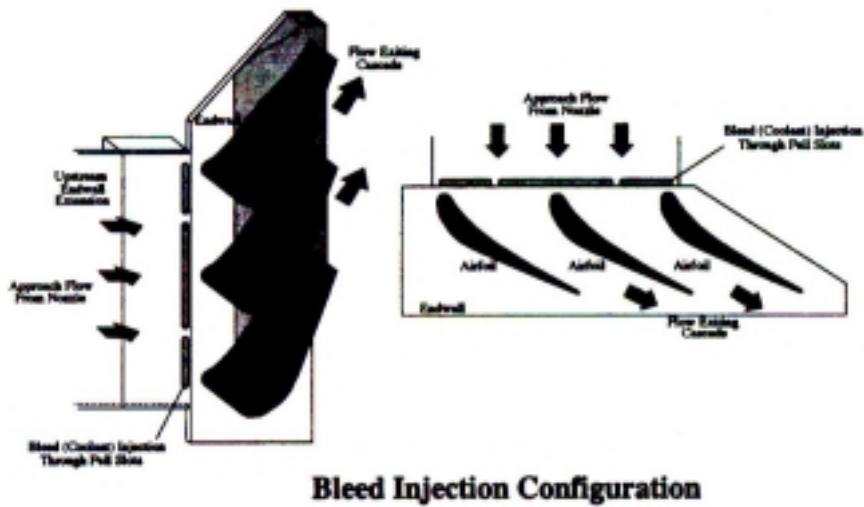
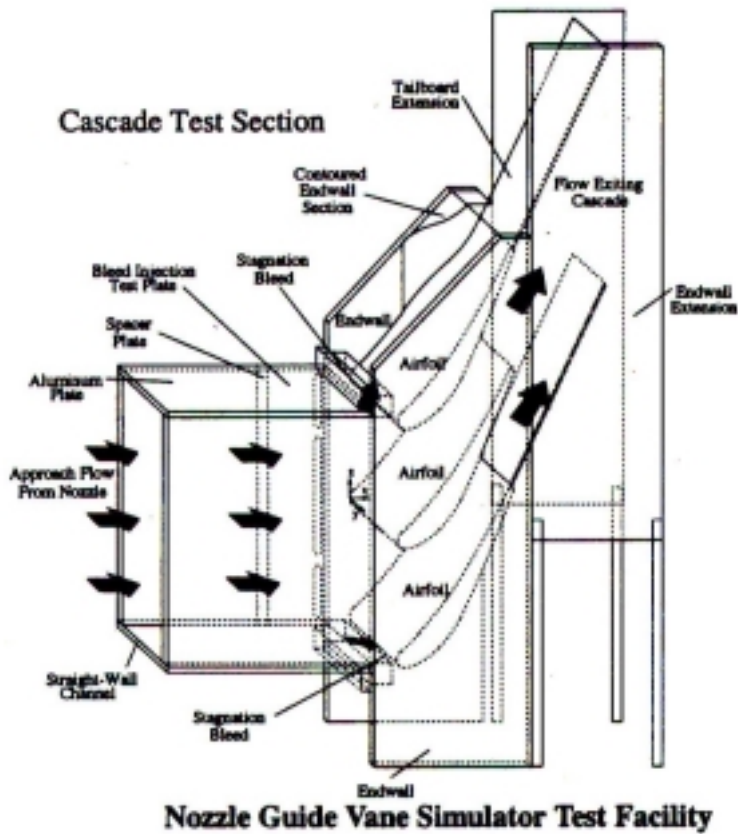


Figure 2-27 Schematic of Burd and Simon (2000) experimental setup.

3. Design of the Combustor Simulator and Instrumentation

The main goals in this study were to design a combustor simulator that could produce flow field conditions similar to those exiting a real combustor in a gas turbine engine, implement the simulator design into an existing wind tunnel facility, and then benchmark its overall performance. The existing wind tunnel facility, shown in Figure 3-1, contained a scaled-up (9x) turbine vane cascade (Radomsky and Thole, 2000a) and represented one sector (two pitches) of a gas turbine engine. The scaling of the cascade allowed for good measurement resolution while matching the inlet Reynolds number between the wind tunnel cascade and an engine turbine.

To design the combustor simulator, an in-depth analysis was required of the combustor in an actual operating gas turbine engine. The following section includes a discussion of the engine combustor that was analyzed and the parameters that were matched for the combustor simulator. Following a discussion of the matched parameters, this chapter presents a description of the overall wind tunnel facility including the provisions made for installing the simulator. This is followed by descriptions of the simulator's primary and secondary flow paths and the test section downstream of the combustor simulator. Finally, all of the instrumentation that was used in benchmarking the facility and the uncertainties associated with the flow and thermal field measurements are then discussed.

3.1 Description of the Engine Combustor

The combustion chamber that was modeled in this study is an annular prototype combustor with the geometry and flow parameters supplied by Pratt & Whitney (Soechting and Cheung, 1999). A schematic of the combustion chamber for the engine with its important geometrical features can be seen in Figure 3-2. The liners on the inner and outer diameters of the combustor are film-cooled and contain two rows of dilution jets. The dilution holes are located in the second and third liners at axial positions 7.6 cm ($X/L = 0.45$) and 10.2 cm ($X/L = 0.60$) from the chamber entrance. Located at the combustor-turbine interface is a cooling slot on both the inner and outer diameter liners. The combustor has an overall axial length of 17 cm with an

inlet height of 8.8 cm and an exit height of 6.1 cm. The coolant mass flow that is injected through the liner panels, dilution holes, and exit slots is distributed in terms of a percentage of the total mass flow rate exiting the combustor. The distribution of this coolant mass flow is shown in Table 3-1. Note that only 38 % of the exit mass flow actually passes through the combustor entrance. The total amount of film-coolant that is used accounts for 25 % of the exit mass flow and the total amount of dilution flow accounts for 35 % of the total exit mass flow.

The total mass flow rate exiting the combustor and entering the downstream nozzle guide vanes of the turbine was determined on a per sector basis (two vane pitches) by using the given engine data shown in Table 3-2 and equations 3-1 through 3-5. These equations include the continuity equation (3-1), an equation of state (3-2), and three gas dynamics equations (3-3 to 3-5).

$$\dot{m} = \rho VA \quad (3-1)$$

$$\rho = \frac{P}{RT} \quad (3-2)$$

$$V = Ma\sqrt{\gamma RT} \quad (3-3)$$

$$P = \frac{P_0}{\left(1 + \frac{\gamma-1}{2} Ma^2\right)^{\frac{\gamma}{\gamma-1}}} \quad (3-4)$$

$$T = \frac{T_0}{\left(1 + \frac{\gamma-1}{2} Ma^2\right)} \quad (3-5)$$

The total mass flow rate exiting the engine combustor was determined to be approximately 1.2 kg/s per sector. This calculation is verified in Appendix B. The flow exiting the combustor can also be quantified in terms of the flow parameter (φ) shown in equation 3-6.

$$\varphi = \frac{\dot{m}\sqrt{T_0}}{P_0} \quad (3-6)$$

Using the mass flow rate per sector and the engine data in Table 3-2, the flow parameter per sector for this combustor is approximately $4.8 \times 10^{-5} \frac{\text{kg} \sqrt{\text{K}}}{\text{Pa} \cdot \text{s}}$. The air loading parameter (*ALP*) for this combustor, defined in equation 3-7 (Lefebvre, 1998), was determined to be 0.66×10^{-4} .

$$ALP = \frac{P_0^{1.75} \cdot A_{ref} \cdot D_{ref}^{0.75} \cdot e^{\frac{T}{300}}}{\dot{m}} \quad (3-7)$$

In equation 3-7, the total pressure (P_0) is in units of kPa and the temperature (T) is in units of Kelvin. The loading parameter η_θ , given by Walsh and Fletcher (1998), is defined in equation 3-8 and for this combustor was determined to be 1.8.

$$\eta_\theta = \frac{\dot{m}}{Vol \cdot P_0^{1.8} \cdot 10^{0.00145(T-400)}} \quad (3-8)$$

The total pressure and temperature in equation 3-8 are in the same units as in equation 3-7.

To accurately simulate the flow field conditions exiting the engine combustor, an analysis of the flow field within the combustor was required. This analysis involved performing flow calculations at several mainstream axial locations within the combustion chamber, as shown in Figure 3-3. To simulate the flow field conditions exiting the engine combustor, several parameters were matched to be consistent between the engine combustor and the wind tunnel combustor simulator. These parameters included the Reynolds number at the combustor exit, the axial acceleration of the mainstream within the combustor, the film cooling and dilution hole momentum flux ratios, and the coolant mass flow percentages based on the total mass flow rate at the combustor exit.

Determining the axial acceleration of the mainstream flow field began with the axial Mach number distribution shown in Figure 3-4. With this distribution and the detailed flow

calculations presented in Appendix C, the mainstream axial velocity distribution was calculated. The axial acceleration of the flow field was then determined by differentiating a second order polynomial that was curve fitted to the velocity distribution and is also shown in Figure 3-4. Note that the acceleration is expressed in terms of a non-dimensional acceleration parameter, K , defined in equation 3-9.

$$K = \frac{v}{V_{\infty}^2} \frac{\partial V_{\infty}}{\partial x} \quad (3-9)$$

Negative values of K indicate that the average mainstream velocity is decelerating and positive values of K indicate that the flow is accelerating. As shown in the figure, the mainstream flow within the combustor experiences positive acceleration throughout the entire axial length of the chamber. The figure also shows that the mainstream flow in the first half of the combustor ($X/L = 0.0$ to 0.5) experiences values of K that are considerably larger than those in the second half. This behavior is expected due to the relatively larger mainstream velocities that are present in the latter half of the chamber.

The momentum flux ratio, defined in equation 3-10, is the ratio of momentum that an injected jet has relative to the momentum of the mainstream cross-flow that it is being injected into.

$$I = \frac{\rho_{jet} V_{jet}^2}{\rho_{\infty} V_{\infty}^2} \quad (3-10)$$

It is expected that with increasing I values the penetration distance of the jet into the mainstream increases. The details involved in determining the momentum flux ratios associated with the film-cooling jets and dilution jets are also presented in Appendix C. The average momentum flux ratios for the dilution holes were given by Pratt & Whitney to be 100 for the first row and 20 for the second row. A summary of these ratios for the film-cooling and dilution jets on both the inner and outer diameter liners is presented in Table 3-3 and Table 3-4. Also shown in these two

tables are the average density ratios (given by Pratt & Whitney) and the average mass flux ratios (M), defined in equation 3-11, associated with the film-cooling jets and dilution jets.

$$M = \frac{\rho_{jet} V_{jet}}{\rho_{\infty} V_{\infty}} \quad (3-11)$$

It can be seen from the two tables that the average velocity ratios, mass flux ratios, and momentum flux ratios for the liner panels are very similar for the inner and outer diameter combustor walls.

The number of film-cooling holes for a given liner per sector was determined by using the mass flow rate through the liner, the density and velocities of jets passing through the liner (determined in Appendix C), and the given film-cooling hole diameter ($D = 0.76$ mm). The total number of film-cooling holes (N) for a given liner was calculated using equation 3-12.

$$N = \frac{\dot{m}_{panel}}{\rho_{jet} V_{jet} A_{jet}} \quad (3-12)$$

The film-cooling holes in all liner panels are arranged in a staggered array that results in an equilateral triangle pattern, shown in Figure 3-5. The number of film-cooling holes in a given liner panel was determined to be larger for the outer diameter liner than the inner diameter liner. This was expected due to the slightly larger coolant mass flow that is delivered to the outer diameter liner. This additional coolant is needed due to the larger surface area of the liner panels (per sector) for the outer diameter wall relative to the inner diameter wall. Tabulated in Table 3-5 is the total film-cooling hole area in each liner panel.

The Reynolds number based on vane chord length, defined in equation 3-13, is the ratio of the flow's inertial forces to viscous forces.

$$Re = \frac{\rho VC}{\mu} \quad (3-13)$$

In equation 3-13, the symbol V denotes the velocity of the gas exiting the combustor. In the real operating engine, the true chord length is approximately 6.6 cm. Under design operating conditions and altitude, the average mainstream velocity exiting the combustor and entering the vane passage is approximately 92.8 m/s and it has a density of approximately 2.1 kg/m^3 and a dynamic viscosity of approximately $5.86 \times 10^{-5} \text{ Pa}\cdot\text{s}$. Therefore, the Reynolds number at the combustor exit based on chord length is approximately 2.2×10^5 . This is in agreement with the calculations performed by Radomsky (2000). A summary of all the conditions used to design the wind tunnel combustor simulator is presented in Table 3-6.

3.2 Overall Design of the Combustor Simulator

The general shape of the combustor simulator was designed to be similar to that of the engine combustor; a constant area cross-section followed by a contraction. One difference between the two, however, was the use of a symmetric contraction for the simulator rather than an asymmetric contraction as shown in Figure 3-6. A symmetric contraction was easier to physically construct and install into the existing facility. Also, symmetric conditions are beneficial for concurrent computational studies. To insure symmetry, however, would require imposing the restriction of generating identical flow conditions on both the inner and outer diameter liners. Also, since the existing turbine vane section in the wind tunnel is a linear cascade with flat endwalls, a two-dimensional geometry was used rather than an annular one as shown in Figure 3-7. For the experiments conducted in this thesis, the flow conditions associated with the inner diameter liner of the engine combustor were simulated. The simulation of the flow conditions associated with the outer diameter liner was considered to be follow-on work.

Due to the temperature limits of the existing fiberglass wind tunnel, the temperature ratio between the mainstream and the coolant within the engine could not be matched. An analysis for thermally conditioning the mainstream and coolant flows was conducted. From this analysis, a reasonable strategy was to heat the primary flow and cool the secondary (coolant) flow giving a

temperature difference of nominally 20 °C. The simulator was designed for a maximum temperature difference of approximately 20 °C between the coolant and the mainstream corresponding to a maximum density ratio (coolant density to mainstream density) of approximately 1.07.

The arrangement of the film-cooling holes in the simulator was kept similar to that in the engine. The diameter of the holes was scaled up nine times to approximately 0.7 cm. The streamwise angle was kept constant at 30 degrees but the compound angle was changed from 45 degrees to zero degrees. If the compound angle had been matched there would have been an accumulation of mass near one side of the simulator resulting in asymmetric exit conditions. Note that several combustor liner designs do have axial cooling holes.

One of the most important considerations in designing the combustor simulator was its installation into the existing wind tunnel facility. For the simulator to be installed upstream of the turbine vane cascade, three existing sections had to be removed. This included the nozzle section, the main test section, and the diffuser section shown in Figure 3-1. The simulator design that replaced these three sections split the mainstream flow into three separate paths including a primary path and two secondary paths. The design consisted of a transition section and combustor simulator sections shown in Figure 3-8.

The primary path delivered flow to the mainstream inlet of the combustor simulator that was designed to heat the main flow by 20 °C above the coolant flow temperature. The secondary paths, located above and below the primary path, provided the coolant to be injected through liner film-cooling holes, dilution holes, and exit slots. To establish a good baseline of the flow and thermal field conditions exiting the combustor simulator without any secondary flow interactions, the downstream vane cascade was removed and replaced with a two-dimensional exit test section.

The combustor simulator's exit geometry needed to be consistent with the inlet geometry of the existing turbine vane cascade to allow for smooth transition of the flow field. For this

reason, the exit dimensions of the simulator were matched to the rectangular inlet cross-section of the vane cascade. This inlet cross-section corresponded to one vane span in height (55 cm) and 2.44 vane pitches (111.8 cm) in width. The width was designed to be slightly larger than one sector (2 vane pitches) to remove any flow affected by the sidewalls. The width of the combustor simulator remained constant throughout its entire axial length.

The first two liner panels in the simulator were designed to have lengths equivalent to the first two engine liner panels scaled up by a factor of nine, which were 40.6 cm each in length. The contraction section (third and fourth liner panels) and the inlet height were designed by matching the mainstream acceleration parameter in the engine while maintaining an overall axial length of the simulator of 161 cm (nine times that of the engine). Calculations at several axial locations within the combustor simulator, similar to those performed in the analysis of the engine combustor, were made to match the axial distribution of the acceleration parameter and the exit Reynolds number. A summary of these flow field calculations is given here.

The average exit velocity was based on the mass averaged temperature of the flow exiting the combustor simulator (29 °C), the local atmospheric pressure, and the desired exit Reynolds number. The mass flow rate exiting the combustor simulator was then calculated and used for determining the flows for the liner panels, dilution holes, and exit slots. Given the mass flow distribution and the combustor simulator's exit height, the inlet height was chosen to match the acceleration parameter of the engine. A contraction angle of 17.1°, with the length of the third liner panel being 37.9 cm and the length of the fourth liner panel being 45.7 cm, produced a mainstream acceleration similar to that of the engine. Figure 3-9 shows a comparison of the acceleration found in the engine combustor and that of the combustor simulator. Good agreement occurs over a large majority of the latter portion of the simulator. This resulted in the overall length of the combustor simulator being 161 cm, which is consistent with the 9x scaling. It is also important to note that the contraction angle that was determined is an approximate average of the contraction angles on the inner and outer diameter liners in the engine combustor. A summary of the overall combustor simulator geometry is presented in Table 3-7.

Having set the overall combustor simulator dimensions as previously described, the liner panels were designed to match the engine's coolant mass flow rates and momentum flux ratios. Knowing the velocity and density of the mainstream along with the coolant density, the average jet velocity was calculated to match a given average momentum flux ratio for each liner using equation 3-10. Since the coolant density, average jet velocity, and coolant mass flow rate were known for the simulator, the total jet area needed for the film-cooling holes for each liner was determined using the mass flow rate equation 3-1. The jet area associated with a single film-cooling hole was determined by using the scaled up diameter of approximately 0.76 cm. The total number of film-cooling holes needed for each liner was determined using equation 3-12. The film-cooling holes were arranged in the previously mentioned pattern of equilateral triangles with the spacing between holes such that the distribution of holes uniformly covered the entire surface area of a given liner panel. A summary of the liner panel geometry and the total film-cooling hole area used in the combustor simulator is presented in Table 3-8. The total mass flow rate and mass averaged freestream velocity at the trailing edge of each liner panel are shown in Table 3-9.

The dilution holes were arranged in a given staggered pattern, shown in Figure 3-10, such that the first row contained holes that were aligned with the stagnation of the downstream nozzle guide vanes and the second row contained holes that were aligned with the center of the vane passage. For the existing turbine vane cascade this resulted in the first row containing three dilution holes and the second row containing two dilution holes. Note that this also resulted in the lower liner dilution holes being aligned with the upper liner dilution holes. The diameter of the dilution holes were designed using the given momentum flux ratios of 100 for the first row and 20 for the second row. Knowing the density and velocity of the mainstream at these axial locations along with the density of the coolant in the simulator, the average jet velocity exiting the dilution holes was determined using equation 3-10. Knowing this average jet velocity, the coolant density, and the mass flow rate through the dilution holes, the total dilution hole area (and diameters) was determined using equation 3-1. A summary of the dilution hole geometry is also presented in Table 3-8.

The film-cooling slots located at the exit of the combustor simulator were directly scaled-up (9x) versions of the film-cooling slots in the engine combustor. The number of feed holes that supplied coolant to the slots was determined to insure the needed mass flow rate.

3.3 Primary Flow Path in the Combustor Simulator

The primary flow path arrangement, shown in Figure 3-11, consisted of a rectangular cross-section entrance followed by a large perforated plate. Following this perforated plate, there were several feet of constant area where the flow passed over an array of heated finned rods to raise its temperature to approximately 40 °C. Following this heater section, the flow then entered a honeycomb and screen section to straighten the flow and reduce turbulence. After the heated flow passed through the honeycomb and screen, it then entered the combustor simulator. This primary flow path represents the hot gas path in the engine combustor.

The perforated plate, located at the inlet of the primary flow path, was designed with two goals in mind. First, it needed to provide the primary flow path with a sufficient pressure drop such that the coolant remainder of the flow was directed to the secondary coolant chambers. Second, it needed to consist of a hole pattern that would distribute the incoming mass flow uniformly across the entire primary path.

This plate was designed by first calculating an estimate of the required open flow area needed to reduce the upstream pressure such that flow rate downstream of the perforated plate provided an average velocity of 1.5 m/s. In flows that are dominated by inertia effects, such as a flow through a perforated plate, pressure drops can be related to the fluid's dynamic pressure through the relationship given in equation 3-14.

$$P_{loss} = K_L \frac{1}{2} \rho V^2 \quad (3-14)$$

In this case, the loss coefficient used was that for a simple jet expansion, $K_L = 1.0$. The desired pressure difference was measured across a previously installed shutter system in the primary flow path with the shutters positioned to produce the desired flow rate. An explanation for the removal of the shutter system and its replacement with the perforated plate is presented in a benchmarking discussion later in Section 4-1. Using equation 3-14, a direct calculation of the fluid jet velocity was obtained. Already knowing the desired primary path mass flow rate from the facility design, approximately 1.83 kg/s, the approximate jet area was then calculated using the mass flow rate relationship given earlier in equation 3-1.

To insure a uniform flow at the inlet to the combustor simulator, tests were conducted to fine-tune the hole sizes in the perforated plate. The final hole pattern is displayed in Figure 3-12. Note that it consists of 2.0 cm, 2.5 cm, and 5.0 cm diameter holes with a more dense hole arrangement towards the outer side wall of the primary flow path to account for the flow turning in the wind tunnel elbow.

After the flow in the primary path passes through the perforated plate it then passes through a bank of 18 Watlow fin-strip heater elements that each deliver approximately 3,050 Watts of power giving a total of 55 kW. The purpose of this heater array was to raise the primary path flow temperature by approximately 20 °C when the wind tunnel was in a closed loop configuration. Since the tests presented in this thesis were made in an open loop tunnel, the temperature difference was not as high at 12.2 °C. The entire heater bank is controlled by three Watlow Series 988 1/8 DIN microprocessor-based temperature/process controllers and a cascade of six type K thermocouples approximately 0.32 cm in diameter. One controller sets the current load passing through the lower six fin-strip heater elements (lower zone), another sets the current load passing through the middle six elements (middle zone), and the third controller sets the current load passing through the upper six elements (upper zone). Two type K thermocouples were placed in each zone, one located approximately 2.5 cm downstream of the heater elements and the other located at the mainstream inlet of the combustor simulator. To obtain the correct flow temperature in a particular zone, the current load passing through the heater elements was adjusted manually in terms of a percentage of the total allowable current load for that heater

element array. The resulting settings for the upper, middle, and lower zones were 96 %, 97 %, and 97 %, respectively.

The primary path flow is then directed through a section containing honeycomb and screens to straighten the flow and reduce turbulence levels. It then enters the combustor simulator section as the mainstream inlet flow.

3.4 Secondary Flow Path in the Combustor Simulator

The flow that does not enter into the primary path is directed through one of two symmetric secondary paths shown in Figure 3-13. The flow that enters the secondary paths is first directed through a water fin and tube exchanger with the intent to further reduce the flow's temperature. It then enters a secondary path supply chamber, shown in Figure 3-14, which supplies the liner panels, dilution jets, and exit slots with coolant flow. As shown in the figure, each supply chamber contains a series of six plenums. These include one plenum for each of the four liner panels and one plenum for each row of dilution holes. The mass flow rates and the difference between the plenum pressure and the mainstream static pressure at that axial location under operating conditions are tabulated in Table 3-10 for each liner panel, both rows of dilution holes, and the exit slots.

The plenums provide independent control of the flow rates to the liner film-cooling holes and dilution holes. The amount of mass flow passing through a given plenum is controlled by an adjustable shutter that is located at the entrance to the plenum. The positioning of this shutter in turn regulates the plenum's supply area and total pressure. Knowing the total pressure within a plenum, the static pressure of the mainstream at that corresponding axial location, and the discharge coefficient of the cooling holes (discussed in more detail in section 4-2), the amount of mass flow exiting the plenum through either the liner film-cooling holes or dilution holes may be determined. For a more in-depth explanation of determining this mass flow rate see Appendix D.

The downstream test plate and each liner panel were made of polyurethane foam having a low thermal conductivity (0.037 W/m-K). Each liner panel was 1.3 cm thick and the downstream test plate was 3.8 cm thick. The foam was used to simulate an adiabatic wall to establish the adiabatic effectiveness, defined in equation 3-15, for the liner panels and downstream endwall.

$$\eta = \frac{T_{\infty} - T_{aw}}{T_{\infty} - T_c} \quad (3-15)$$

In equation 3-15, the variable denoted as T_{∞} is the mass averaged temperature of the mainstream at the combustor simulator exit and T_c is the coolant temperature. Each liner panel and the test plate were repeatedly sanded to provide a smooth boundary and was then lightly spray-painted black to obtain a high emissivity for infrared camera imaging.

The remainder of the coolant in the secondary path supply exits the chamber through a slot at the combustor-turbine interface. Feed holes direct the coolant flow through a pin fin arrangement prior to exiting a slot as shown in Figure 3-15. The purpose of this exit slot is to provide the endwall region with coolant to reduce heat transfer from the heated mainstream to the endwalls and vanes. The pin fins were constructed using 127 small wooden pegs that were 1.0 cm in diameter and 1.6 cm in height and evenly distributed across the entire width of the slot. The purpose of these pegs was twofold. First, they provided the flow exiting the feed holes with a pressure drop for flow regulation in the engine. Second, they provided a means to conduct heat away from the pin fin plate of the exit slot. For the simulator this pin fin plate was also made of polyurethane foam, approximately 1.0 cm thick, and was sanded and painted black.

3.5 Test Section Downstream of the Combustor Simulator

A constant area test section was placed downstream of the combustor simulator to establish a baseline of the flow and thermal field conditions exiting the combustor without any

secondary flow interactions with the vane cascade. This test section, shown in Figure 3-16, consists of an endwall made of a flat layer of polyurethane foam approximately 1.6 m long, 1.12 m wide, and 3.8 cm thick. The thermal conductivity of the foam was 0.037 W/m-K to again provide an adiabatic boundary condition. The surface of the foam exposed to the flow was repeatedly sanded in order to establish a smooth boundary and was then airbrushed with black paint to obtain a high emissivity for infrared camera imaging. This layer of foam is supported by a 2 cm thick piece of birch plywood and is enclosed inside a rectangular channel made of Plexiglas. The entire section is supported using Unistrut and is securely fastened to the exit of the combustor simulator using aluminum angle irons around its inlet perimeter.

The piece of Plexiglas covering the top of the test section contains 15 removable ports, shown in Figure 3-17, that were used to take infrared camera pictures of the endwall surface temperature. Thirty type E thermocouples (0.25 mm diameter) were embedded in the endwall plate to calibrate the infrared camera. The thermocouples were positioned such that they were flush with the endwall surface as shown in Figure 3-18. A small amount of highly thermally conductive Omega paste (OmegaTherm 201) was used to fill in the small grooves made in the endwall foam that contained the thermocouple beads.

3.6 Instrumentation

Several types of measurements were made in the benchmarking of the combustor simulator facility. Total pressure measurements were taken at the combustor simulator exit and within the supply plenums. Static pressure measurements were made on the surface of the liner panels. Temperature measurements were taken at the combustor simulator inlet and exit, in the supply plenums, and on the adiabatic surface downstream of the combustor simulator. Velocity measurements were taken at the combustor simulator inlet and exit and at the exit of the film-cooling and dilution holes. Turbulence and length scale measurements were taken at the combustor simulator inlet and exit. This section gives a complete description of the instrumentation that was used in conducting these measurements.

Total pressure measurements were taken at the exit of the combustor simulator using a 1.6 mm diameter United Sensor Keil probe (Type KA). An enlarged schematic view of the head of this Kiel probe is shown in Figure 3-19. The Kiel probe is less sensitive to the streamwise orientation of the probe head than a typical pressure probe, for example a pitot-static tube, due to the shroud that covers the probe head. The probe specifications indicate insensitivity to the direction of flow within a yaw range of $\pm 52^\circ$ and a pitch range from $+47^\circ$ to -40° . This probe was connected to the high pressure port on an Omega PX 653 differential pressure transducer using 1.6 mm inner diameter vinyl tubing. This transducer had a pressure range of 0 to 498 Pa with an accuracy of 0.5% full scale. The low pressure port was left open to the atmosphere. A Setra Digital Pressure Gage (Model 370) was used to measure the atmospheric room pressure. This gage had a pressure range of 80,000 to 110,000 Pa with an accuracy of 0.02% full scale. Pressure measurements were acquired using LabView data acquisition software. A typical pressure measurement involved an average of 20,000 samples acquired at 1 kHz.

Static pressure taps were used to take total pressure measurements within each film-cooling plenum and static pressure measurements of the mainstream at the leading edge of each liner. The taps were made of 0.8 mm inner diameter brass tubing and were connected by 1.6 mm inner diameter vinyl tubing to the high pressure port on a Setra Systems Model 264 differential pressure transducer. This transducer had a range of 0 to 498 Pa with an accuracy of 0.5% full scale. The low pressure port was left open and atmospheric pressure was determined as previously mentioned. Pressure measurements were acquired using LabView data acquisition software. A typical static pressure measurement involved an average of 10,000 samples acquired at 1 kHz.

Temperature measurements were taken at the combustor simulator inlet and exit using a thermocouple rake. The rake, shown in Figure 3-20, contained five thermocouples that were spaced 2.5 cm apart. The thermocouple wire was type E with an approximate diameter of 0.3 mm. The thermocouple wire transmitted its voltage signal to a data acquisition system. This system included a Dell personal computer with a National Instruments (NI) AT-MIO-16E-2 data

acquisition board that was connected to a NI SCXI 1000 chassis. The chassis contained two NI SCXI 1100 32 channel multiplexer amplifiers that each contained one NI SCXI-1303 32 Channel Isothermal Terminal Blocks. The voltage signal from the thermocouple was directed to the terminal blocks that contained a high accuracy thermistor, cold-junction temperature sensor, and an isothermal copper plane to minimize the temperature gradients across screw terminal connections. The voltage signal was then directed into the multiplexer amplifier that amplified the μV signal and then directed it into the PC data acquisition system where it was processed using LabView software. A typical temperature measurement involved an average of 3000 samples acquired at 100 Hz. The temperature within the plenums and secondary path supply chambers were measured using the same type E thermocouples and NI data acquisition system.

Temperature measurements were also taken on the adiabatic endwall surface of the flat test section located downstream of the combustor simulator using an infrared camera. The camera, an Inframetrics Model 760, was calibrated over the full range of endwall temperatures in situ using one type E thermocouple (0.3 mm diameter wire) that was embedded in and positioned flush with the endwall surface. This was done in order to determine the endwall emissivity and the background temperature. It was found that an emissivity of approximately $\varepsilon = 0.90$ and a background temperature of approximately $22.0\text{ }^\circ\text{C}$ needed to be set on the camera system to obtain good agreement with the thermocouple readings. A typical temperature image taken with the camera involved a spatial integration over a circle approximately 0.37 cm in diameter with an overall rectangular viewing area of approximately 21.5 cm by 16 cm. Each temperature measurement was an average of 16 images and from an uncertainty analysis it was determined that five of these 16-averaged images were sufficient to obtain a good average. The location of each image was identified using small cross marks placed on the endwall surface. The temperature data information in each image was extracted into ASCII formatted text using the camera's imaging software and a MATLAB routine was written to process the individual images and to assemble them into one complete surface temperature distribution.

Velocity measurements were taken at the combustor simulator inlet and exit, at the exit of the film-cooling holes and across the diameters of the dilution holes. The velocity measurements

at the simulator inlet and exit as well as at the trailing edge of the first liner panel were taken using a single sensor hot-wire. The hot-wire sensor had a diameter of approximately 5 μm and a length of approximately 1.3 mm. The operating resistance was set at 9.57 Ω . This hot-wire was connected to a Thermo-Systems Inc. (TSI) Constant Temperature Anemometer (Model 1010A) by a BNC coaxial cable. The output voltage signal from the anemometer was transmitted to an analog-to-digital converter that directed the signal into the data acquisition system. The frequency response of the hot-wire probe was analyzed using the anemometer's built-in square wave generator and directing the anemometer's output voltage signal into the input terminal of a Tektronix 2 Channel Digital Real Time Oscilloscope (Model TDS 220). The anemometer's stability control and loop gain settings were adjusted to achieve a signal time constant, detectable on the oscilloscope screen, of approximately 10 μs . This corresponded to a frequency response, defined in equation 3-16, of 100 kHz, however the analog output was filtered at 10 kHz.

$$f_{resp} = \frac{1}{\tau_s} \quad (3-16)$$

The hotwire was calibrated over the full range of operating velocities using a TSI hot-wire calibration unit. This unit received flow from a high pressure airline within the laboratory and regulated it to the desired pressure level. The unit passed the air through a small cylindrical chamber containing multiple highly dense screens that reduced turbulence levels. A pressure port located axially downstream of the last screen was used to monitor the chamber pressure (relative to atmosphere). The flow exited the chamber as a jet through a small nozzle with an exit diameter of approximately 0.4 cm. The hot-wire was positioned such that the junction was located in the center of this exit jet approximately 0.15 cm away from the hole exit. Using the chamber pressure and the method presented in Appendix D, the average jet velocity exiting the hole and passing over the hot-wire junction was determined. A relationship between the velocity of the air and the voltage signal across the hot-wire was then established. A typical calibration, shown in Figure 3-21, involved 25 to 30 data points. The data was then curve fit with a fourth order polynomial. This curve fit between hot-wire voltage and air velocity was then entered into

a LabView data acquisition program that acquired the hot-wire voltage information. A typical velocity measurement involved an average of 100,000 samples taken at 10 kHz.

The velocity of the air entering the combustor simulator was relatively low (1.5 m/s). This meant that the velocity measurements at this location required a hot-wire probe calibration over relatively low pressures within the chamber of the calibration unit. Therefore, the pressure within the chamber was acquired using a Setra Systems Model 264 differential pressure transducer that had a range of 0 to 125 Pa and an accuracy of 0.5% full scale. The velocity measurements taken at the exit of the simulator were relatively high (6.8 m/s) and therefore the pressure within the chamber was acquired using the Omega PX 653 differential pressure transducer that had a range of 0 to 498 Pa and an accuracy of 0.5% full scale.

The velocity measurements just at the exit of the film-cooling holes were taken with a pitot-static tube with a 1.6 mm diameter probe head. This probe was connected to the Omega PX 653 differential pressure transducer with a range of 0 to 498 Pa using 1.6 mm inner diameter vinyl tubing. A typical velocity measurement involved an average of 10,000 samples taken at 1 kHz. The velocity measurements taken across the diameters of the dilution holes were taken with a pitot-static tube that had a 3.1 mm diameter probe head. This probe was connected to the Omega PX 653 differential pressure transducer with a range of 0 to 498 Pa using 3.1 mm inner diameter vinyl tubing. A typical velocity measurement involved an average of 10,000 samples taken at 1 kHz.

The turbulence measurements were calculated using the hot-wire velocity data. Turbulence measurements were taken at the combustor simulator inlet and exit as well as at the trailing edge of first liner panel. Turbulence intensity was defined in two different ways. The measurements taken at the combustor simulator inlet and exit were quantified according to the ratio of u_{rms} to the local velocity U . The turbulence measurements taken at the trailing edge of the first liner panel were quantified according to the ratio of u_{rms} to the freestream velocity U_{∞} .

The turbulence energy spectra and length scale measurements involved acquiring eight velocity data samples at ten different locations. Each data sample contained 80,000 data points sampled at a frequency of 20 kHz. The highest frequency that can be resolved for a given sampling frequency (f_s) is determined by the Nyquist frequency (f_{Nyq}) defined in equation 3-17.

$$f_{Nyq} = \frac{f_s}{2} \quad (3-17)$$

A signal containing frequencies lower than the Nyquist frequency is accurately sampled. A signal containing frequencies greater than the Nyquist frequency is not accurately sampled and the frequencies above f_{Nyq} appear incorrectly as lower frequencies in the discrete sample (Beckwith et al., 1993). This phenomenon is known as aliasing. To avoid this problem, the sampling frequency was chosen to be at least twice the signal's highest frequency. Since the analog output on the anemometer was filtered at 10 kHz, a sampling frequency of 20 kHz was used.

The integral length scales were determined by evaluating an autocorrelation curve of a given velocity sample. The autocorrelation coefficient of a continuous velocity function $u(t)$ is defined in terms of the velocity fluctuations defined in equation 3-18. The autocorrelation coefficient is defined in equation 3-19.

$$u' = u - U \quad (3-18)$$

$$R_u(\tau) = \frac{\overline{u'(t) \cdot u'(t + \tau)}}{(u'_{rms})^2} \quad (3-19)$$

Since the velocity measurements taken with the hot-wire were sampled at a constant time interval, Δt , the definition of the root-mean-square and the autocorrelation coefficient for the discrete sample become the expressions shown in equations 3-20 and 3-21.

$$u'_{rms} = \sqrt{\frac{1}{N} \left(\sum_{i=1}^N (u'_i)^2 \right)} \quad (3-20)$$

$$R(\tau) = \frac{1}{N} \left(\frac{\sum_{j=1}^N u'_i \cdot u'_{i+j}}{(u'_{rms})^2} \right) \quad \text{where } \tau = j \cdot \Delta t \quad (3-21)$$

The expression in equation 3-21 was evaluated using Matlab at each time lag from $\tau = 0$ to $N \cdot \Delta t$ in order to produce an autocorrelation curve for each of the eight velocity samples. A typical autocorrelation curve of a velocity data sample for a turbulence level of 15 % is shown in Figure 3-22. It can be seen that the autocorrelation curve is a plot of the autocorrelation coefficient versus the time lag. Since $R(\tau)$ is dimensionless and τ has units of time, the area underneath the curve is the integral time scale of the turbulence. This is also stated in mathematical form in equation 3-22.

$$T = \int_{\tau=0}^{\tau=\infty} R(\tau) d\tau \quad (3-22)$$

This expression is evaluated only to the first zero crossing of $R(\tau)$ due to the finite time increment between velocity data samples. If the autocorrelation curve associated with a particular data sample did not cross zero at any time lag, the expression in equation 3-21 was evaluated for time lags up to where the autocorrelation function was approximately 0.05. An integral time scale was determined for each of the eight velocity samples. An average integral time scale was determined by taking a linear average of the eight individual integral time scales. An average local mean velocity (U) was determined by taking a linear average of the eight individual local mean velocities. Knowing the average integral time scale of the turbulence and the average local mean velocity, Taylor's hypothesis, defined in equation 3-23, was used to determine the associated integral length scale of the turbulent eddies.

$$A_x = U \cdot T \quad (3-23)$$

Sauer (1996) showed that this autocorrelation method with the invoking of Taylor's hypothesis was a valid technique for turbulence levels up to 20% using an active grid turbulence generator.

In addition to the integral length scales, the hotwire measurements allowed for the determination of the energy spectra. The turbulent kinetic energy (u'^2) associated with the frequency (f) of the fluctuations (u') is denoted as $E_{11}(f)$ and is defined in equation 3-24.

$$E_{11}(f) = \frac{|FFT(u')|^2}{\Delta f_s} \quad (3-24)$$

The frequency bandwidth (frequency resolution) of the data sample is denoted as Δf_s and is defined in equation 3-25.

$$\Delta f_s = \frac{f_s}{N_s} \quad (3-25)$$

A data sample containing 80,000 points sampled at 20,000 Hz gives a frequency bandwidth of 0.25 Hz. The numerator of the expression given in equation 3-24 is determined by first performing a discrete Fourier transform of the velocity fluctuations (u') using Matlab. Entering the expression given in equation 3-26 into Matlab returns the discrete Fourier transform of the vector u' , computed with a fast Fourier transform (FFT) algorithm.

$$\xi = fft(u') \quad (3-26)$$

The expression given in equation 3-26 must then be normalized by the number of data points in the sample (N_s), in this case 80,000, as shown in equation 3-27.

$$\omega = \frac{\xi}{N_s} \quad (3-27)$$

The expression denoted as ω in equation 3-27 is then multiplied by its complex conjugate ω^* and then this quantity is multiplied by a factor of two as shown in equation 3-28.

$$\Psi = 2 \times (\omega \cdot \omega^*) \quad (3-28)$$

The expression denoted as Ψ in equation 3-28 is equivalent to the expression in the numerator of equation 3-24, i.e. $\Psi = |FFT(u')|^2$. The multiplication by two in equation 3-28 is a Matlab amplitude correction factor.

The energy spectra is typically presented in a form such that the energy $E_{11}(f)$ is normalized by the factor $\frac{U}{(u'_{rms})^2 \cdot \Lambda_x}$ and plotted versus the quantity $\kappa_1 \cdot \Lambda_x$ where the wave number (κ_1) is defined in equation 3-29.

$$\kappa_1 = \frac{2\pi f}{U} \quad (3-29)$$

A comparison is also usually made between the energy spectra of the data and the von Karman energy spectra defined in equation 3-30.

$$\frac{E_{11}(f) \cdot U}{(u'_{rms})^2 \cdot \Lambda_x} = \frac{4}{\left[1 + \left(\frac{8\pi f \cdot \Lambda_x}{3U}\right)^2\right]^{5/6}} \quad (3-30)$$

A traverse system, shown in Figure 3-23, was used to position the thermocouple rake, pressure probes, and the hot-wire to the desired measurement locations. The system consisted of a Velmex bi-slide assembly that provided 88 cm of linear movement in both the pitch and span directions and could be positioned at several axial locations using the guide rail supports. The bi-slide assembly was equipped with two motor controlled screws (one for pitch movement and one for span movement) that were computer controlled using a Velmex VP9000 Controller.

Each traverse screw was approximately 0.9 cm in diameter with a pitch of approximately 7.9 turns/cm. Both motors allowed for an incremental screw movement as small as 6.0×10^{-3} mm in either the pitch or span directions.

3.7 Uncertainty Analysis

The uncertainties associated with the flow and thermal field measurements were determined using the Kline and McClintock (Moffat, 1988) propagation of uncertainty method. The total uncertainty of a variable U is defined in equation 3-31 to be the square root of the sum of the squares of the bias and precision uncertainties.

$$U_{total} = \sqrt{U_{bias}^2 + U_{precision}^2} \quad (3-31)$$

The precision uncertainty in a measurement was based upon a 95% confidence interval (two standard deviations). The uncertainty in a variable Y depends on the uncertainties in the independent variables that define Y through the relationship defined in equation 3-32.

$$U_Y = \pm \sqrt{\left(\frac{\partial Y}{\partial x_1} \cdot u_{x_1}\right)^2 + \left(\frac{\partial Y}{\partial x_2} \cdot u_{x_2}\right)^2 + \dots + \left(\frac{\partial Y}{\partial x_n} \cdot u_{x_n}\right)^2} \quad (3-32)$$

In equation 3-32, x_i represent the n independent variables that define Y and the u subscripted by x_i denotes the uncertainty in the specific independent variable.

The bias uncertainties associated with the pressure transducer measurements were given to be 0.5% of full scale. The precision uncertainty of a specific measurement was determined by taking five independent data samples. The bias uncertainties associated with the temperature measurements were determined by referencing an average of three thermocouples, located upstream of the combustor simulator, under design flow conditions at constant temperature. The

uncertainty associated with the infrared camera temperature measurements was determined using equation 3-31 where the bias uncertainty was determined from the thermocouples used to calibrate the camera and the precision uncertainty was based on five camera images each of which was an average of 16 frames.

A summary of the uncertainties that were determined in the experimental variables is presented in Table 3-11. A more in-depth analysis of the experimental uncertainties can be found in Appendix E.

Table 3-1 Distribution of Mass Flow in the Engine Combustor

Combustor Component	Percent of Total Mass Flow Rate Exiting the Combustor	
	Inner Diameter Liner	Outer Diameter Liner
Mainstream Inlet	38.3	
Liner Panel 1	1.5	2.75
Liner Panel 2	3.5	4.75
Liner Panel 3	3.5	4.75
Liner Panel 4	1.5	2.75
Dilution Row 1	8.75	8.75
Dilution Row 2	8.75	8.75
Exit Slot	0.7	1.0

Table 3-2 Engine Data at Combustor Exit

Ratio of specific heats, γ	1.28
Gas constant, R (J/kg-K)	292.4
Total Temperature (K)	1,666
Total Pressure (Pa)	1,034,200
Mach Number	0.1175
Exit Area per Sector (cm ²)	62.1
Reynolds Number (based on vane chord length)	2.2×10^5

Table 3-3 Flow Field Parameters in the Engine Combustor (Inner Diameter Liner)

Combustor Component	$\frac{\rho_{jet}}{\rho_{\infty}}$	$\frac{V_{jet}}{V_{\infty}}$	M	I
Liner Panel 1	3.3	2.0	6.6	13.2
Liner Panel 2	3.3	1.4	4.6	6.5
Liner Panel 3	2.3	1.1	2.4	2.5
Liner Panel 4	2.3	0.8	1.9	1.5
Dilution Row 1	3.3	5.5	18.2	100
Dilution Row 2	2.3	2.9	6.8	20

Table 3-4 Flow Field Parameters in the Engine Combustor (Outer Diameter Liner)

Combustor Component	$\frac{\rho_{jet}}{\rho_{\infty}}$	$\frac{V_{jet}}{V_{\infty}}$	M	I
Liner Panel 1	3.3	1.9	6.1	11.4
Liner Panel 2	3.3	1.3	4.3	5.7
Liner Panel 3	2.3	1.0	2.3	2.3
Liner Panel 4	2.3	0.8	1.8	1.4
Dilution Row 1	3.3	5.5	18.2	100
Dilution Row 2	2.3	2.9	6.8	20

Table 3-5 Total Film-Cooling Hole Area (per sector) in the Engine Combustor

Liner Panel	Inner Diameter Liner	Outer Diameter Liner
1	0.71 cm. ²	1.40 cm. ²
2	1.61 cm. ²	2.34 cm. ²
3	1.47 cm. ²	2.11 cm. ²
4	0.55 cm. ²	1.06 cm. ²

Table 3-6 Summary of Flow Field Conditions Used to Design the Combustor Simulator

Combustor Simulator Component	I	Percent of Total Exit Mass Flow Rate
Liner Panel 1	13.2	1.5
Liner Panel 2	6.5	3.5
Liner Panel 3	2.5	3.5
Liner Panel 4	1.5	1.5
Dilution Row 1	100	8.75
Dilution Row 2	20	8.75
Exit Slot	-	0.7
Exit Reynolds Number	2.2×10^5	

Table 3-7 Summary of the Combustor Simulator Geometry

Inlet Height (cm)	99.1
Axial Length (cm)	161.0
Width (cm)	111.8
Contraction Exit Height (cm)	49.8
Total Exit Height (cm)	55.0
Contraction Angle (degrees)	17.1

Table 3-8 Liner Panel and Dilution Hole Geometry in the Combustor Simulator

Combustor Simulator Component	Length (cm)	Total Hole Area (cm. ²)	S_p / D	S_s / D
Liner Panel 1	40.6	92.1	10.1	5.8
Liner Panel 2	40.6	217.9	6.1	3.5
Liner Panel 3	37.9	188.3	6.1	3.5
Liner Panel 4	45.7	78.4	10.1	5.8
Film-Cooling Hole Diameter (cm)	0.76	-	-	-
Dilution Hole Diameter (cm) – 1 st Row	8.5	170.2	60 (5.4 D_1)	90.2 (8.1 D_1)
Dilution Hole Diameter (cm) – 2 nd Row	12.1	229.9	60 (3.8 D_2)	120.8 (7.6 D_2)

Table 3-9 Total Mass Flow Rate and Mass Averaged Freestream Velocity at the Trailing Edge of Each Liner Panel

Liner Panel	Mass Flow Rate (kg/s)	Velocity (m/s)
1	1.95	1.6
2	2.98	2.4
3	4.01	4.2
4	4.13	6.8

Table 3-10 Plenum Pressure Drops and Mass Flow Rates in the Combustor Simulator

Combustor Simulator Component	$\Delta P_{pl} = P_{0_{pl}} - P_{\infty}$ (Pa)	Mass Flow Rate (kg/s)
Panel 1	38.0	0.06
Panel 2	37.4	0.15
Panel 3	50.1	0.15
Panel 4	54.8	0.06
Dilution Row 1	-	0.37
Dilution Row 2	-	0.37
Exit Slot	770.0	0.03

Table 3-11 Uncertainties in the Flow and Thermal Field Measurements

Variable	Percent Uncertainty
U (hot-wire)	2.6
U (pitot-tube)	1.2
U_{rms}	4.4
Tu (15%)	5.1
$\Delta P = -0.52$	4.5
$\Delta P = 0.11$	16.7
$\eta = 0.98$	4.6
$\eta = 0.23$	17.8
$\theta = 0.94$	5.0
$\theta = 0.25$	18.6
T	14.4
A_x	14.6

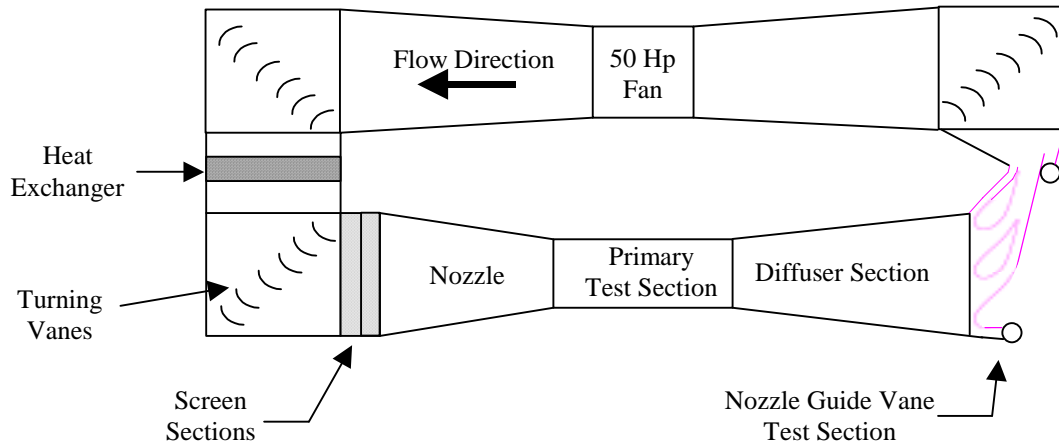


Figure 3-1 Schematic shows a plan view of the existing wind tunnel facility with its scaled-up (9x) turbine vane cascade.

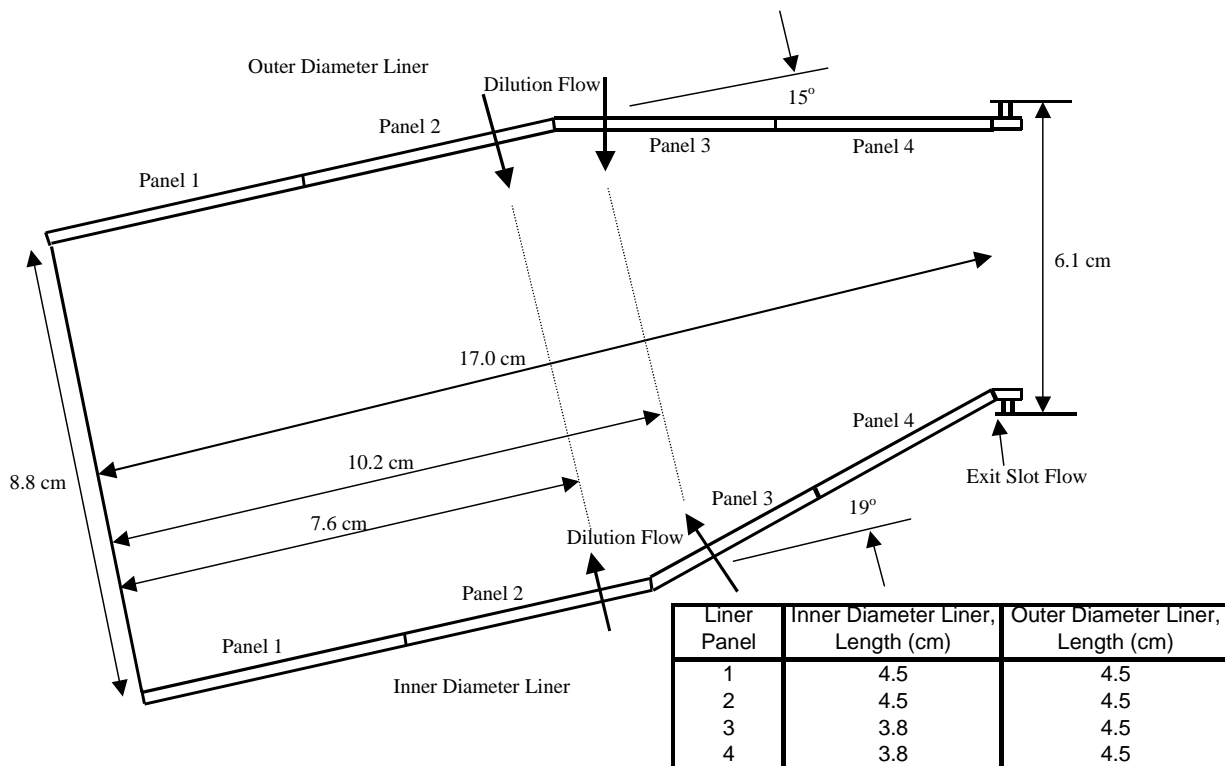


Figure 3-2 Schematic shows a cross-sectional view of a Pratt & Whitney annular combustor geometry.

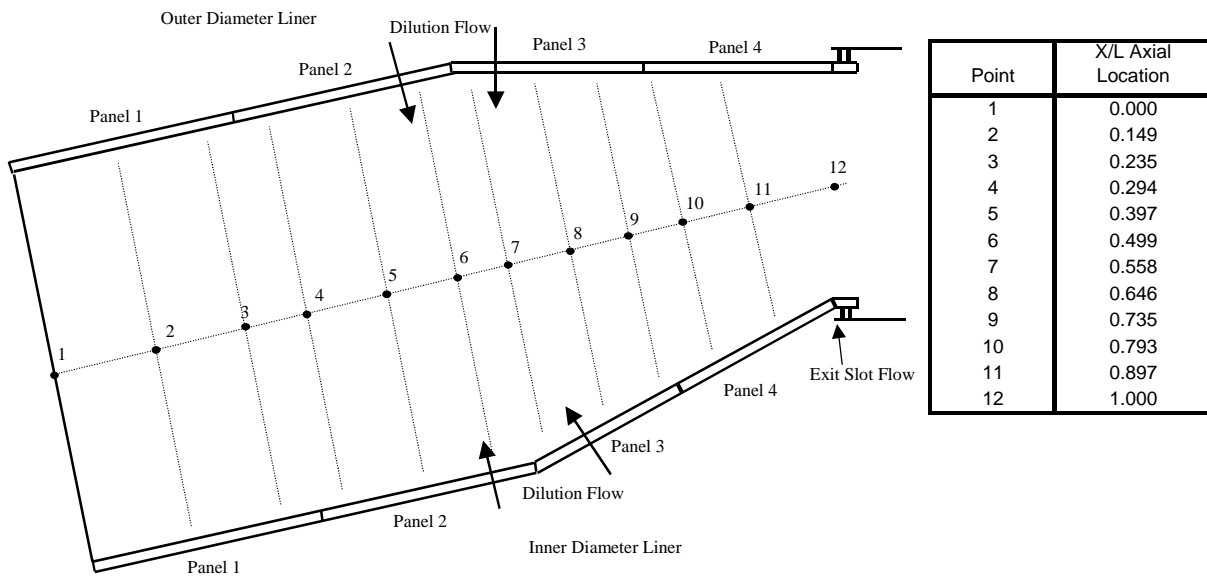


Figure 3-3 Schematic of the engine combustor indicating the axial locations used to perform flow calculations.

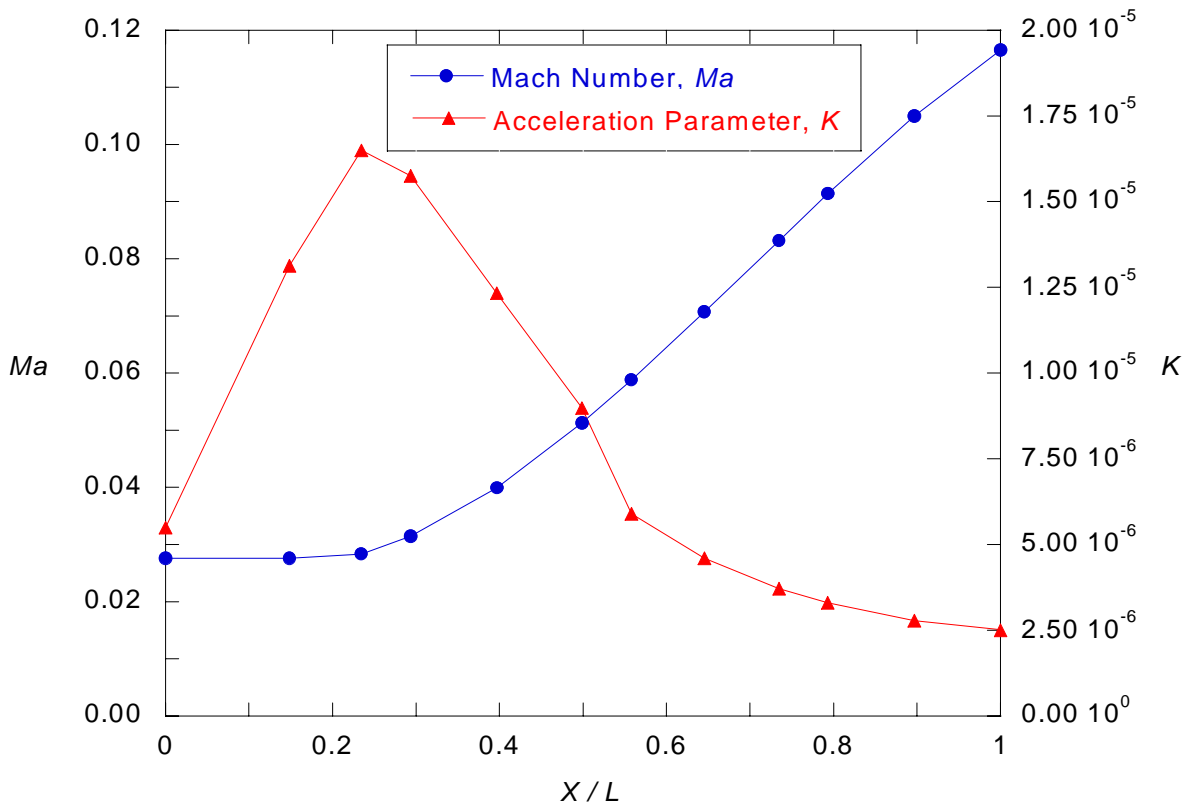


Figure 3-4 Graph indicating the axial Mach number distribution and the acceleration of the mainstream flow in the engine combustor.

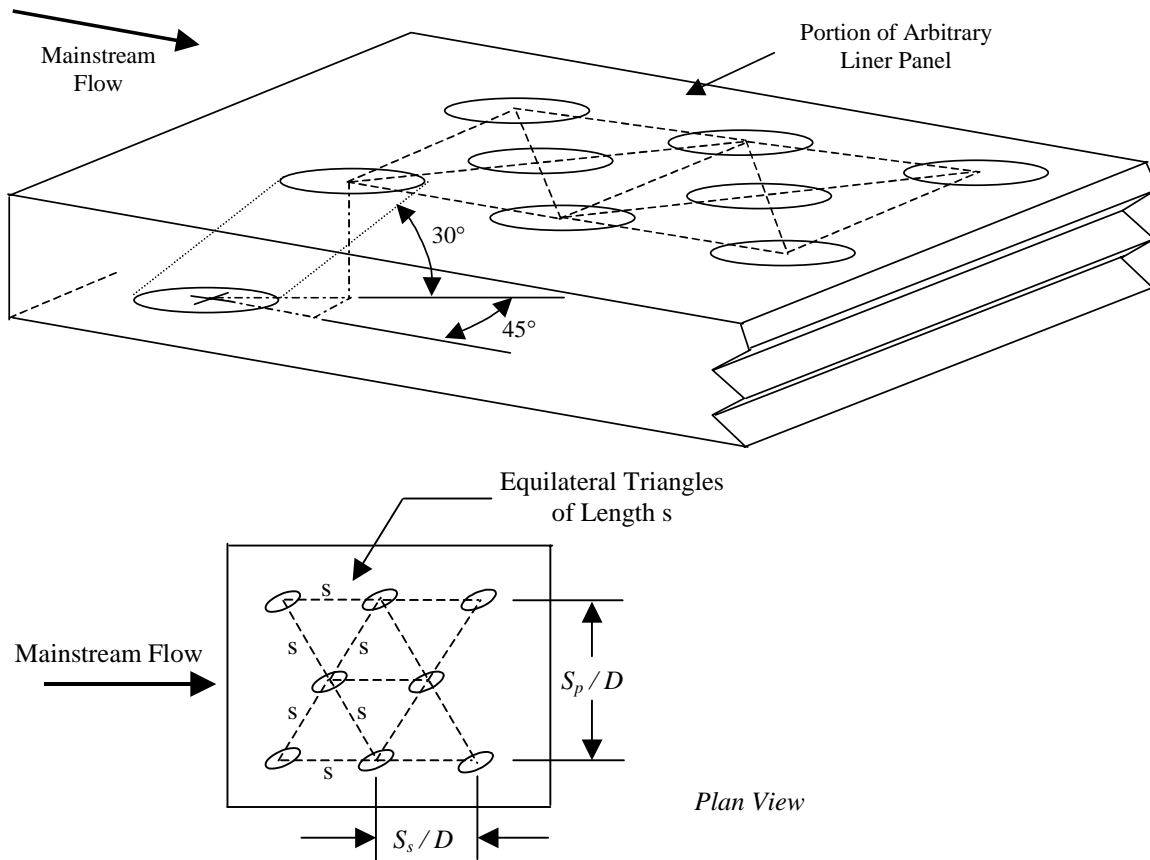


Figure 3-5 Schematics showing portions of an arbitrary liner panel indicating film-cooling hole pattern.

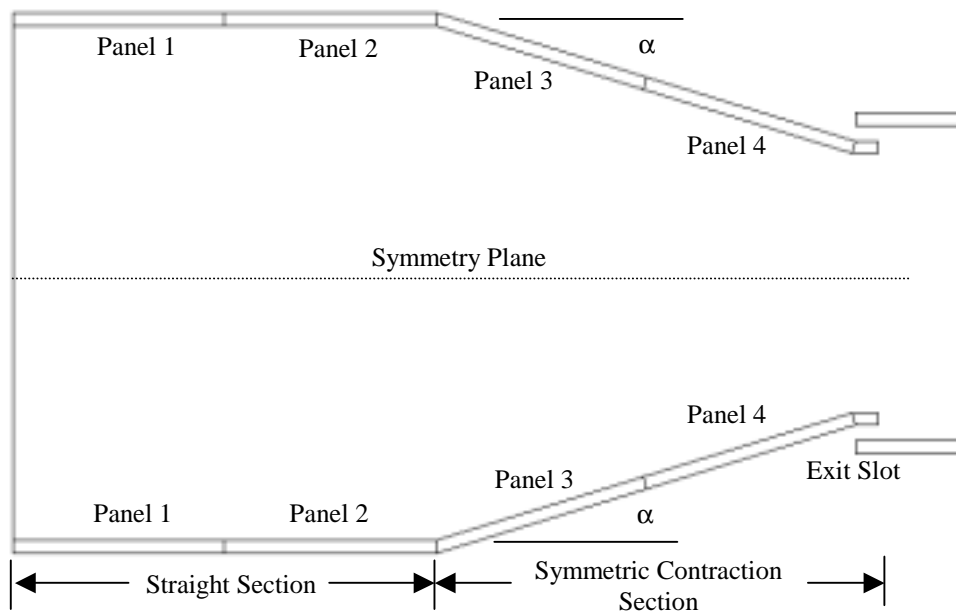


Figure 3-6 Schematic showing the general shape of the combustor simulator.

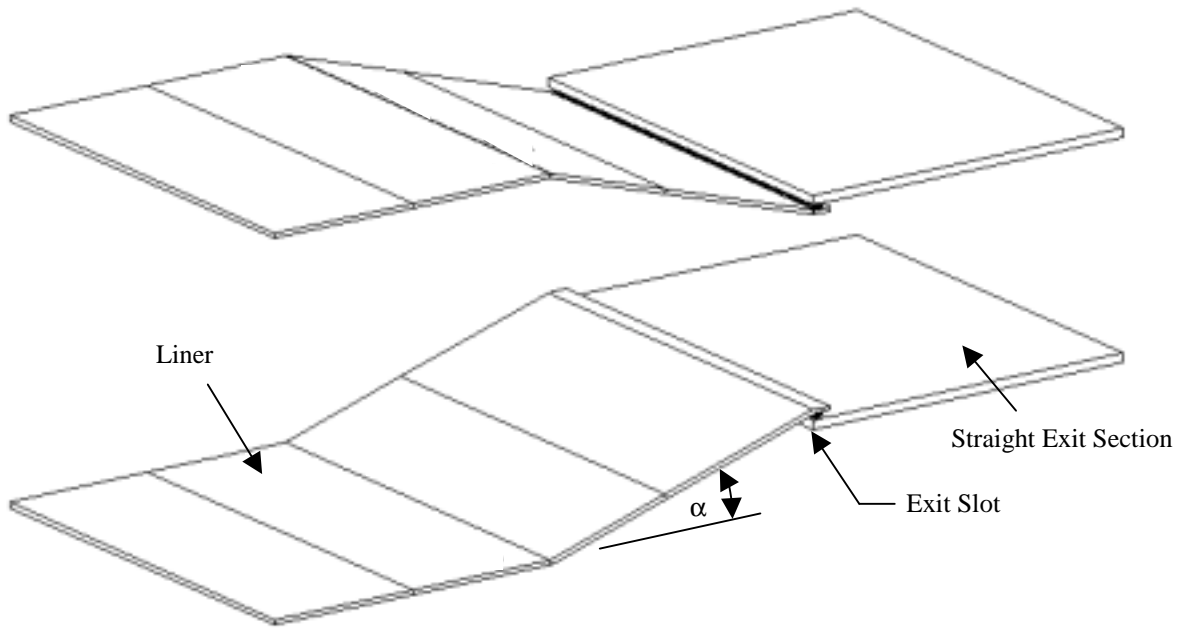


Figure 3-7 Schematic indicating the flat liner panels and straight exit section.

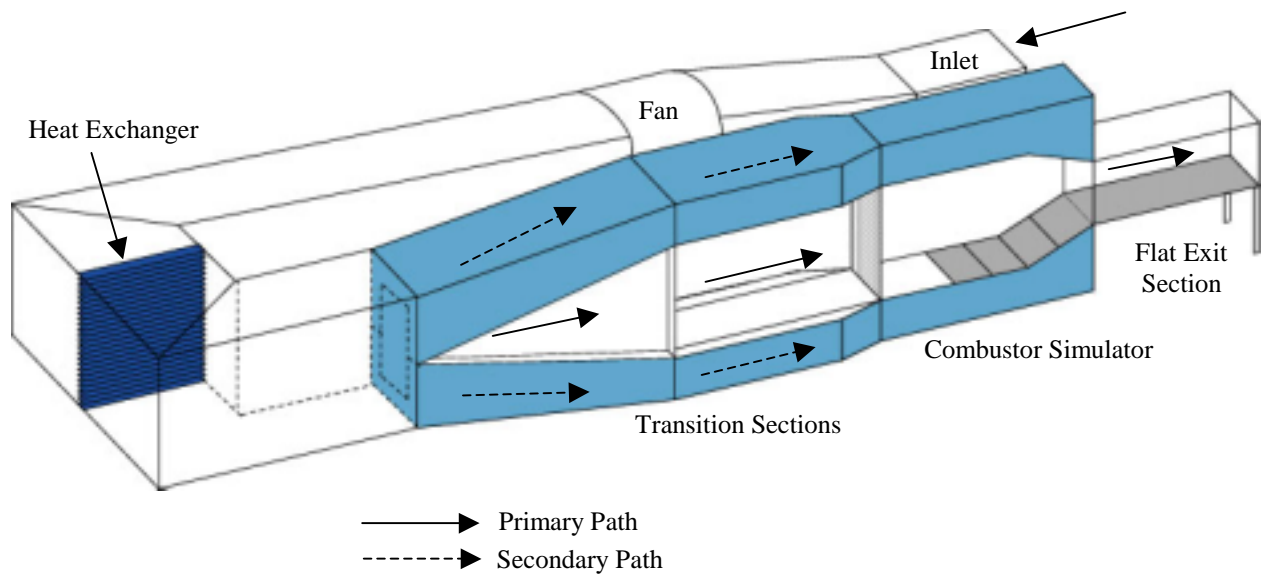


Figure 3-8 Schematic indicating design concept modifications to the existing facility.

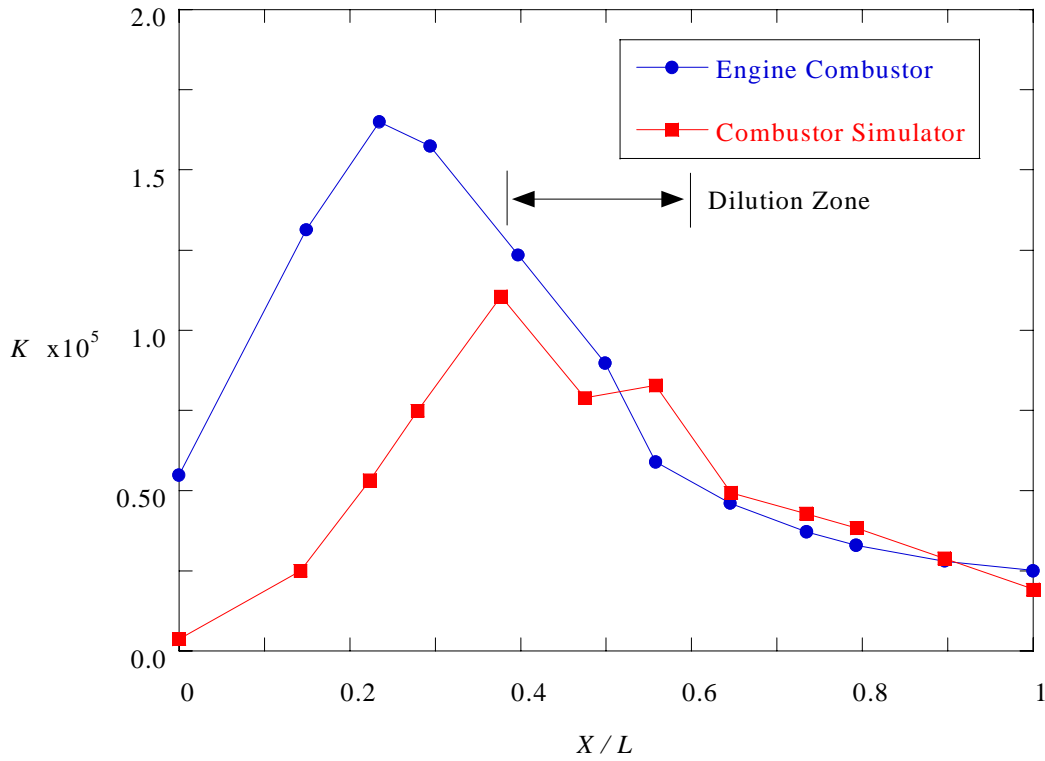


Figure 3-9 Graph showing a comparison of the acceleration in the engine combustor and the combustor simulator.

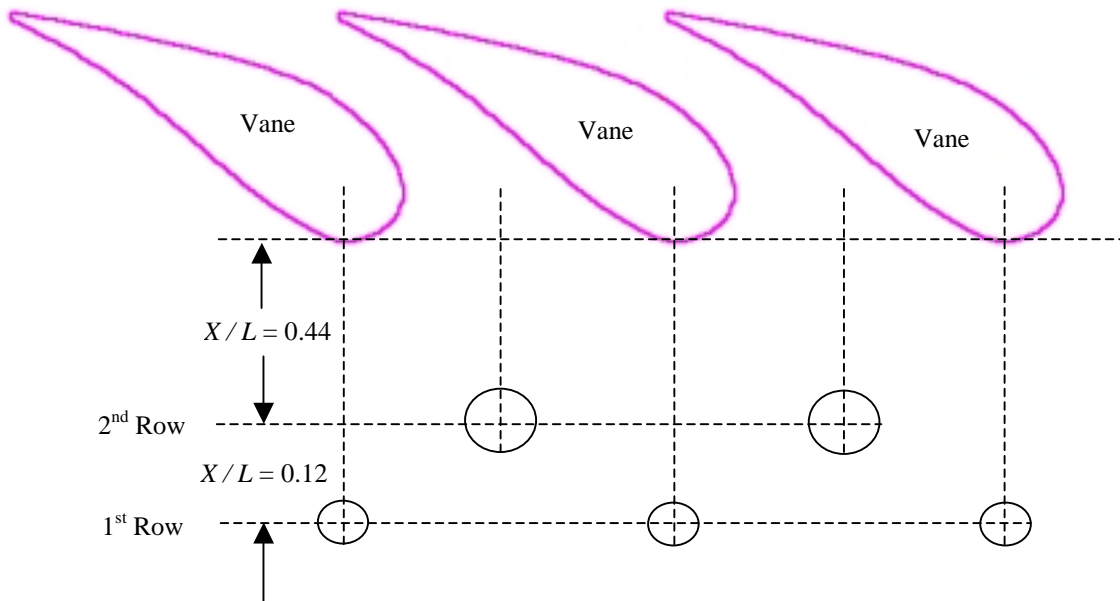


Figure 3-10 Schematic indicating the dilution hole pattern relative to the down stream vanes.

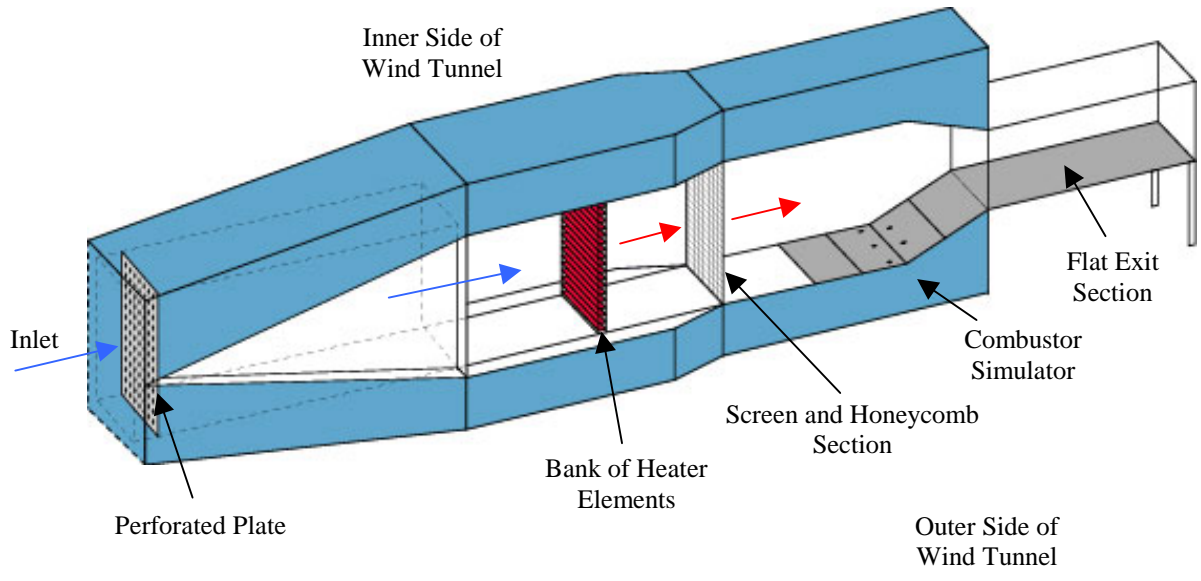


Figure 3-11 Schematic indicating the primary flow path arrangement.

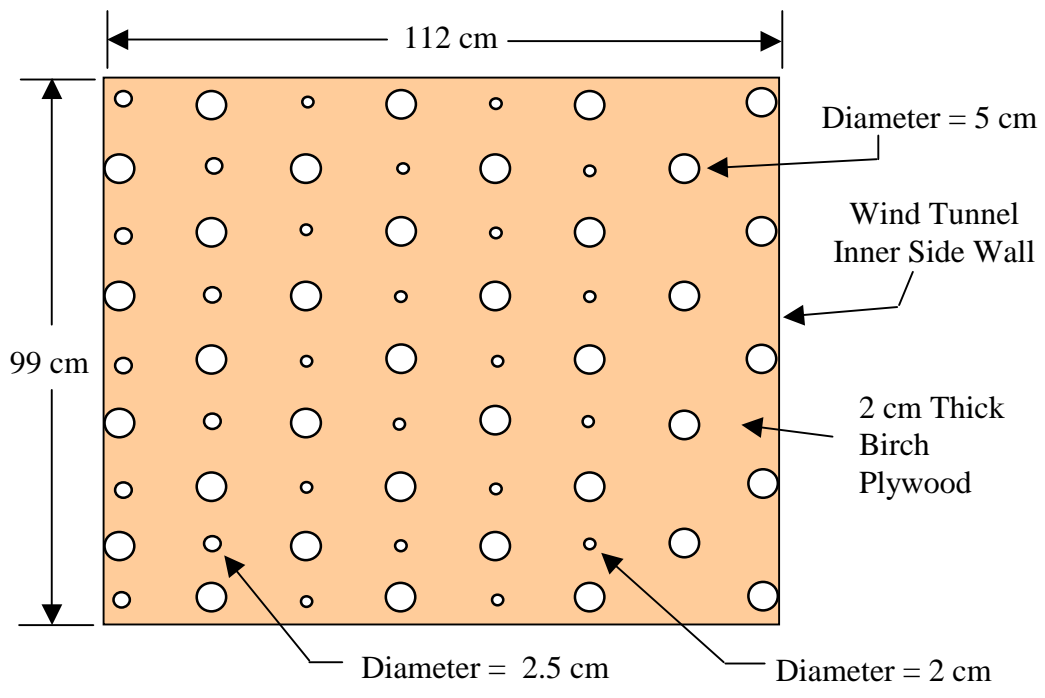


Figure 3-12 Schematic of the perforated plate design with the final hole pattern.

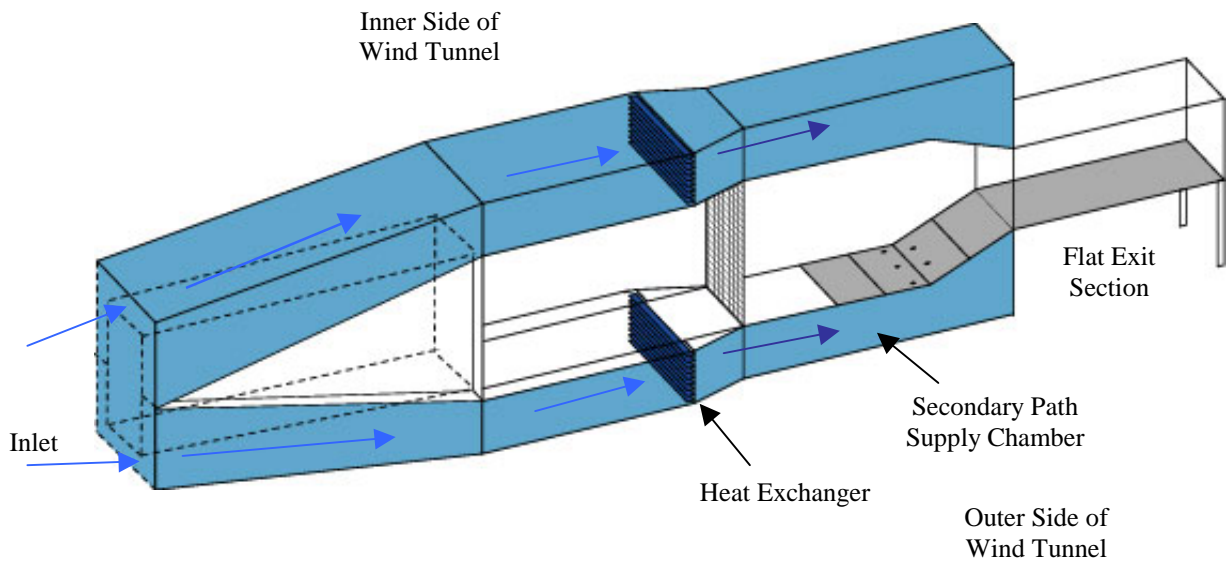


Figure 3-13 Schematic indicating the secondary flow path arrangement.

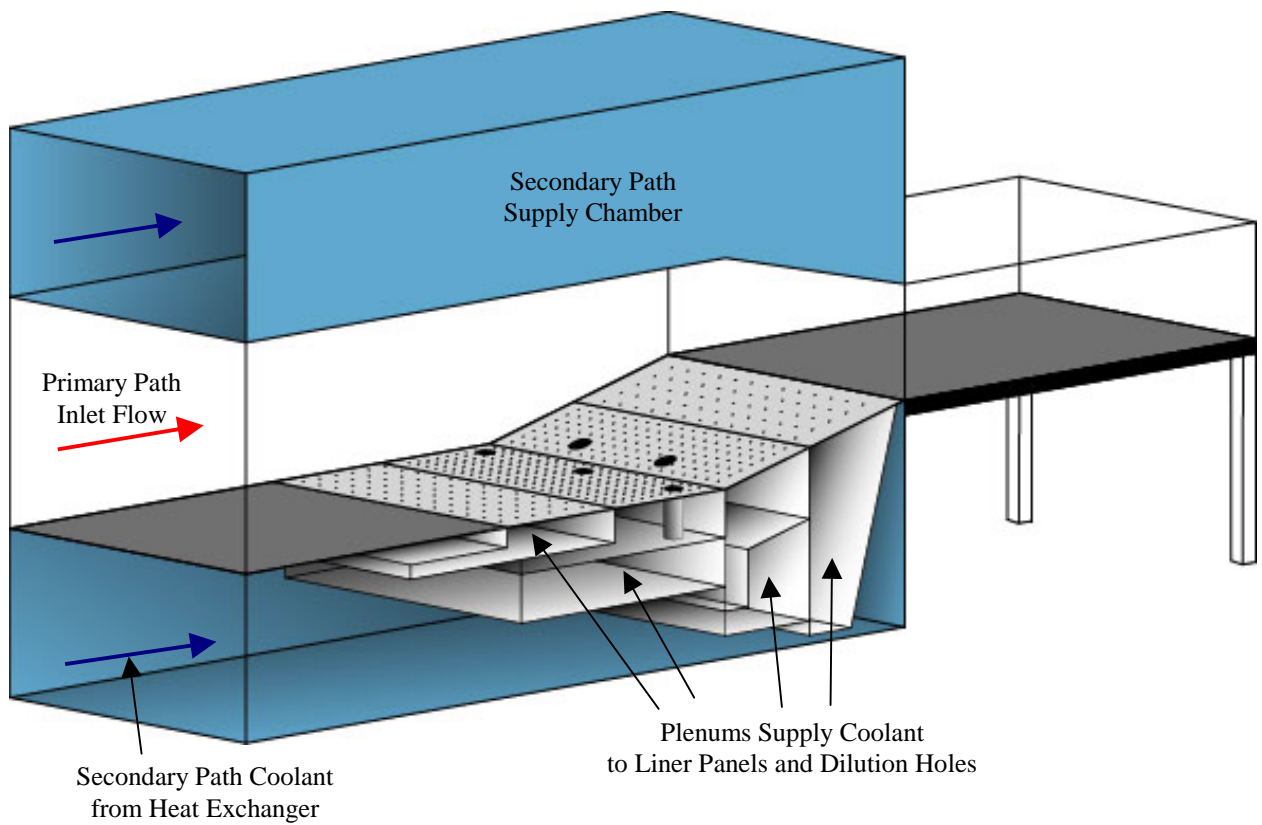


Figure 3-14 Schematic of the combustor simulator illustrating the components within the secondary path supply chamber.

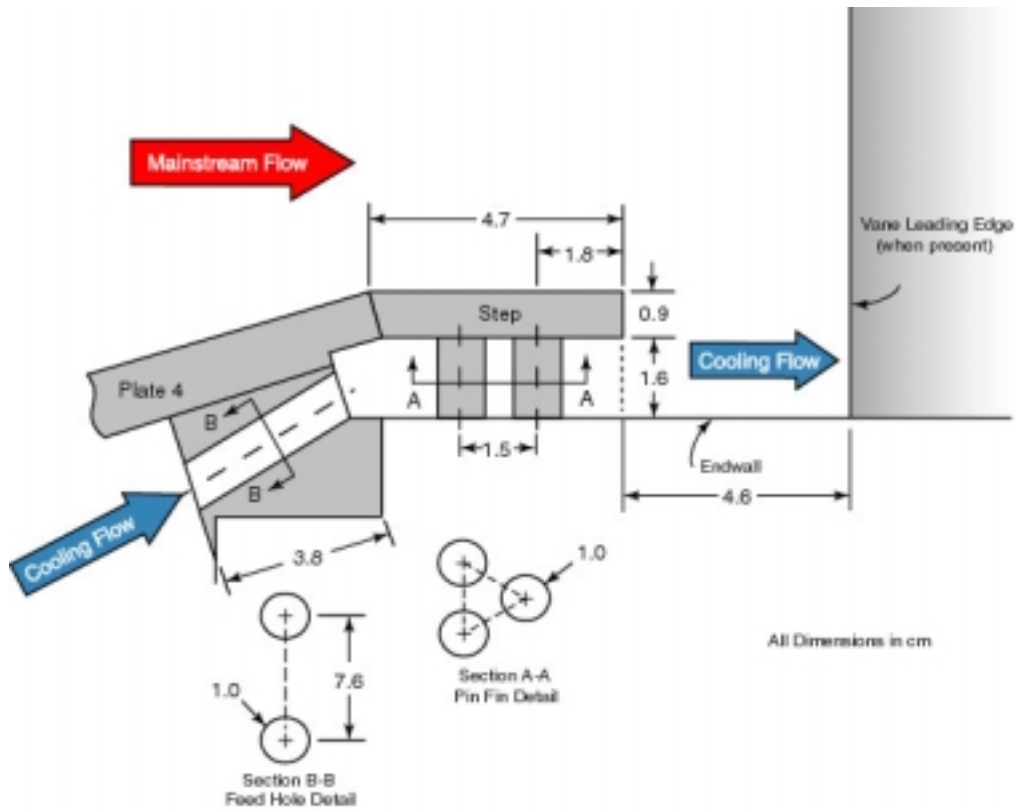


Figure 3-15 Schematic indicating the details of the exit slot region (Stitzel, 2001).

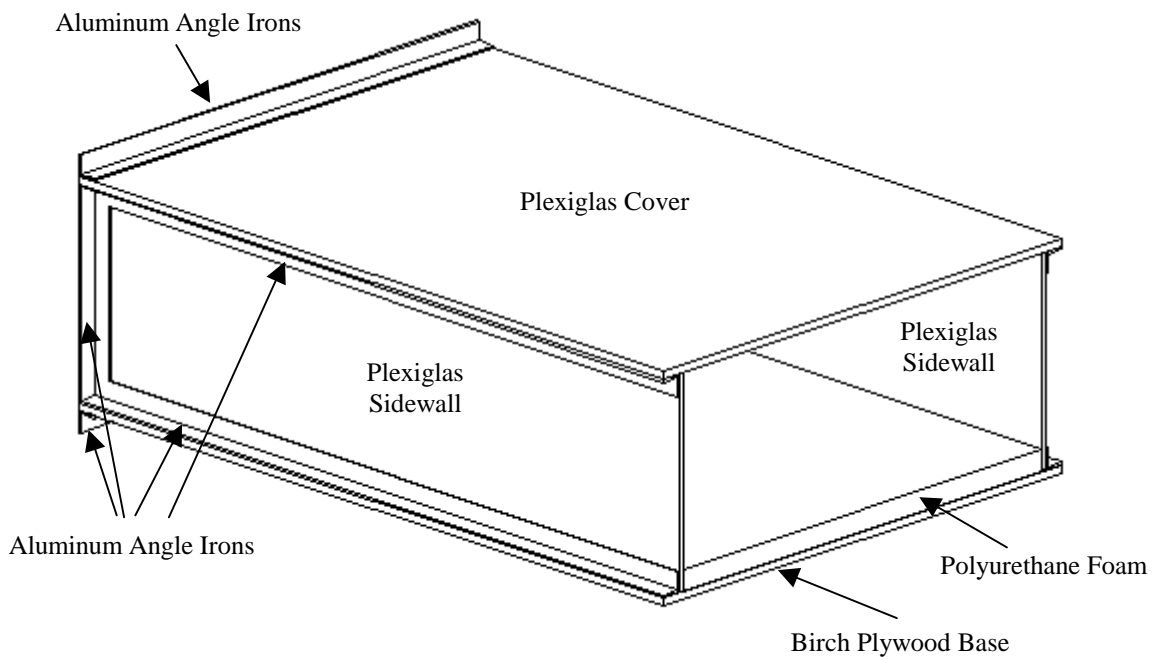


Figure 3-16 Schematic of the straight test section downstream of the combustor simulator.

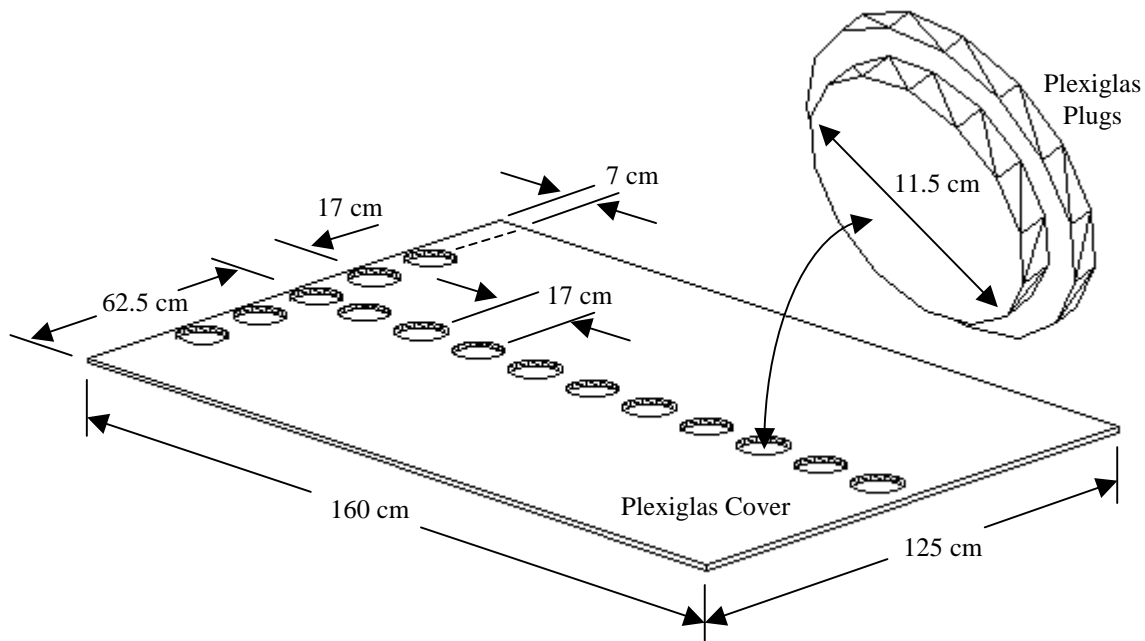


Figure 3-17 Schematic of the Plexiglas cover indicating the locations of the infrared camera ports.

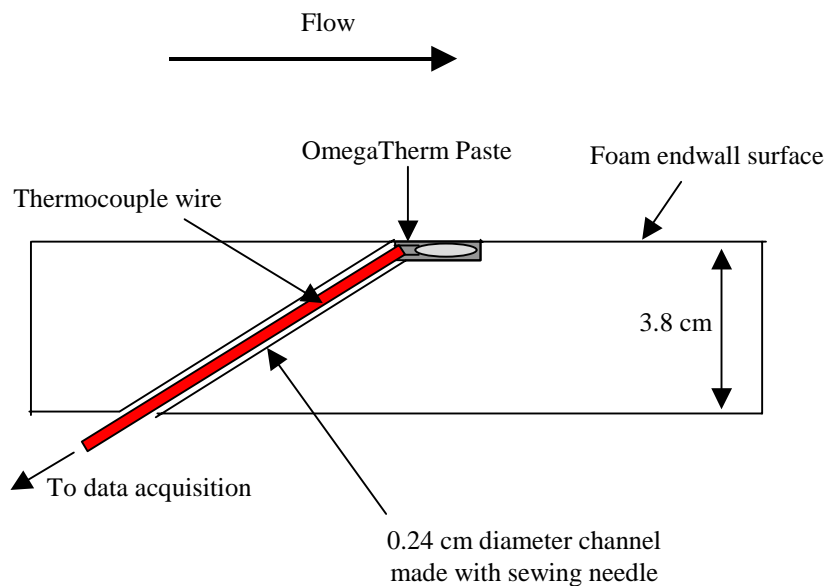


Figure 3-18 Schematic of a thermocouple embedded in a portion of the flat foam endwall.

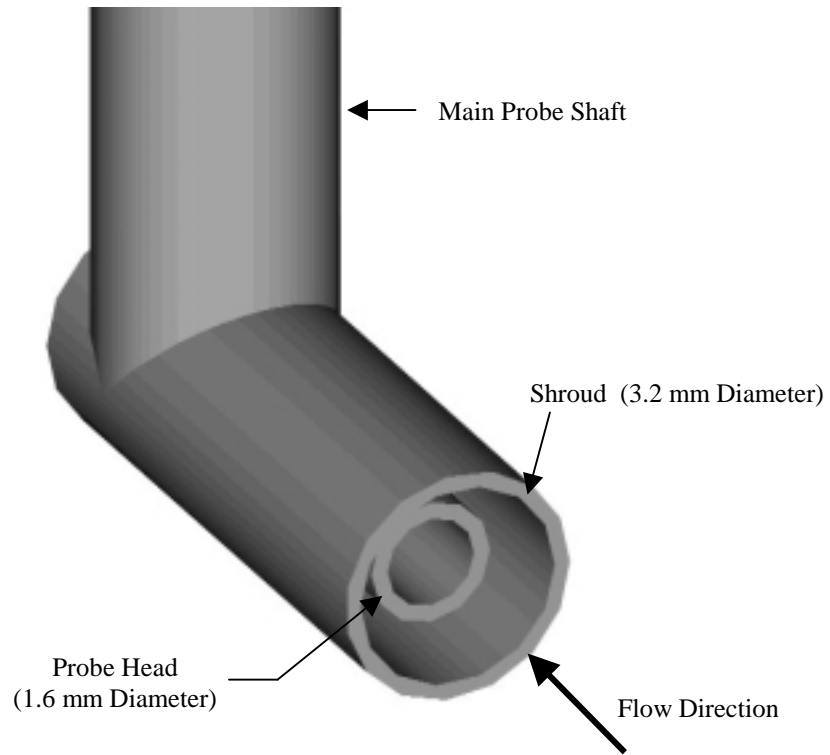


Figure 3-19 Schematic showing an enlarged view of the head of a Keil Probe.

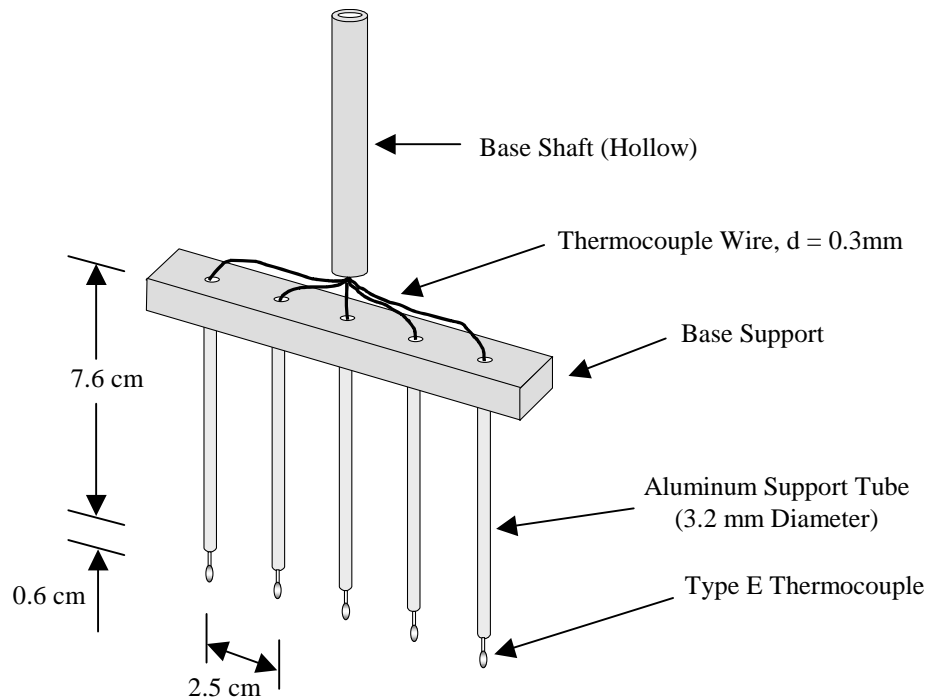


Figure 3-20 Schematic of the thermocouple rake.

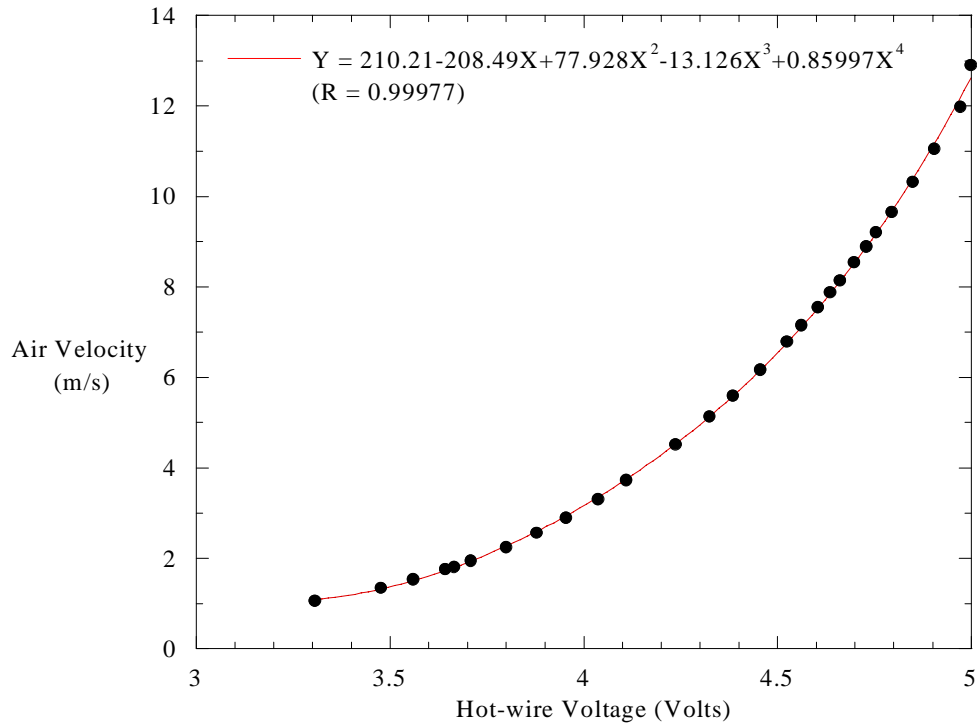


Figure 3-21 Graph of a typical hot-wire calibration curve.

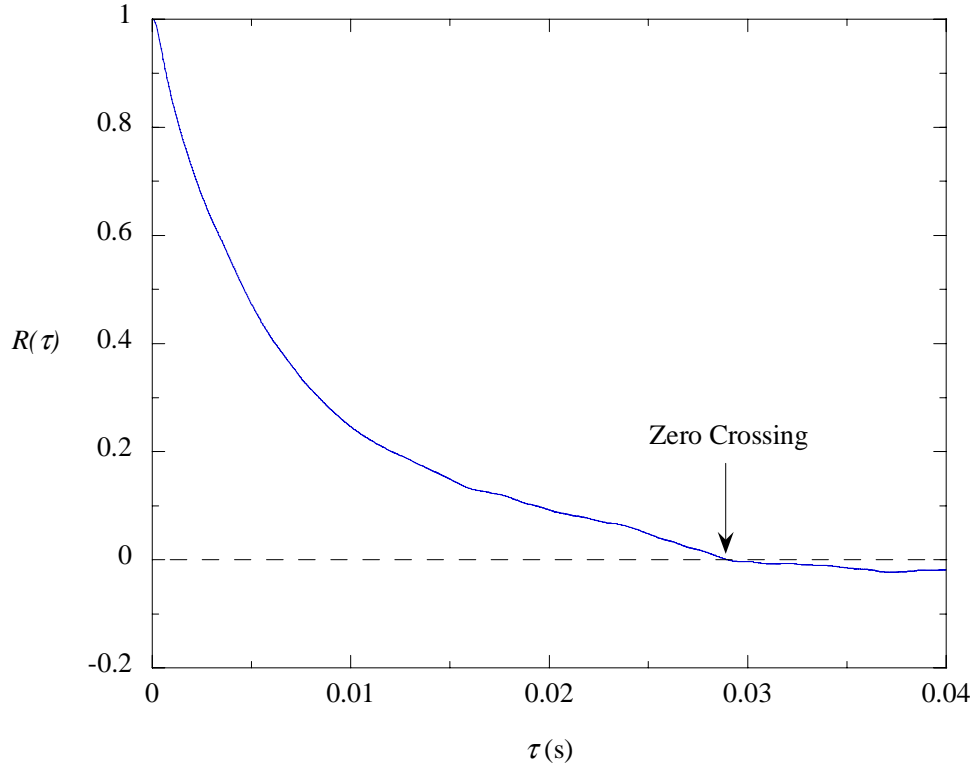


Figure 3-22 Graph showing a typical autocorrelation curve for a turbulence level of 15 %.

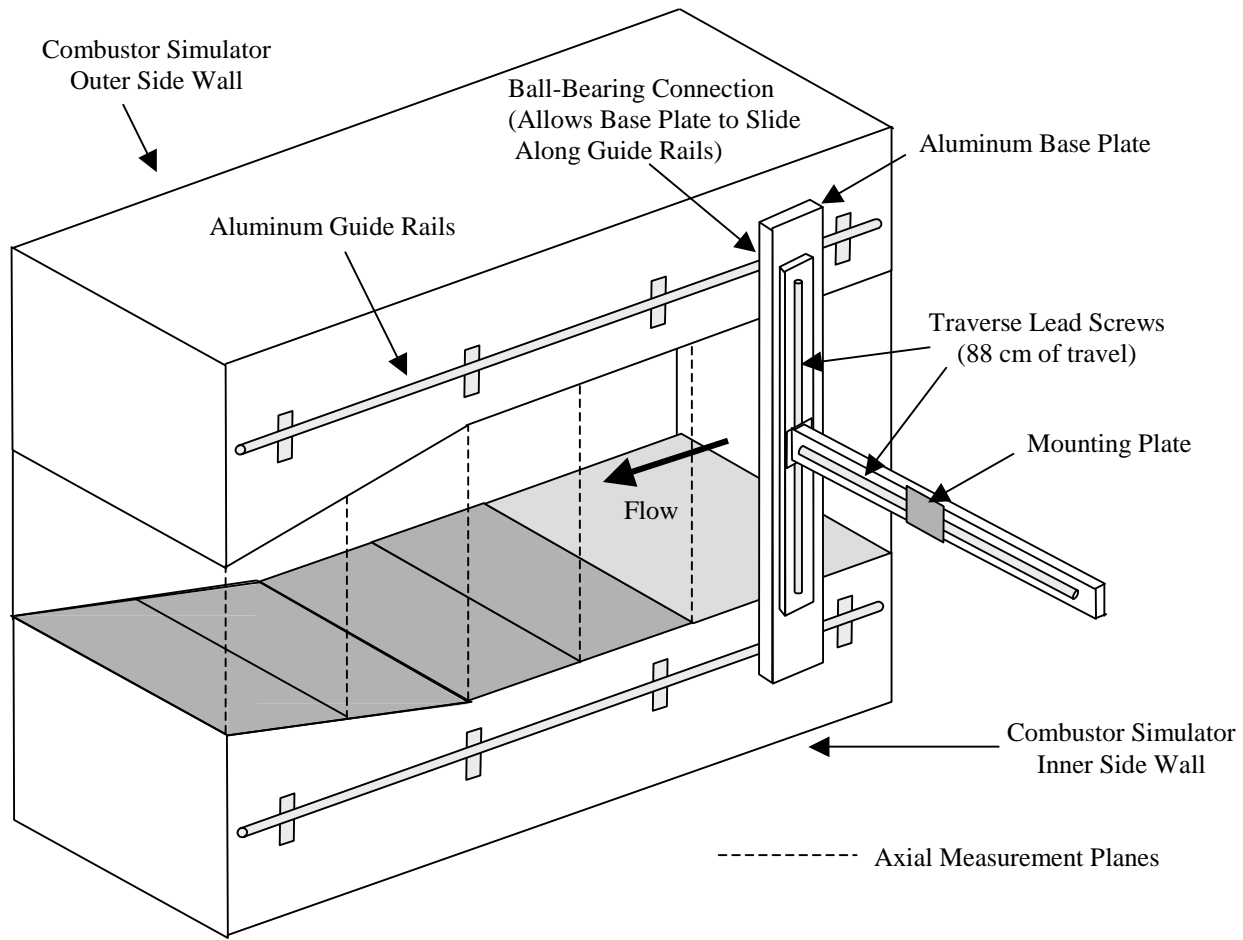


Figure 3-23 Schematic of the traverse system.

4. Benchmarking of the Combustor Simulator

To insure the proper design flow conditions throughout the combustor simulator, several flow quality and benchmarking studies were made in both the primary and secondary flow paths. Since the combustor simulator described in this thesis is a new facility, benchmarking of this facility was particularly important. The first section in this chapter discusses the benchmarking and flow conditions in the heated primary flow path. This is followed by discussions of the cooled secondary flow path benchmarking including the liner panels and dilution holes. The last section in this chapter focuses on the flow benchmarking of the combustor exit slot.

4.1 Primary Flow Benchmarking

The primary flow path inlet conditions were measured in both the spanwise (Z) and pitchwise (Y) directions to establish the flow quality entering the combustor simulator. This included measurements of velocity, temperature, and turbulence intensity. These measurements were taken in a pitchwise plane, shown in Figure 4-1, located approximately five film-cooling hole diameters (3.8 cm) axially upstream of the leading edge of the first combustor liner panel. The following discussion focuses on the flow quality benchmarking of the primary path inlet and the final achieved inlet conditions.

Prior to installing the perforated plate in the primary flow path, a shutter system for controlling the flow was tested, as shown in Figure 4-2. Mean velocity profiles measured in the plane shown in Figure 4-3 indicated non-uniform flows in the pitchwise direction at the inlet to the combustor simulator for various shutter positions. These profiles, measured with a pitot-static probe, indicated that a relatively low velocity was present near the outer wall of the simulator while a higher velocity existed toward the inner wall. One example of these profiles in which the average streamwise velocity corresponded to the desired combustor inlet velocity of 1.5 m/s is shown in Figure 4-3. Note that the location $y/W = 0$ corresponds to the middle of the simulator which is also the pitchwise location of the stagnation point on the center downstream

vane (when present). The pitch locations $y/W = 1.0$ and -1.0 correspond to the endpoints of one sector (stagnation points on the adjacent vanes when present). The pitch location $y/W = -1.22$ corresponds to the inner combustor side wall and $y/W = 1.22$ corresponds to the outer combustor side wall. The skewed velocity profiles were a result of more mass flow near the inner wall of the wind tunnel. The higher velocities near the inner wall were a result of the flow being turned by ninety degrees in the upstream corner wind tunnel section. This is analogous to flow around a corner in which the flow path of least resistance is the shorter path near the inner wall. The flow non-uniformities were corrected by removing the aluminum shutters and constructing a perforated plate, as was discussed in Chapter 3, and positioning it near the entrance to the primary flow path.

With the perforated plate in place, inlet velocity profiles were taken in the plane shown in Figure 4-1. These profiles were taken at mid-span across the entire pitch and at mid-pitch taken across the entire span. These velocity profiles were taken with a single component hot-wire, which measured the streamwise velocity component and are shown in Figure 4-3. Note that the figure displays the normalized streamwise velocity in both pitch and span directions. The profiles indicate that the inlet velocity for the primary path is uniform over the entire span and pitch. The average measured inlet velocity was approximately 1.5 m/s with a maximum deviation from the mean of 1.7%. The average measured inlet turbulence intensity was approximately 3.0 %.

Temperature profiles were also taken at mid-span and mid-pitch of the combustor simulator inlet in the same pitchwise plane and at the same axial location as the velocity measurements. To obtain a uniform temperature profile at the combustor simulator inlet the current load passing through each zone of the heater element array had to be adjusted manually in terms of a percentage of the total allowable current load for that set of heater elements. The adjustment procedure involved first setting the current load at 100 % for all three zones. The system was then allowed approximately 1.5 hours to warm up. A manual fine tuning of the current load was then performed by lowering and/or raising the amount of current passing through a given zone until the temperature profile was nearly uniform. The final achieved

current settings were 97 % for the lower zone, 97 % for the middle zone, and 96 % for the upper zone. The temperature profiles were taken with a thermocouple rake and are shown in Figure 4-4. The typical driving temperature for these profiles is approximately 12.2 °C. Note that the figure displays a temperature difference ratio θ in both pitch and span directions. This temperature difference ratio is given by equation 4-1.

$$\theta = \frac{T_{ave} - T}{T_{ave} - T_c} \quad (4-1)$$

The average measured inlet temperature is denoted as T_{ave} , the local measured temperature is denoted as T , and the coolant supply temperature is denoted as T_c . The reason for using a temperature difference ratio rather than just a temperature ratio, for example, T / T_{ave} , was that the profile shape was then a function of the temperature units that were used, i.e. Celsius or Kelvin. Using an expression involving temperature differences, however, eliminates this problem. It can be seen from the figure that the temperature profiles indicate that the primary path inlet temperature is uniform over the entire span and pitch of the combustor simulator. The average measured inlet temperature was 37.6 °C with a maximum deviation of $\theta = 0.058$.

4.2 Liner Flow Benchmarking

Secondary coolant flow was injected into the primary hot gas path through liner panels containing a large number of film-cooling holes, as discussed in Chapter 3. Each liner panel has its own supply plenum in which the desired flows were set using discharge coefficients, the total pressure measured in each of the liner supply plenums, and the local static pressure measured in the primary flow path. A series of experiments were conducted prior to the construction of the combustor simulator to determine the discharge coefficients for each liner panel.

The discharge coefficient, defined in equation 4-2, is the ratio of the actual mass flow rate to the theoretical mass flow rate.

$$C_d = \frac{\dot{m}_{actual}}{\dot{m}_{theoretical}} \quad (4-2)$$

The actual mass flow rate is the experimentally measured mass flow rate and the theoretical mass flow rate is that calculated using simple fluid mechanic relationships. For a plenum flow injected through an orifice to a mainstream cross-flow, this theoretical calculation involves using the Bernoulli equation under the assumptions of steady, incompressible, inviscid flow, and being applied along a streamline. The important result is given in equation 4-3.

$$V_{theoretical} = \sqrt{\frac{2}{\rho} (P_{plenum} - P_{\infty static})} \quad (4-3)$$

Knowing the hole area and the fluid density, a direct calculation of the theoretical mass flow rate can be performed using equation 3-1. Subsequently, the discharge coefficient can then be determined.

The discharge coefficient experiments consisted of a five horsepower fan that directed coolant flow through a laminar flow element and then into a large plenum chamber attached directly to a film-cooling panel. The coolant was injected through the panel into the main test section of the wind tunnel prior to the combustor simulator modifications. A schematic of the experimental setup is shown in Figure 4-5. Experimental measurements included the flow rate measured across the laminar flow element, the total pressure within the plenum, and the static pressure at the exit of the film-cooling holes.

In order to validate the experimental methodology, the first set of experiments were compared with those presented in the literature by Burd and Simon (1999). Figure 4-6 compares the results from conducting these initial tests with those found by Burd and Simon. It can be

seen that good agreement does occur thus establishing experimental verification. It can also be seen in the figure that the first and fourth combustor liner panels, in which $S_s/D = 5.8$ and $S_p/D = 10.1$, the average discharge coefficient near design pressure conditions was approximately 0.74. The experiments indicated that the second and third combustor liner panels, in which $S_s/D = 3.5$ and $S_p/D = 6.1$, the discharge coefficient was approximately 0.73. The tests including multiple rows of film-cooling holes resulted in larger discharge coefficients than those determined for a single row of film-cooling holes. For the case with multiple rows of film-cooling holes, the cooling flow passing through the holes located downstream of the first row experienced less resistance to the mainstream flow due to the disturbance of the mainstream boundary layer with the first row cooling flow.

The total pressure in each of the liner supply plenums is directly related to the individual plenum's mass flow rate. The amount of mass flow entering a liner supply plenum is controlled through the adjustment of a shutter located at the plenum's entrance. The shutter functions by varying the entrance flow area. Pressure taps were located within the plenums to measure total pressure and pressure taps were located at the start of each liner panel to measure the mainstream static pressure. The static pressure taps were embedded in the liner panels and were positioned flush with the external surface. The static pressures were verified by placing a pitot-static tube in the vicinity of the pressure taps and taking measurements of static pressure directly from the pitot-static tube.

The film-cooling flow uniformity through the liner panels was checked by taking vertical velocity measurements with a hot-wire at the trailing edge of the panel. Figure 4-7 shows the vertical velocity profiles that were taken approximately 7.7 film-cooling hole diameters downstream of the last row of film cooling holes in the first lower liner panel. These velocity profiles were taken at three different pitch locations including $y/W = -0.5$, $y/W = 0.0$, and $y/W = 0.5$. This figure illustrates that the flow exiting from the first lower liner panel is uniform in the pitch direction. From this figure it can also be seen that two distinct regions appear within the velocity profiles. The first region exists between $z/D = 0.0$ and $z/D = 2.5$. This region contains a velocity peak associated with the last row of film-cooling holes in the first liner panel.

The coolant velocity within this region has a peak velocity approximately 3.6 times greater than the freestream velocity at that same axial position. The second region exists between $z/D = 2.5$ and $z/D = 8$. This second region is the coolant flow that has been injected through the upstream film-cooling holes. It can also be seen that the overall film-cooling jet penetration depth at the trailing edge of the first panel ($I = 14$) is approximately eight film-cooling hole diameters above the liner panel surface. The velocity at z/D values larger than 8.0 coincides with the combustor simulator freestream velocity at that axial location which is equivalent to the combustor simulator inlet velocity. Figure 4-8 shows turbulence profiles based on the mainstream velocity at the same three measurement locations. This figure indicates that the turbulence profiles associated with the flow exiting the liner are very similar in the pitch direction.

Another method that was used to investigate the film-cooling flow uniformity through each of the panel liners was to take peak velocity measurements within several individual film-cooling holes. A relatively small diameter (0.16 cm) pitot-static tube was inserted into the film-cooling hole and the peak velocity of the flow was measured. These measurements were taken across several rows and columns of film-cooling holes in each of the liner panels and indicated that good uniformity was obtained.

4.3 Dilution Flow Benchmarking

Coolant exiting the secondary path was also injected into the primary hot gas path through the combustor dilution holes. Each axial row of dilution holes has its own supply plenum and the desired flow rates exiting the dilution holes are controlled through the adjustment of shutters located at each plenum entrance.

The flow rates for each of the dilution holes were initially set using previous experimentally determined discharge coefficients, the total pressure in each of the dilution supply plenums, and the local static pressure in the main gas path. It was found, however, that

the desired mass flow rates entering the dilution hole plenums were too large for the previously assembled plenums to actually be considered plenums. There was appreciable velocity detected within the plenums thus indicating that the plenum dynamic pressure was not negligible and that the pressure taps within the plenums did not measure true total pressure. This meant that the flow rates exiting the dilution holes could not be determined in the same manner as the liner panels. Instead, velocity profiles were taken across the diameter of each of the dilution holes to determine a cross-sectional average velocity exiting each hole.

The results of performing these velocity profiles initially indicated that non-uniformities existed at the exit of the first row of dilution holes. These non-uniformities can be seen in Figure 4-9 in which deviations from the mean velocity were recorded as high as 37%. These skewed exit profiles were ultimately linked to the plenum conditions mentioned above along with the fact that the plenum's entrance was physically located directly underneath the dilution supply pipes. In order to correct for this problem the plenum's entrance section was elongated in order to allow the entering flow a longer development length.

Figure 4-9 shows the velocity profiles taken across the diameters of the center holes in the first row of dilution holes before and after the plenum entrance modifications. It can be seen that good uniformity existed over the majority of the diameter of each hole. Figure 4-10 shows the velocity profiles taken across the diameters of the second row of dilution holes. It can also be seen that good uniformity existed over the majority of the diameter of each hole. The maximum deviation from the mean velocity exiting the first row of dilution holes was approximately 11% and that for the second row of dilution holes was approximately 8.1%. Knowing the coolant density and dilution hole area along with the average velocity, the mass flow rate exiting the dilution holes was determined.

4.4 Combustor Exit Flow Conditions

Benchmarking the combustor exit flow conditions first involved establishing the desired flow conditions upstream. This included setting the desired velocity in the primary path at the combustor simulator inlet as well as setting the mass flows for the liner panels and the dilution holes. Having set the upstream conditions, a mass flow rate balance was performed at the combustor exit. This mass balance was performed by taking several velocity profiles in both the pitch and span directions in the plane upstream of the exit slot shown in Figure 4-11. These velocity profiles, shown in Figure 4-12 and Figure 4-13, were used to determine a representative cross-sectional average velocity exiting the combustor simulator. The first figure plots the vertical location non-dimensionalized by the total exit height (H) versus the local velocity. The second figure plots the local velocity versus the pitch location non-dimensionalized by one pitch (W). Each profile was integrated to obtain four spatially averaged velocities. These average velocities were then linearly averaged to obtain a characteristic cross-sectional average velocity of 6.98 m/s. This corresponds to only a 2.6% deviation from the design cross-sectional average velocity at the combustor simulator exit (within the plane upstream of the exit slot) of 6.8 m/s. Considering these four velocity profiles do not take into account the slightly lower mass flow located near the four corners of the exit plane, due to boundary layer effects, the average velocity determined here was a conservative estimate. The results from performing this mass flow rate balance indicated that the proper upstream mass flow rate conditions had been met. Note that the cross-sectional average velocity in a plane located $6 D$ downstream of the exit slot (corresponding to the vane leading edges when present) is lower at 6.3 m/s due to the exit slot flow having a much lower average velocity of 1.5 m/s. The upper and lower exit slots combined account for approximately 10 % of the total exit height.

The coolant within the secondary path supply chambers that does not enter into any of the liner panel or dilution hole plenums exits the supply chambers through the exit slots at the combustor exit. The mass flow rate exiting the lower and upper slots combined is approximately 1.4 % of the total exit mass flow rate. The exit slot mass flow rate is set and monitored using

discharge coefficients, the total pressure in the secondary path supply chamber, and the static pressure at the exit of the slot feed holes.

Total pressure taps are located in the supply chamber plenum region that supplies flow to the exit slot. The static pressure taps are located in the downstream side of the slot feed-hole plate. Static pressure taps are also located in the endwall on the downstream side of the pin-fins. Based on the L/D and pressure ratios of the feed holes a typical literature discharge coefficient of 0.7 was used in determining the flow rate passing through these holes.

Pitchwise total pressure profiles were taken with a Keil probe in the exit slot region downstream of the pin fins. Figures 4-14 and 4-15 show schematics of the exit slot region with the location of the Keil probe used for the profiles. The probe head was located vertically 0.32 cm below the pin-fin plate bottom surface and axially at the trailing edge of the pin-fin plate. The probe was traversed in the pitch direction in increments of 0.32 cm from $y/W = 0.0$ to 1.22. The total pressure measurements are shown in Figure 4-16. Note that the exit total pressure was non-dimensionalized by the mid-span average total pressure at that axial location and the average dynamic pressure of the coolant exiting through the slot. It can be seen from the figure that the slot exit flow conditions were highly non-uniform. This non-uniformity was due to the alignment, which was part of the engine design, of the slot feed holes with the first row of pin-fins. The alignment, also shown in Figure 4-16, was such that some feed holes injected flow directly into the body of a pin-fin located in the first row while others injected flow into the gap between two adjacent pin-fins in the first row, thus directing the flow into the body of a pin-fin located in the second row. This flow arrangement led to sporadic variation in slot cooling flow coverage near the endwall, which agreed with the computations performed by Stitzel (2001).

To complete the benchmarking process, the flow and thermal fields exiting the combustor simulator and entering the straight test section needed to be fully examined. This involved taking total pressure, velocity, temperature, and turbulence measurements in both the pitch and span directions at axial locations just upstream of the exit slot and corresponding to the leading edges of the vanes (when present). In addition to these tests, adiabatic effectiveness

measurements were taken on the flat endwall. All of these tests were conducted while operating the combustor simulator with and without dilution flow. The case involving no dilution flow required adjustment of the upstream flow conditions to produce the desired design exit conditions. A summary of the flow field conditions for the two test cases with and without dilution flow is presented in Table 4-1.

Table 4-1 Summary of the Flow Field Conditions for the Two Flow Cases

Combustor Component	Engine (I.D.)		Dilution On		Dilution Off	
	\dot{m}_{exit} (%)	I	\dot{m}_{exit} (%)	I	\dot{m}_{exit} (%)	I
Panel 1	1.5	13	1.5	14	2	9
Panel 2	3.5	7	3.5	8	4.5	8
Panel 3	3.5	3	3.5	4	4.5	7
Panel 4	1.5	1.5	1.5	1.5	2	3
Dilution Row 1	8.75	100	8.75	100	-	-
Dilution Row 2	8.75	20	8.75	20	-	-
Exit Slot	0.7	-	0.7	-	1.1	-

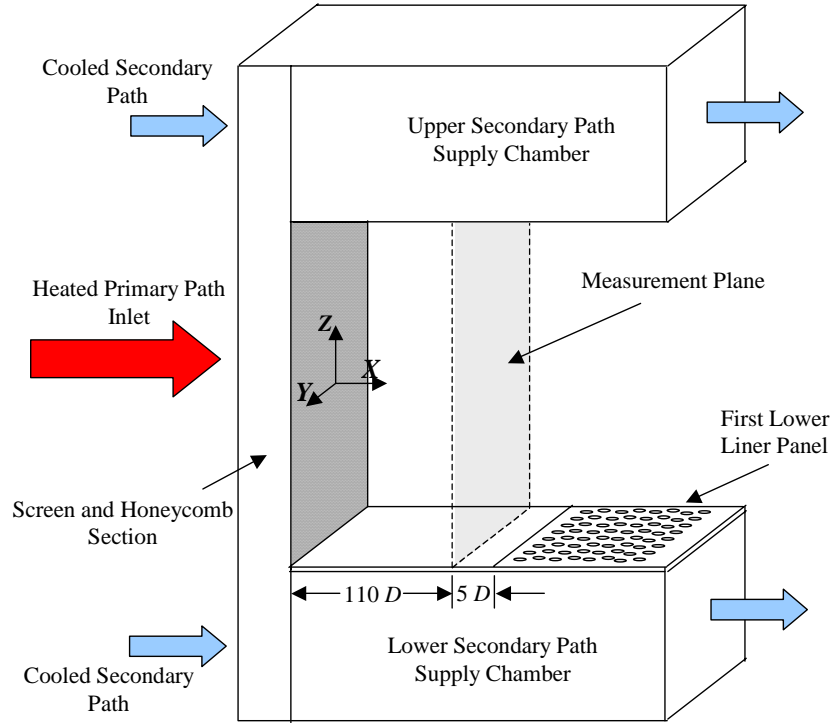


Figure 4-1 Schematic indicating the location of the measurement plane for benchmarking the primary path of the combustor simulator.

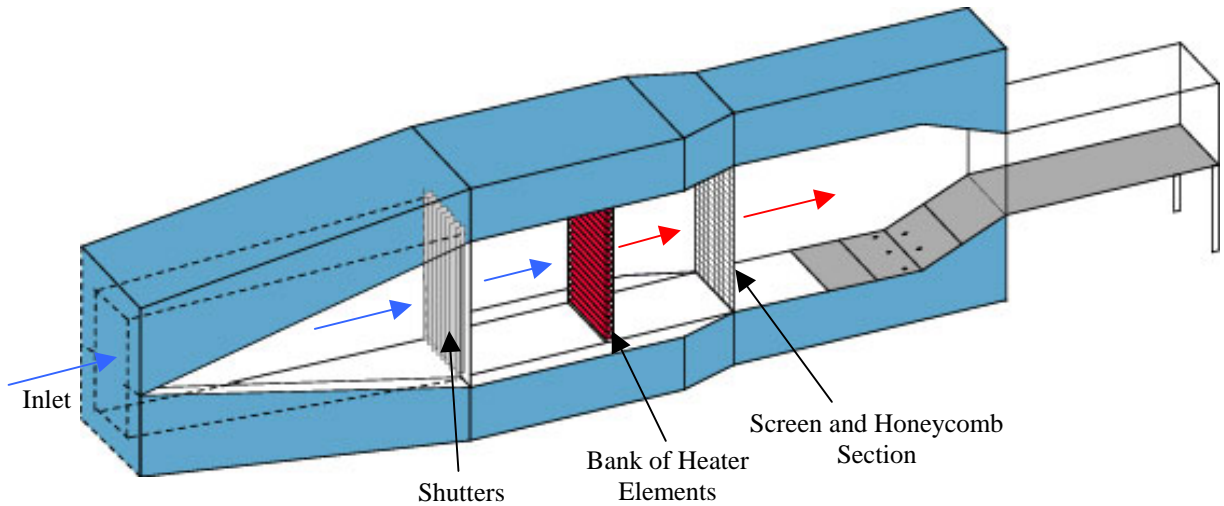


Figure 4-2 Schematic of the initial primary path flow arrangement.

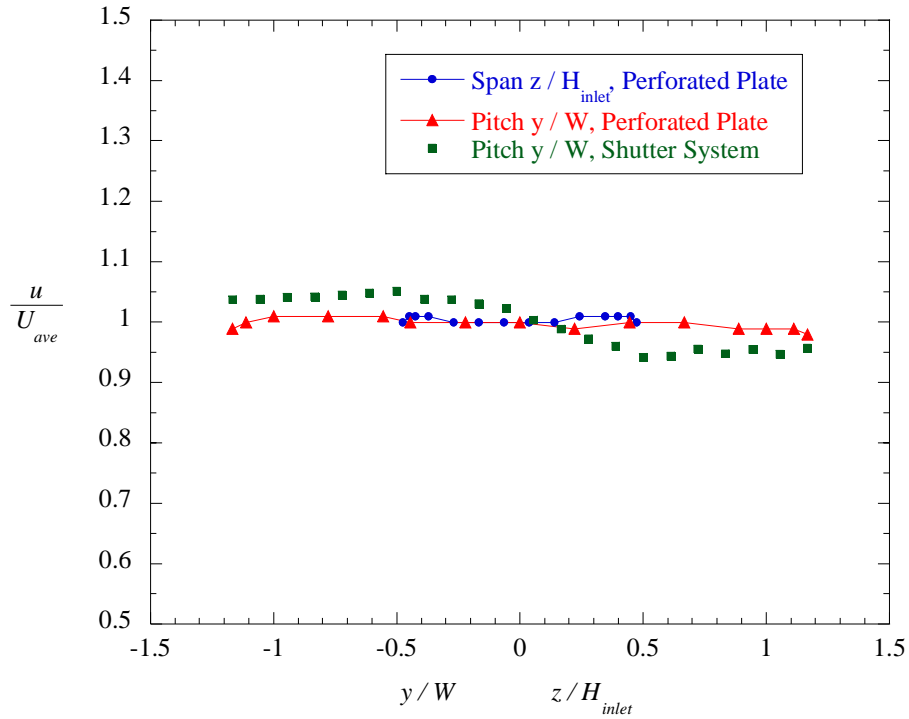


Figure 4-3 Graph of the velocity profiles at the combustor simulator inlet in both the pitch and span directions.

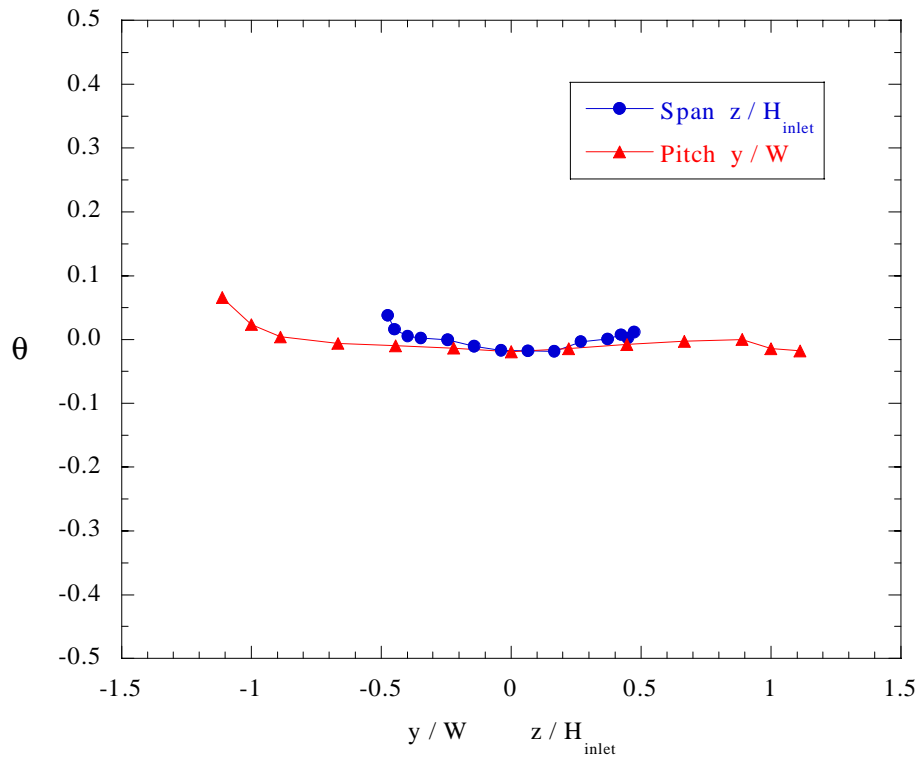


Figure 4-4 Graph of the pitch and span temperature profiles at the combustor simulator inlet.

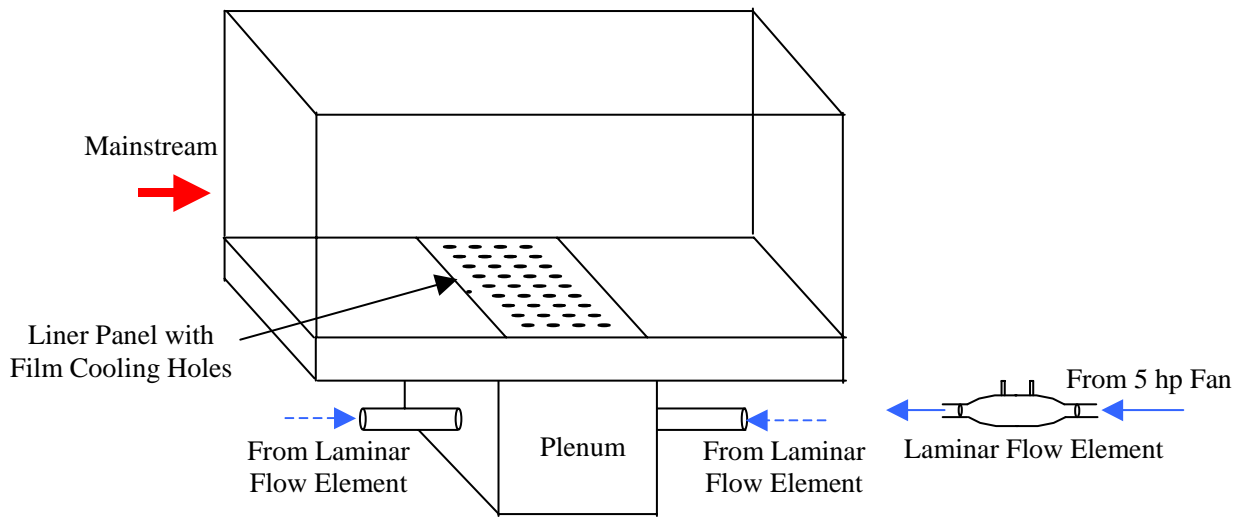


Figure 4-5 Schematic of the discharge coefficient experiment setup.

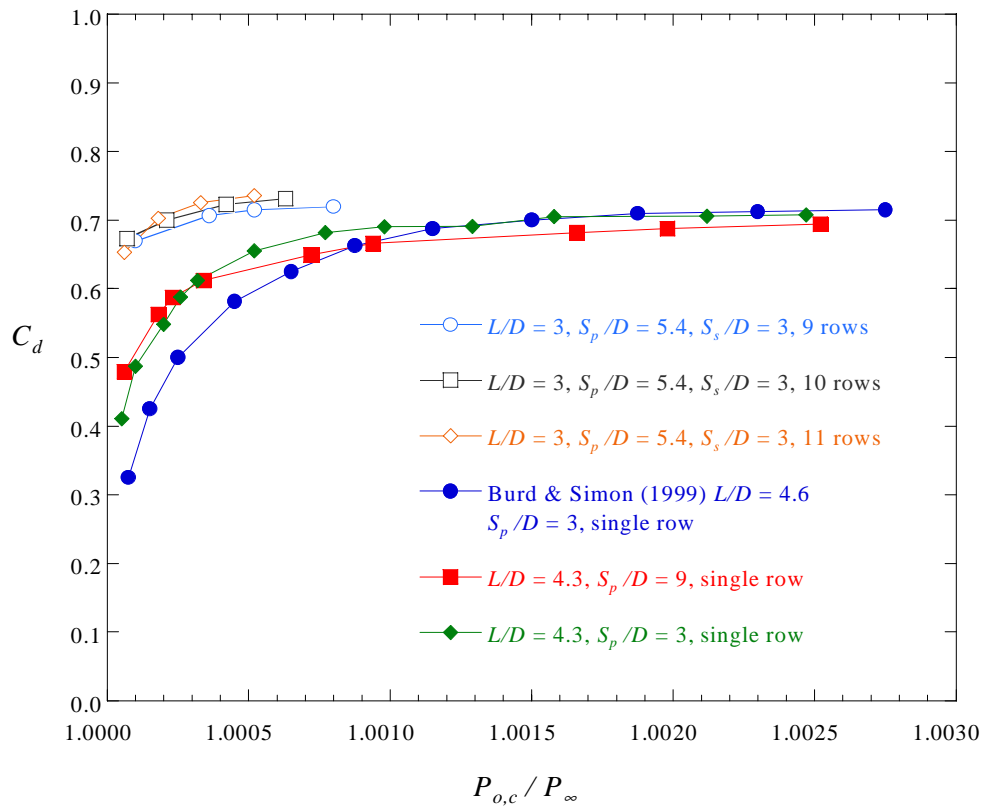


Figure 4-6 Graph of the discharge coefficient data.

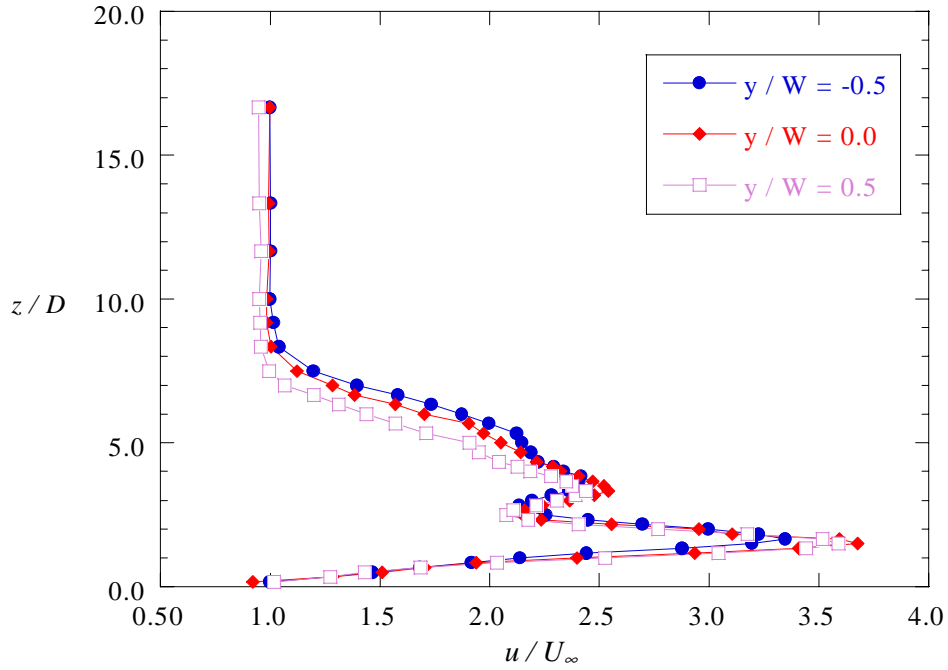


Figure 4-7 Graph of the vertical velocity profiles indicating uniform film-cooling conditions at the end of the first liner panel ($x/D = 7.7$ downstream of the last row of film-cooling holes)

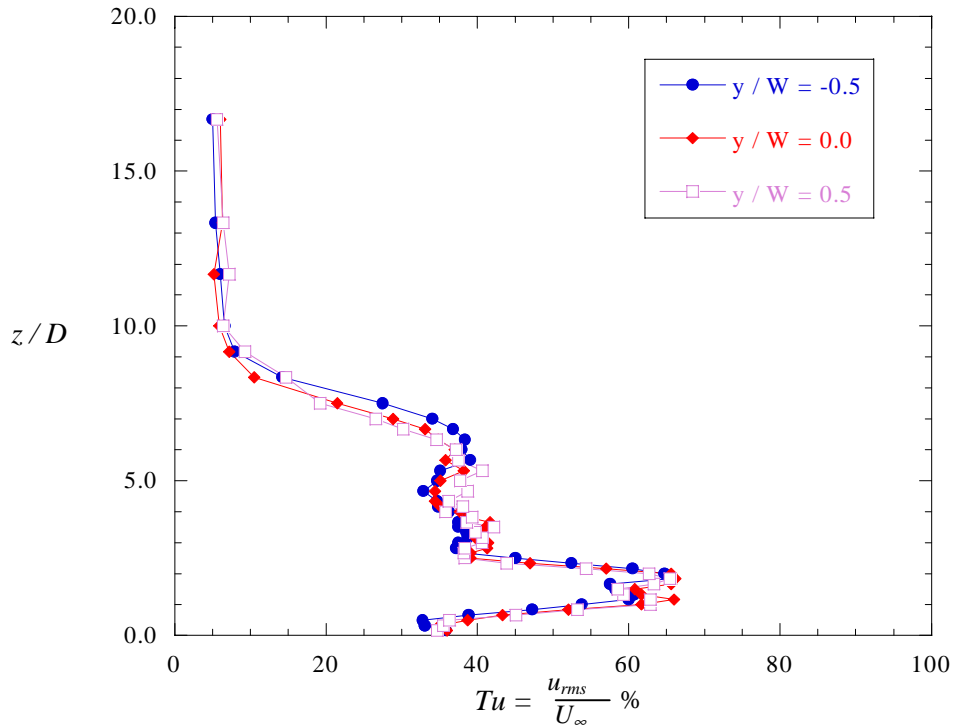


Figure 4-8 Graph of the vertical turbulence profiles indicating uniform film-cooling conditions at the end of the first liner panel ($x/D = 7.7$ downstream of the last row of film-cooling holes)

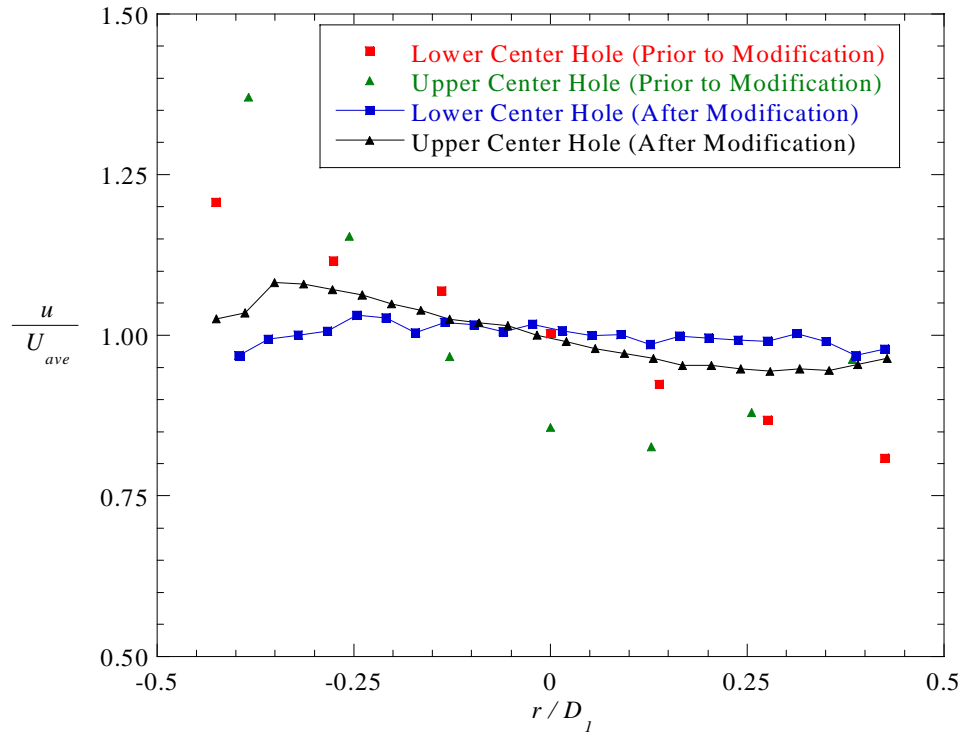


Figure 4-9 Graph of velocity profiles taken across the diameters of the first row of dilution holes.

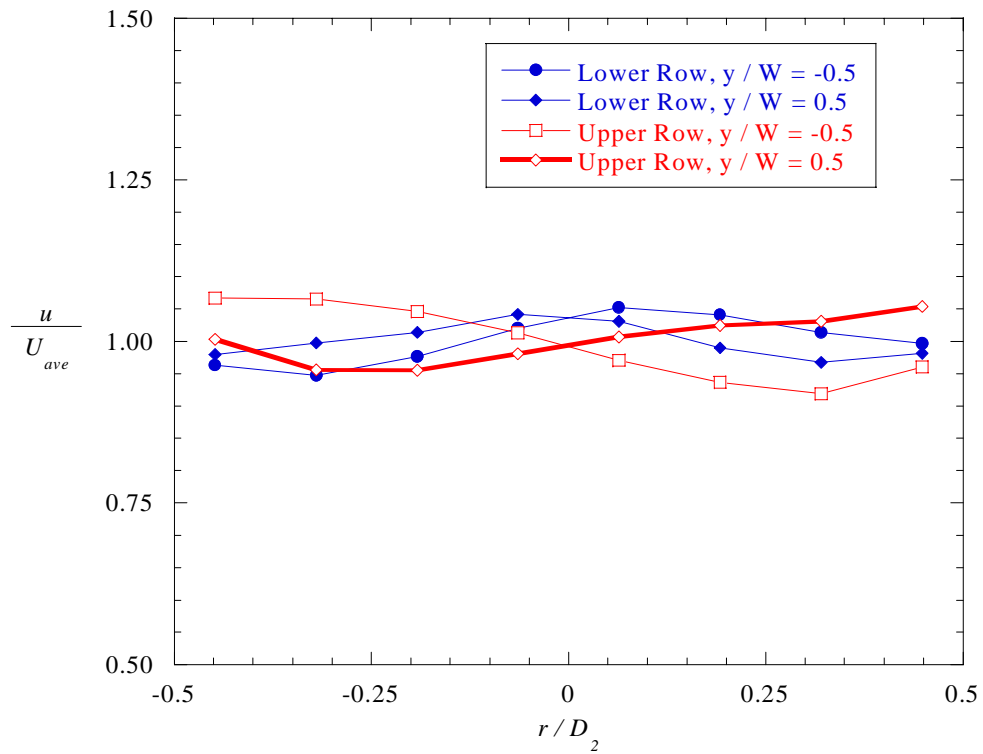


Figure 4-10 Graph of velocity profiles taken across the diameters of the second row dilution holes.

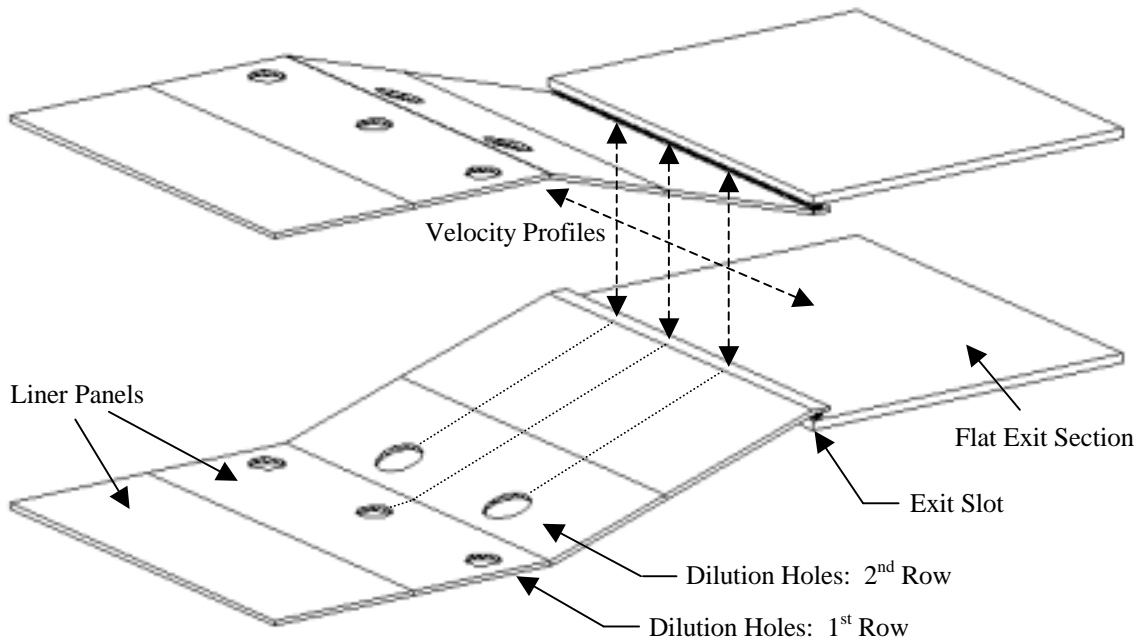


Figure 4-11 Schematic of the combustor simulator indicating the measurement locations used for the mass balance study.

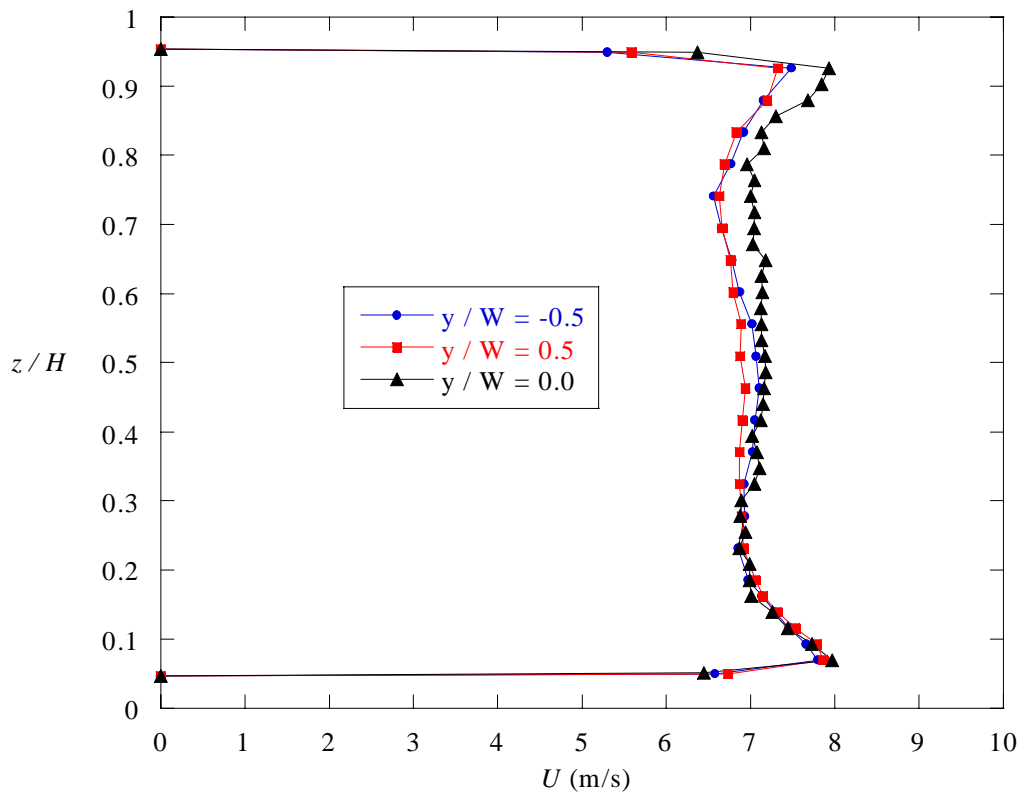


Figure 4-12 Graph of the spanwise velocity profiles taken at combustor simulator exit (upstream of exit slot) indicating proper upstream mass flow rate conditions.

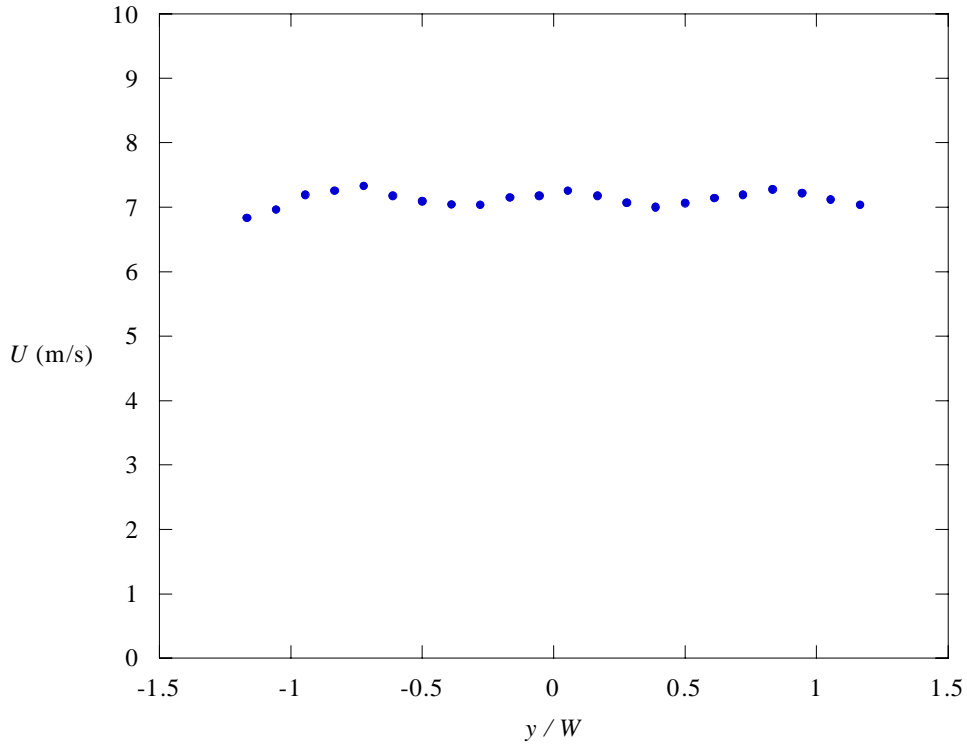


Figure 4-13 Graph of the pitchwise velocity profile taken at the combustor simulator exit (upstream of exit slot) indicating proper upstream mass flow rate conditions (data taken at $z/H = 0.0$).

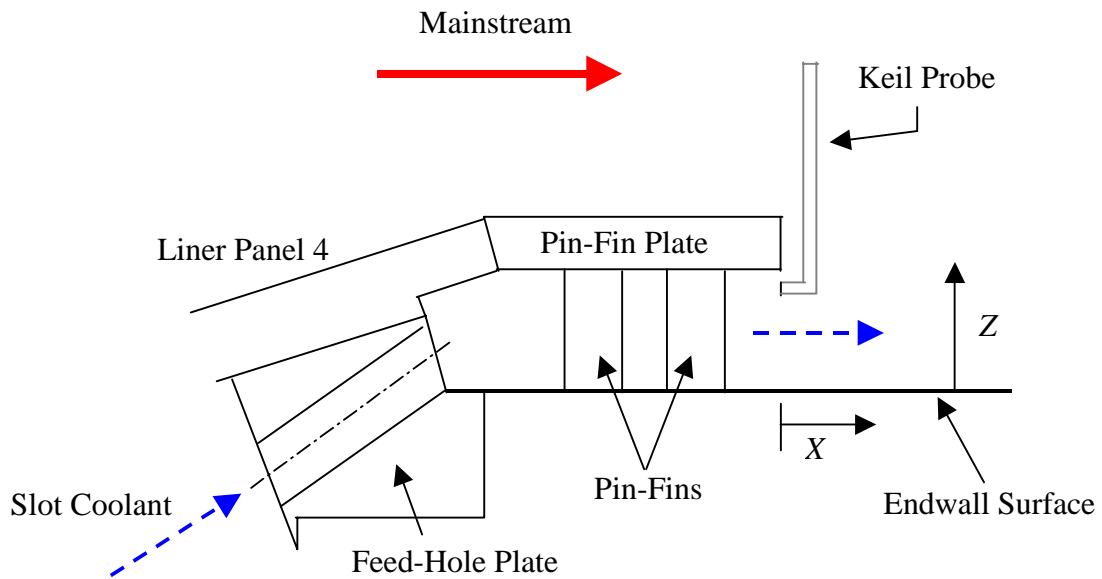


Figure 4-14 Schematic showing the exit slot flow region and the measurement location.

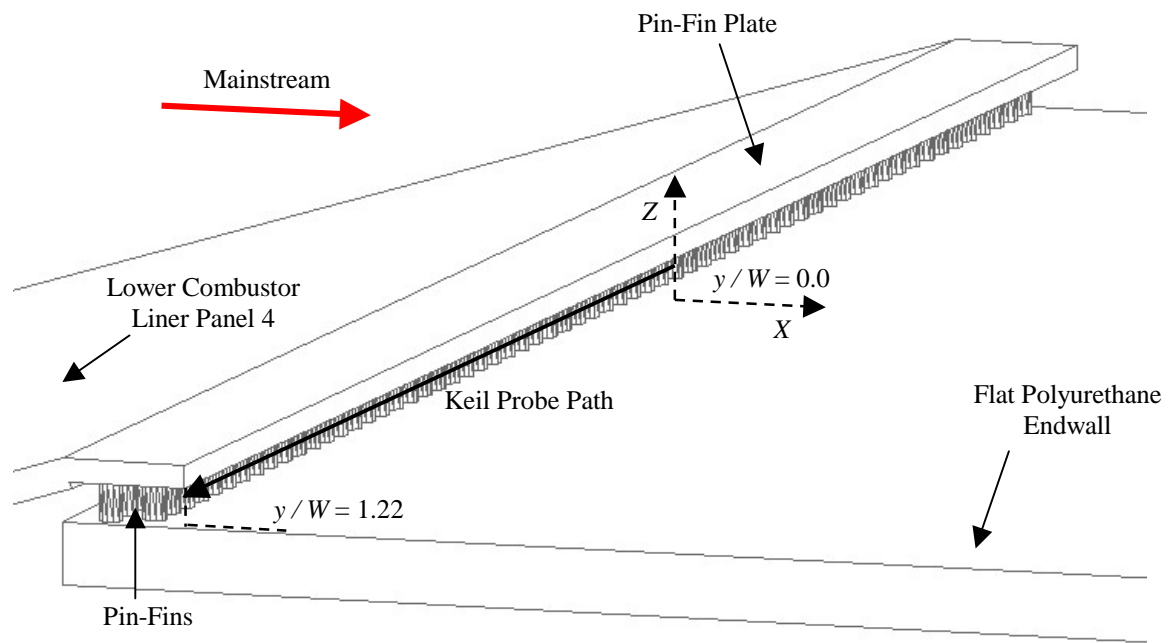


Figure 4-15 Schematic of the exit slot region indicating the measurement locations.

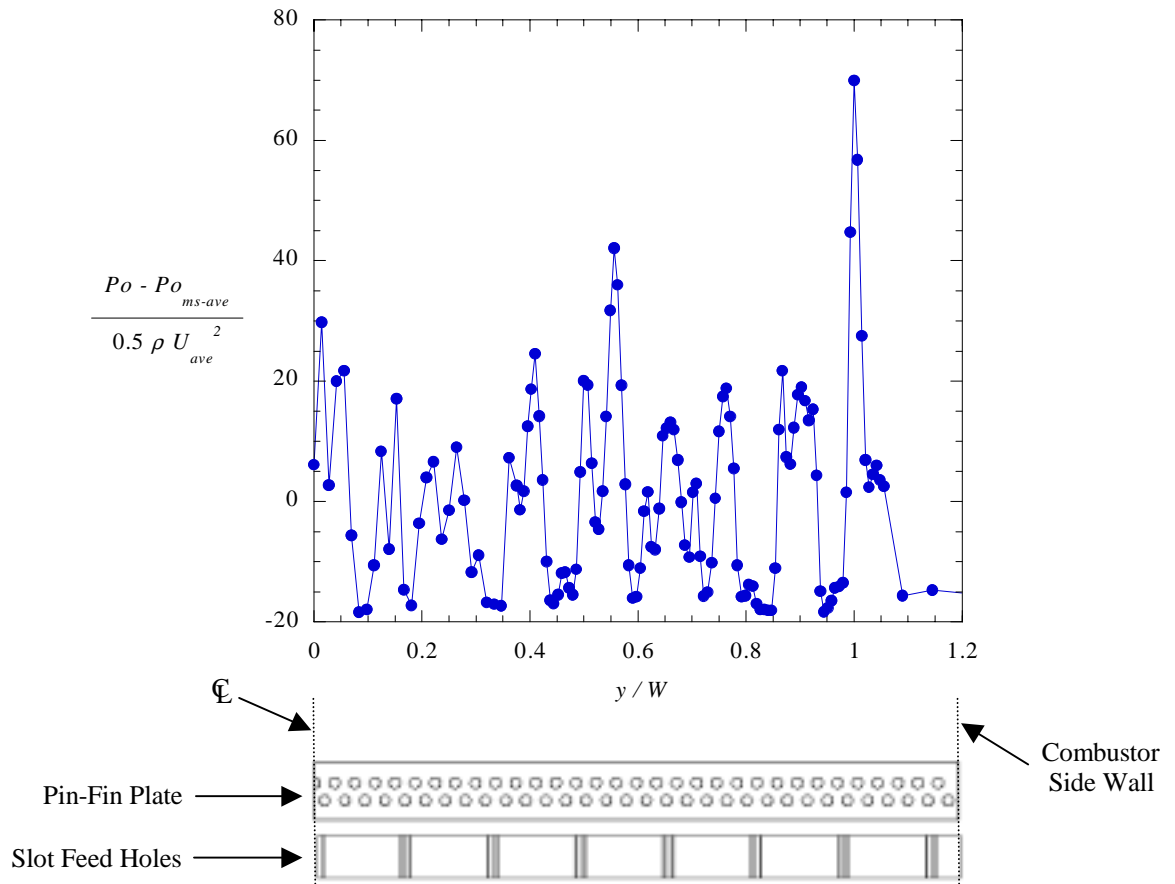


Figure 4-16 Graph of the exit slot total pressure profile with a schematic of the upstream component orientation.

5. Flow and Thermal Field Measurements at the Combustor Simulator Exit

The measurements taken within the straight exit test section were conducted to establish a baseline of the flow and thermal fields exiting the combustor simulator without any secondary flow interactions with the vanes. The following sections discuss all of the flow and thermal measurements that were performed for the two cases with and without dilution flow. These included velocity, total pressure, temperature, and turbulence measurements taken in both the pitch and span directions in the plane, shown in Figure 5-1, located upstream of the exit slot (Plane A). Since the velocity profiles taken at the combustor simulator exit were found to be nearly symmetric in both the pitch and span directions, note that sometimes only a partial plane was mapped. Total pressure and temperature measurements were also performed in both the pitch and span directions in the streamwise plane, shown in Figure 5-2, corresponding to the leading edge location of the vanes when present (Plane B). The chapter then discusses the adiabatic effectiveness measurements that were performed on the endwall.

5.1 Flow Field Measurements

Velocity measurements were taken in Plane A with the single component hot-wire. These measurements were taken for the cases with and without dilution flow. Figure 5-3 shows two profiles that were taken in the pitch direction at mid-span ($z/H = 0.5$) with and without dilution flow. It can be seen from the figure that the velocity profiles exiting the combustor simulator and entering the two-dimensional test section differ significantly between the cases with and without dilution flow. When the dilution flow is turned off the velocity profile exiting the simulator in the pitch direction is uniform except in the vicinity of the combustor simulator sidewalls ($y/W = \pm 1.22$) where boundary layer effects become dominate. When the dilution

flow is turned on the velocity profile in the pitch direction is non-uniform containing three peaks and two valleys centered about mid-pitch ($y/W = 0.0$). The two valleys correspond to the general pitch locations of the upstream second row dilution holes ($y/W = \pm 0.5$). These dilution holes are vertically inclined at 17° and inject coolant in a direction slightly opposite of the mainstream flow direction. The peaks correspond to the general pitch locations of the first row dilution holes ($y/W = 0.0, \pm 1.0$) which are not inclined. The maximum deviation from the average velocity for this velocity profile was 3.0 %. An important similarity between the two profiles is that both are nearly symmetric about mid-pitch.

Two velocity profiles were also taken in Plane A in the span direction at mid-pitch ($y/W = 0.0$) with and without dilution flow. These two profiles, shown in Figure 5-4, are also significantly different. When the dilution flow is turned off the velocity profile within this plane in the span direction takes the form of a parabola with a minimum velocity at mid-span and maximum velocities near the pin fin plate ($z/H = 0.05$ and 0.95). This behavior can be explained by the injection of mass flow (coolant) through the liners in which the velocity ratio of the coolant jet to the mainstream varies from 1.2 near the combustor entrance to 3.7 near the combustor exit. When the dilution flow is turned on the velocity profile in the span direction is more uniform and has two peaks near the pin fin plate. The relatively uniform velocities measured from $z/H = -0.3$ to 0.3 were a result of the presence of a nearly flat total pressure field in this region. The total pressure field was dictated primarily by the dilution flow and will follow later in this chapter. The velocity peaks measured near the pin fin shroud walls were a result of the mass flow injection through the upstream liners. Both of the velocity profiles, however, are nearly symmetric about mid-span. The overall effects of the dilution flow on the mid-pitch and mid-span velocity profiles entering the two-dimensional test section were to reduce variation in the span direction and to produce variation in the pitch direction.

The velocity profiles for the case without dilution flow contained little to no variation in the pitch direction and therefore the velocity profile measured in the span direction at mid-pitch for this case became representative of the entire flow field in the pitch direction. For this reason,

a complete mapping of the velocity field for the case without dilution flow was considered unnecessary. The velocity profiles for the case with dilution flow contained variations in both the pitch and span directions. These variations, however, were nearly symmetric about mid-pitch and mid-span and therefore only a partial mapping of the velocity field in Plane A was needed for the case with dilution flow. This partial mapping, shown as a contour plot in Figure 5-5, consisted of taking velocity profiles in the span direction at several pitch locations from $y/W = 0.0$ to 0.5 . The contour is a plot of normalized streamwise velocity (u/U) and indicates that a region of relatively high velocity existed between the pin fin plate and about 13 % of the total exit height (H). It can also be seen that this region of flow was nearly uniform in the pitch direction and was directly linked to the coolant injection through the upstream liners. The contour indicates that relatively lower velocities existed from $z/H = 0.13$ to 0.5 and the profiles varied slightly in both the span and pitch directions. These variations were, however, consistent with the mid-pitch and mid-span profiles discussed previously.

Total pressure measurements were taken with and without dilution flow in Plane A and Plane B using a Keil probe. Since the flow field was shown to be symmetric about mid-pitch and mid-span, the contour mapping procedure discussed previously was also used for the total pressure measurements to create contours of the total pressure fields. The local total pressure was non-dimensionalized according to the expression shown in equation 5-1.

$$\Delta P = \frac{P_o - P_{o_{ms-ave}}}{0.5 \rho U_{ave}^2} \quad (5-1)$$

In equation 5-1, ΔP relates the local total pressure to the average total pressure measured at mid-span and the average dynamic pressure measured within the plane. This definition implies that $\Delta P = 0.0$ corresponds to a local total pressure that is equivalent to the average total pressure measured at mid-span and $\Delta P = \pm 1.0$ corresponds to a local total pressure that is equivalent to one average dynamic pressure above or below the average mid-span total pressure.

The total pressure measurements taken in Plane A and Plane B without dilution flow are shown in the contours in Figure 5-6. The measurements taken within Plane A indicated that the total pressure varied significantly from $\Delta P = 0.0$ to 1.0 in the region from $z/H = 0.07$ to 0.2. This region of the total pressure field represents the total pressure associated with the film coolant that is injected through the upstream liners. The largest total pressures that were measured were within this small region, which is in agreement with the velocity profiles presented earlier. It was found that at span locations greater than $z/H = 0.25$ the total pressure did not vary and therefore measurements were taken only to 33% of the total exit height. It can be seen from the figure that within similar span and pitch regions the total pressure fields in Plane A and Plane B appear very similar. This implied that the total pressure field of the mainstream flow (Plane A) was not significantly affected by the sudden expansion it experienced at the trailing edge of the pin fin plate (located in the straight test section). The measurements taken in Plane B included the total pressure associated with the flow passing through the exit slot region from $z/H = 0.0$ to 0.05. The total pressure in this region was seen to be highly non-uniform and at much lower total pressures than those measured above $z/H = 0.2$. This behavior, however, was expected due to an inconsistency in the pitchwise orientation of the feed holes in relation to the arrangement of the pin fins. The alignment, discussed in Chapter 4, was such that some feed holes inject flow directly into the body of a pin-fin located in the first row while others inject flow into the gap between two adjacent pin-fins in the first row, thus directing the flow into the body of a pin-fin located in the second row. This flow arrangement led to sporadic variation in slot cooling flow coverage near the endwall. Note that the scale of the contours in this figure was chosen to allow a direct comparison between the cases with and without dilution flow. Overall, there was a large variation in total pressure from the endwall to mid-span with the majority of the variation concentrated within the first 20 % of the total exit height.

Total pressure measurements were also taken in Plane A and Plane B for the case with dilution flow, as shown in Figure 5-7. The measurements taken within Plane A indicated that the total pressure field had become significantly more uniform in the region from $z/H = 0.07$ to 0.5 as compared to the case without dilution. The measurements taken within this region indicated a

significantly lower and smaller ΔP range from -0.05 to 0.15 compared to the case without dilution in which the ΔP range was from 0.0 to 1.0. This is an 80% reduction in the overall total pressure range. For the case with dilution flow a larger pressure gradient was observed to be concentrated in a small region from $z/H = 0.05$ to 0.07 in which the total pressure varied from $\Delta P = -0.5$ to -0.1 . These trends are consistent with the velocity profiles discussed previously in which a large velocity gradient was observed near the pin fin plate and a relatively flat velocity gradient existed towards the mid-span region. Although the ΔP range in the region from $z/H = 0.07$ to 0.5 was significantly reduced for the case with dilution, variation in total pressure was still evident in this region. This variation can be seen in Figure 5-8 which shows a comparison between the total pressure measurements taken in Plane A with the original contour scale and a more refined contour scale. The contour with the more detailed scale reveals the small total pressure variations that the original scale masked.

The total pressure fields in Plane A and Plane B appear almost identical from $z/H = 0.07$ to 0.5 (similar to the case without dilution flow) indicating that the sudden expansion in the two-dimensional test section did not significantly alter the total pressure field between these two streamwise planes. The total pressure field associated with the flow passing through the exit slot region from $z/H = 0.0$ to 0.05 was measured in Plane B. The total pressure in this region was also seen to be highly non-uniform and at much lower total pressures than those measured above $z/H = 0.07$. These measurements in the slot flow region indicated a pressure range from $\Delta P = -1.2$ to -0.5 which was significantly lower than the range measured for the case without dilution ($\Delta P = -0.7$ to 0.3). For the case with dilution flow, the average total pressure at mid-span was higher than for the case without dilution flow. Overall, there was a large variation in total pressure from the endwall to mid-span with the majority of the variation concentrated within the first 10 % of the total exit height.

The contours of total pressure were then spatially averaged in the pitch direction. Figure 5-9 shows the spatially averaged profiles for the cases with and without dilution flow in both Plane A and Plane B. Also shown in the figure is the total pressure profile associated with a

typical turbulent boundary layer. In comparing the results between the two measurement planes for a given flow case it can be seen from the figure that very little difference was detected in the spatially averaged profiles. The profiles for the case without dilution flow are characterized by relatively low total pressures below $z/H = 0.05$ and a large peak from $z/H = 0.05$ to 0.2 with total pressures well above the mid-span average total pressure. The profiles for the case with dilution flow are also characterized by relatively low total pressures below $z/H = 0.05$. For $z/H \geq 0.05$, however, the spatially averaged total pressures for the case with dilution flow are much more uniform and close to the mid-span average total pressure. The overall effect of the dilution flow was to reduce the variation in total pressure in both measurement planes. It is important to note that all four spatially averaged profiles differ significantly from the turbulent boundary layer profile. This is important because the total pressure profile exiting the combustor dictates the development of the flow field in the nozzle guide vane passages in the turbine.

Turbulence measurements were taken in Plane A with the single component hot-wire. These measurements were taken for the cases with and without dilution flow. The turbulence intensity was defined to be the ratio of the local root-mean-square velocity to the local average velocity (u_{rms}/U). Figure 5-10 shows two turbulence profiles that were taken in the pitch direction at mid-span ($z/H = 0.5$) with and without dilution flow. It can be seen from the figure that the turbulence profiles entering the straight test section differed significantly between the two cases. The turbulence profile in the pitch direction without dilution flow was nearly uniform at 1.0% except in the vicinity of the combustor simulator sidewalls ($y/W = \pm 1.22$) where the maximum turbulence level measured was 1.7%. The turbulence profile in the pitch direction with dilution flow was non-uniform containing two peaks and one valley centered about mid-pitch ($y/W = 0.0$). The intensity of the turbulence ranged from 14.5% to 18.5% which was significantly larger than the case without dilution flow. The higher turbulence levels were measured in the general pitch locations of the second row dilution holes and the lower turbulence levels were measured in the general pitch locations of the first row dilution holes. This distribution was expected since the turbulent flow associated with the second row dilution jets

had less time to decay than the turbulent flow associated with the first row dilution jets due to the second row dilution jets being located closer axially to the measurement plane.

Two turbulence profiles were also taken in Plane A in the span direction at mid-pitch with and without dilution flow. These two profiles, shown in Figure 5-11 from $z/H = 0.05$ to $z/H = 0.5$, are also significantly different. When the dilution flow was turned off the turbulence profile within this plane in the span direction contained an inflection point located near $z/H = 0.13$. At span locations larger than the inflection point the turbulence profile gradually decreased to the mainstream turbulence level (1.0 %). Turbulence profiles of this type occur with high-velocity tangential injection through upstream slots or holes in the wall into a turbulent boundary layer. Therefore, the region of the profile from $z/H = 0.05$ to 0.25 was the turbulence associated with the upstream coolant that was injected through the liner walls. The turbulence intensity was measured to be about 4.5 % near the pin fin plate. It then increased sharply from $z/H = 0.05$ to 0.13 to about 10% at $z/H = 0.13$ and then reduced sharply from $z/H = 0.13$ to 0.25 to about 1.0 % at $z/H = 0.25$. Overall, the turbulence associated with velocity field in Plane A without dilution flow was concentrated within the first 25 % of the total exit height. When the dilution flow was turned on the turbulence profile within this plane in the span direction was considerably more uniform. The turbulence intensity was measured to be about 13.0 % near the pin fin plate. It then gradually increased from $z/H = 0.1$ to 0.2 to about 14.5 % at $z/H = 0.2$ and then remained nearly uniform from $z/H = 0.2$ to 0.5 .

A turbulence contour was generated, shown in Figure 5-12, for the case with dilution flow by taking spanwise turbulence profiles at several pitch locations. The contour illustrates that the turbulence levels varied in both the span and pitch directions. At a pitch location corresponding to a first row dilution hole ($y/W = 0.0$) the turbulence intensity varied in the span direction from 13.0 % near the pin fin plate to 14.5 % from $z/H = 0.25$ to 0.5 . As the pitch location was increased the variation of the turbulence level also increased. The spanwise profile taken at $y/W = 0.5$ (corresponding to a second row dilution hole) resulted in turbulence levels that varied from 13.0 % near the pin fin plate to 17.5 % near mid-span. The turbulence levels

were much more uniform in the pitch direction for span locations in the range $z/H = 0.05$ to 0.2 . This behavior was attributed to the layer of coolant that was injected through the upstream liners which is distributed nearly evenly in the pitch direction. At span locations greater than $z/H = 0.2$ the turbulence levels varied significantly in the pitch direction. This variation was produced by the dilution flow as was previously discussed. The contour of turbulence intensity was then spatially averaged in the pitch direction. Figure 5-13 shows the spatially averaged profile for the case with dilution flow. This figure shows that in general the turbulence levels increased from 12.5 % near the pin fin plate to 15 % at $z/H = 0.2$. Overall, the dilution flow resulted in turbulence profiles that were nearly uniform in the span direction (at a given pitch location) for span locations larger than $z/H = 0.2$. These uniform levels, however, increased significantly with pitch location from $y/W = 0.0$ to 0.5 . The dilution flow also resulted in turbulence profiles that were nearly uniform in the pitch direction for span locations within the region $z/H = 0.05$ to 0.20 .

The turbulent length scale and energy spectra measurements consisted of taking a series of data sets at several pitch locations. The data sets were taken at mid-span ($z/H = 0.5$) in Plane A at ten evenly spaced pitch locations from $y/W = 0.0$ to 0.5 . The length scale analysis discussed in Chapter 3 was performed on the acquired data and resulted in the turbulent length scales shown in Figure 5-14. The length scales have been non-dimensionalized by the diameter of the first row of dilution holes. The length scale of the turbulent eddies near mid-pitch ($y/W = 0.0$) were about 0.75 of the diameter D_1 . The length scales gradually increased with increasing pitch location to about 80 % of D_1 at $y/W = 0.4$. The length scales then sharply increased in the region $y/W = 0.4$ to 0.5 to about 93 % of D_1 . This gradual and then sharp increase in the length scale was attributed to the distribution of the dilution flow field from $y/W = 0.0$ to 0.5 . The larger length scales were measured at pitch locations near the second row of dilution holes and the smaller length scales were measured at pitch locations near the first row of dilution holes which were smaller in diameter. It can be seen that the characteristic length of the turbulent eddies scaled with the diameter of the dilution holes.

The energy spectra analysis discussed in Chapter 3 was also performed on the acquired data and resulted in a series of turbulent energy spectra at each of the ten pitch locations. Due to the close similarity between the spectra plots for a given pitch location, only two energy spectra plots are given. These two plots are shown in Figure 5-15 and they represent the turbulent energy spectra for the pitch locations with the largest and smallest turbulent length scales ($y/W = 0.0$ and 0.5). It can be seen from the figure that the two energy spectra profiles are very similar and that good agreement occurs with the von Karman profile at low wave numbers. At higher wave numbers, however, viscous dissipation of the turbulent kinetic energy in the turbulent eddies becomes increasingly important. The von Karman model does not take into account this importance and therefore the energy spectra of the measured data deviates from the von Karman profile with increasing wave numbers.

5.2 Thermal Field Measurements

The thermal field entering the straight test section was quantified by taking temperature measurements in Plane A and Plane B using the thermocouple rake. Since the flow field was shown to be symmetric about mid-pitch and mid-span, the contour mapping procedure used for the total pressure measurements was also used for the temperature measurements to create contours of the thermal fields within in these two planes. The temperature measurements are expressed in terms of the dimensionless temperature parameter θ that was defined in Chapter 4. Large values of θ indicate that the temperature of the flow is representative of the coolant temperature and small values of θ imply that the temperature of the flow is indicative of the mass averaged freestream temperature. A negative value of θ implies that the flow temperature is warmer than the mass averaged freestream temperature.

A contour of the temperature measurements taken in Plane B without dilution flow is shown in Figure 5-16. These measurements indicated that the temperature varied significantly from $\theta = 0.0$ to 1.0 in the region from $z/H = 0.0$ to 0.33 . It was found that at span locations

greater than $z/H = 0.25$ the temperature did not vary and therefore measurements were again taken only to 33% of the total exit height. The contour shows that there were non-uniformities in the exit slot flow by revealing a pitchwise variation of the flow temperature in the region $z/H = 0.0$ to 0.05 from $\theta = 0.8$ to 1.0 . This non-uniformity of temperature in the pitch direction, however, was expected due to the misalignment of the feed holes and pin fins discussed previously. The region from $z/H = 0.05$ to 0.25 represents the temperature associated with the film coolant that is injected through the upstream liners. Within this region there was a large variation in temperature from $\theta = 0.0$ to 0.8 . Note that the scale of the contour in this figure was chosen to allow a direct temperature comparison between the cases with and without dilution flow. Overall, it is important to note that all temperature gradients that were measured for the case without dilution were within the first 25 % of the total exit height.

The temperature measurements taken in Plane A and Plane B with dilution flow are shown in the contours in Figure 5-17. The measurements taken in Plane A appear almost identical to those measured in Plane B. A slightly cooler region just above the step was noticed, however, in the span direction between the two planes. This was explained by the additional turbulent mixing that the freestream experienced with the coolant layer (associated with the upstream liners) between Plane A and Plane B and the additional coolant that was injected through the slot that was located between Plane A and Plane B. A small temperature gradient in the pitch direction can also be seen in the figure in the region from $y/W = 0.25$ to 0.5 and $z/H = 0.05$ to 0.5 . This gradient was associated with the coolant that was injected through the second row dilution hole (located at $y/W = 0.5$). This region was slightly cooler than the corresponding region from $y/W = 0.0$ to 0.25 and $z/H = 0.05$ to 0.5 because the coolant injected through the second row dilution hole had less time to mix out with the surrounding warmer flow than the coolant injected through the first row dilution hole that is located further upstream.

The temperature varied from $\theta = 0.4$ to 1.0 in the slot region from $z/H = 0.0$ to 0.05 for the case with dilution flow. Within the same region and without dilution flow, the temperature varied only from $\theta = 0.8$ to 1.0 . The dilution flow therefore greatly increased the overall

temperature gradient within this region. This behavior is in contrast, however, to that experienced in the region $z/H = 0.05$ to 0.25 . Within this region the temperature varied from $\theta = -0.05$ to 0.45 for the case with dilution flow and varied from $\theta = 0.2$ to 1.0 for the case without dilution flow. The dilution flow therefore greatly reduced the overall temperature gradient within this region. A negative value of θ indicated that the flow was warmer than the mass-averaged temperature at the combustor simulator exit. At span locations greater than $z/H = 0.25$ the temperature did not vary for the case without dilution flow and only varied from $\theta = -0.05$ to 0.05 for the case with dilution flow.

The contours of temperature were then spatially averaged in the pitch direction. Figure 5-18 shows the spatially averaged profiles for the cases with and without dilution flow. In comparing the results between the two measurement planes for the case with dilution flow it can be seen from the figure that the two spatially averaged profiles are very similar. The profile for the case without dilution flow (Plane B) is characterized by large values of θ from $\theta = 0.95$ near $z/H = 0.0$ to $\theta = 0.88$ at $z/H = 0.05$ which can be attributed to the exit slot flow. This same profile also shows that in general a very large gradient and reduction in θ occurs from $\theta = 0.88$ at $z/H = 0.05$ to $\theta = 0.08$ at $z/H = 0.25$ which can be attributed to the upstream film-coolant. This profile also indicates that very little variation occurs at vertical locations above $z/H = 0.25$ where θ ranges between $\theta = 0.1$ to $\theta = 0.0$. The profile for the case with dilution flow (Plane B) is characterized by much lower values of θ ranging sharply from $\theta = 0.87$ near $z/H = 0.0$ to $\theta = 0.35$ at $z/H = 0.05$. This same profile also shows that θ varies from $\theta = 0.35$ at $z/H = 0.05$ to $\theta = 0.0$ at $z/H \geq 0.25$. The overall effect of the dilution flow was to significantly increase mixing between the mainstream and the film-coolant thereby considerably reducing the θ values over the full range of vertical location. It was also shown that in both flow cases the majority of the temperature variation occurred within the first 25 % of the total exit height.

5.3 Endwall Adiabatic Effectiveness Measurements

The adiabatic effectiveness levels on the endwall surface were determined by taking temperature measurements of the adiabatic endwall with the infrared camera. The adiabatic effectiveness (η) of a particular flow field is defined according to the expression given in equation 5-2.

$$\eta = \frac{T_{\infty} - T_{aw}}{T_{\infty} - T_c} \quad (5-2)$$

The adiabatic effectiveness level has lower and upper bounds of zero and one, respectively. A value of one implies that the temperature of the adiabatic wall (T_{aw}) is indicative of the coolant temperature (T_c). A value of zero implies that the temperature of the adiabatic wall is representative of the mass averaged freestream temperature (T_{∞}).

Adiabatic effectiveness levels were determined for the cases with and without dilution flow. Two contours were made for each case. The first contour shows the leading edge region of the endwall near the exit slot. This rectangular region included one full pitch by an axial length that included 15 D downstream of the trailing edge of the pin fin plate. The second contour shows a larger axial region that is 140 D (1.8 C) in length and 17 D in width centered about $y/W = 0.0$.

The adiabatic effectiveness levels that were measured in the near exit slot region for both flow cases are displayed in Figure 5-19. It can be seen that the adiabatic effectiveness levels on the endwall for the case without dilution flow were high and ranged from $\eta = 0.93$ to 1.0. It also shows that there was a slight variation of the adiabatic effectiveness levels in the pitch direction. This variation of η was attributed to the sporadic coverage of the cooling flow passing through the exit slot. The leading edges of the vanes (when present) are approximately 6 D downstream of the trailing edge of the pin fin plate. The contour shows that at this axial location the endwall surface temperature is indicative of the coolant temperature. The contour also shows that the

adiabatic effectiveness levels on the pin fin plate were high and ranged from $\eta = 0.88$ to 0.93 thus indicating that the upstream film-cooling holes were providing sufficient cooling.

Figure 5-19 also shows the adiabatic effectiveness levels in the near exit slot region for the case with dilution flow. It can be seen that adiabatic effectiveness levels were nearly symmetric on the pin fin plate and varied from $\eta = 0.5$ to 0.7 . The contour also indicates that the adiabatic effectiveness levels on the endwall were not as symmetric as those on the pin fin plate. This variation of η in the pitch direction was again attributed to the sporadic coverage of the cooling flow passing through the exit slot. The contour shows that in the near exit slot region, even with the variation of coolant in the pitch direction, the adiabatic effectiveness levels were high and ranged from $\eta = 0.7$ to 1.0 . The overall effect of the dilution flow was to significantly reduce the adiabatic effectiveness levels.

Figure 5-20 shows the adiabatic effectiveness levels downstream of the exit slot for both flow cases. It can be seen that for the case without dilution flow η varied in the axial direction from $\eta = 1.0$ at $x/D = 0.0$ to 0.85 at $x/D = 140$. It is also important to note that at one chord length downstream of the pin fin plate η varied between 0.89 and 0.91 . This implied that the cooling potential of exit slot coolant and film-coolant was still present at an axial location equivalent to one vane chord length downstream of the exit slot. It can also be seen in the figure that the adiabatic effectiveness levels for the case with dilution flow varied significantly in the axial direction from $\eta = 1.0$ at $x/D = 0.0$ to 0.25 at $x/D = 140$. Also note that at one chord length downstream of the pin fin plate η varied between 0.3 and 0.35 . This implied that the cooling potential of exit slot coolant and film-coolant was still present, although significantly reduced, at an axial location equivalent to one vane chord length downstream of the exit slot.

Adiabatic effectiveness measurements were also taken with thermocouples located near mid-pitch down the axial length of the straight exit test section. Figure 5-21 shows that there was good agreement between the infrared camera measurements and the thermocouples used for calibration. The figure verifies that the overall effect of the dilution flow was to appreciably

reduce the adiabatic effectiveness levels on the endwall with increasing axial distance from the exit slot.

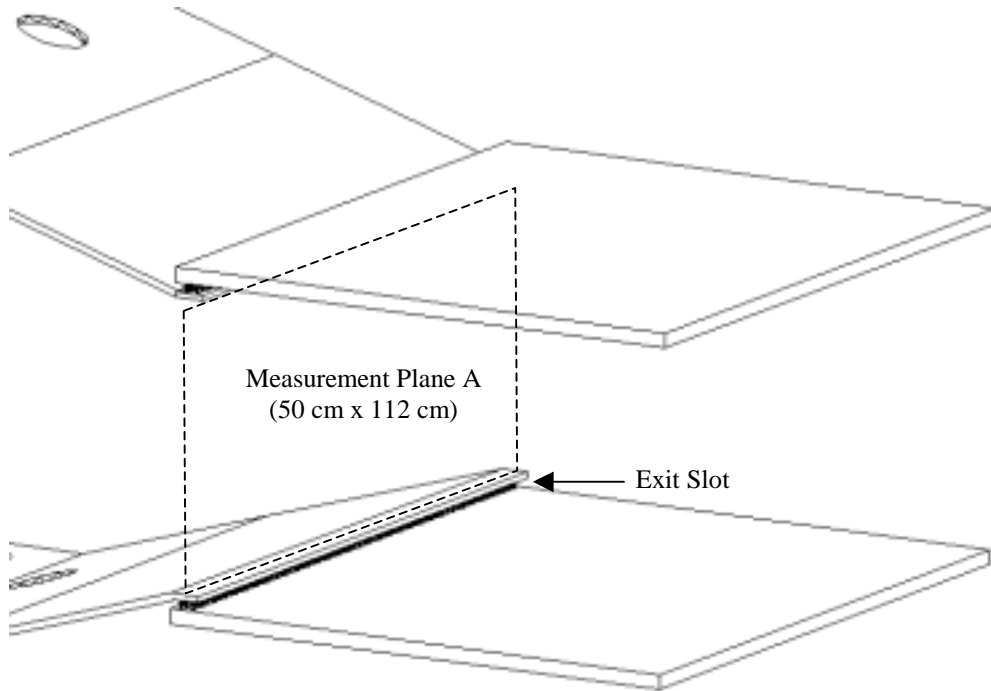


Figure 5-1 Schematic indicating the measurement Plane A located upstream of the exit slot.

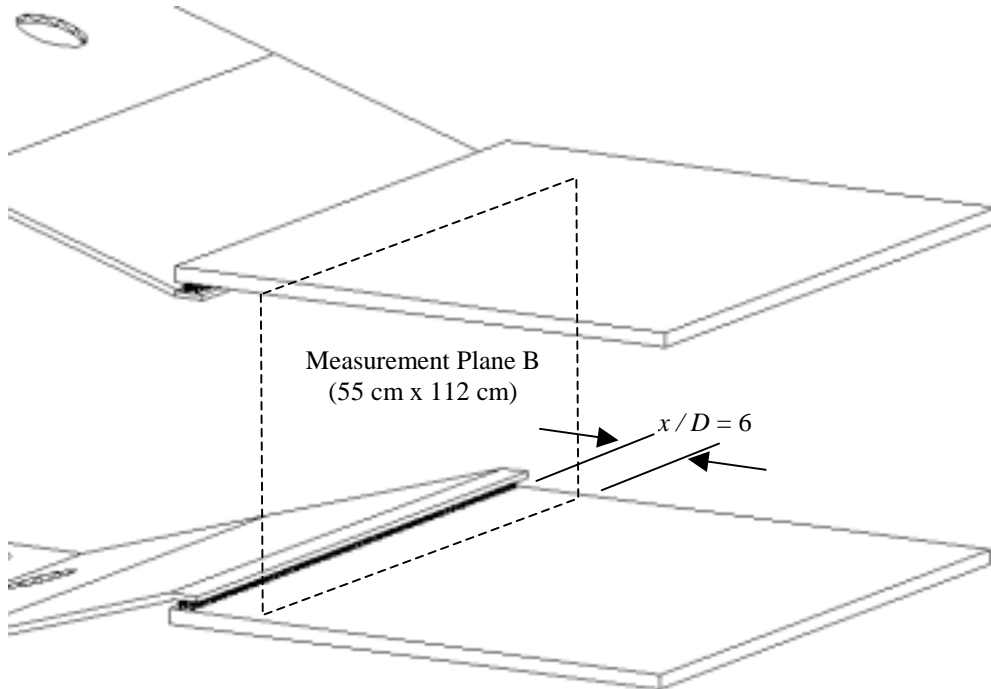


Figure 5-2 Schematic indicating the measurement Plane B located downstream of exit slot.

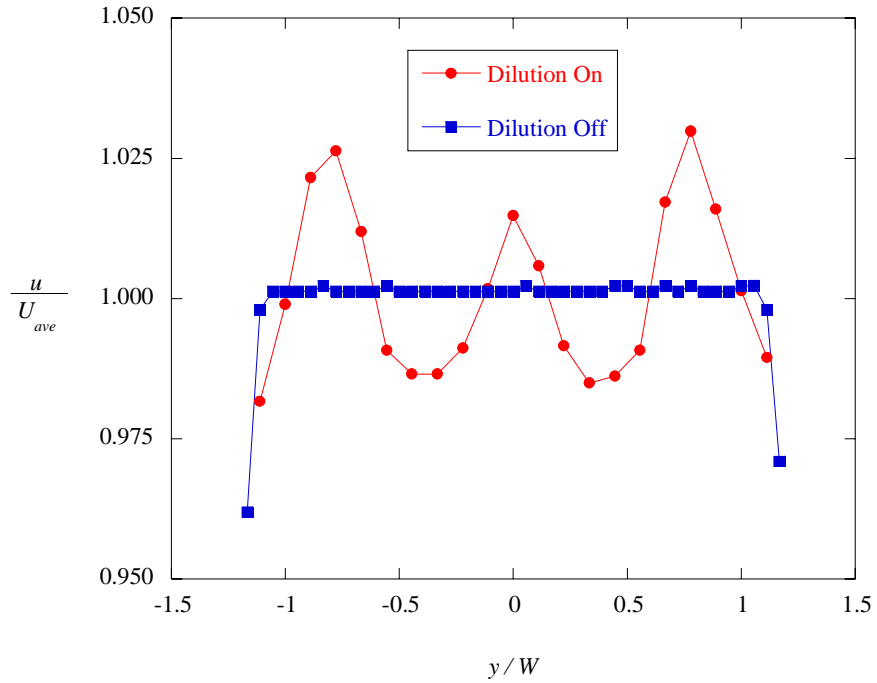


Figure 5-3 Graph comparing pitchwise velocity profiles in Plane A at mid-span ($z/H = 0.5$) with and without dilution flow.

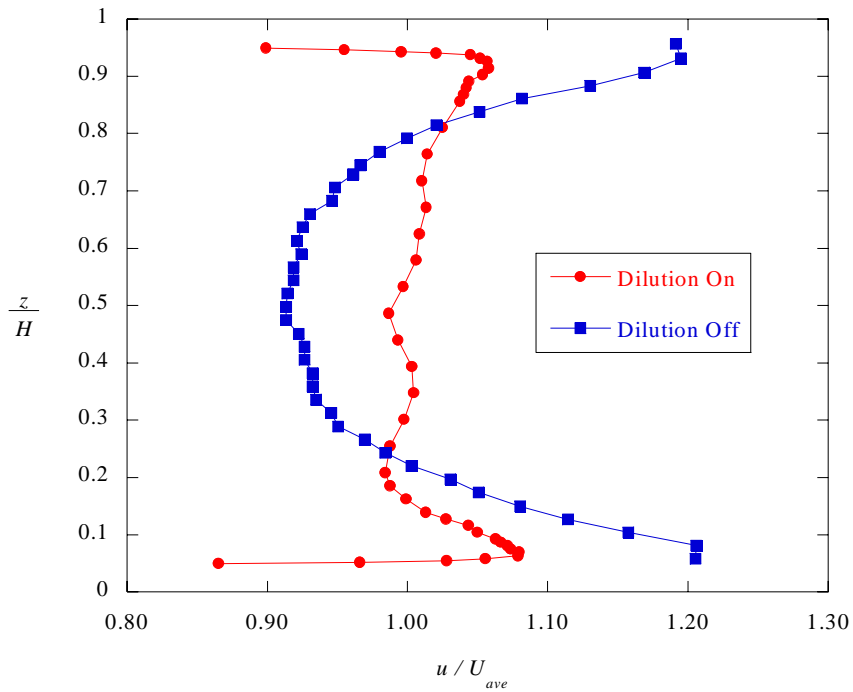


Figure 5-4 Graph comparing spanwise velocity profiles in Plane A at mid-pitch ($y/W = 0.0$) with and without dilution flow.

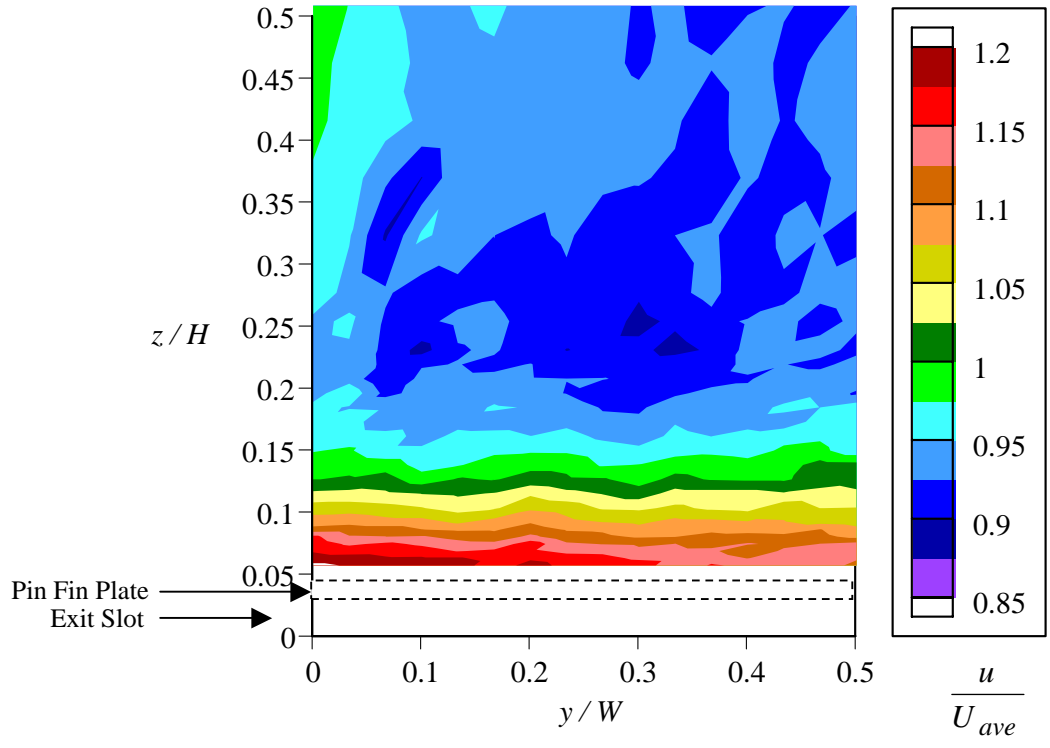


Figure 5-5 Contour plot showing normalized streamwise velocity with dilution flow in Plane A.

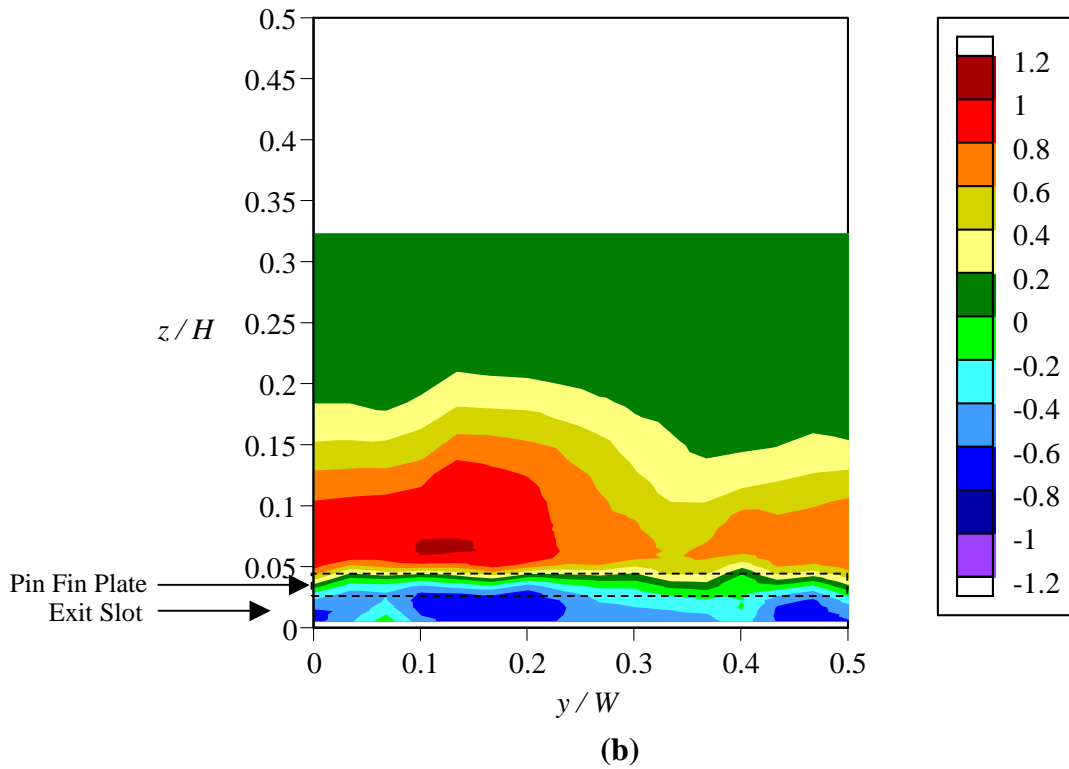
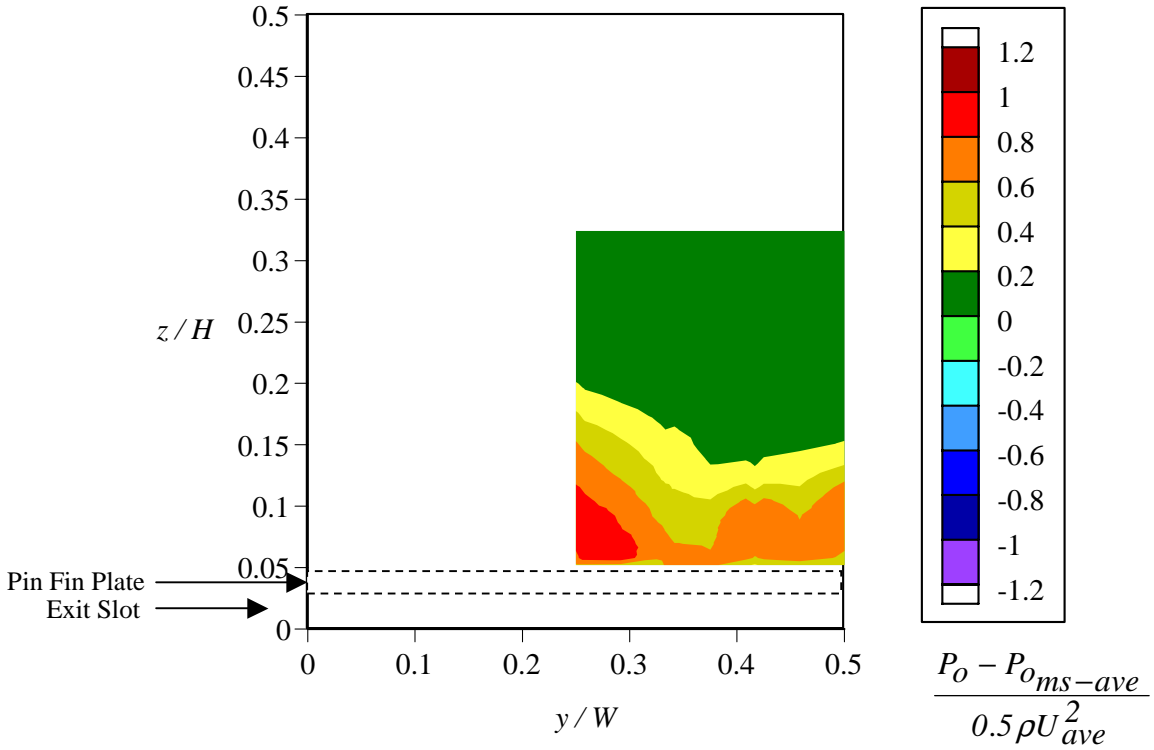


Figure 5-6 Contour plots of non-dimensional total pressure without dilution flow in (a) Plane A and (b) Plane B.

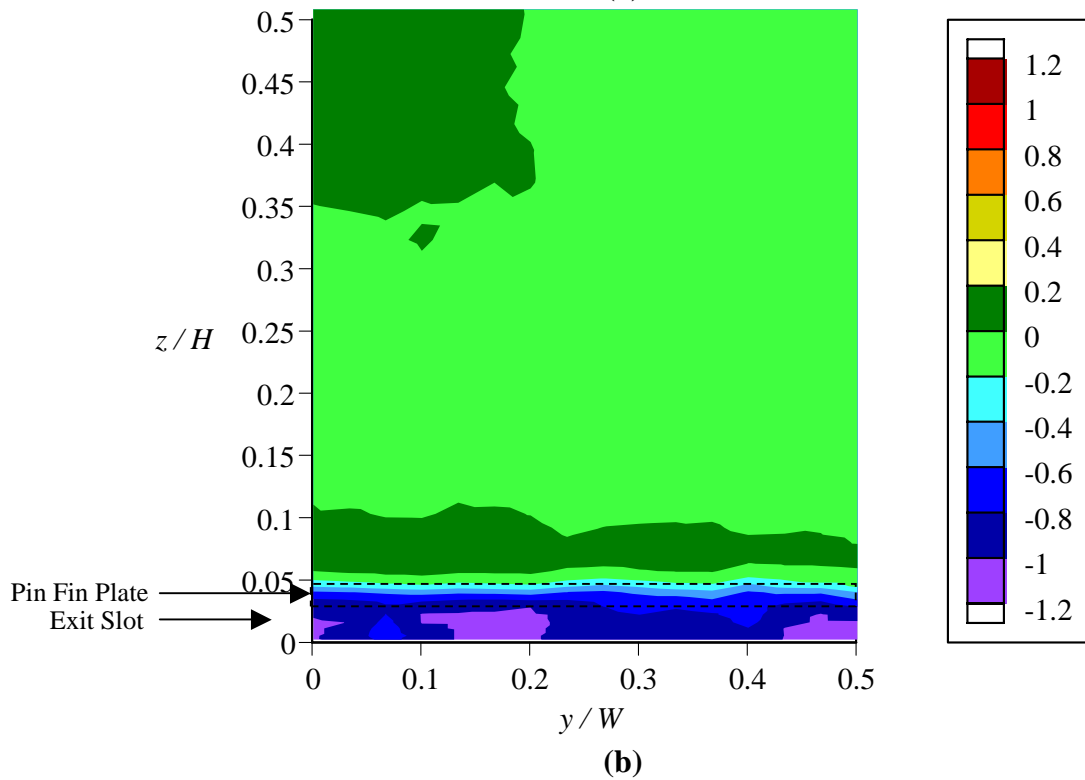
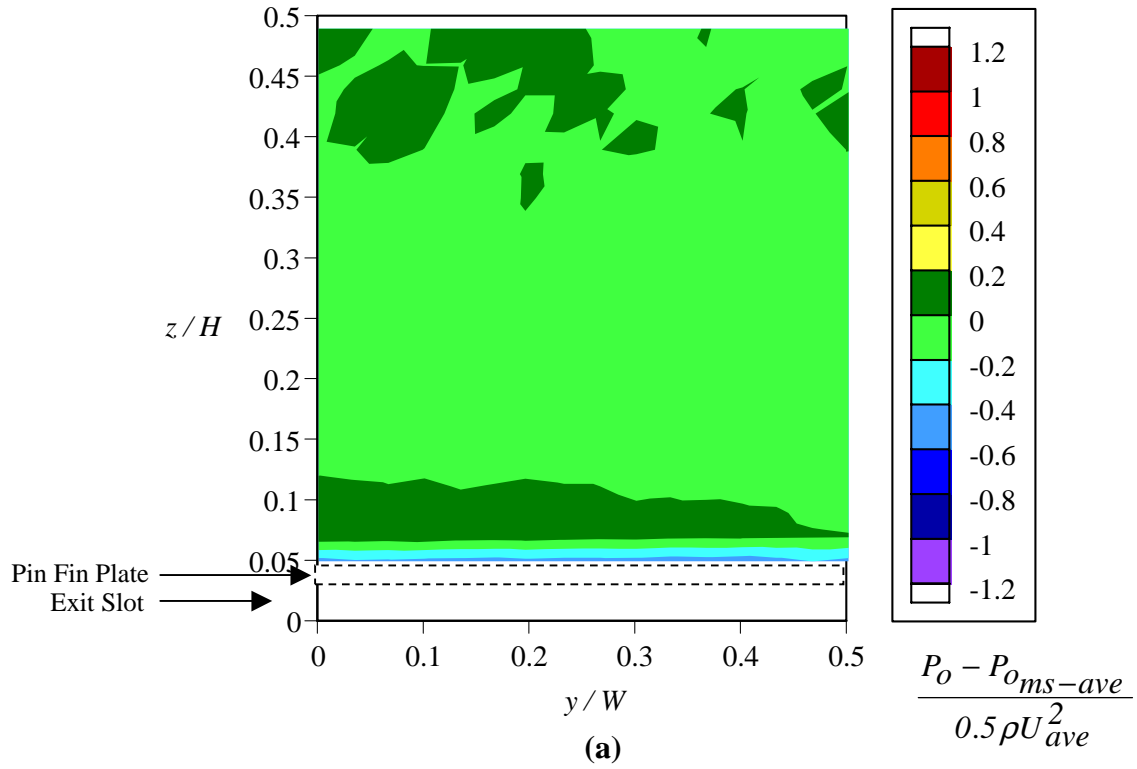


Figure 5-7 Contour plots of non-dimensional total pressure with dilution flow in (a) Plane A and (b) Plane B.

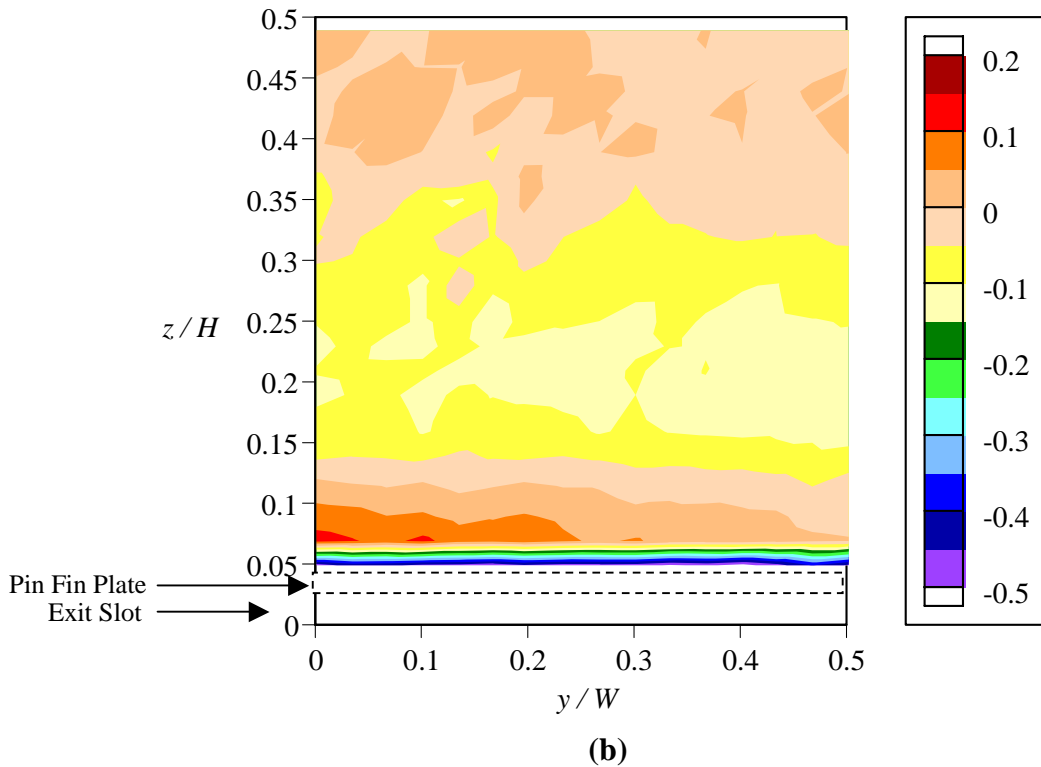
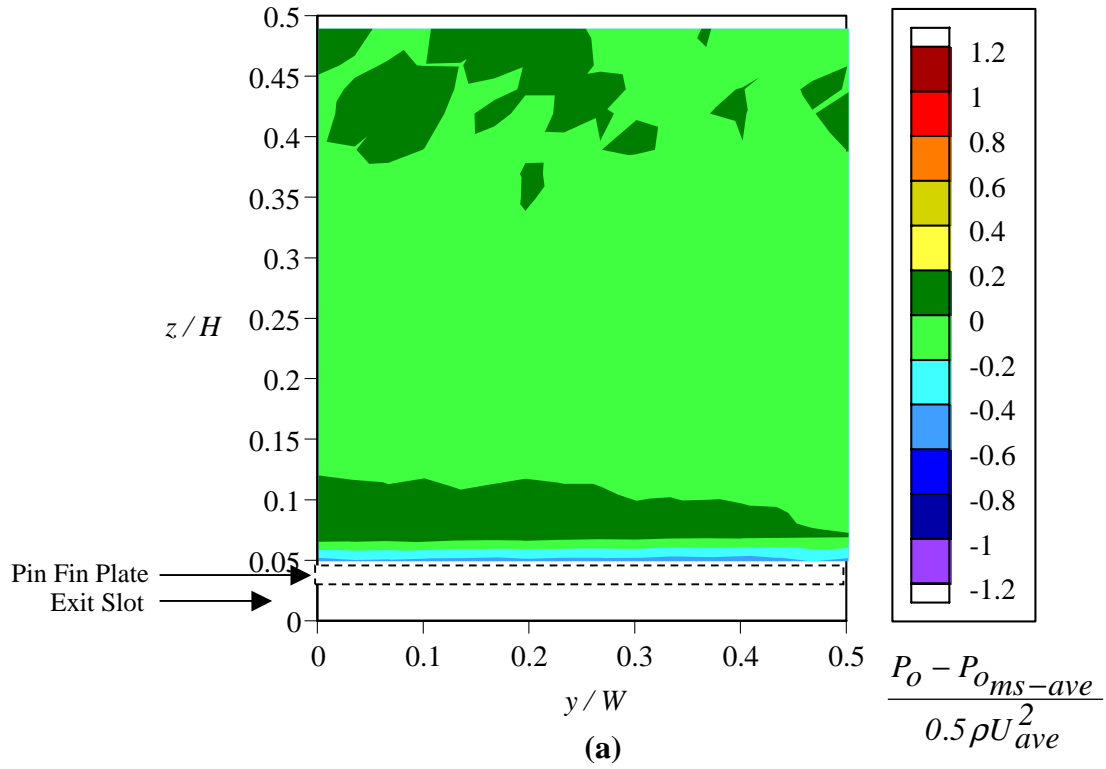


Figure 5-8 Comparison of non-dimensional total pressure contours with dilution flow in Plane A indicating the variation of pressure on (a) original scale and (b) refined scale.

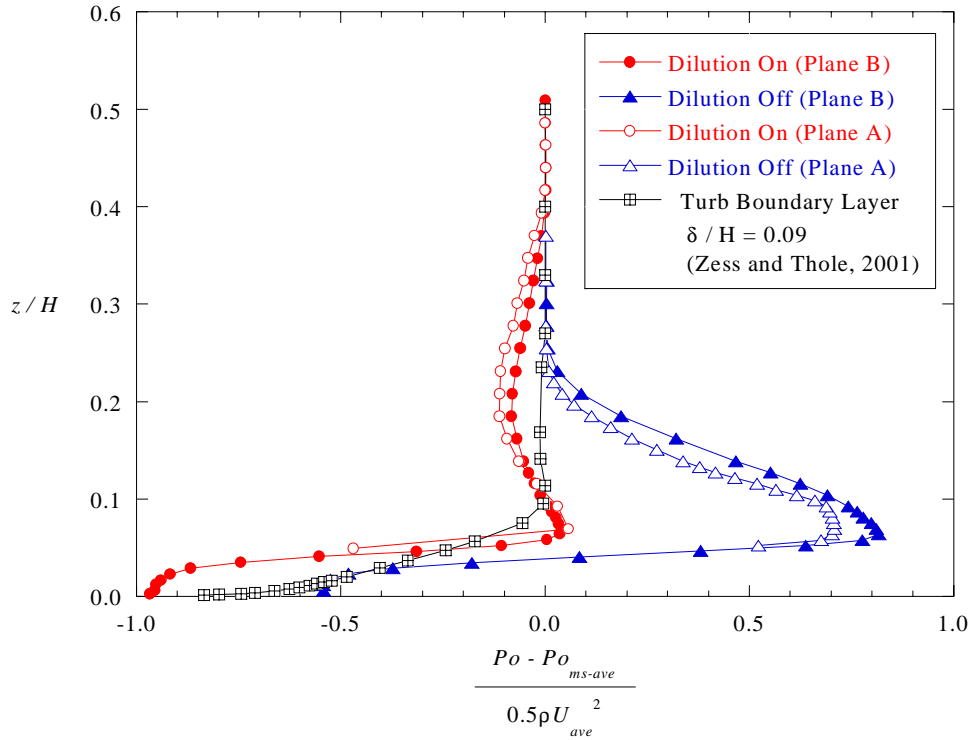


Figure 5-9 Graph showing the spatially averaged non-dimensional total pressure profiles.

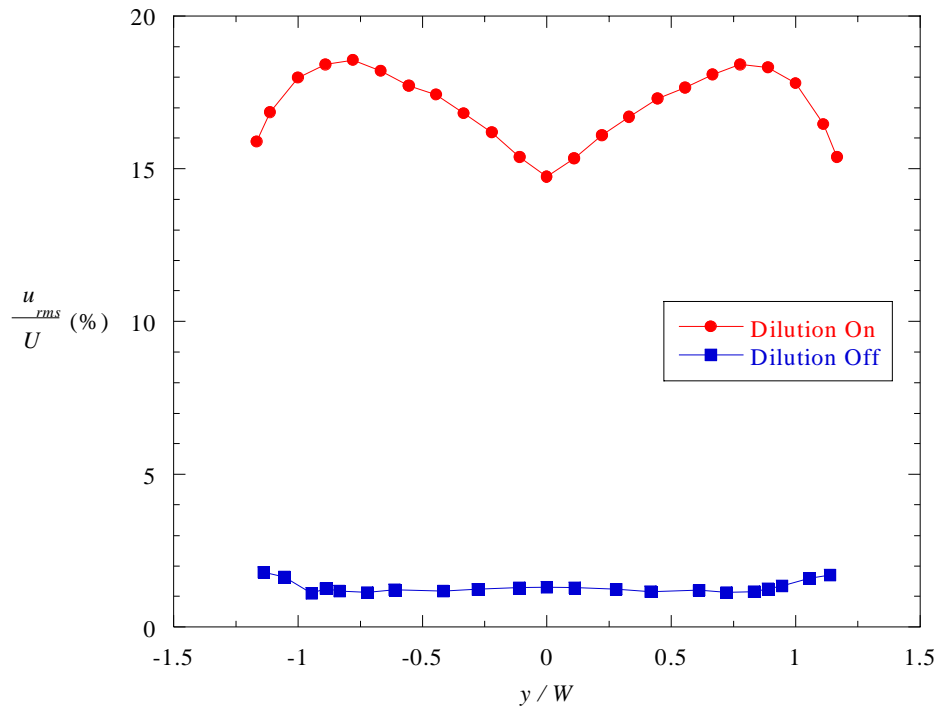


Figure 5-10 Graph showing a comparison of pitchwise turbulence intensity with and without dilution flow in Plane A ($z/H = 0.5$).

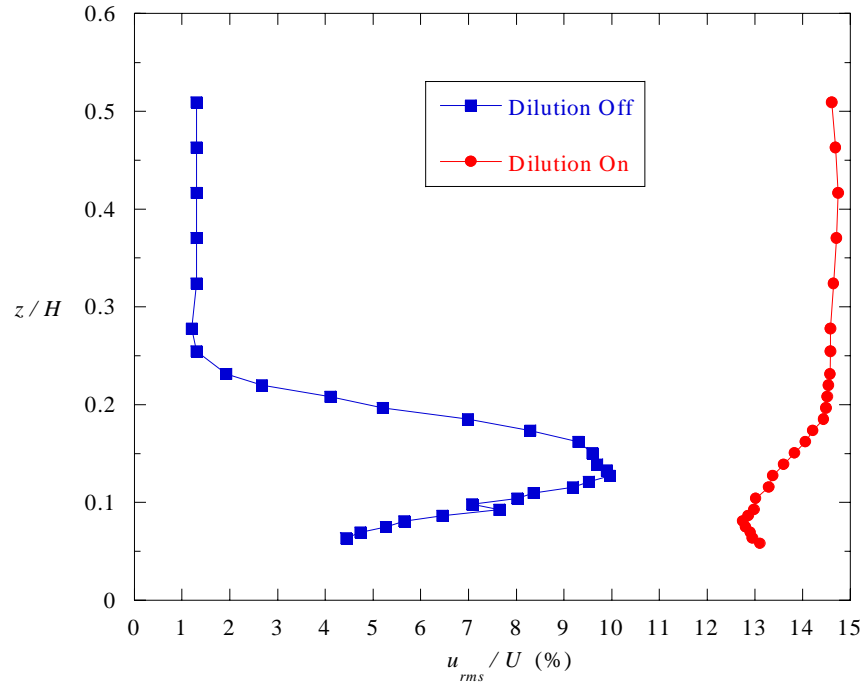


Figure 5-11 Graph showing a comparison of spanwise turbulence intensity for the cases with and without dilution flow in Plane A ($y/W = 0.0$).

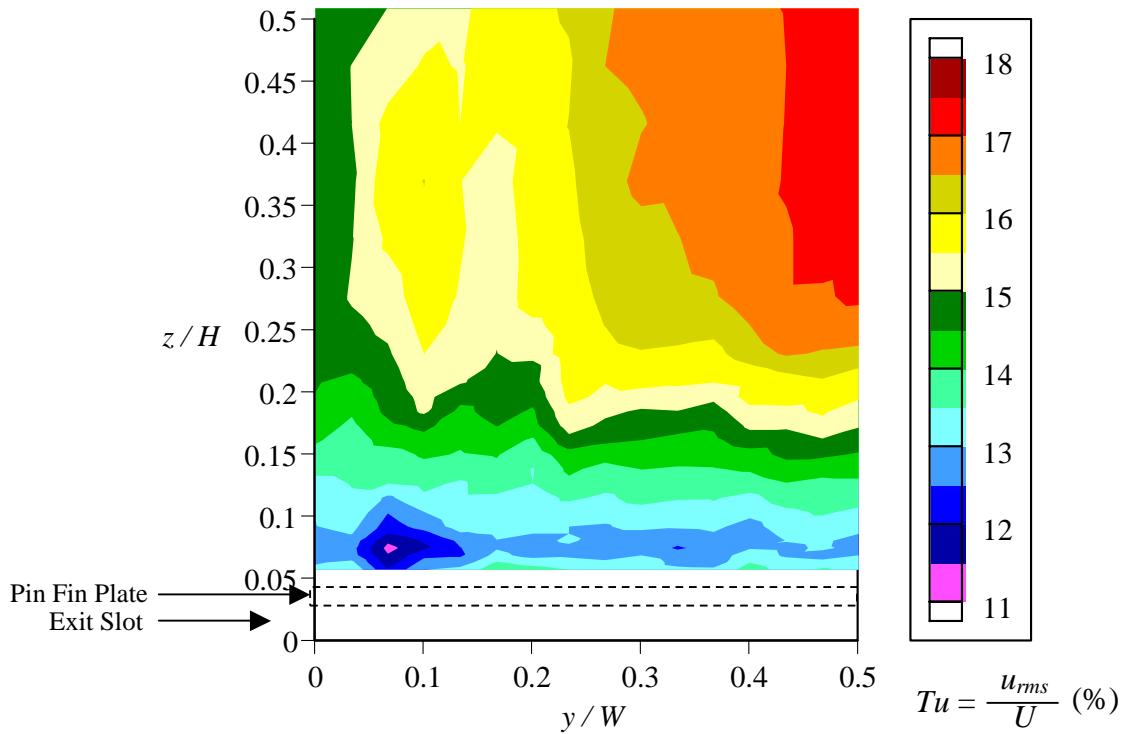


Figure 5-12 Contour plot of the turbulence intensity with dilution flow in Plane A.

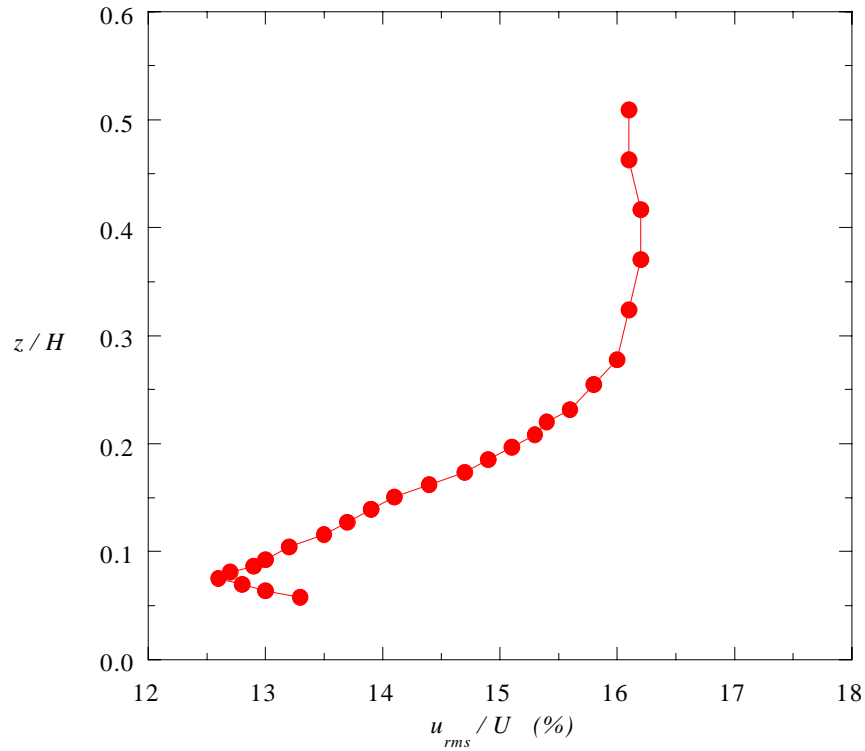


Figure 5-13 Graph showing the spatially averaged turbulence intensity profile with dilution flow in Plane A.

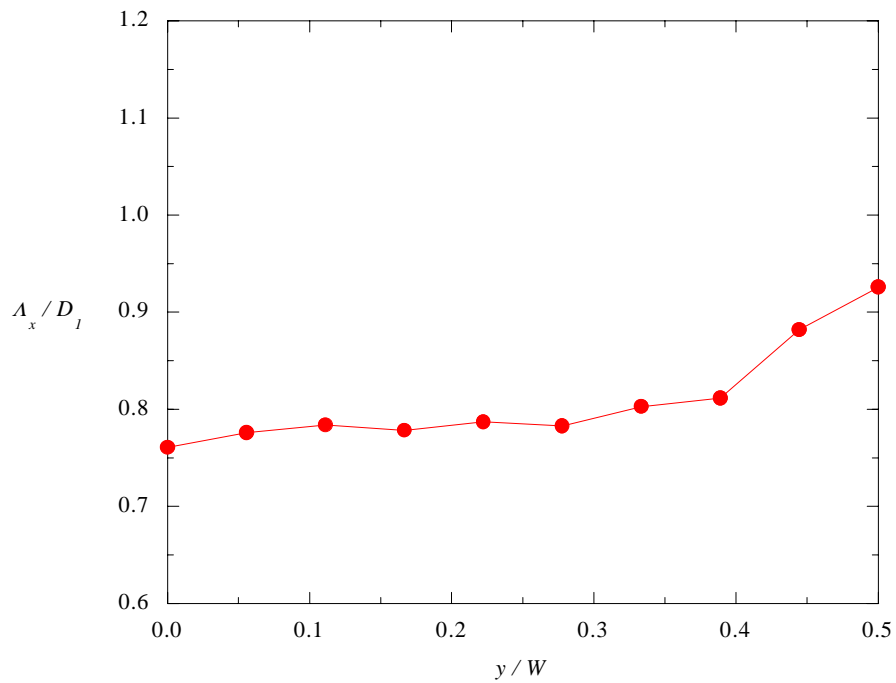


Figure 5-14 Plot of the integral length scales in Plane A ($z/H = 0.5$) with dilution flow.

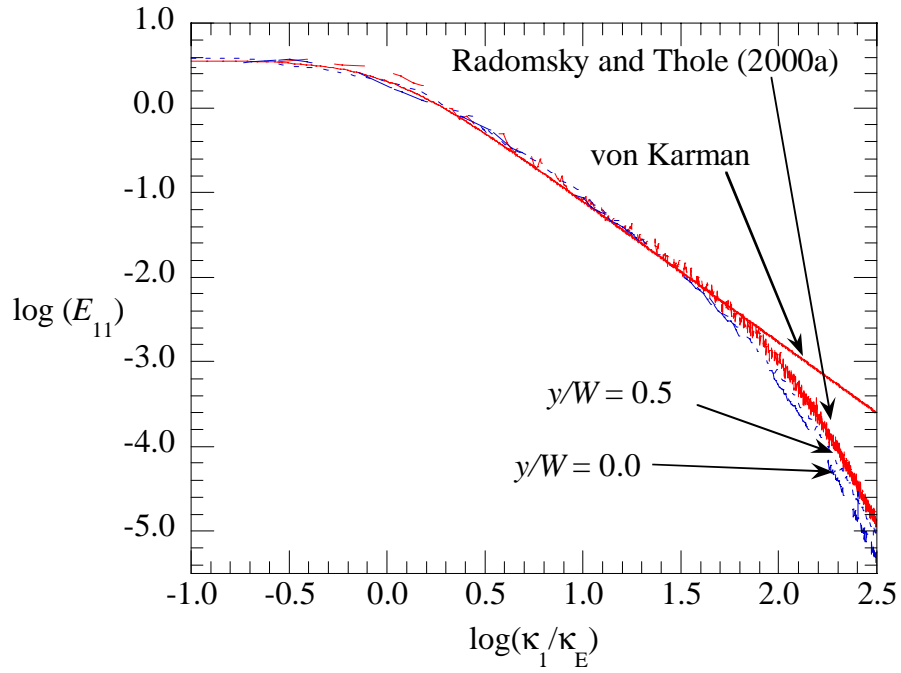


Figure 5-15 Plot of the turbulent energy spectra at $y/W = 0.0$ and 0.5 in Plane A ($z/H = 0.5$) with dilution flow.

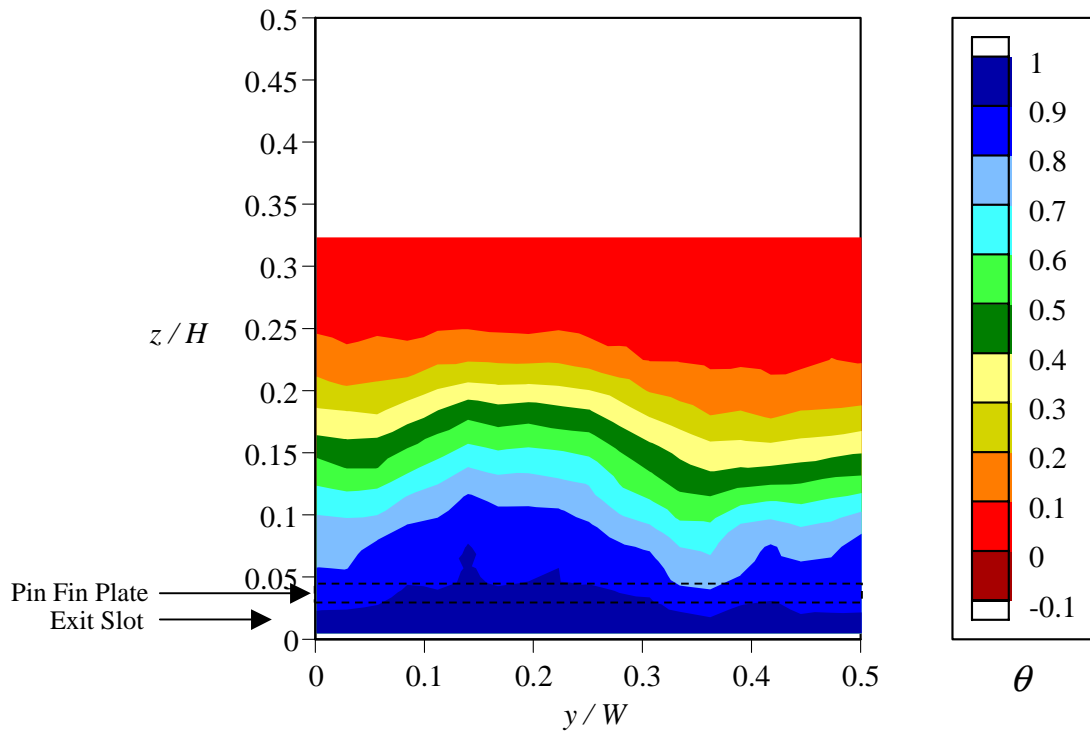


Figure 5-16 Contour plot of non-dimensional temperature without dilution flow in Plane B.

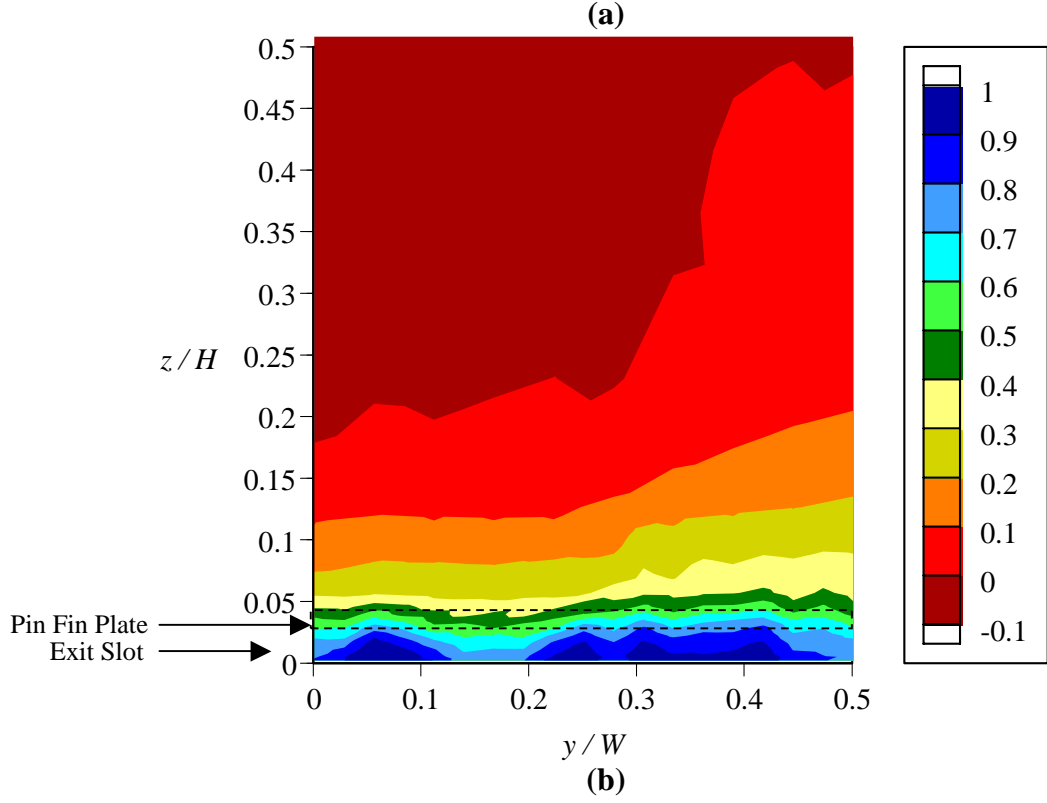
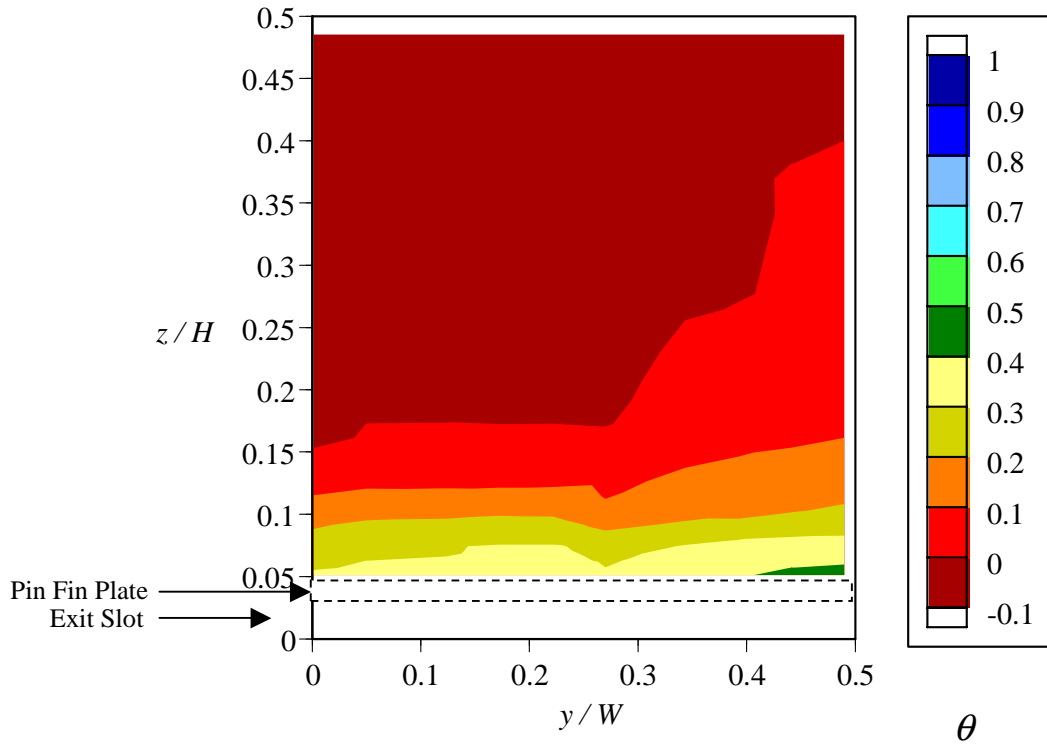


Figure 5-17 Contour plots of non-dimensional temperature with dilution flow in (a) Plane A and (b) Plane B.

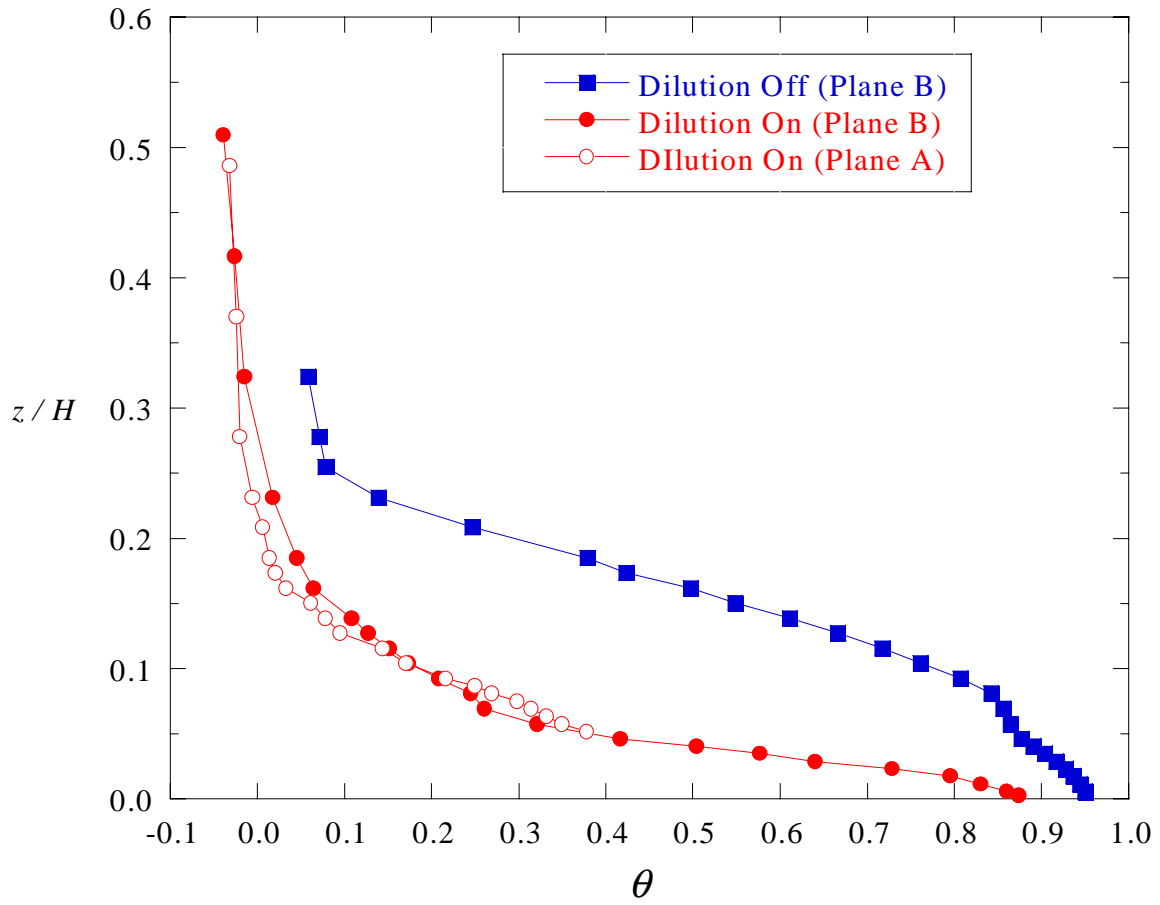


Figure 5-18 Graph showing the spatially averaged non-dimensional temperature profiles.

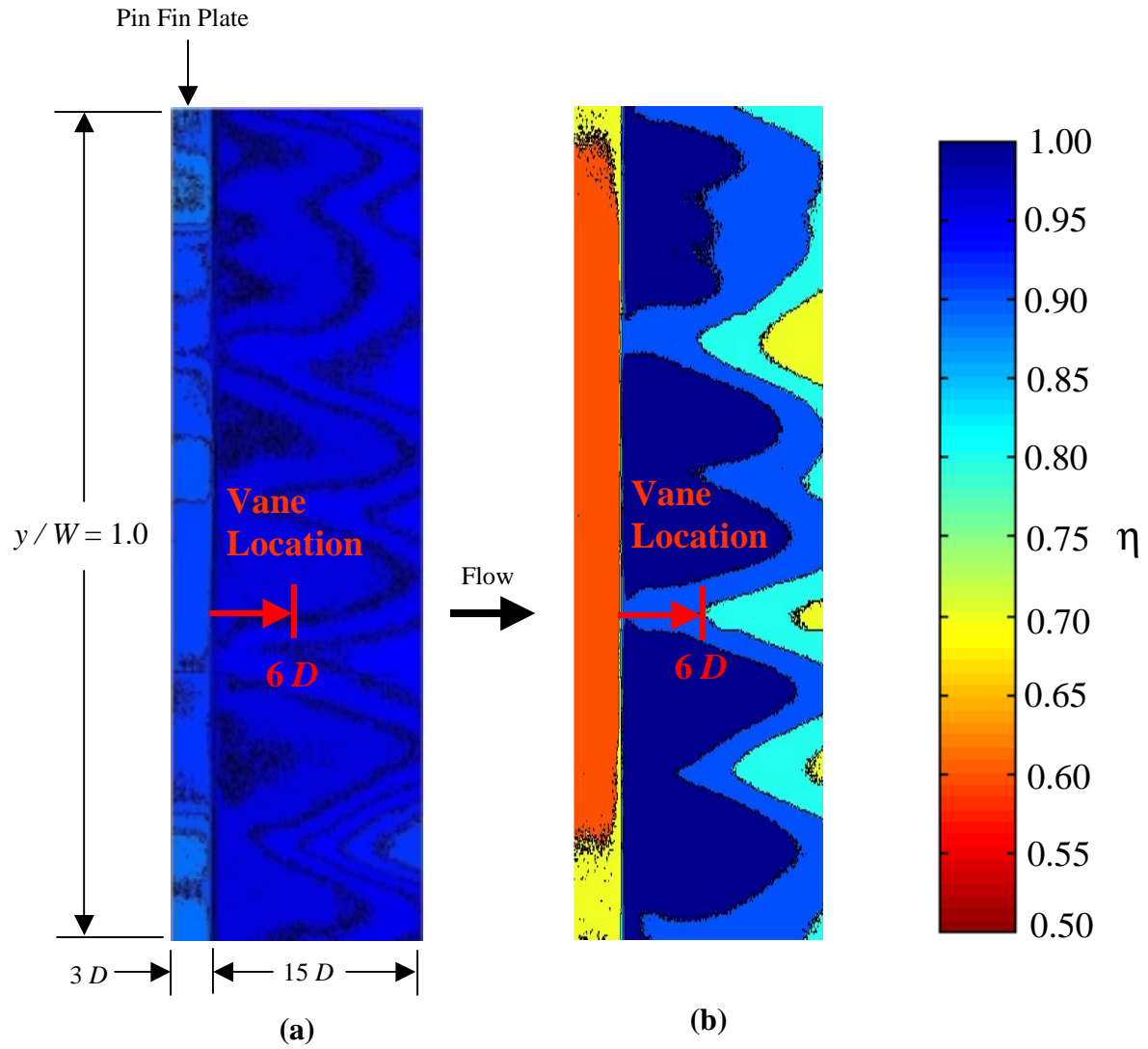


Figure 5-19 Contours of adiabatic effectiveness levels in the near exit slot region for (a) without dilution flow and (b) with dilution flow.

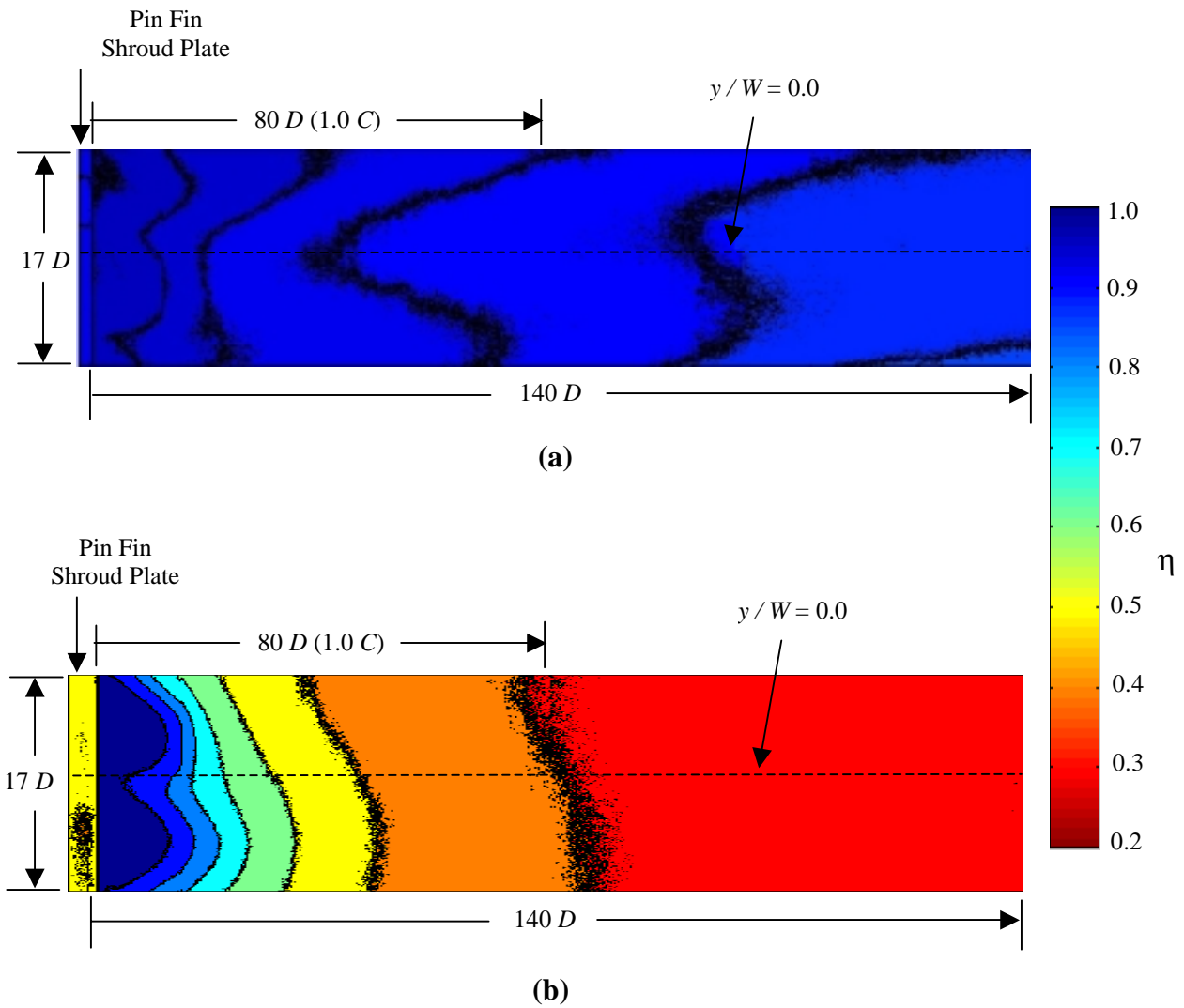


Figure 5-20 Contours of adiabatic effectiveness levels downstream of the exit slot for the cases (a) without dilution flow and (b) with dilution flow.

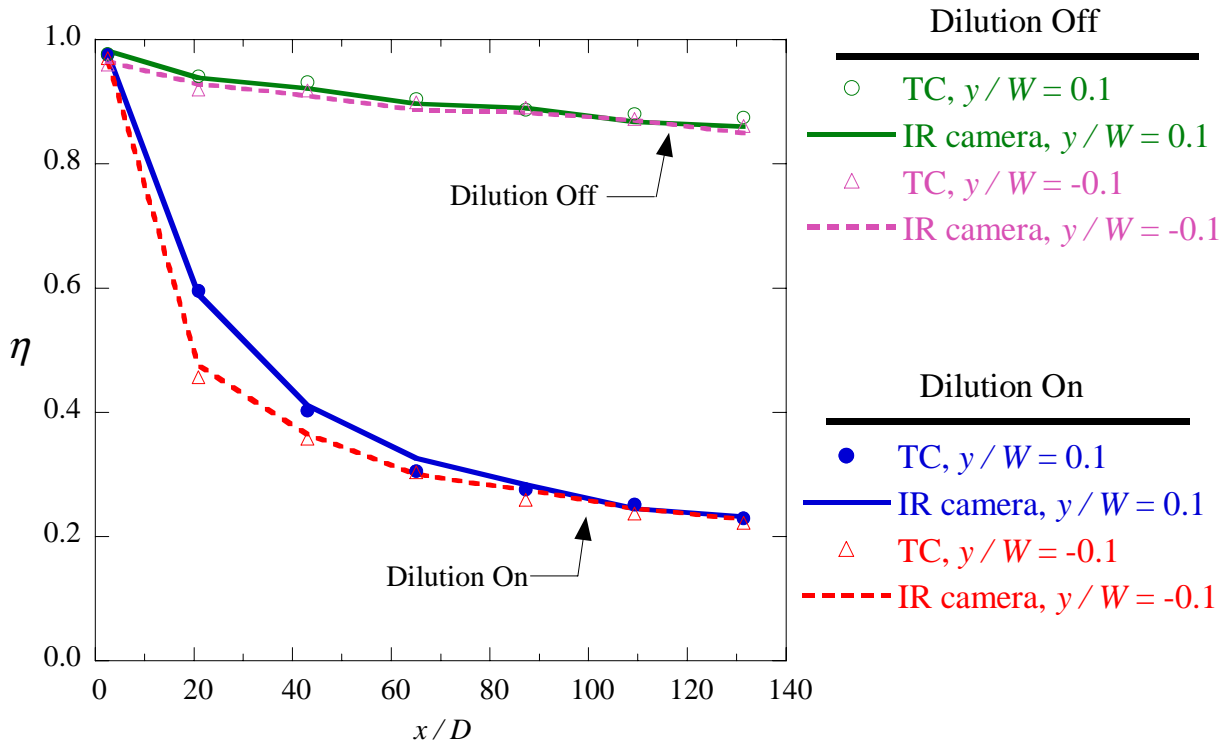


Figure 5-21 Graph showing adiabatic effectiveness levels downstream of the exit slot taken with thermocouples and the infrared camera for the cases with and without dilution flow (data taken at mid-pitch).

6. Conclusions and Future Work

A new experimental facility was designed to simulate the flow field conditions present in a commercial gas turbine engine. Upon completion of the design, modifications were made to an existing wind tunnel facility to allow for the installation of the combustor simulator. The overall performance of the facility was then benchmarked through velocity, pressure, temperature, and turbulence measurements. Conclusions with respect to benchmarking the combustor simulator are discussed in the next section. Following the benchmarking discussion, the flow and thermal field profiles that were measured at the combustor simulator exit are discussed. Finally, some recommendations for future work involving the combustor simulator facility are given.

6.1 Facility Benchmarking

To insure the proper design flow conditions throughout the entire combustor simulator, several flow quality and benchmarking studies were performed in both the primary and secondary flow paths. Since the combustor simulator described in this thesis is a new facility, benchmarking of this facility was important. It was ultimately found that the momentum flux ratios of the film-cooling holes and the dilution holes were consistent with the design conditions. A mass flow rate balance was performed at the combustor simulator exit. This mass balance resulted in a cross-sectional average velocity that was consistent with the design velocity at the combustor simulator exit, thus indicating that the proper upstream mass flow rate conditions had been met. This average exit velocity also indicated that the design exit Reynolds number had been matched. The exit slot flow conditions were found to be highly non-uniform, which was attributed to the alignment of the slot feed holes with the pin-fins. This flow arrangement, which was part of the engine design, lead to sporadic variation in slot flow coverage near the endwall.

6.2 Combustor Simulator Exit Profiles

Flow and thermal field measurements were taken at the combustor simulator exit with and without dilution flow. The flow and thermal field measurements indicated non-uniformities in velocity, turbulence, pressure, and temperature in both the pitch and span directions. The velocity profiles were found to be nearly symmetric about mid-span and mid-pitch for both flow cases. The overall effects of the dilution flow on the velocity profiles at the combustor simulator exit were to significantly reduce variation in the vertical direction and to produce small variations in the pitch direction.

There was a large variation in total pressure for both flow cases from the endwall to mid-span with the majority of the variation concentrated within the first 20 % of the total exit height. The total pressure measurements indicated that with dilution flow the total pressure field became significantly more uniform in the region above the slot flow region as compared to the case without dilution flow. The pressure measurements taken within this region indicated significantly lower total pressures within a smaller pressure range compared to the case without dilution flow. Overall, there was an 80 % reduction in the total pressure range in the vertical region from the pin fin plate to mid-span. For the case with dilution flow, a higher pressure gradient was observed to be concentrated just above the pin fin plate. These trends are consistent with the velocity profiles in which a high velocity gradient was observed near the pin fin plate and a relatively flat velocity profile existed towards the mid-span region. There was a large variation in total pressure in the pitch direction in the slot flow region from the endwall to the pin fin plate for both flow cases due to the non-uniform exit slot flow conditions. The behavior of the spatially averaged total pressure profiles for both flow cases differed significantly from the turbulent boundary layer profile. This is very important because the total pressure profile exiting the combustor dictates the development of the secondary flow field in the nozzle guide vane passages of the turbine. The commonly made assumption of a turbulent boundary layer entering the nozzle guide vane passages in modeling turbine vane flows is put into question.

The dilution flow significantly increased the turbulence intensity levels at the combustor simulator exit in both the pitch and span directions. The turbulence intensity measurements for the case with dilution flow indicated that turbulence levels were as high as 18.5 % with increasing values near the mid-span. These levels are consistent with the results from studies mentioned earlier involving reacting and non-reacting combustor flow fields. The measurements also showed that turbulence levels increased in the pitch direction for vertical locations above 20 % of the exit height with maximum levels aligned with the second row of dilution holes. Since increased turbulence levels in general lead to increased heat transfer between the hot gas and the component surface, this could be an indication that gas turbine engine designers should avoid clocking the downstream nozzle guide vanes in the turbine with the last row of dilution holes in the combustor.

The length scale of the turbulent eddies were consistent with the dilution hole sizes. These results are consistent with those presented in the literature review. The increase in the length scale in the pitch direction was attributed to the distribution of the dilution flow field in the pitch direction. The larger length scales were measured at pitch locations that were aligned with the second row of dilution holes and the smaller length scales were measured at pitch locations that were aligned with the first row of dilution holes, which were smaller in diameter. It can be seen that the characteristic length of the turbulent eddies scaled well with the diameter of the dilution holes.

The energy spectra analysis showed that no dominant frequencies occurred in the profiles and that they agreed well with the behavior of isotropic turbulence. Good agreement was obtained with the von Karman profile at low wave numbers. At higher wave numbers, however, viscous dissipation of the turbulent kinetic energy in the turbulent eddies becomes increasingly important. The von Karman model does not take into account this importance and therefore the energy spectra of the measured data deviates from the von Karman profile with increasing wave numbers.

The temperature measurements indicated that the majority of the temperature gradients that were measured for both flow cases were within the first 25 % of the total exit height. There was a large variation in temperature for both flow cases in the pitch direction for a vertical region from the endwall to the pin fin plate due to the non-uniform exit slot flow conditions. The overall effect of the turbulence generated by the dilution jets was to significantly increase the mixing of the coolant flow with the hot mainstream flow.

Contours of adiabatic effectiveness in the near exit slot region indicated that non-uniformities existed with and without the dilution flow. This variation of adiabatic effectiveness was attributed to the sporadic coverage of the cooling flow passing through the exit slot. The contours show that in the near exit slot region, even with the variation of coolant in the pitch direction, the adiabatic effectiveness levels on the endwall were high for both flow cases. The overall effect of the dilution flow was to reduce the adiabatic effectiveness levels in the near exit slot region.

The contours of adiabatic effectiveness downstream of the exit slot indicated that for the case without dilution flow the cooling potential of exit slot coolant and film-coolant was still present at an axial location equivalent to one vane chord length downstream of the exit slot where $\eta = 0.9$. For the case with dilution flow, the cooling potential of exit slot coolant and film-coolant was also still present, although significantly reduced to $\eta = 0.3$, one vane chord length downstream of the exit slot.

6.3 Recommendations for Future Work

The author believes that the benchmarking information and the measurements of the flow and thermal fields at the combustor simulator exit using the straight exit test section will be a useful data base for future experiments. These future experiments will consist of placing a linear turbine vane cascade just downstream of the combustor simulator. Direct comparisons of the flow and thermal fields can be made between the two test geometries to help further understand how to best integrate the combustor with the turbine.

To reduce the uncertainties associated with the thermal field measurements the author believes that the driving temperature between the primary and secondary flow paths should be increased. This could be accomplished by installing additional heater elements to further raise the primary flow path's temperature. This could also be accomplished by directing chilled water through the heat exchangers in the secondary flow path to further reduce the secondary flow path's temperature.

References

- Agrawal, A., Kapat, J., and Yang, T. (1998) "An Experimental/Computational Study of Airflow in the Combustor-Diffuser System of a Gas Turbine for Power Generation," *Journal of Engineering for Gas Turbines and Power*, Vol. 120, pp. 24-33.
- Ahmed, S.A. (1998) "Velocity Measurements and Turbulence Statistics of a Confined Isothermal Swirling Flow," *Experimental Thermal and Fluid Science*, Vol. 17, pp. 256-264.
- Ames, F.E. and Moffat, R.J. (1990) "Effects of Simulated Combustor Turbulence on Boundary Layer Heat Transfer," Heat Transfer in Turbulent Flow 1990: AIAA/ASME Thermophysics and Heat Transfer Conference, Seattle, Washington, June 18-20, 1990.
- Anacleto, P., Heitor, M., and Moreira, A. (1996) "The Mean and Turbulent Flowfields in a Model RQL Gas-Turbine Combustor," *Experiments in Fluids*, Vol.22, pp. 153-164.
- Anand, M., Zhu, J., Connor, C., and Razdan, M. (1999) "Combustor Flow Analysis Using an Advanced Finite-Volume Design System," ASME Paper No. 99-GT-273.
- Bain, D., Smith, C., Liscinsky, D., and Holdeman, J. (1999) "Flow Coupling Effects in Jet-in-Crossflow Flowfields," *Journal of Propulsion and Power*, Vol. 15, No. 1, pp.10-16.
- Barringer, M., Richard, O., Stitzel, S., Walter, J., and Thole, K. (2001) "Flow Field Simulations of a Gas Turbine Combustor," ASME Paper No. 2001-GT-170 (accepted to the *Journal of Turbomachinery*).
- Beckwith, T., Marangoni, R., and Lienhard, J., 1993, Mechanical Measurements Fifth Edition. New York: Addison-Wesley Publishing Company, Inc.
- Bicen, A., Tse, D., and Whitelaw, J. (1988) "Flow and Combustion Characteristics of an Annular Combustor," *Combustion and Flame*, Vol. 72, pp. 175-192.

- Blomeyer, M., Krautkremer, B., Hennecke, D., and Doerr, T. (1999) "Mixing Zone Optimization of a Rich-Burn/Quick-Mix/Lean-Burn Combustor," *Journal of Propulsion and Power*, Vol. 15, No. 2, pp. 288-295.
- Burd, S.W. and Simon, T.W. (1999) "Measurements of Discharge Coefficients in Film Cooling," *Journal of Turbomachinery*, Vol. 121, pp. 243-248.
- Burd, S.W., and Simon, T.W. (2000) "Effects of Slot Bleed Injection Over a Contoured End Wall on Nozzle Guide Vane Cooling Performance: Part I – Flow Field Measurements," ASME Paper No. 2000-GT-199.
- Burd, S.W., Satterness, C.J., and Simon, T.W. (2000) "Effects of Slot Bleed Injection Over a Contoured End Wall on Nozzle Guide Vane Cooling Performance: Part II – Thermal Measurements," ASME Paper No. 2000-GT-200.
- Busnaina, A.A. (1987) "Lateral Jet Injection into Isothermal Combustor Flowfields," *Chemical Engineering Communications*, 54 (1-6): 265-278.
- Cameron, C., Brouwer, J., Wood, C., and Samuelson, G. (1989) "A Detailed Characterization of the Velocity and Thermal Fields in a Model Can Combustor with Wall Jet Injection," *Journal of Engineering for Gas Turbines and Power*, Vol. 111, pp. 31-35.
- Carrotte, J. and Stevens, S. (1990) "The Influence of Dilution Hole Geometry on Jet Mixing," *Journal of Engineering for Gas Turbines and Power*, Vol. 112, pp. 73-79.
- Cline, M., Micklow, G., Yang, S., and Nguyen, H. (1995) "Numerical Analysis of the Flowfields in a Staged Gas Turbine Combustor," *Journal of Propulsion and Power*, Vol. 11, No. 5, pp. 894-898.

- Cohen, H., Rogers, G., and Saravanamuttoo, H., 1996, Gas Turbine Theory Fourth Edition. England: Addison Wesley Longman Limited.
- Chung, J. and Simon, T. (1993) "Effectiveness of the Gas Turbine Endwall Fences in Secondary Flow Control at Elevated Freestream Turbulence Levels," ASME Paper No. 93-GT-51.
- Crocker, D., Smith, C., and Myers, G. (1994) "Pattern Factor Reduction in a Reverse Flow Gas Turbine Combustor Using Angled Dilution Jets," ASME Paper No. 94-GT-406.
- Doerr, T., Blomeyer, M., and Hennecke, D. (1997) "Optimization of Multiple Jets Mixing With a Confined Crossflow," *Journal of Engineering for Gas Turbines and Power*, Vol. 119, pp. 315-321.
- Ebbinghaus, A. and Swithenbank, J. (1995) "Mixing of Multiple Jets in a Can Combustor," ASME Paper No. 95-GT-257.
- Goebel, S., Abuaf, N., Lovett, J. and Lee, C. (1993) "Measurements of Combustor Velocity and Turbulence Profiles," ASME Paper No. 93-GT-228.
- Gritsch, M., Martiny, M., Schulz, A., Kim, S., and Wittig, S. (1998) "Gas Turbine Heat Transfer: Newest Developments in Components Performance," Heat Transfer 1998: Proceedings of the 11th International Heat Transfer Conference (IHTC), Kyongju, Korea, August 23-28, 1998.
- Gulati, A., Tolpadi, A., VanDeusen, G., and Burrus, D. (1995) "Effect of Dilution Air on the Scalar Flowfield at Combustor Sector Exit," *Journal of Propulsion and Power*, Vol. 11, No. 6, pp. 1162-1169.
- Halls, B.A. (1970) "Nozzle Guide Vane Cooling," AGARD, CP No. 73, Paper 25.

- He, G., Guo, Y., Hsu, A., Brankovic, A., Syed, S., and Liu, N. (1999) "The Effect of Schmidt Number on Turbulent Scalar Mixing in a Jet-In-Crossflow," ASME Paper No. 99-GT-0137.
- Hermanson, K. and Thole, K. (2000) "Effect of Inlet Conditions on Endwall Secondary Flows," AIAA Paper 99-0241.
- Hill, P., and Peterson, C., 1992, Mechanics and Thermodynamics of Propulsion Second Edition. New York: Addison-Wesley Publishing Company, Inc.
- Holdeman, J.D. (1993) "Mixing of Multiple Jets with a Confined Subsonic Crossflow," *Prog. Energy Combust. Sci.*, Vol. 19, pp. 31-70.
- Jones, J. and Dugan, R., 1996, Engineering Thermodynamics. New Jersey: Prentice Hall, Inc.
- Koutmos, P., and McGuirk, J. (1989) "Isothermal Flow in a Gas Turbine Combustor – A Benchmark Experimental Study," *Experiments in Fluids*, Vol. 7, pp 344-354.
- Krishnamoorthy, V., Pai, B., and Sukhatme, S. (1988) "Influence of Upstream Flow Conditions on the Heat Transfer to Nozzle Guide Vanes," *Journal of Turbomachinery*, Vol. 110, pp. 412-416.
- Lawson, R.J. (1993) "Computational Modeling of an Aircraft Engine Combustor to Achieve Target Exit Temperature Profiles," ASME Paper No. 93-GT-164.
- Lefebvre, A.H., 1998, Gas Turbine Combustors. New York, Taylor and Francis.
- Liou, T.M., and Wu, Y.Y. (1992), "LDV Measurements of the Flowfield in a Simulated Combustor with Axial and Side Inlets," *Experimental Thermal and Fluid Science*, Vol. 5, pp. 401-409.

- Malecki, R., Rhie, C., McKinney, R., Ouyang, H., Syed, S., Colket, M., and Madabhushi, R. (2001) "Application of an Advanced CFD-Based Analysis System to the PW6000 Combustor to Optimize Exit Temperature Distribution – Part I: Description and Validation of the Analysis Tool," ASME Paper No. 2001-GT-0062.
- Mattingly, J. D., 1996, Elements of Gas Turbine Propulsion. New York: McGraw-Hill, Inc.
- McGuirk, J. and Palma, J. (1993) "The Flow Inside a Model Gas Turbine Combustor: Calculations," *Journal of Engineering for Gas Turbines and Power*, Vol. 115, pp. 594-602.
- Moffat, J. R. (1988) "Describing the Uncertainties in Experimental Results," *Experimental Thermal and Fluid Science*, Vol. 1, pp.3-17.
- Moss, R.W. (1992) "The Effects of Turbulence Length Scale on Heat Transfer," Ph.D. Dissertation, Department of Engineering Science, University of Oxford, Report No. OUEL 1924/92.
- Radomsky, R. (2000) "High Freestream Turbulence Studies on a Scaled-Up Stator Vane," Ph.D. Dissertation, Mechanical Engineering Department, University of Wisconsin-Madison.
- Radomsky, R. and Thole, K. (2000a) "Highly Turbulent Flowfield Measurements in the Endwall Leading Edge Region," *Journal of Turbomachinery*, Vol. 122, pp.255-262.
- Richards, C. and Samuelson, G. (1992) "The Role of Primary Jets in the Dome Region Aerodynamics of a Model Can Combustor," *Journal of Engineering for Gas Turbines and Power*, Vol. 114, pp. 20-26.
- Rolls-Royce, 1992, The Jet Engine. Derby, England: The Technical Publications Department, Rolls-Royce plc.

- Rydholm, H.A. (1998) "An Experimental Investigation of the Velocity and Temperature Fields of Cold Jets Injected into a Hot Crossflow," *Journal of Turbomachinery*, Vol. 120, pp. 320-326.
- Sauer, J. (1996) "The SUDI Turbulence Generator – A Method to Generate High Freestream Turbulence Levels and a Range of Length Scales," German Diplom Thesis, University of Wisconsin-Madison.
- Schwab, J., Stabe, R. and Whitney, W. (1983) "Analytical and Experimental Study of Flow Through an Axial Turbine Stage With a Nonuniform Inlet Radial Temperature Profile," AIAA Paper 83-1175.
- Shyy, W., Braaten, M., and Burrus, D. (1989) "Study of Three-Dimensional Gas-Turbine Combustor Flows," *International Journal of Heat and Mass Transfer*, Vol. 32, No. 6, pp. 1155-1164.
- Snyder, T., Stewart, J., Stoner, M., and McKinney, R. (2001) "Application of an Advanced CFD-Based Analysis System to the PW6000 Combustor to Optimize Exit Temperature Distribution – Part II: Comparison of Predictions to Full Annular Rig Test Data," ASME Paper No. 2001-GT-0064.
- Soechting, F. and Cheung, A. (1999), Private communication at Pratt & Whitney.
- Stabe, R., Whitney, W., and Moffit, T. (1984) "Performance of High-Work Low-Aspect Ratio Turbine Tested with a Realistic Inlet Radial Temperature Profile," AIAA Paper 84-1161.
- Stevens, S.J., and Carrotte, J.F. (1990) "Experimental Studies of Combustor Dilution Zone Aerodynamics, Part I: Mean Flowfields," *Journal of Propulsion*, Vol.6, No.3, pp. 297-304.

- Stevens, S.J., and Carrotte, J.F. (1990) "Experimental Studies of Combustor Dilution Zone Aerodynamics, Part II: Jet Development," *Journal of Propulsion*, Vol.6, No.4, pp. 504-511.
- Stitzel, S., (2001) "Flow Field Computations of Combustor-Turbine Interaction in a Gas Turbine Engine," thesis, Mechanical Engineering Department, Virginia Polytechnic Institute and State University.
- Sturgess, G.J. (1980) "Account of Film Turbulence for Predicting Film Cooling Effectiveness in Gas Turbine Combustors," *Journal of Engineering for Power*, Vol.102, pp.524-534.
- Walsh, P., and Fletcher, P., 1998, Gas Turbine Performance. New Jersey, Blackwell Science LTD.
- Wittig, S., Elbahar, O., and Noll, B. (1984) "Temperature Profile Development in Turbulent Mixing of Coolant Jets with a Confined Hot Crossflow," *Journal of Engineering for Gas Turbines and Power*, Vol. 106, pp. 193-197.
- Wittig, S., Bauer, H., and Noll, B. (1987) "On the Application of Finite-Difference Techniques for the Computation of the Flow Field in Gas Turbine Combustors with Complex Geometries," PEP 70th Symposium on Combustion and Fuels in Gas Turbine Engines, Chania, Greece, October 19-23, 1987.
- Yang, S. and Cline, M. (1994) "Efficient Mapping Topology for Turbine Combustors with Inclined Slots/Staggered Holes," *Journal of Propulsion*, Vol. 11, No. 3, pp. 572-574.
- Zess, G. and Thole, K. (2001) "Computational Design and Experimental Evaluation of a Leading Edge Fillet on a Gas Turbine Vane", ASME Paper No. 2001-GT-404.

Appendix A

Combustor Models

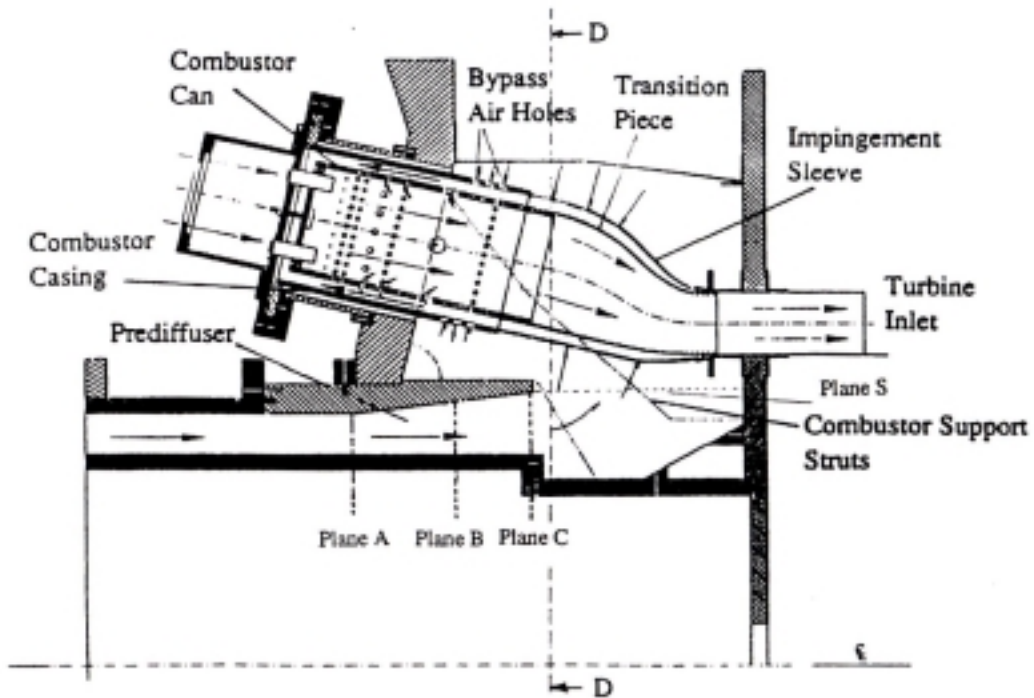


Figure A-1 Schematic of Agrawal et al. (1998) combustor model.

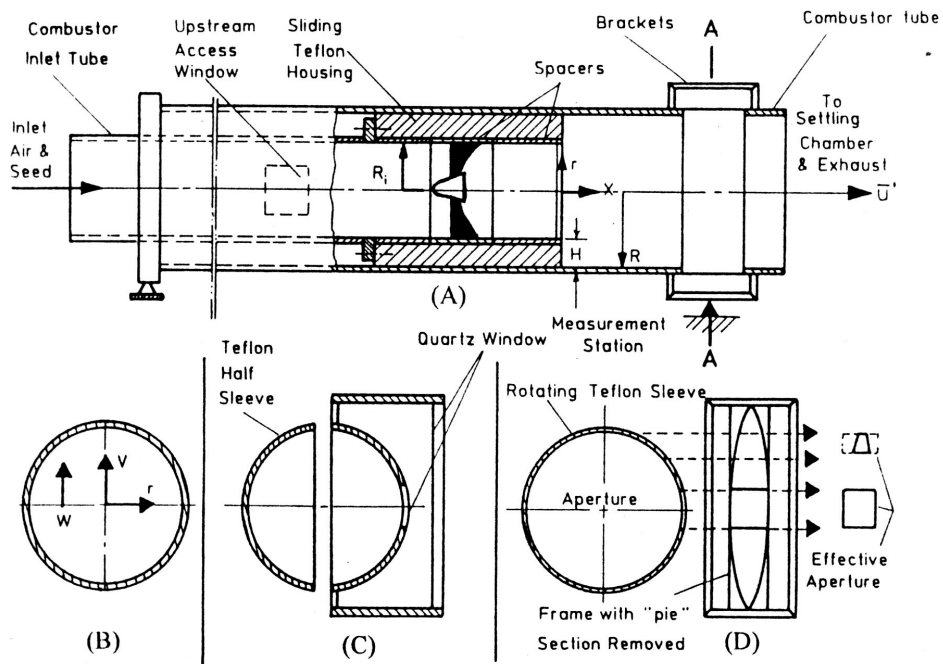


Figure A-2 Schematic of Ahmed (1998) combustor model.

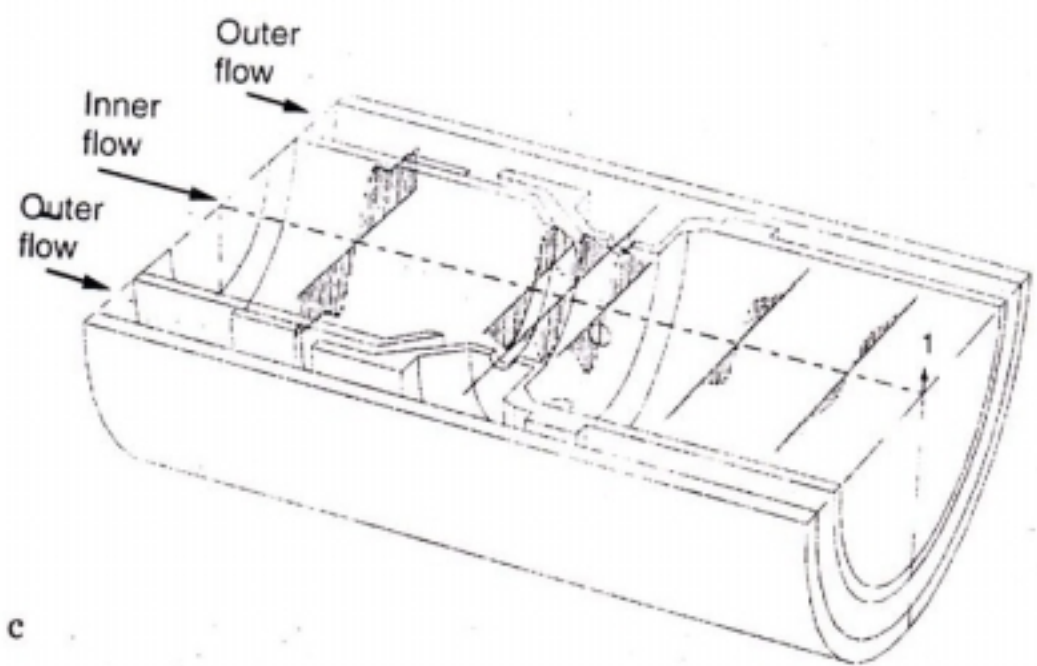
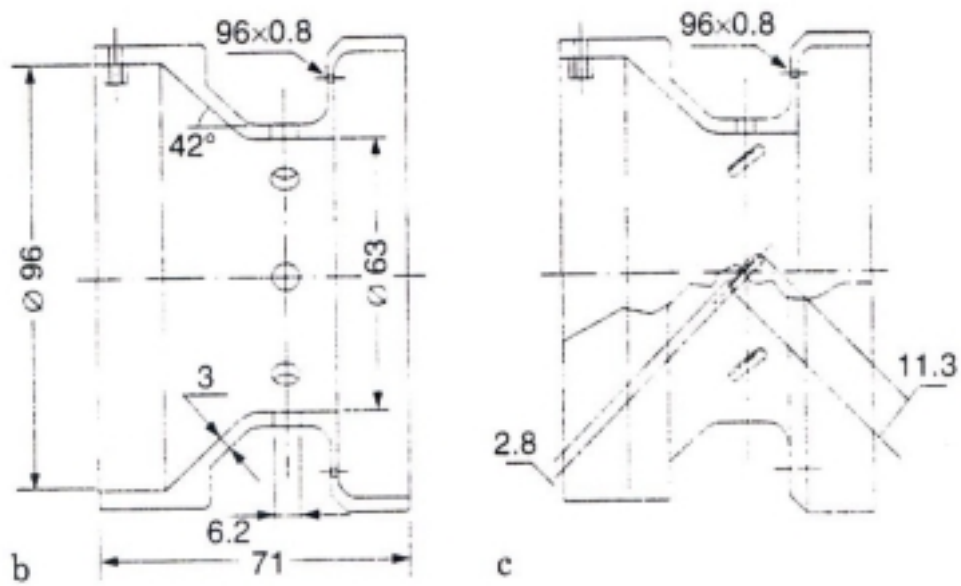


Figure A-3a Schematic of Anacleto et al. (1996) combustor model.

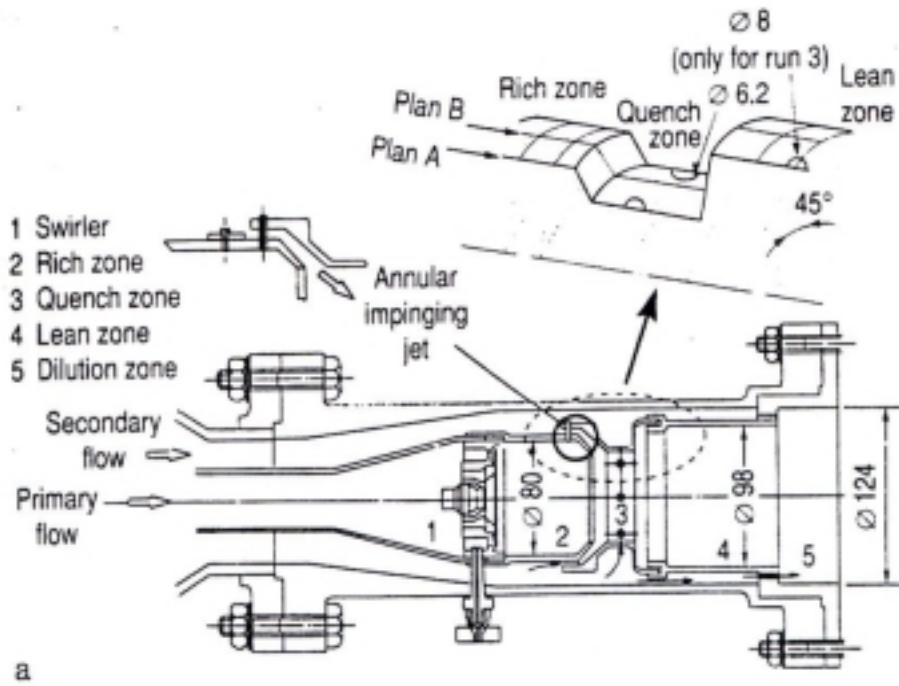


Figure A-3b Schematic of Anacleto et al. (1996) combustor model.

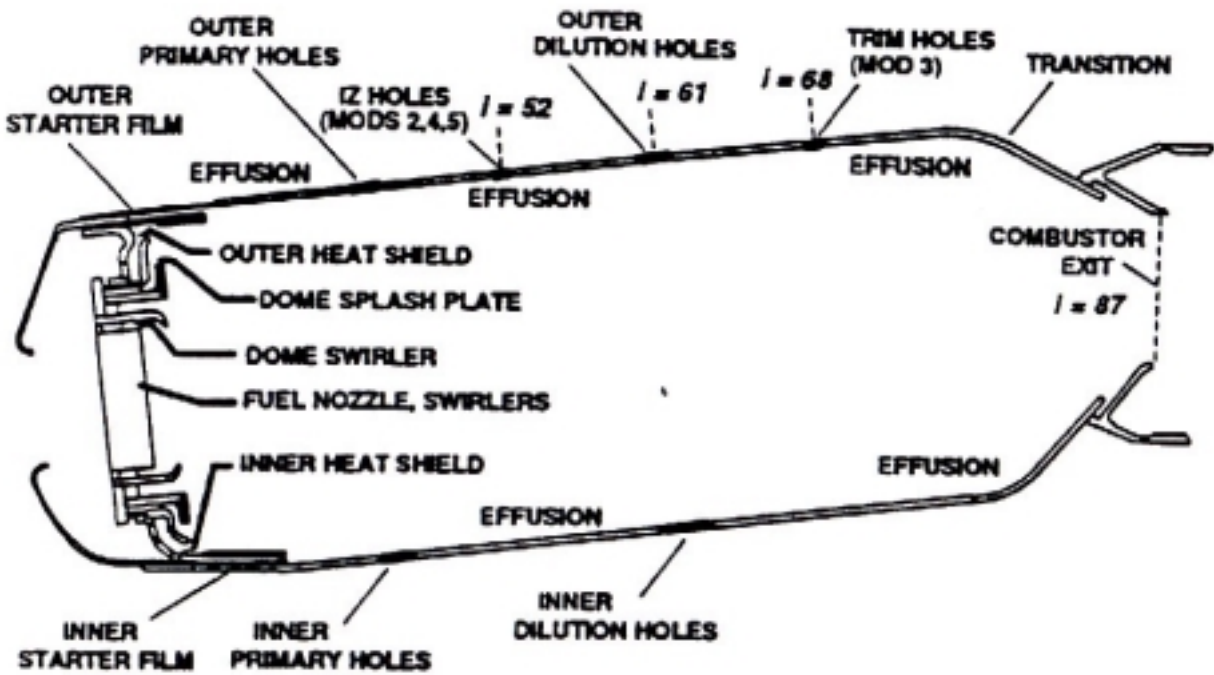


Figure A-4 Schematic of Anand et al. (1999) combustor model.

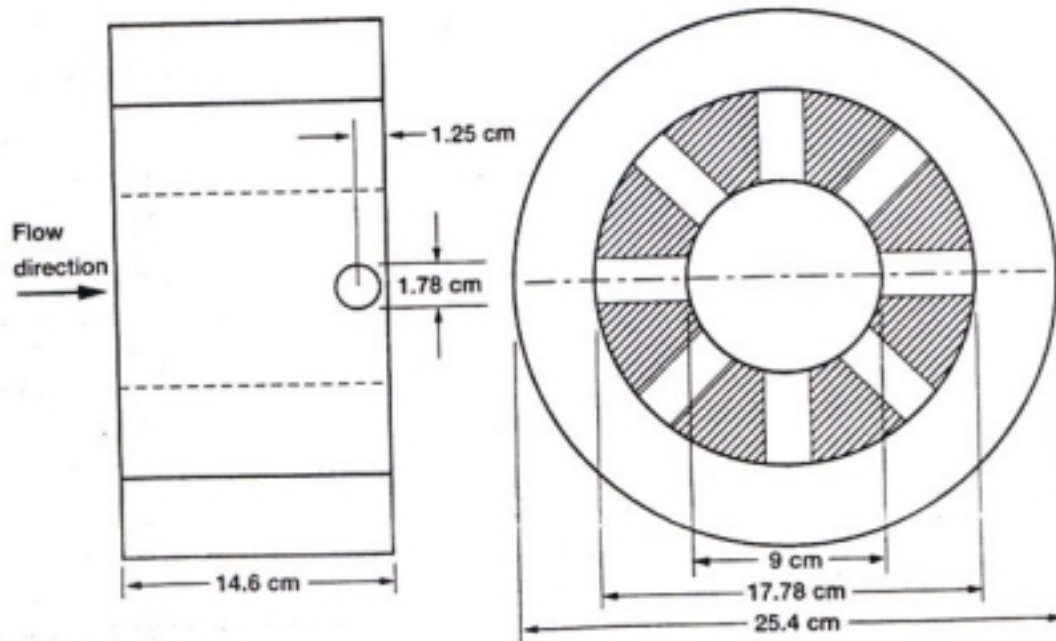
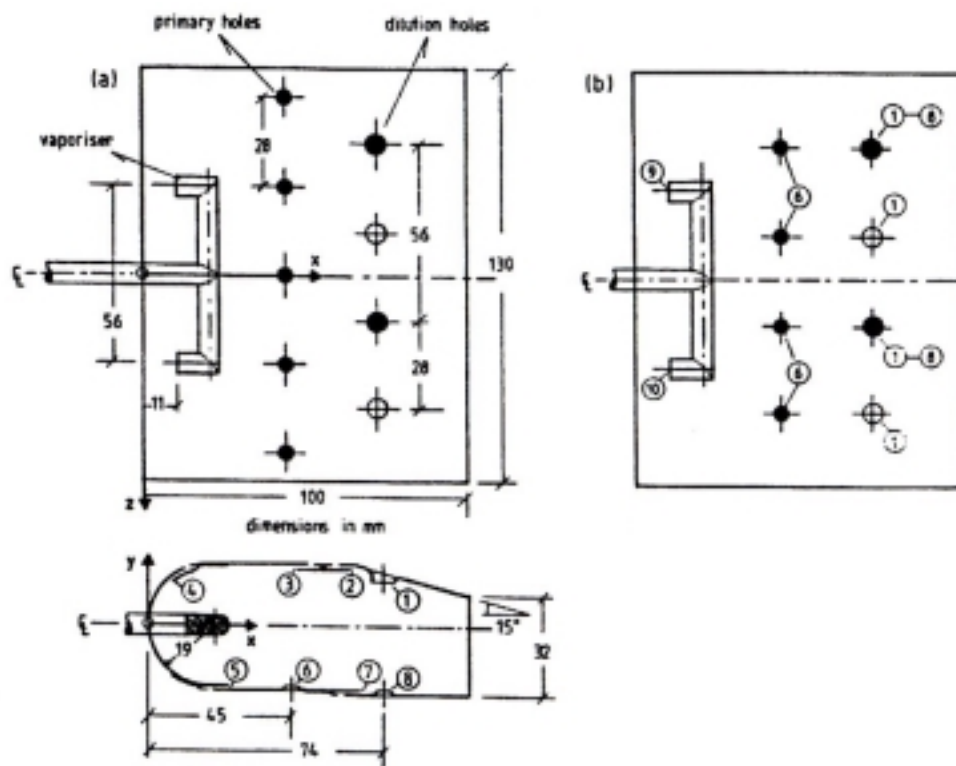


Figure A-5 Schematic of Bain et al. (1999) combustor model.



Combustor geometries: (a) Combustor 1; (b) Combustor 2.

Figure A-6 Schematic of Bicen et al. (1988) combustor model.

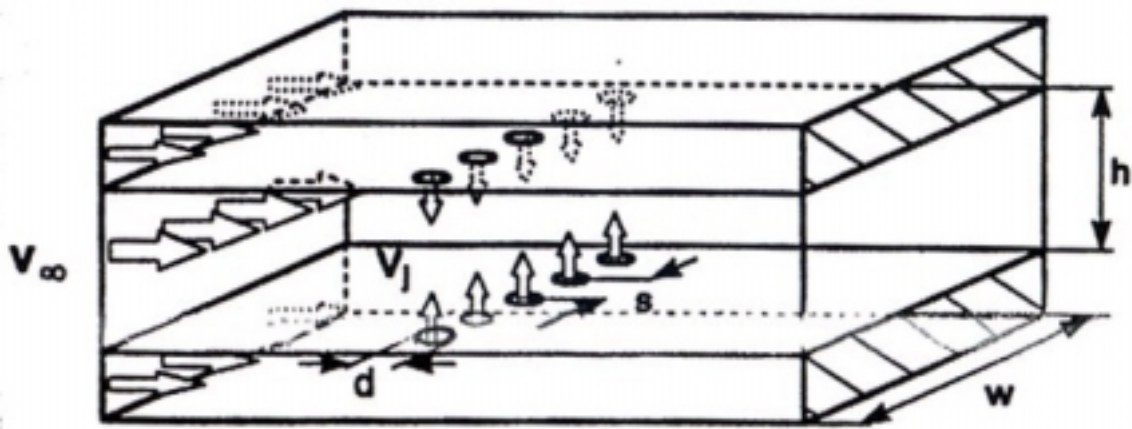


Figure A-7 Blomeyer schematic of multiple jet mixing

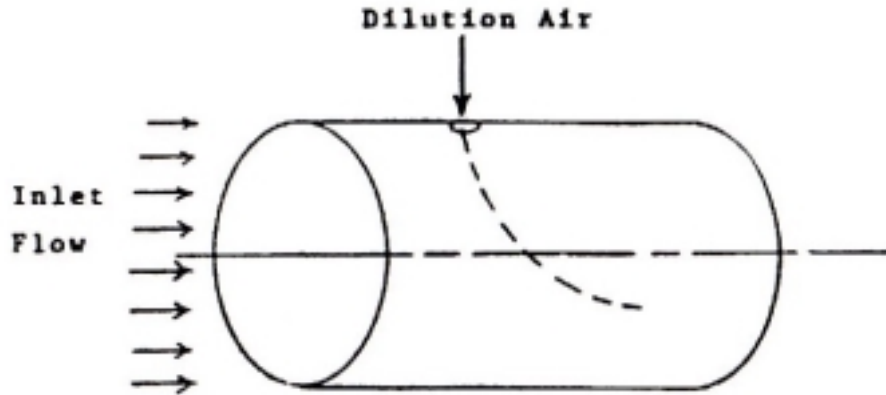
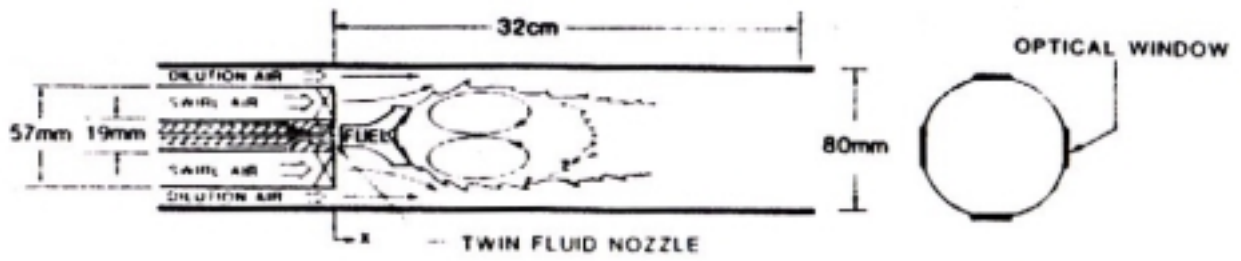
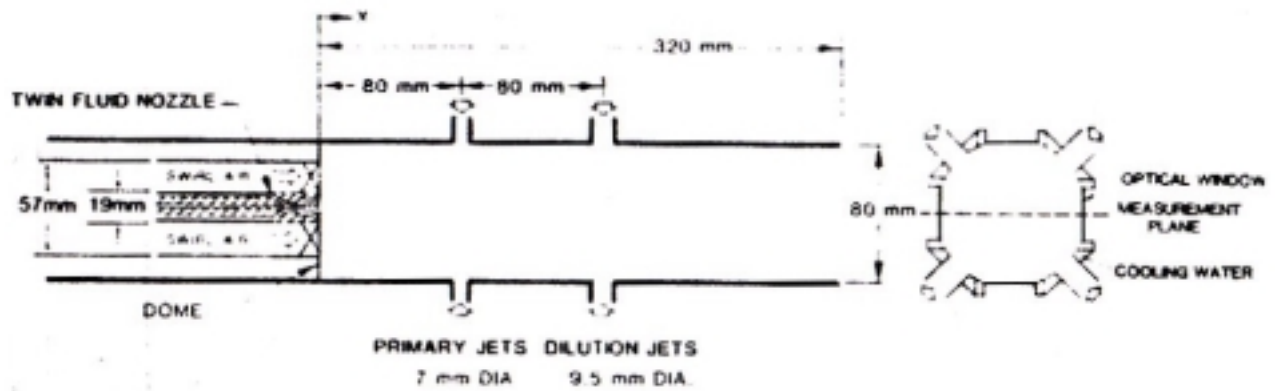


Figure A-8 Schematic of Busnania (1987) combustor model.



1(a) The axisymmetric can combustor (ASCC)



1(b) The wall jet can combustor (WJCC)

Figure A-9 Schematic of Cameron et al. (1989) combustor model.

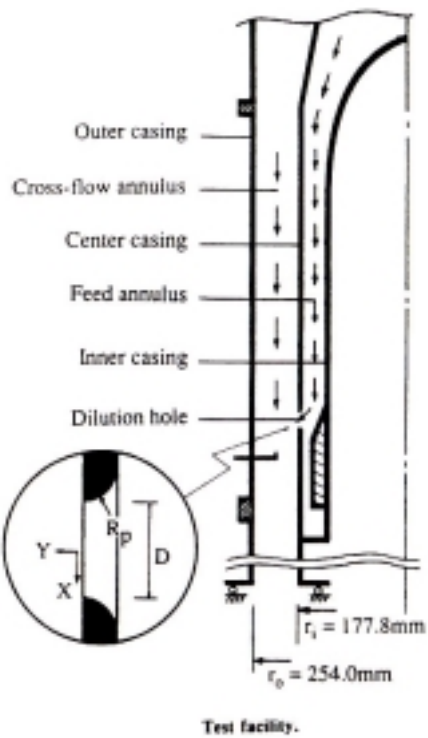


Figure A-10 Schematic of Carrotte and Stevens (1990) combustor model.

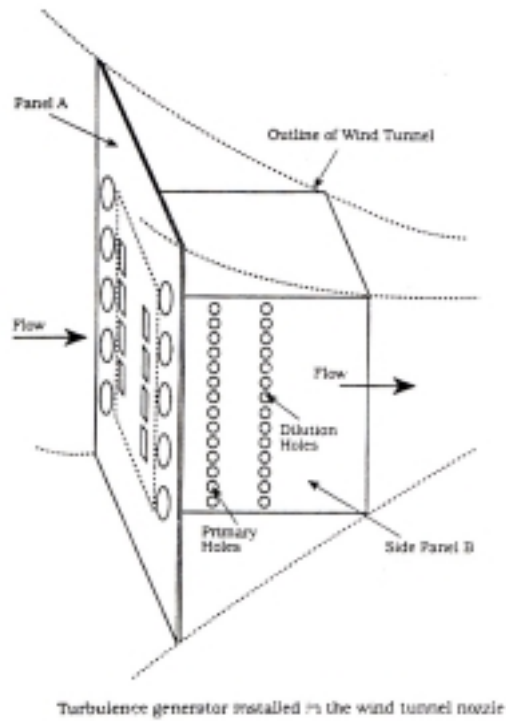


Figure A-11 Schematic of Chung and Simon (1993) combustor model.

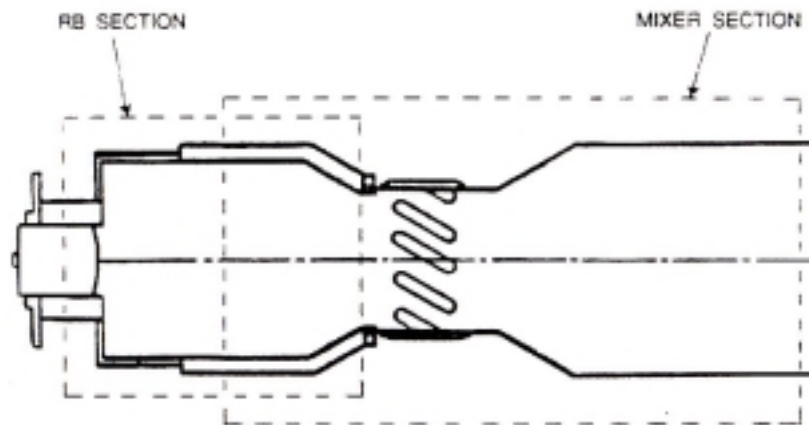


Figure A-12 Schematic of Cline et al. (1995) combustor model.

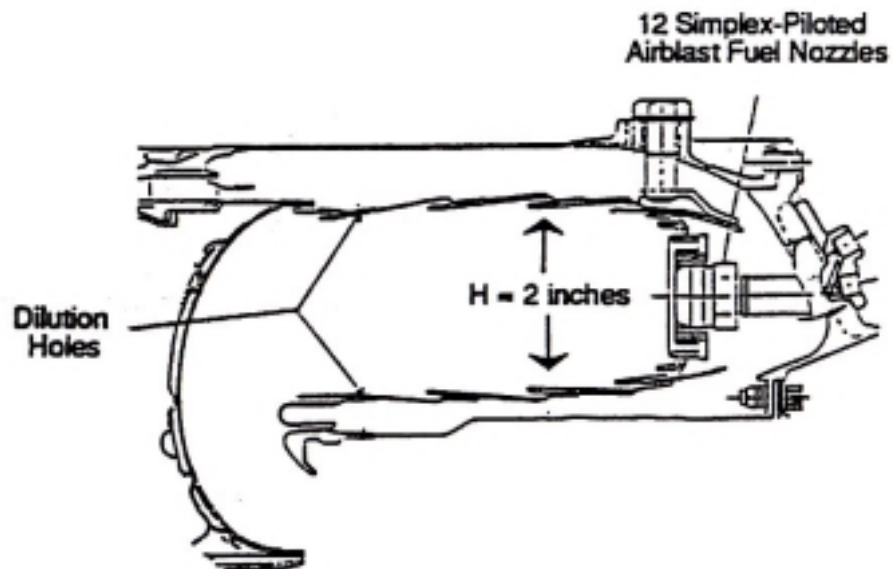


Figure A-13 Schematic of Crocker et al. (1994) combustor.

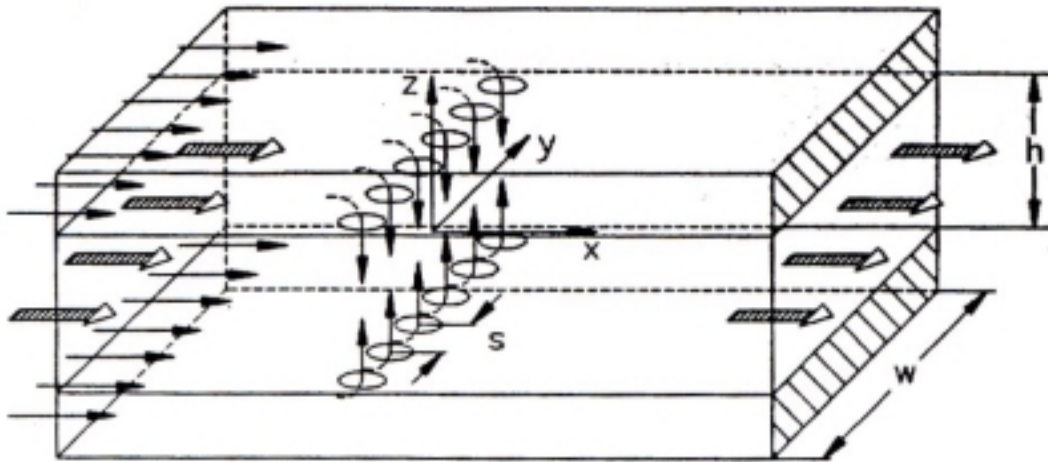


Figure A-14 Schematic of Doerr et al. (1997) combustor model.

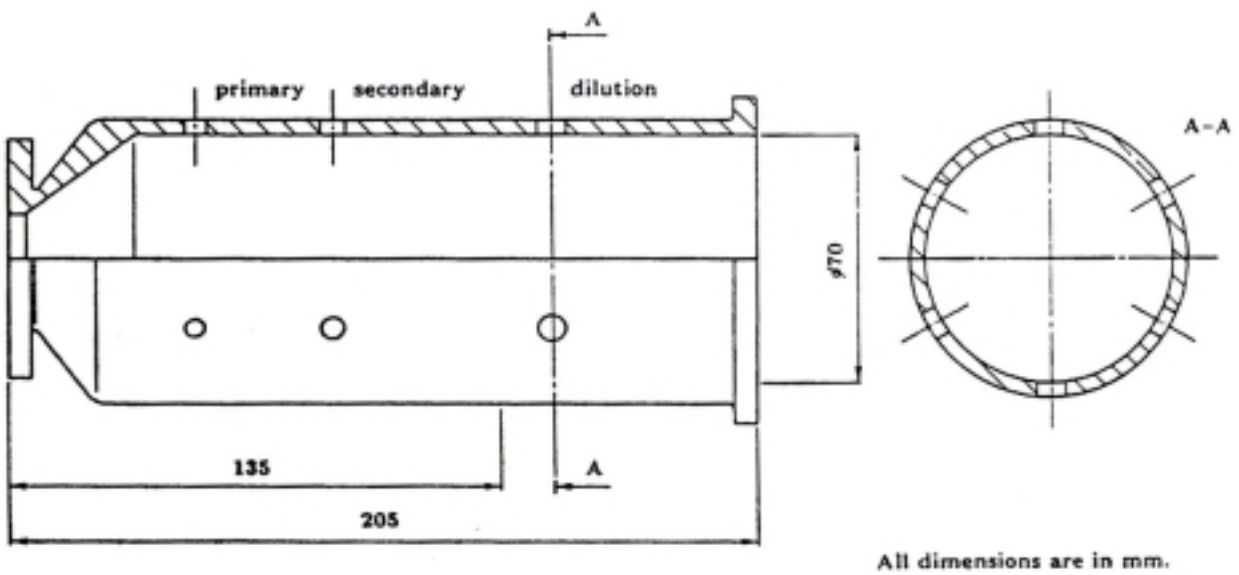


Figure A-15 Schematic of Ebbinghaus and Swithenbank (1995) combustor model.

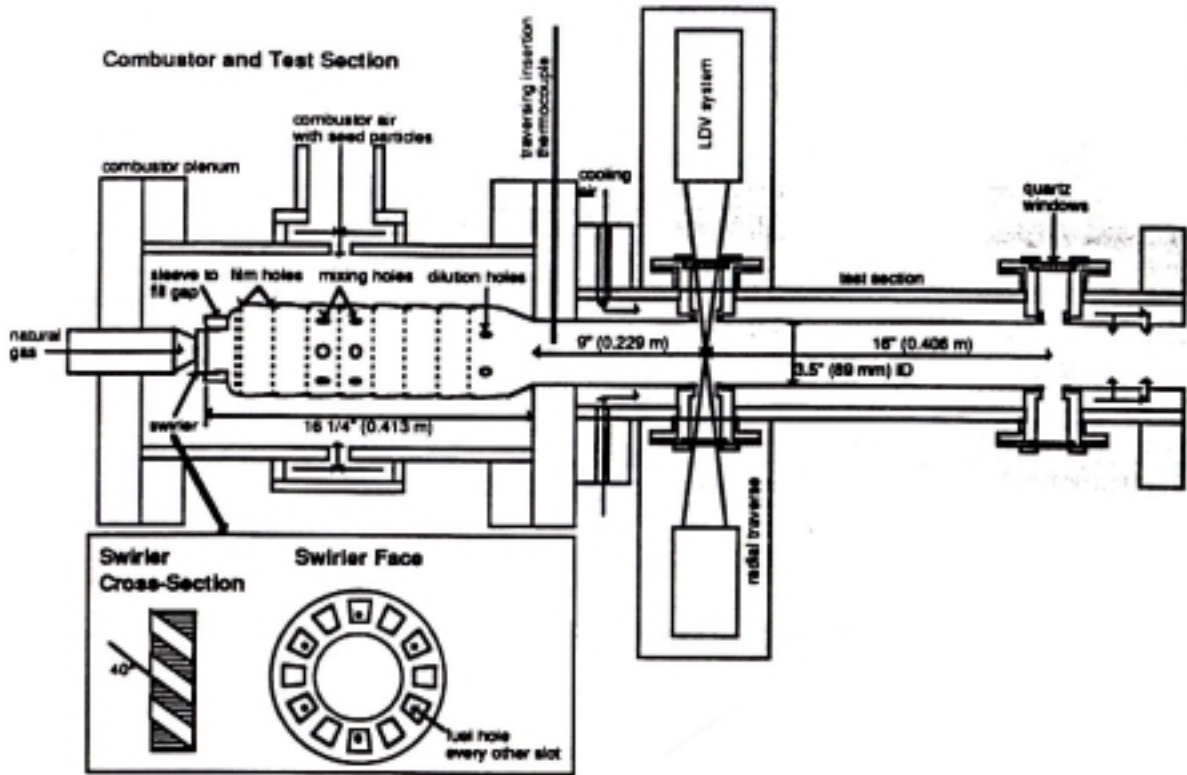


Figure A-16 Schematic of Geobel et al. (1993) combustor model.

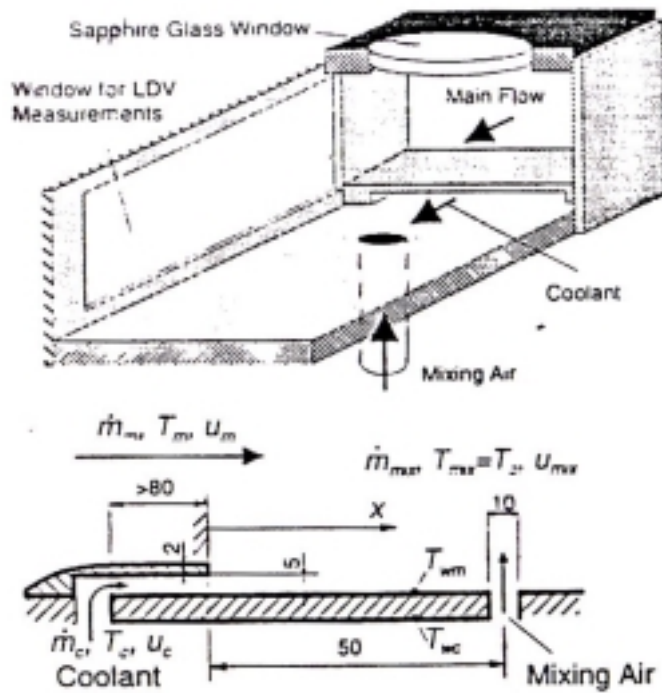


Figure A-17a Schematic of Gritsch et al. (1998) combustor model.

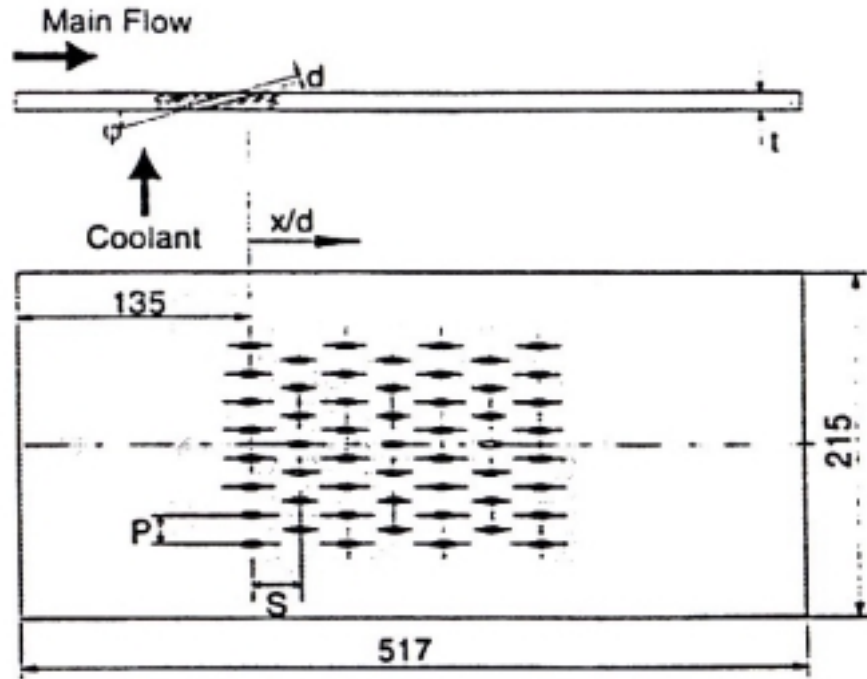


Figure A-17b Schematic of Gritsch et al. (1998) combustor model.

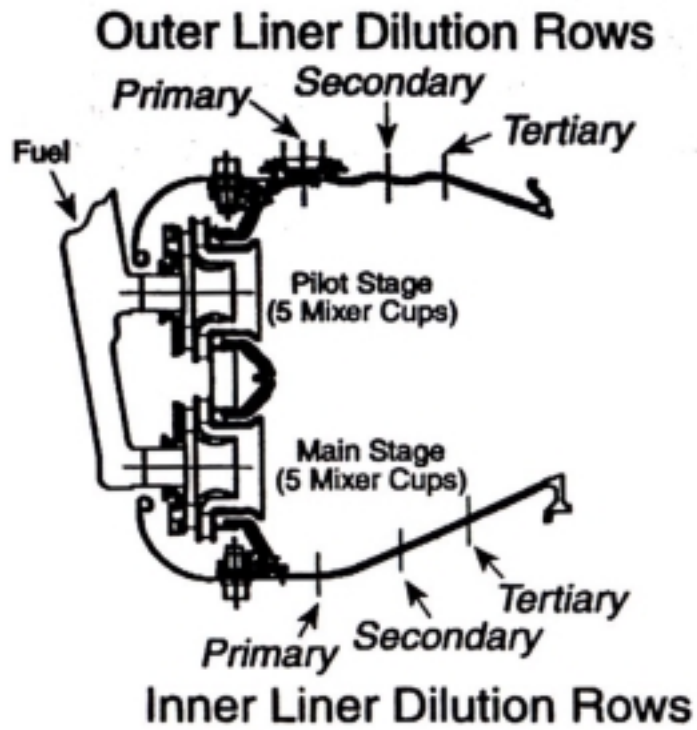


Figure A-18 Schematic of Gulati et al. (1995) combustor.

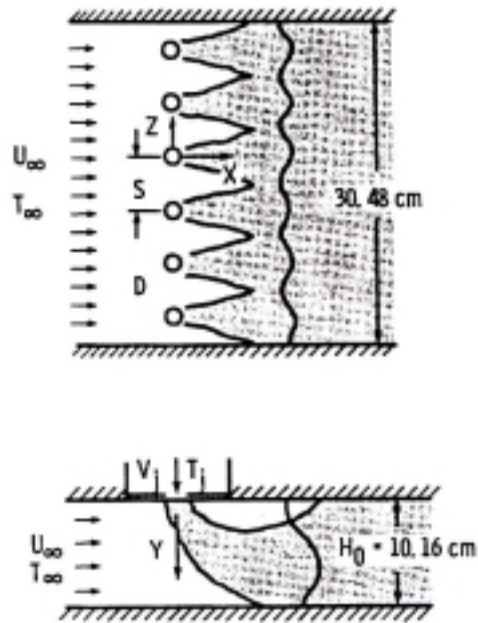


Figure A-19a Schematic of Holdeman (1993) combustor model.

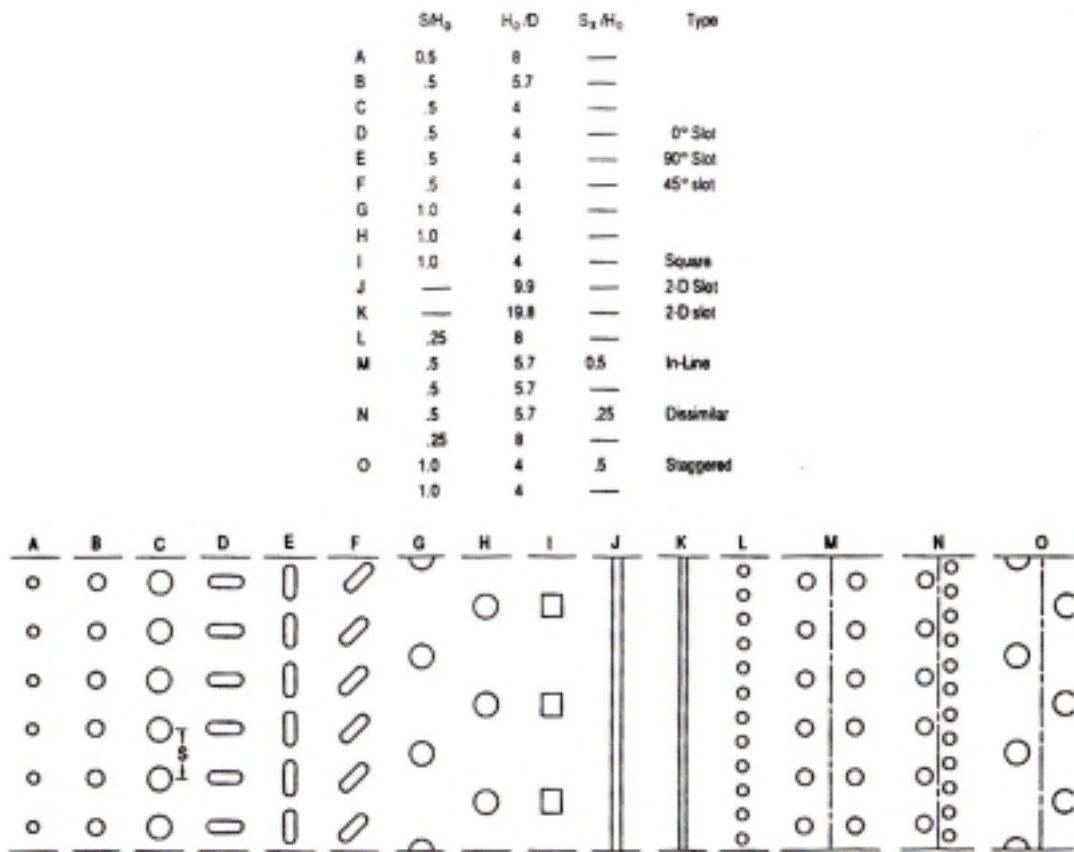


Figure A-19b Schematic of Holdeman (1993) orifice configurations

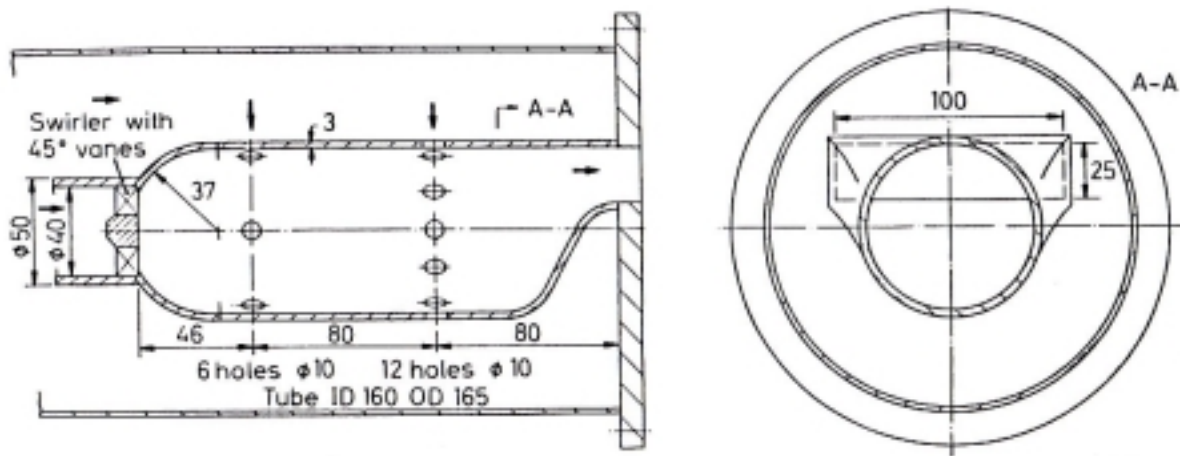


Figure A-20 Schematic of Koutmos and McGuirk (1989) combustor model.

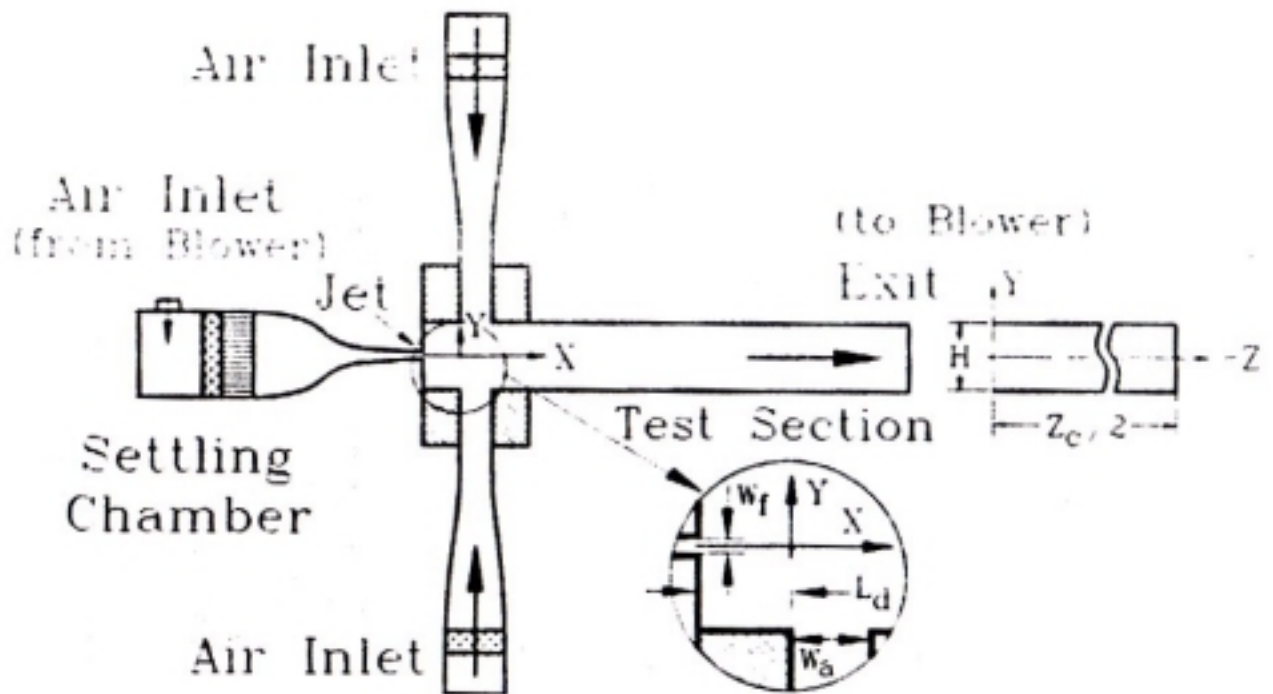


Figure A-21 Schematic of Liou and Wu (1992) combustor model.

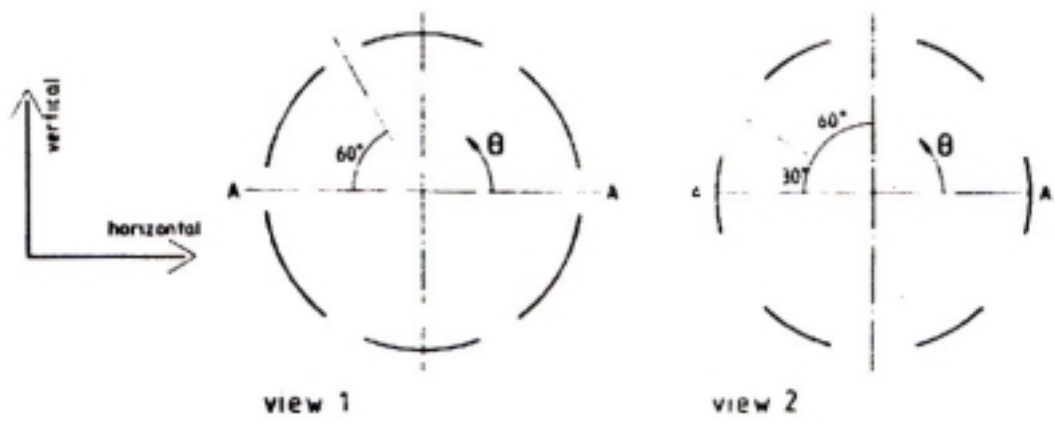
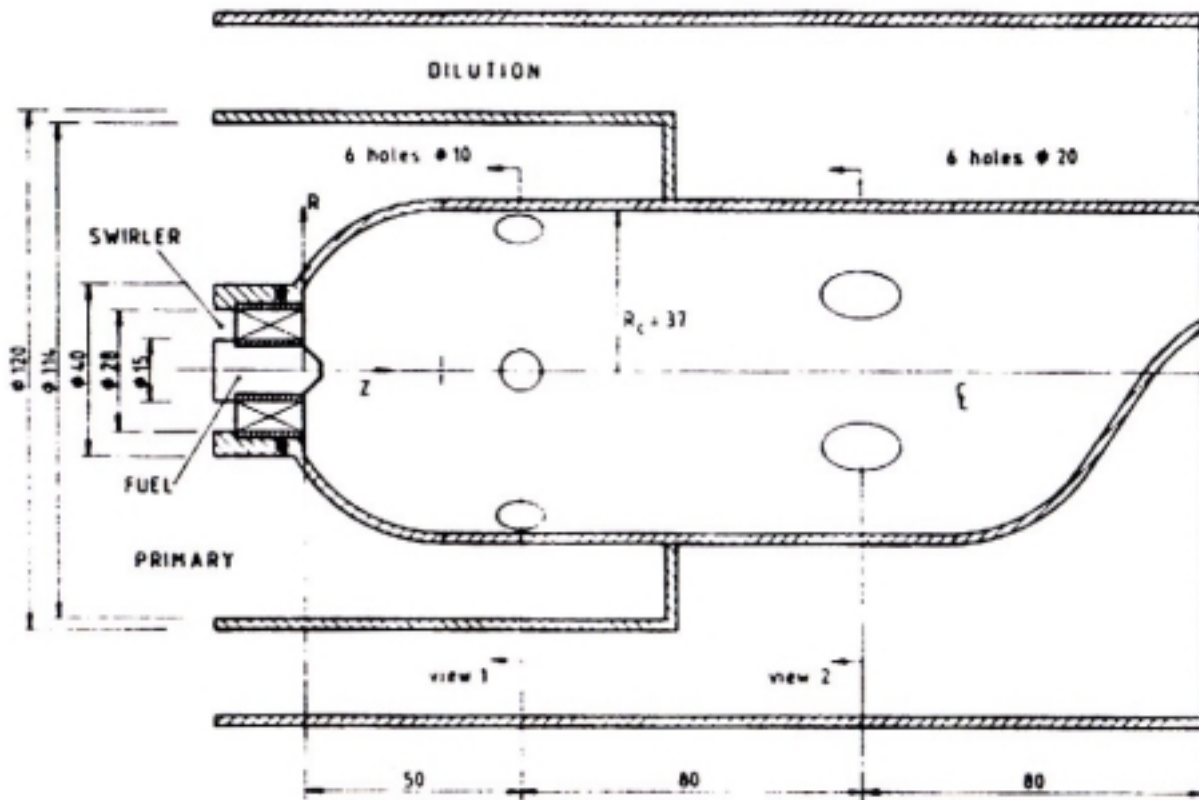
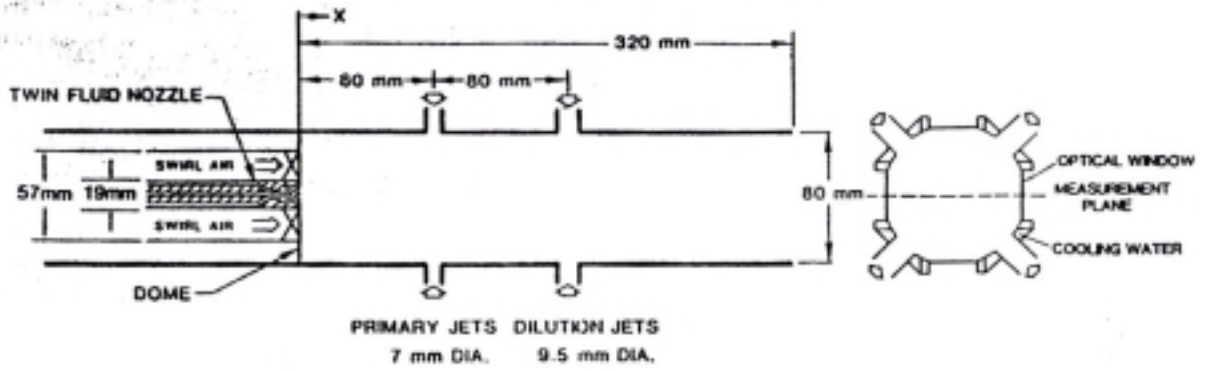
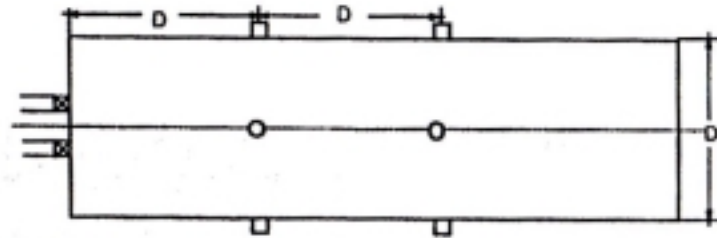


Figure A-22 Schematic of McGuirk and Palma (1993) combustor model.

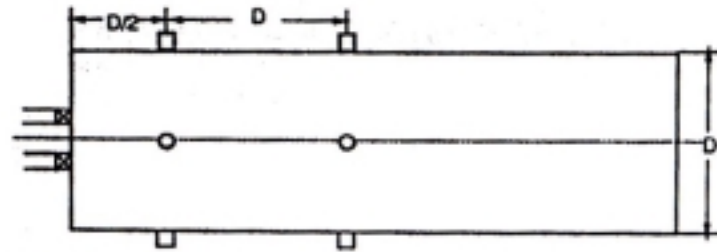
a) The Wall Jet Can Combustor (WJCC).



b) Module 1.



c) Module 2.



d) Module 3.

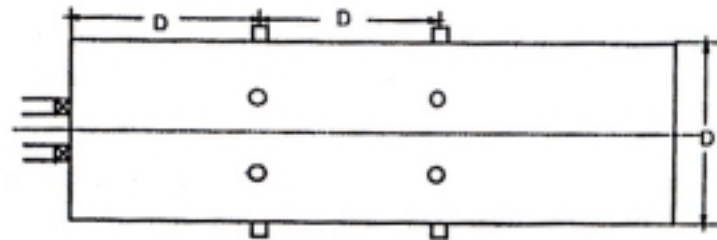


Figure A-23 Schematic of Richards and Samuelsen (1992) combustor model.

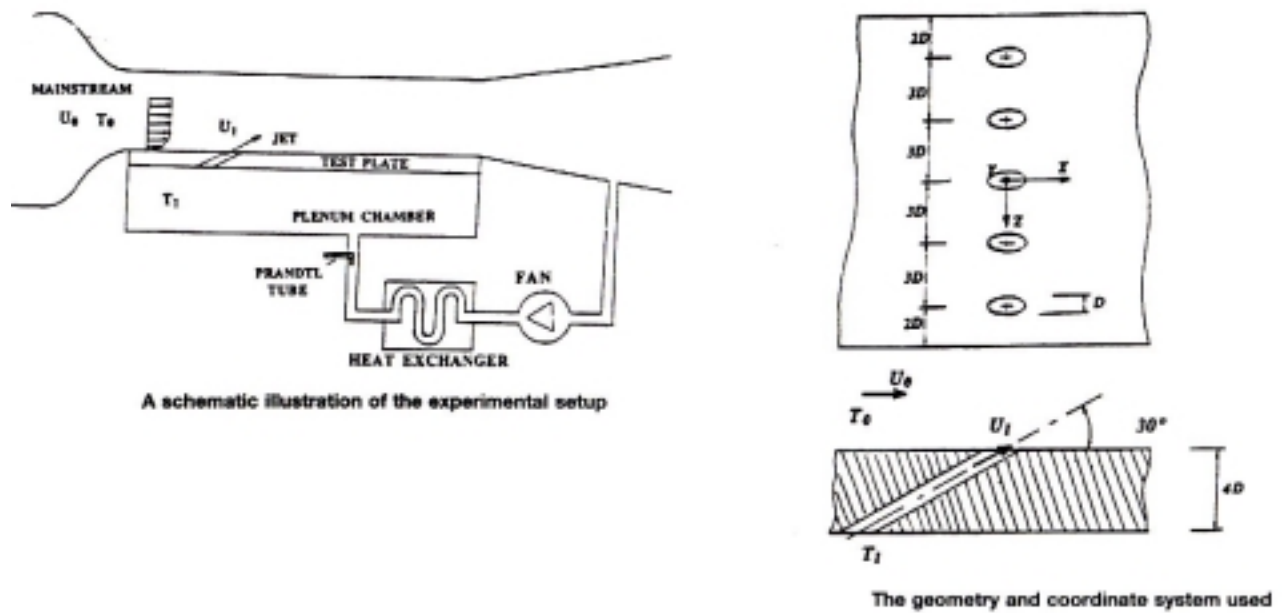


Figure A-24 Schematic of Rydholm (1998) combustor model.

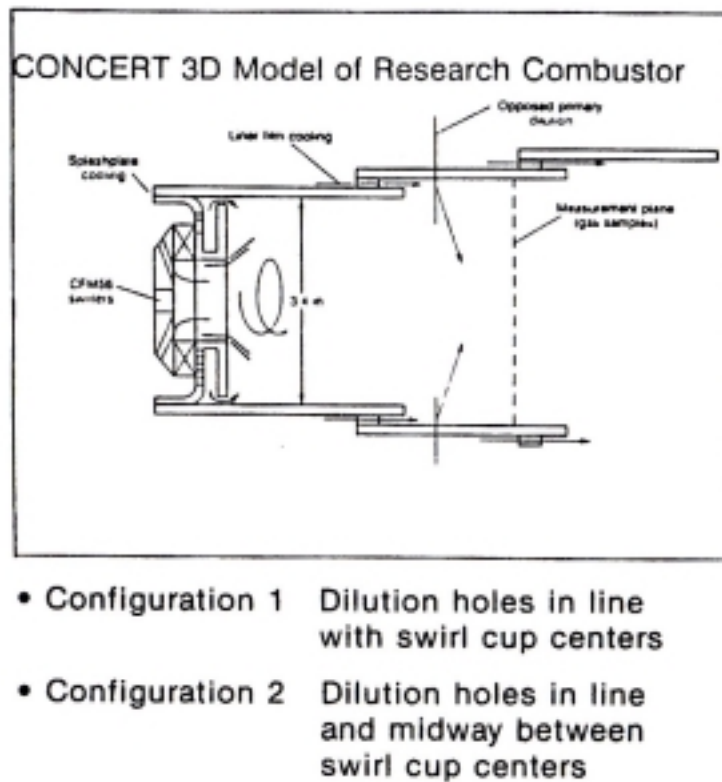


Figure A-25 Schematic of Shyy et al. (1989) combustor model.

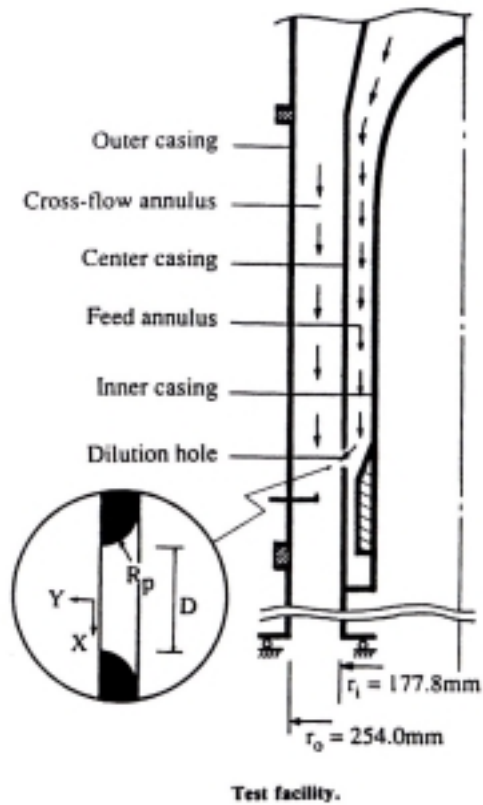
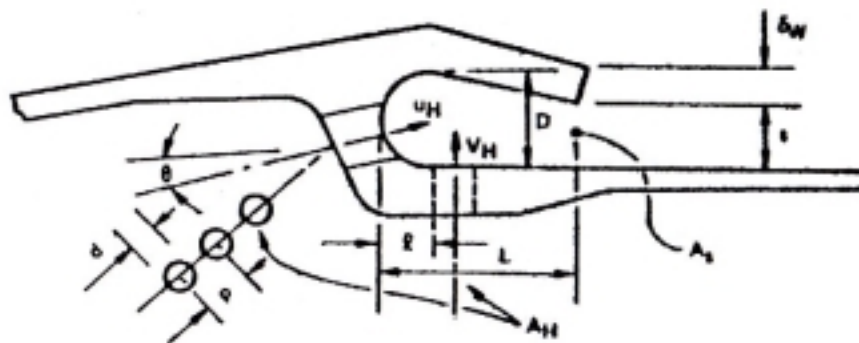


Figure A-26 Schematic of Stevens and Carrotte (1990) combustor model.



- | | |
|--|--|
| δ_W - Lip Trailing-Edge Thickness | θ - Angle of Axial Metering Holes to Cooled Wall |
| s - Slot Outlet Height | D - Height of Mixing Chamber at Coolant Inlet |
| A_s - Slot Outlet Area, (Geometric) | d - Metering Port Diameter |
| u_H - Coolant Velocity from Axial Holes | p - Metering Port Pitch, (Axial/Normal, Indexed $n/2$) |
| v_H - Coolant Velocity from Normal Holes | L - Mixing Chamber Length |
| A_H - Total Coolant Metering Area, (Geometric) | R - Downstream Position of Leading Edge of Metering Port in Mixing Chamber |

Figure A-27 Schematic of Sturgess (1980) combustor model.

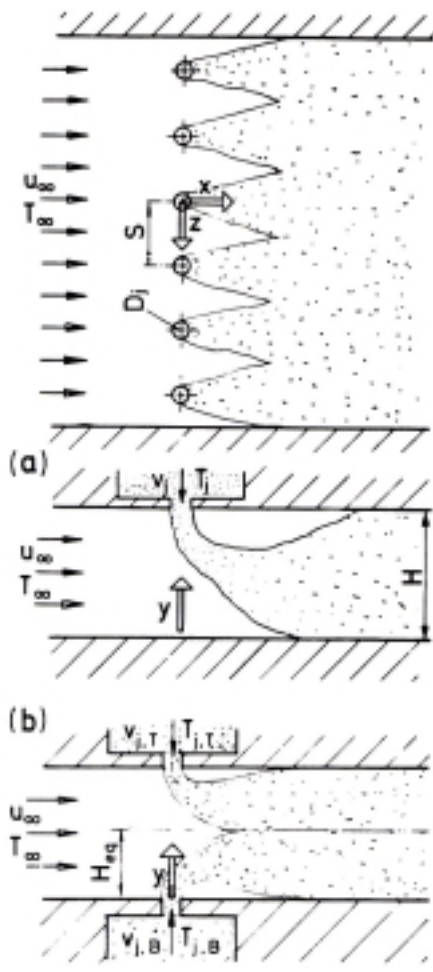


Figure A-28a Schematic of Wittig et al.(1984) combustor model.

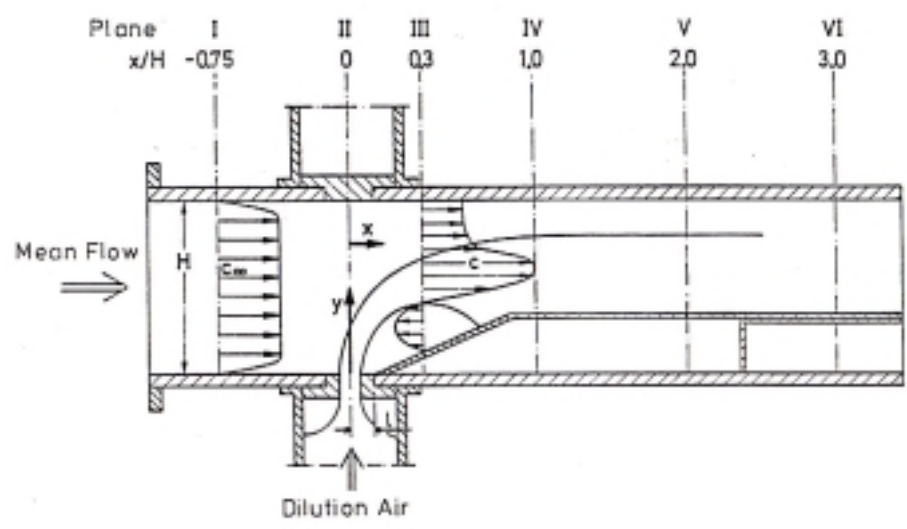


Figure A-28b Schematic of Wittig et al. (1987) combustor model.

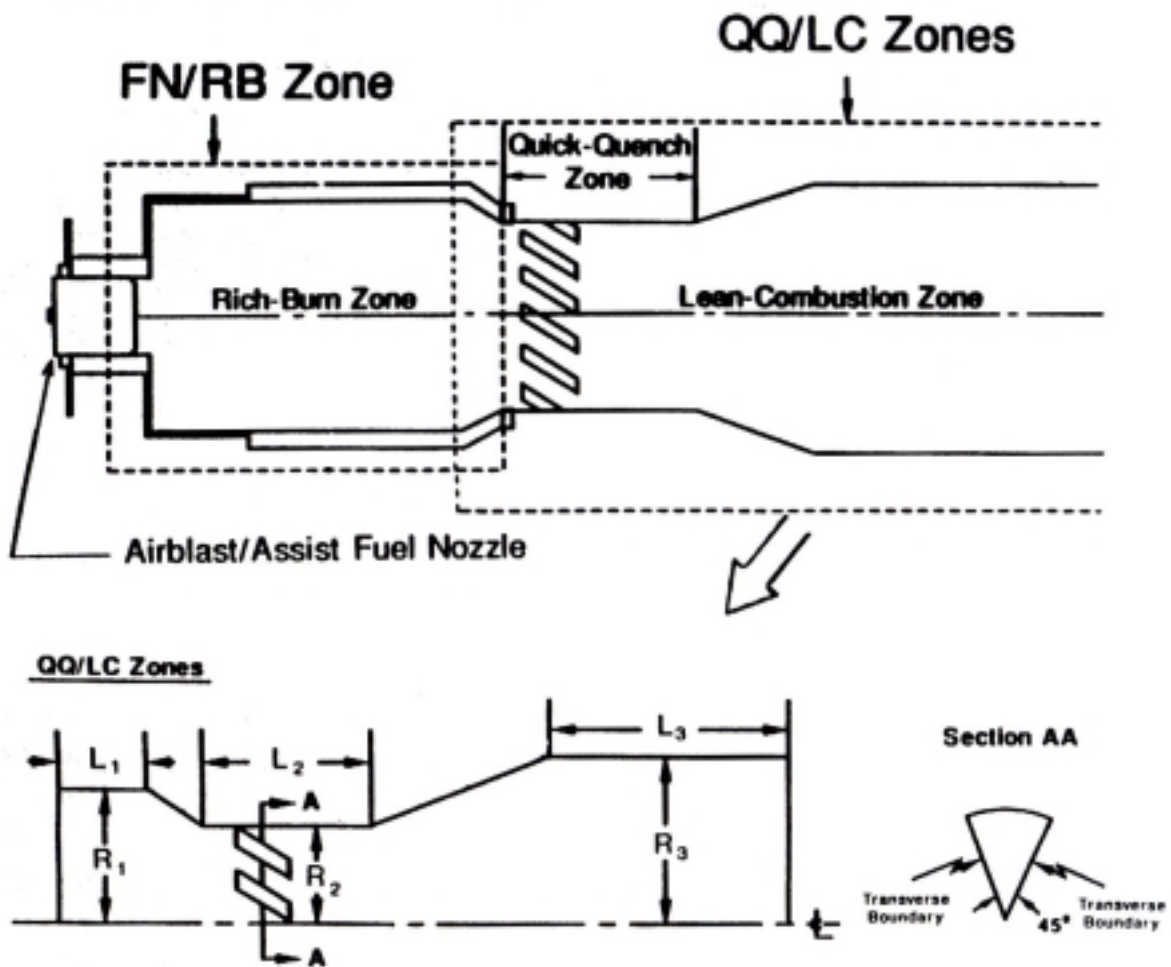


Figure A-29 Schematic of Yang and Cline (1994) combustor model.

Appendix B

Verification of Total Mass Flow Rate Exiting the Engine Combustor

The following flow field analysis of the turbine vane cascade is presented to verify the total mass flow rate exiting the engine combustor per sector.

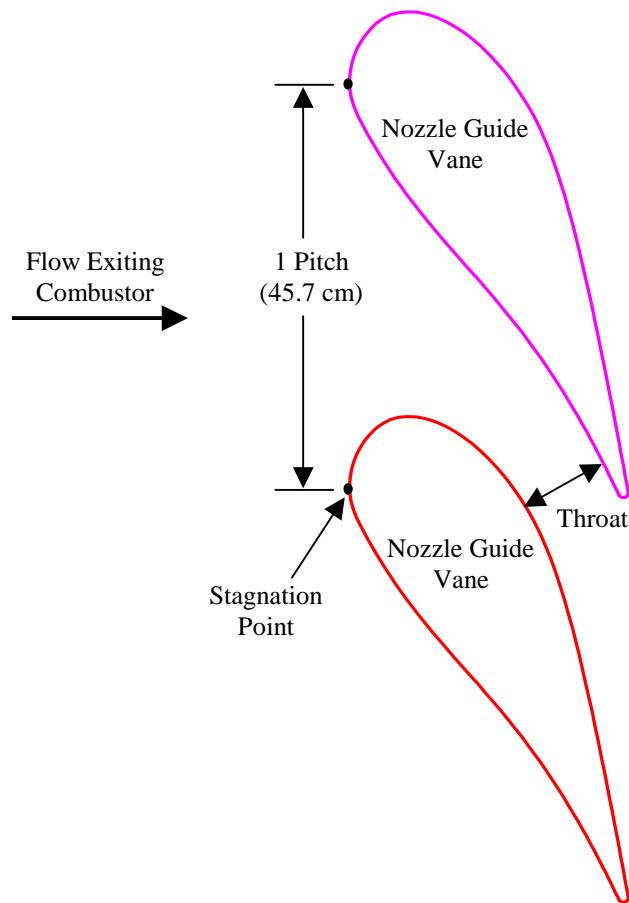
- Mass flow rate through two adjacent nozzle guide vanes, $\dot{m} = \rho_{\text{throat}} V_{\text{throat}} A_{\text{throat}}$

A_{throat} = minimum cross-sectional area between adjacent nozzle guide vanes

ρ_{throat} = density of air at the throat of the nozzle guide vane passage

V_{throat} = velocity of air at the throat of the nozzle guide vane passage

- Schematic of two adjacent nozzle guide vanes



- Geometric parameters
 - Nozzle Guide Vane Pitch = 5.08 cm
 - Nozzle Guide Vane Span = 6.11 cm

- Nozzle Guide Vane Inlet Conditions
 - Inlet Area, $A_{inlet} = (\text{Pitch}) \times (\text{Span})$
 $= (5.08 \text{ cm}) \times (6.11 \text{ cm}) = 31.04 \text{ cm}^2$
 $= 0.003104 \text{ m}^2$
 - Inlet Mach Number, $Ma_{inlet} = 0.1175$
 - Ratio of Specific Heats, $\gamma = 1.2826$
 - Total Temperature, $T_0 = 1666\text{K}$
 - Total Pressure, $P_0 = 1.0342 \times 10^6 \text{ Pa}$
- According to Compressible Fluid Dynamics by B.K. Hodge and Keith Koenig, for a convergent nozzle with these flow conditions $\frac{A_{inlet}}{A^*} = 5.0300$, where A^* represents the location (nozzle throat area) of the nozzle where $Ma = 1$. The flow conditions can then be determined at the nozzle throat.
 - Throat Area, $A^* = 6.16895 \times 10^{-4} \text{ m}^2$
 - Throat Static Temperature, $T_{th} = \frac{T_{0_{th}}}{1 + \frac{\gamma-1}{2} Ma_{th}^2} = 1459.7 \text{ K}$
 - Throat Static Pressure, $P_{th} = \frac{P_{0_{th}}}{\left(1 + \frac{\gamma-1}{2} Ma_{th}^2\right)^{\frac{\gamma}{\gamma-1}}} = 567,664 \text{ Pa}$
 - Throat Density, $\rho_{th} = \frac{P_{th}}{RT_{th}} = \frac{567,664\text{Pa}}{\left(292.43 \frac{\text{J}}{\text{kg} - \text{K}}\right)(1459.7\text{K})} = 1.33 \text{ kg/m}^3$
 - Throat Velocity, $V_{th} = Ma_{th} \sqrt{\gamma RT_{th}} = 739.97 \text{ m/s}$
 - Mass Flow Rate at Throat, $\dot{m}_{th} = (1.33 \text{ kg/m}^3)(739.97 \text{ m/s})(6.16895 \times 10^{-4} \text{ m}^2)$
 $= 0.607 \text{ kg/s}$
 - Total Mass Flow Rate per Sector, $\dot{m}_{sector} = 2 (\dot{m}_{th}) = 2 (0.607 \text{ kg/s})$
 $= 1.21 \text{ kg/s}$
 (This is in agreement with calculation presented in section 3-2)

Appendix C

Detailed Flow Calculations within Engine Combustor

- Determining the Mainstream Acceleration Parameter
 - Given pressure information:

Total pressure of mainstream at exit, $P_{0_{exit}} = 1,034,200$ Pa

Total pressure of coolant supply, $P_{0_{sup ply}} = 1,043,973$ Pa (Inner Diameter Liner)

$P_{0_{sup ply}} = 1,042,577$ Pa (Outer Diameter Liner)

** Since the coolant supply pressures are very similar for the inner and outer diameter liners (less than 0.15% difference) the following calculations are presented only for the inner diameter liner.

- Static pressure distribution of mainstream is determined from the given Mach number distribution of the mainstream and the assumption of constant axial total pressure.

$$P_{\infty} = \frac{P_{0_{\infty}}}{\left(1 + \frac{\gamma - 1}{2} Ma_{\infty}^2\right)^{\frac{\gamma}{\gamma - 1}}}$$

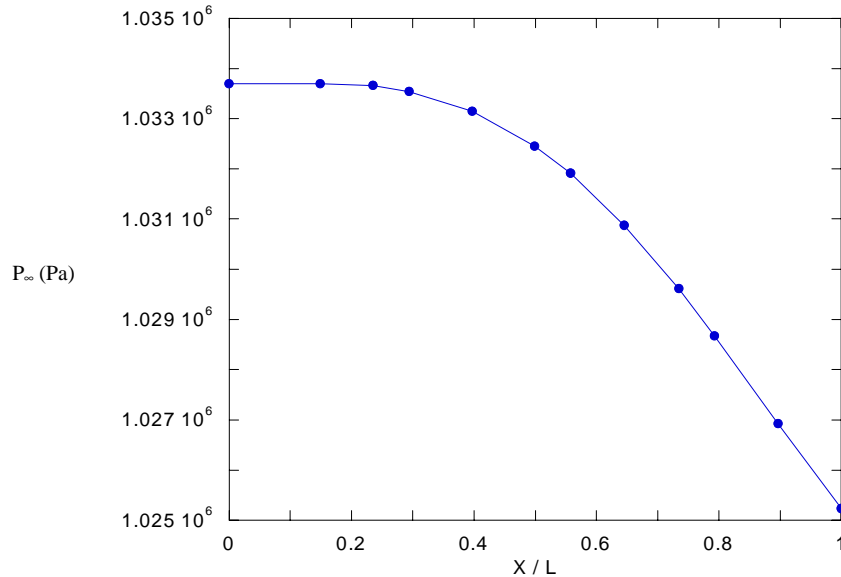


Figure B-1 Graph of the static pressure distribution in the mainstream.

- Static temperature at the combustor exit is determined.

$$T_{\infty_{exit}} = \frac{T_{0_{\infty_{exit}}}}{1 + \frac{\gamma-1}{2} Ma_{\infty_{exit}}^2} = \frac{1666K}{1 + \frac{1.2826-1}{2} (0.1175)^2} = 1662.8 K$$

- The static temperature of the jet coolant at the exit of the film cooling holes at the trailing edge of the fourth liner panel (assuming negligible difference in R between coolant and mainstream)

$$P_{jet_{exit}} = \rho_{jet_{exit}} \times R \times T_{jet_{exit}} \quad \text{and} \quad P_{jet_{exit}} = P_{\infty_{exit}} = \rho_{\infty_{exit}} \times R \times T_{\infty_{exit}}$$

$$\therefore T_{jet_{exit}} = \frac{\rho_{\infty_{exit}} T_{\infty_{exit}}}{\rho_{jet_{exit}}} = \frac{1662.8K}{2.3} = 722.9K$$

- The density of jet coolant near the combustor exit (trailing edge of fourth liner panel).

$$\rho_{jet_{exit}} = \frac{P_{jet_{exit}}}{RT_{jet_{exit}}} = \frac{P_{\infty_{exit}}}{RT_{jet_{exit}}} = \frac{1,025,093Pa}{\left(292.43 \frac{J}{kg \cdot K}\right)(722.9K)} = 4.85 \text{ kg/m}^3$$

Density of coolant supply to all four liner panels:

$$\rho_{jet} = 4.85 \text{ kg/m}^3$$

- The Mach number of film-cooling jets can then be calculated.

$$Ma_{jet} = \left[\left(\left(\frac{P_{0_{sup\ ply}}}{P_{\infty}} \right)^{\frac{\gamma-1}{\gamma}} - 1 \right) \frac{2}{\gamma-1} \right]^{0.5}$$

Example, at trailing edge of the fourth liner panel the jet Mach number is:

$$Ma_{jet} = \left[\left(\left(\frac{1,043,973Pa}{1,025,093Pa} \right)^{\frac{1.2826-1}{1.2826}} - 1 \right) \frac{2}{1.2826-1} \right]^{0.5} = 0.169$$

- The total temperature of film-cooling jets can then be determined.

$$T_{0_{jet}} = T_{jet} \left(1 + \frac{\gamma-1}{2} Ma_{jet}^2 \right) = \text{constant for all film cooling jets in all liner panels}$$

Example, at trailing edge of the fourth liner panel the total temperature of the film-cooling jet is:

$$T_{0_{jet}} = 722.9K \left(1 + \frac{1.2826-1}{2} (0.169)^2 \right) = 725.8 \text{ K}$$

- Static temperatures of the film-cooling jets can then be calculated.

$$T_{jet} = \frac{T_{0_{jet}}}{1 + \frac{\gamma-1}{2} Ma_{jet}^2}$$

- The distribution of mainstream static temperature is then determined.

$$\text{From previously, } T_{\infty} = T_{jet} \frac{\rho_{jet}}{\rho_{\infty}}$$

- The mainstream velocity distribution is then determined.

$$U_{\infty} = M_{\infty} \sqrt{\gamma R T_{\infty}}$$

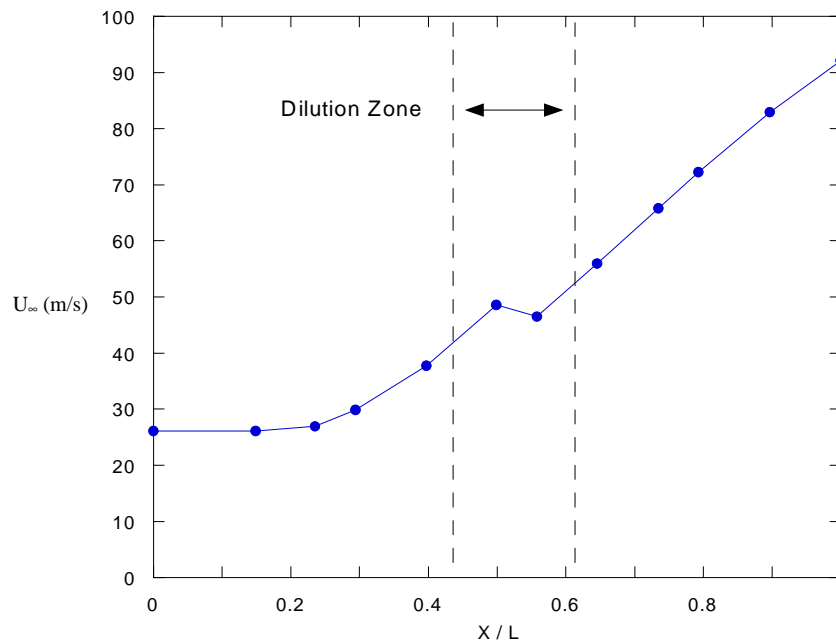


Figure B-2 Graph of the mainstream velocity distribution.

- The mainstream acceleration parameter is obtained by curve fitting a second order polynomial to the velocity distribution and evaluating K.

$$K = \frac{v}{U_{\infty}^2} \frac{dU_{\infty}}{dx}$$

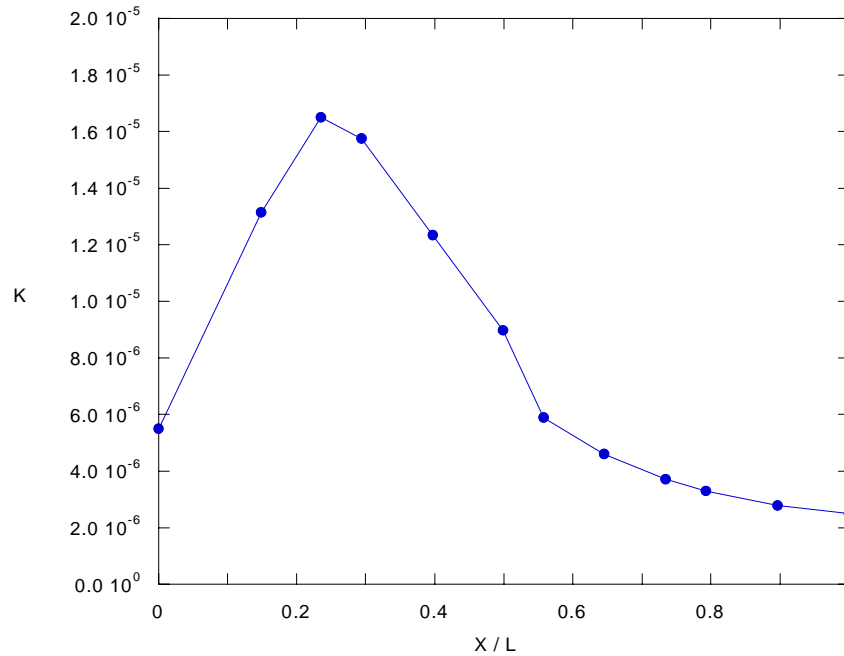


Figure B-3 Graph of the mainstream acceleration parameter.

- Determining the momentum flux ratios and number of film-cooling holes for the inner diameter liner
 - The average density of the mainstream is determined over each liner panel.

$$\text{Liner panel 1: } \rho_{\infty} = \frac{4.85 \text{ kg/m}^3}{3.3} = 1.47 \text{ kg/m}^3$$

$$\text{Liner panel 2: } \rho_{\infty} = \frac{4.85 \text{ kg/m}^3}{3.3} = 1.47 \text{ kg/m}^3$$

$$\text{Liner panel 3: } \rho_{\infty} = \frac{4.85 \text{ kg/m}^3}{2.3} = 2.11 \text{ kg/m}^3$$

$$\text{Liner panel 4: } \rho_{\infty} = \frac{4.85 \text{ kg/m}^3}{2.3} = 2.11 \text{ kg/m}^3$$

- The theoretical jet velocities may be determined according to Appendix D.

$$U_{jet,theo} = \sqrt{\frac{2}{\rho_{jet}}(P_{0,supply} - P_{\infty})}$$

An average theoretical jet velocity is then determined per liner panel by averaging the theoretical jet velocities over each liner panel

- Mass flow rates through each liner panel:

$$\text{Panel 1} = 1.5 \% \text{ of } \dot{m}_{exit} = 0.015 \times 1.214 \text{ kg/s} = 0.01821 \text{ kg/s}$$

$$\text{Panel 2} = 3.5 \% \text{ of } \dot{m}_{exit} = 0.035 \times 1.214 \text{ kg/s} = 0.04249 \text{ kg/s}$$

$$\text{Panel 3} = 3.5 \% \text{ of } \dot{m}_{exit} = 0.035 \times 1.214 \text{ kg/s} = 0.04249 \text{ kg/s}$$

$$\text{Panel 4} = 1.5 \% \text{ of } \dot{m}_{exit} = 0.015 \times 1.214 \text{ kg/s} = 0.01821 \text{ kg/s}$$

- Given coolant to mainstream density ratio, $\frac{\rho_{jet}}{\rho_{\infty}}$, for each liner panel:

$$\text{Panel 1} = 3.3$$

$$\text{Panel 2} = 3.3$$

$$\text{Panel 3} = 2.3$$

$$\text{Panel 4} = 2.3$$

- The required total film-cooling hole area per liner panel is then determined.

$$A_{holes} = \frac{\dot{m}_{panel}}{C_d V_{jet,theo} \rho_{jet}} \quad \text{where } C_d \text{ is the discharge coefficient of the film-cooling}$$

holes given to be 0.81 for all film-cooling holes in all four liner panels.

- Determining the number of film-cooling holes in each liner panel:

$$D = 8.38 \text{ cm}$$

$$N = \frac{A_{holes}}{\frac{\pi}{4} D^2}$$

$$\text{Panel 1: } N = 129$$

$$\text{Panel 2: } N = 292$$

$$\text{Panel 3: } N = 266$$

$$\text{Panel 4: } N = 100$$

- The actual average jet velocities per liner panel are determined:

$$U_{jet} = \frac{\dot{m}_{panel}}{A_{holes} \rho_{jet}}$$

Panel 1: $U_{jet} = 52.77$ m/s

Panel 2: $U_{jet} = 54.37$ m/s

Panel 3: $U_{jet} = 59.66$ m/s

Panel 4: $U_{jet} = 67.83$ m/s

- The average momentum flux ratios for each liner panel are determined:

$$I = \frac{\rho_{jet} U_{jet}^2}{\rho_{\infty} U_{\infty}^2}$$

Panel 1: $I = 13$

Panel 2: $I = 7$

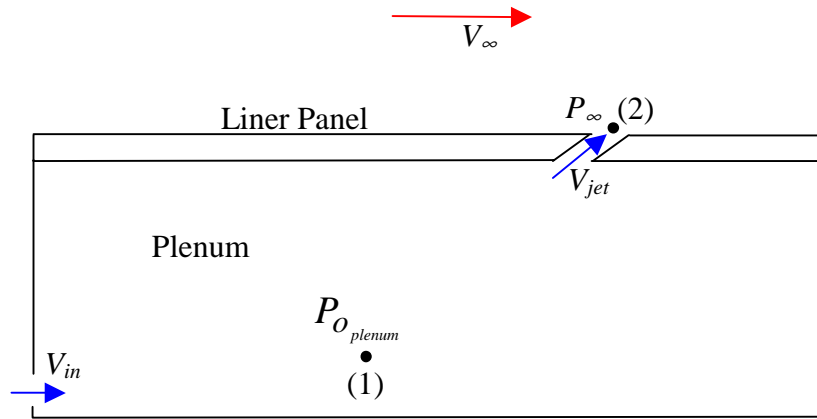
Panel 3: $I = 3$

Panel 4: $I = 1.5$

- The above procedure can be repeated for the outer diameter liner flow field information.

Appendix D

Determining the Mass Flow Through the Plenums



- Under the assumptions of steady, inviscid, incompressible flow along a streamline, using the Bernoulli equation from (1) to (2) yields the following result:

$$P_1 + \frac{1}{2} \rho V_1^2 + \rho g h_1 = P_2 + \frac{1}{2} \rho V_2^2 + \rho g h_2 \quad (D-1)$$

- Assuming negligible changes in density and elevation from (1) to (2) the above equation reduces to the following:

$$P_{o\ plenum} + \frac{1}{2} \rho V_1^2 = P_{\infty} + \frac{1}{2} \rho V_{jet}^2 \quad (D-2)$$

- Solving for the jet velocity yields the following:

$$V_{jet} = \sqrt{\frac{2}{\rho} (P_{o\ plenum} - P_{\infty})} \quad (D-3)$$

- The theoretical mass flow rate then becomes the following:

$$\dot{m}_{theoretical} = \rho V_{jet} A_{jet} \quad (D-4)$$

where A_{jet} = area of hole that jet passes through

Appendix E

Experimental Uncertainties

- Velocity Measurements Made with Pitot-Tube

$U_{ave} = 7.045 \text{ m/s}$					
Variable	Value	Total Uncertainty	Partial	U*P	(U*P)^2
$\rho \text{ (kg/m}^3\text{)}$	1.1	-	-	-	-
Po - Ps (Pa)	27.300	0.657	0.129	0.085	0.007
				U _v (m/s)	0.0848
				% Uncertainty	1.2

Example of Precision uncertainty in velocity measurement (Velocity taken at the slot typical of U_{ave})		
Number	Po - Ps (" H ₂ O)	
1	0.1096	
2	0.1085	
3	0.1093	
4	0.1088	
5	0.1091	
Average	0.10906	
Std. Dev.	0.000428	
Uncertainty	0.000838	Inches H ₂ O
Uncertainty	0.209	Pascals

- Total Pressure Measurements

High ΔP		0.1173			
Variable	Value	Uncertainty	Partial	U*P	(U*P)^2
ρ (kg/m ³)	1.1	-	-	-	-
U_{ave} (m/s)	7.045	0.084751627	-0.0332877	-0.002821186	7.9591E-06
Po (Pa)	30.015345	0.374920815	0.03663324	0.013734564	0.00018864
Po-msave (Pa)	26.8145385	0.374920815	-0.03663324	-0.013734564	0.00018864
				$U_{\Delta P}$	0.0196
				% Uncertainty	16.7

Small ΔP		-0.5188			
Variable	Value	Uncertainty	Partial	U*P	(U*P)^2
ρ (kg/m ³)	1.1	-	-	-	-
U_{ave} (m/s)	7.045	0.0848	0.1473	0.0125	0.0002
Po (Pa)	12.65	0.3749	0.0366	0.0137	0.0002
Po-msave (Pa)	26.81	0.3749	-0.0366	-0.0137	0.0002
				$U_{\Delta P}$	0.0231
				% Uncertainty	4.5

- Temperature Measurements

High η		0.980				
Variable	Value ($^{\circ}\text{C}$)	Uncertainty ($^{\circ}\text{C}$)	Partial	U*P	(U*P) ²	
T_{∞}	29.06	0.2	0.0034945	0.0006989	0.0000005	
T_{aw}	23.32	0.173	-0.1706485	-0.0294987	0.0008702	
T_{jet}	23.2	0.2	0.1671540	0.0334308	0.0011176	
					U_{η}	0.0446
					% Uncertainty	4.6

Low η		0.227				
Variable	Value ($^{\circ}\text{C}$)	Uncertainty ($^{\circ}\text{C}$)	Partial	U*P	(U*P) ²	
T_{∞}	29.06	0.2	0.1319177	0.0263835	0.0006961	
T_{aw}	27.73	0.173	-0.1706485	-0.0294987	0.0008702	
T_{jet}	23.2	0.2	0.0387308	0.0077462	0.0000600	
					Ueta	0.0403
					% Uncertainty	17.8

High θ		0.939				
Variable	Value ($^{\circ}\text{C}$)	Uncertainty ($^{\circ}\text{C}$)	Partial	U*P	(U*P) ²	
T_{∞}	29.06	0.2	0.010483523	0.002096705	0.000004396	
T	23.56	0.2	-0.170648464	-0.034129693	0.001164836	
T_{jet}	23.2	0.2	0.160164941	0.032032988	0.001026112	
					U_{θ}	0.046854503
					% Uncertainty	5.0

Low θ		0.257				
Variable	Value ($^{\circ}\text{C}$)	Uncertainty ($^{\circ}\text{C}$)	Partial	U*P	(U*P) ²	
T_{∞}	28.85	0.2	0.13922204	0.027844408	0.000775311	
T	27.48	0.2	-0.187265918	-0.037453184	0.001402741	
T_{jet}	23.51	0.2	0.048043878	0.009608776	0.000092329	
					U_{θ}	0.047648511
					% Uncertainty	18.6

- Turbulence Measurements

Turbulence Measurements			
Example Data Sets at $y / W = 0.0$			
Number	U (m/s)	U_{rms} (m/s)	Tu
1	7.0679	1.0631	15.04
2	7.1559	1.0775	15.058
3	7.2842	1.0317	14.163
4	7.2072	1.0369	14.387
5	7.2148	1.0437	14.466
6	7.1459	1.05106	14.708
7	7.1843	1.0892	15.161
8	7.2268	1.0191	14.102
Average	7.19	1.05	14.64
Std Dev	0.06442	0.02375	
1.96 sigma	0.12627	0.04655	
	% Uncertainty in U_{rms}	4.4	
		Uncertainty in Tu	0.00746
		% Uncertainty in Tu	5.1

- Integral Time and Length Scale Measurements

Integral Time and Length Scale Test		
Example Data Sets at $y / W = 0.0$		
Number	Integral Time Scale (s)	Integral Length Scale (m)
1	0.01076	0.07635
2	0.01020	0.07194
3	0.00976	0.06856
4	0.00962	0.06702
5	0.00838	0.05924
6	0.01007	0.06951
7	0.00965	0.06724
8	0.00916	0.06247
Average	0.00970	0.06779
Std Dev	0.00071	
1.96 Sigma	0.00140	
% Uncertainty	14.4	
	Uncertainty	0.00992
	% Uncertainty	14.6

Vita

Michael Barringer

Michael D. Barringer was born in Newport News, Virginia. He began his engineering education at Virginia Polytechnic Institute and State University in the fall of 1995. Michael graduated from Tech with a Bachelor of Science degree in Mechanical Engineering in May, 1999. During his education at Virginia Tech he spent two summers at the NASA Langley Research Center working as an intern in the Structural Acoustics Branch under the direction of Dr. Stephen Rizzi and one summer working in the mechanical engineering department at Virginia Tech as a heat transfer laboratory technician under the direction of Dr. Elaine Scott. He continued his education as a graduate student at Virginia Tech by working in the Experimental and Computational Convection Laboratory (VT ExCCL) under the direction of Dr. Karen Thole and received his Master of Science degree in mechanical engineering in the fall of 2001. Michael is currently pursuing his doctorate degree in mechanical engineering at Virginia Tech.